Design and construction of electroconductive ink based textile sensors for sensing weak bio-signals

A thesis submitted to the University of Manchester for the degree of

Doctor of Philosophy

In the faculty of Science and Engineering

2018

Yuhua WANG

School of Material

TABLE OF CONTENTS

Table of Contents 2

List of Figures 6

List of Tables 12

List of Acronyms 13

Abstract 15

Declaration 16

Copyright Statement 17

Acknowledgement 18

Chapter One: Introduction 19

1.1 Background 19

1.2 Problem definition 20

1.3 Research aim and objectives 21

1.4 The scope of the research 22

1.5 The layout of this thesis 22

Chapter Two: Literature Review 24

2.1 Introduction 24

2.2 Bio-signals and cardiorespiratory monitoring 24

2.2.1 Methods of cardiorespiratory monitoring 25

2.2.2 Smart textile materials for sensory applications 28

2.3 Portable/wearable cardiorespiratory sensors 30

2.3.1 Inductive cardiorespiratory sensor 30

2.3.2 Fibre optic cardiorespiratory sensors 33

2.3.3 Capacitive/piezoelectric material based cardiorespiratory sensors 35

2.3.4 Piezo-resistive material based cardiorespiratory sensors 38

2.4 Electroconductive inks 42

2.4.1 Metallic electroconductive inks 43

2.4.2 Carbon/graphene-based electroconductive ink 45
2.4.3 Impregnation methods 46
2.4.4 Sintering process 54
2.5 Summary 57
Chapter Three: Methodology 58
3.1 Introduction 58
3.2 The operational principle of nonwoven fabric based piezo-resistive pressure sensor 58
3.3 Materials and sample preparation 59
3.3.1 List of the fabric materials 59
3.3.2 Thermally bonded nonwoven materials 62
3.3.3 Preparation of the nanoscale silver particle-based electroconductive ink 65
3.3.4 Dip-coating impregnation and thermal sintering 68
3.3.5 Piezo-resistive sensor design and fabrication 70
3.3.6 Piezo-resistive nonwoven fabric based sensors 72
3.4 Test procedures 73
3.4.1 Measurement of electrical resistance 73
3.4.2 Characterisation of nanoscale silver particle-based piezo-resistive nonwoven materials 78
3.4.3 Cardiorespiratory signal capturing 80
3.4.4 Investigation of the reliability and accuracy of the nonwoven piezo-resistive sensor 83
3.4.5 Response and recovery time of the piezo-resistive nonwoven sensor 83
3.5 Summary 83
Chapter Four: Microscopy analysis of the nanoscale silver particle-based piezo-resistive nonwoven materials 84
4.1 Introduction 84

4.2 Nonwoven materials with a smooth surface structure 84
4.2.1 Thin nonwoven materials (sample A and B) 84
4.2.2 Thick nonwoven materials (sample C and E) 87
4.2.3 Laboratory-made thermally bonded nonwoven fabrics (sample F to I) 91
4.3 Nonwoven material with an embossed dot pattern (sample D) 94
4.4 Knitted fabric and woven fabric 98
4.5 Summary 100
Chapter Five: Characterisation and optimisation of the nanoscale silver particle-based piezo-resistive sensor 101
5.1 Introduction 101
5.2 Characterisation of nanoscale silver particle-based piezo-resistive nonwoven materials 101
5.2.1 Preliminary tests 102
5.2.2 Electromechanical characterisations 109
5.3 Cardiorespiratory signals capturing 122
5.3.1 Respiratory signal capturing 122
5.3.2 Cardiac signal capturing 132
5.4 Investigation of the reliability and accuracy of the nonwoven piezo-resistive sensor 135
5.4.1 Heartbeat signal matching 139
5.4.2 Breathing signal matching 142
5.4.3 Response and recovery time of the piezo-resistive nonwoven sensor 144
5.5 Development of a nonwoven sensor with directional electroconductive monofilament/yarns and its empirical modelling 145
5.5.1 Design and fabrication of the nonwoven piezo-resistive sensor with directional monofilaments/yarns 145
5.5.2 Nanoscale silver particle-based electroconductive ink impregnation 147

5.5.3 Electromechanical characterisation and cardiorespiratory signal acquisition……148

5.5.4 Empirical modelling……155

5.6 Summary……161

Chapter Six: Conclusions and future work……163

6.1 Conclusions……163

6.2 Recommendations for future work……166

References……169

Appendix A: Cyclic compressive loading……191

Appendix B: Hysteresis analysis of sample D, E, G, J and K……194

Appendix C: RTD analysis……196

Appendix D: Respiratory signal capturing……199

Appendix E: Cardiac signal capturing……201

Appendix F: Cardiorespiratory captured with bandpass filter……203

Appendix G: Matlab programme for cardiorespiratory signal peak justification and validation……207

Appendix H: Matlab programme for creating the empirical models……209

Appendix I: Data points used to calculate empirical models and their verifications……210

The final word count, including footnotes and endnotes: 32,337.

LIST OF FIGURES

Figure 2-1. Possible cardiorespiratory monitoring methods. 25

Figure 2-2. Differences and similarities in waveforms acquired from different BCG systems.[34] 26

Figure 2-3. ECG of a heart in normal sinus rhythm.[41] 27

Figure 2-4. BCG and ECG signals of a single heart-cycle.[40] 28

Figure 2-5. The diagram of co-woven-knitted fabric.[53] 29

Figure 2-6. Schematic diagram (a) and mechanical sketch (b) of the inductive sensor.[67] 31

Figure 2-7. The sketch of a cantilever type inductive cardiorespiratory sensor.[72] 32

Figure 2-8. (a): Flexpock device. (b): Flexpock device fit into a shirt pocket.[73] 32

Figure 2-9. Refraction of light between two materials at different incident angles. Left: normal refraction of light. Middle: no refraction of light at a critical angle. Right: total internal reflection. 33

Figure 2-10. The cross-section of an optical fibre. 34

Figure 2-11. (a) top LCP layer with metallised patterns; (b) middle LCP layer with space holes;(c) bottom LCP layer with metallised patterns on the other side; (d) the fabricated sensor.[89] 36

Figure 2-12. Piezoelectric effect in a quartz crystal.[98] 37

Figure 2-13. PVDF based flexible sensor. (a): bending in-sensitive. (b): bending sensitive.[103] 37

Figure 2-14. Relationship curve of carbon black content and resistivity of conductive rubber.[107] Zone A: Insulation zone. Zone B: Percolation zone. Zone C: Conductive zone. 38

Figure 2-15. The fabricated sensor array.[108] 39

Figure 2-16. Electrical-wire-stitched technique.[113] 40

Figure 2-17. Sensor setup for clinical, exercise and gravitational conditions.[119] 41

Figure 2-18. Carbon-coated fibre twisted yarn. (a): Single wrapped; (b) Double wrapped.[123] 42

Figure 2-19. Schematic diagram of silver coating on a copper nanoparticle.[140] 43

Figure 2-20. The concept of the separation of gold agglomerates.[150] 44

Figure 2-21. The concept of self-healing silver ink. (a): before scratching; (b): immediately after scratching; (c): after restoration.[159] 45

Figure 2-22. A comparison of the processing steps involved in subtractive microfabrication and additive direct write printing. (a): traditional microfabrication. (b): inkjet printing technique.[172] (c): a theoretical model of an ink droplet deposits on a solid substrate. 47

Figure 2-23. Ink suitability for printing using non-dimensional numbers.[173] 48

Figure 2-24. Optical image and typical cross-section sketch for annealed silver precursor lines printed at a dot-to-dot spacing of (a) 20 μm, (b) 40 μm, and (c) 80 μm.[177] 49

Figure 2-25. A schematic of the continuous dip coating process. 51

Figure 2-26. The relationship between dip coating thickness and speed.[202] 51

Figure 2-27. Printing sequence of a capacitive cantilever.[207] 52

Figure 2-28. Schematic of the gravure and screen printed pressure sensor.[210] 53

Figure 2-29. Thermal sintering process.[212] 54

Figure 2-30. The resistance of UV-cured (1, 2, 4, 8 and 16 runs) and thermally sintered silver tracks on three different substrate materials (Polyimide, Polycarbonate, Liquid Crystal Polymer).[216] 55

Figure 2-31. Microwave sintering on a silver paste printed Polyimide substrate.[218] 56

Figure 3-1. A schematic diagram of the operational principle of the nonwoven fabric based piezo-resistive material. 59

Figure 3-2. The (a) carding machine and (b) thermal bonding machine. 63

Figure 3-3. The flat surface mould used to create flat thermally bonded nonwoven fabric. 64

Figure 3-4. The photos of the preparation procedure of nanoscale silver particle ink; (a): before 24-hour standing; (b): after 24-hours standing; (c): syringe filtering. (d): filtered nanoscale silver particle ink. 67

Figure 3-5. (a): the nonwoven fabric immersed in the nanoscale silver particle-based ink; (b): Werner Mathis CH-8155 Pad Mangle. 68

Figure 3-6. The nanoscale silver ink impregnated nonwoven fabric, (a) before thermal sintering; (b): during thermal sintering; (c): thermal sintered and cut into a smaller size designed for sensor fabrication. 70

Figure 3-7. (a) The dimensions of designed sensor layers; (b) and (c): the layer schematic of the nonwoven piezo-resistive sensor. 71

Figure 3-8. A schematic of two-wire resistance measurement.[229] 73

Figure 3-9. A schematic of four-wire resistance measurement.[229] 74

Figure 3-10. The Wheatstone half bridge circuit diagram for the NI 9219. The dotted lines are the circuit built into the data acquisition card.[231] 74

Figure 3-11. The Wheatstone half bridge circuit diagram used to measure the resistance of the piezo-resistive sensor in this research. 75

Figure 3-12. NI-9219 data acquisition card. 77

Figure 3-13. Zwick 050 tensile tester under compression test settings. 79

Figure 3-14. Sensor setups for cardiorespiratory signal capturing. 81

Figure 3-15. On-body setup of the nonwoven sensor. 81

Figure 3-16. The 40 mm by 40 mm thin flat block. 82

Figure 4-1. (a) and (b): The SEM images of sample A with different magnifications; (c) and (d): the EDX elemental mapping of (a); (e): the EDX elemental spectrum. 85

Figure 4-2. (a) and (b): The SEM images of sample B with different magnifications; (c) and (d): the EDX elemental mapping of (a); (e): the EDX elemental spectrum. 86

Figure 4-3. The SEM images of sample C with different magnifications. (a): surface SEM image; (b): inner layer SEM image; (c): cross-section SEM image. 88

Figure 4-4. (a) and (b): the EDX elemental mapping of the surface on sample C; (c): the EDX elemental spectrum. 89

Figure 4-5. (a) and (b): the EDX elemental mapping of the inner layer of sample C; (c): the EDX elemental spectrum. 90

Figure 4-6. The SEM images of sample E under different magnifications. 90

Figure 4-7. The SEM images of sample F; (a) and (b): under 140x and 1600x magnification. 92

Figure 4-8. The SEM images of the sample G; (a) and (b): under 200x and 1000x magnification. 92

Figure 4-9. The SEM images of the sample H; (a) and (b): under 200x and 650x magnifications. 92

Figure 4-10. The SEM images of sample I; (a) and (b): under 140x and 550x magnifications. 93

Figure 4-11. The EDX elemental mappings of (a): sample F, (b): sample G, (c): sample H and (d): sample I. 93

Figure 4-12. Photos of (a) dot embossed nonwoven fabric and (b) smooth surface nonwoven. (c): a schematic of dot embossed nonwoven fabric. 95

Figure 4-13. SEM images of the dotted pattern nonwoven (sample D); (a): surface SEM image; (b): embossed area SEM image. 96

Figure 4-14. (a) and (b): the EDX elemental mapping of the surface structure of sample D; (c): the EDX elemental spectrum. 97

Figure 4-15. (a) and (b): the EDX elemental mapping of the embossed area of sample D; (c): the EDX elemental spectrum. 97

Figure 4-16. The SEM images of knitted fabric sample J and woven fabric sample K, under different magnifications: (a) 45x; (b) 140x; (c): 45x; (d): 700x. 99

Figure 4-17. The EDX elemental mapping of knitted fabric sample J and woven fabric sample K. 99

Figure 5-1. Compressive strength test results. 102

Figure 5-2. The quasi-static resistance-pressure curves of Sample C with a smooth surface structure. 103

Figure 5-3. The quasi-static resistance-pressure curves of Sample D with a dot embossed surface structure. 104

Figure 5-4. The piezo-resistive sensitivity of Sample C with a smooth surface structure. 105

Figure 5-5. The piezo-resistive sensitivity of Sample D with a dot embossed surface structure. 106

Figure 5-6. Sensor C with different silver take-up percentages. 108

Figure 5-7. Sensitivity of sensor C with different silver take-up percentages. 108

Figure 5-8. Resistance vs. pressure of sample A and B. 110

Figure 5-9. Resistance vs. pressure of sensor samples with different thicknesses..... 110

Figure 5-10. Sensitivity of smooth surface nonwoven material fabricated sensors..... 111

Figure 5-11. Resistance vs. pressure curves of sample D, E, G, J and K..... 112

Figure 5-12. Sensitivity of sample D, E, G, J and K. 112

Figure 5-13. Cyclic compressive load resistance vs. pressure curve of sample D..... 114

Figure 5-14. Cyclic compressive load resistance vs. pressure curve of sample E. 115

Figure 5-15. Cyclic compressive load resistance vs. pressure curve of sample G..... 115

Figure 5-16. Cyclic compressive load resistance vs. pressure curve of sample J. 116

Figure 5-17. Cyclic compressive load resistance vs. pressure curve of sample K..... 116

Figure 5-18. Diagram of a typical cyclic force-extension curve of a textile material.. 117

Figure 5-19. The resistance hysteresis loss of sample D, E, G, J and K of each cycle of the cyclic compressive loading test. 118

Figure 5-20. The resistance loss percentage of sample D, E, G, J and K of each cycle of the cyclic compressive loading test. 118

Figure 5-21. The change of peak resistance in each cycle. 120

Figure 5-22. The change of trough resistance in each cycle. 121

Figure 5-23. RTD of sample D, E, G, J and K. 122

Figure 5-24. Breathing signal curve from the commercially available breathing belt sensor and the piezo-resistive nonwoven sensor D (dot pattern embossed nonwoven fabric based). 123

Figure 5-25. Arm movements during respiratory signal capturing (sample D). Red circles: the breathing signals captured by the piezo-resistive nonwoven sensor but missed by the Plux sensor. 123

Figure 5-26. Scaled peaks during normal breathing (sample D)..... 124

Figure 5-27. Rapid breathing signal capturing (sample D). 124

Figure 5-28. Breathing signal curve from the commercially available breathing belt sensor and the piezo-resistive nonwoven sensor G (smooth surface nonwoven fabric based). 126

Figure 5-29. Arm movements during respiratory signal capturing (sample G). 127

Figure 5-30. Scaled peaks during normal breathing (sample G)..... 127

Figure 5-31. Rapid breathing signal capturing (sample G). The signal from the piezo-resistive nonwoven sensor is full of fluctuations. 128

Figure 5-32. Breathing signal curve from the commercially available breathing belt sensor and the piezo-resistive nonwoven sensor E (commercial conductive nonwoven fabric based). 128

Figure 5-33. Arm movements during respiratory signal capturing (sample E). 129

Figure 5-34. Breathing signal curve from the commercially available breathing belt sensor and the piezo-resistive sensor J (knitted fabric based)..... 130

Figure 5-35. Rapid breathing signal capturing (sample J). 130

Figure 5-36. Breathing signal curve from the commercially available breathing belt sensor and the piezo-resistive sensor K (woven fabric based). 131

Figure 5-37. Heartbeat signal curve from the commercially available BCG sensor and the piezo-resistive nonwoven sensor D (dot pattern embossed surface)..... 132

Figure 5-38. The successful cardiac signal acquisition using sensor D. 133

Figure 5-39. Heartbeat signal curve from the commercially available BCG sensor and the piezo-resistive nonwoven sensor G (smooth surface nonwoven based). 133

Figure 5-40. The peaks that correspond to the correct heartbeat from piezo-resistive sensor G..... 134

Figure 5-41. The bandpass filtered cardiac signal from piezo-resistive nonwoven sensor D. 136

Figure 5-42. Bandpass filtered cardiac signal from commercially available piezo-resistive nonwoven sensor E. 137

Figure 5-43. Heart signal peak detection and location matching between the nonwoven piezo-resistive sensor and commercially available BCG sensor..... 140

Figure 5-44. Breathing signal peak detection and location matching between the nonwoven piezo-resistive sensor and commercially available breathing belt sensor. (Marked: false peaks detected)..... 143

Figure 5-45. Recovery time of the piezo-resistive nonwoven sensor. 144

Figure 5-46. A schematic of the monofilament layered structure. 146

Figure 5-47. Photos of the monofilament layered structure. Left: during construction; right: finished nonwoven sensor with directional monofilaments. 147

Figure 5-48. SEM image of the monofilament laid structure. 148

Figure 5-49. EDX elemental mapping of carbon and silver. 148

Figure 5-50. Electromechanical compressive strength test. 149

Figure 5-51. The sensitivity of the directional monofilament laid nonwoven sensor.. 149

Figure 5-52. Resistance vs. pressure cyclic loading curve of 20 cycles on the HDPE nonwoven structure. 150

Figure 5-53. Cardiac signal captured by directional monofilament laid nonwovens sensor. (a) Monofilament laid structure; (b) Plux sensor; (c) peak location validation.152

Figure 5-54. Photo of the nonwoven sensor fabricated with directional silver coated polyester yarns. 154

Figure 5-55. Compressive cyclic loading on the nonwoven structure made from silver coated polyester yarns. 154

Figure 5-56. A Messmer micrometer. 156

Figure 5-57. The empirical model and verification curve for sensor conductance against variable pressure and sensor area; verification sensor area: 12.25 cm^2. 157

Figure 5-58. The empirical model and verification curve for sensor sensitivity against variable pressure and sensor area; verification sensor area: 12.25 cm^2. 158

Figure 5-59. The empirical model and verification curve for sensor resistivity against variable pressure and sensor area; verification sensor area: 12.25 cm^2. 159

LIST OF TABLES

Table 3-1. The functional fabrics. 60

Table 3-2. The purchased fabric materials. 62

Table 3-3. Laboratory-made thermally bonded nonwoven fabrics with different thickness and area densities. 65

Table 3-4. Chemicals used in the preparation of nanoscale silver particle ink. 66

Table 3-5. The piezo-resistive nonwoven fabric based sensors. 72

Table 4-1. The weight percentages of carbon, hydrogen, oxygen and silver elements in the piezo-resistive nonwoven fabric A and B. 87

Table 4-2. The weight percentages of carbon, hydrogen, oxygen and silver elements in the piezo-resistive nonwoven fabric C, on the surface and inner layer. 88

Table 4-3. Silver element weight% of sample F, G, H and I. 94

Table 4-4. Silver element weight% of sample D. 96

Table 5-1. The piezo-resistive nonwoven fabric based sensors. 101

Table 5-2. The times of sensor C being mangled and the corresponding silver take-up %. 107

Table 5-3. Cardiorespiratory data of the male subjects. 138

Table 5-4. Cardiorespiratory data of the female subjects. 139

Table 5-5. Heart rate (number of beats per minute) comparison 141

Table 5-6. Breathing rate (number of breaths per minute) comparison 142

Table 5-7. The resistance hysteresis of the HDPE nonwoven structure 151

Table 5-8. The resistance hysteresis of the silver coated yarn based nonwoven structure 155

Table 5-9. The RMSE and correlation coefficients of the empirical models for the sensor conductance, sensitivity and resistivity. 161

LIST OF ACRONYMS

ABR	Auditory Brainstem Response
ADC	Analogue-To-Digital Converter
BCG	Ballistocardiography
BSE	Backscattered Electrons
CNT	Carbon Nanotubes
CVD	Cardiovascular Diseases
ECG	Electrocardiography
EDX	Energy-Dispersive X-Ray Spectroscopy
ENG	Electroneurogram
FORP	Fibre Optic Respiratory Plethysmograph
GO	Graphene Oxide
HDPE	High-Density Polyethylene
HMDS	Hexamethyldisilazane
HR	Heart Rate
HRV	Heart Rate Variability
LCP	Liquid Crystal Polymer
LDPE	Low Density Polyethylene
LTCC	Low-Temperature Co-Fired Ceramic
MAIN	Magnetic Induction
PDAC	Poly(Diallydimethylammonium Chloride)
PDMS	Polydimethylsiloxane
PEDOT	Poly(3,4-Ethylenedioxythiophene)
PET	Polyester
PP	Polypropylene
PVDF	Polyvinylidenefluoride

PVP	Polyvinylpyrrolidone
RGO	Reduced Graphene Oxide
RIP	Respiratory Inductive Plethysmography
RMSE	Root-mean-square Error
RR	Respiratory Rate
RTD	Resistance Time Drift
SEM	Scanning Electron Microscopy
TFT	Thin-Film-Transistor
TIR	Total Internal Reflection
TME	Trimethylolethane

ABSTRACT

This research work has been carried out in order to develop electroconductive ink based electroconductive textile sensors for weak bio-signal capturing. Among the broad range of bio-signals, the cardiorespiratory signal was found as one of the most important physiological signals to people's health. Also, the increasing demand for the development of wearable/portable cardiorespiratory monitoring system has drawn more and more attention from the researchers. Much work has been carried out in order to investigate the feasibility of capturing cardiorespiratory signals based on the inductance, piezoelectricity or capacity of a sensor material. However, little work was found in the literature that using piezo-resistive nonwoven materials as a cardiorespiratory sensor. Therefore, there is a need for developing a nonwoven fabric based piezo-resistive sensor for weak bio-signal (cardiorespiratory signal) monitoring.

The morphology of the silver deposition in the nonwoven materials was studied by Scanning Electron Microscopy (SEM) and Energy-dispersive X-ray Spectroscopy (EDX) analysis in order to evaluate the impregnation performance. The nanoscale silver particle ink impregnated nonwovens were then fabricated into pressure sensors by sandwiching between four layers of functional fabrics. The fabricated sensors were studied by electromechanical characterisations under quasi-static and cyclic conditions. The factors that may affect the piezo-resistivity of the sensor have been investigated in this research. The hysteresis and resistance time drift phenomenon was studied through experiments.

Additionally, the electroconductive nonwoven material based sensors were used to acquire the cardiorespiratory signals in laboratory conditions. Effects of motion artefacts and resistance drift have been studied. In order to improve the accuracy and reliability of the nonwoven based cardiorespiratory sensors, a Matlab programme was developed with the justifications for picking up cardiac and respiratory signals. The response time and recovery time of the nonwoven based sensor were studied as well. It is concluded that the piezo-resistive sensor based on the nonwoven fabric with dot pattern embossed surface had the best performance in obtaining the cardiorespiratory signals, with an accuracy of 87.25% and 95.13% for respiratory and cardiac signal, respectively. The response time for the sensor to capture the cardiac signal was 12.65 seconds and 17.24 seconds for the respiratory signals. The recovery time for the sensor to recover from motion artefacts was 10.37 seconds for cardiac signal and 25.83 seconds for the respiratory signal.

In order to understand the engineering of piezo-resistive sensors and further understand the capability of the sensor to function in different settings, a piezo-resistive sensor was manually fabricated by laying silver coated electroconductive monofilaments/yarns at 0-degree and 90-degree angles. Thereafter the conductance, the piezo-resistive sensitivity, and the resistivity of this sensor was empirically modelled over the investigating limits of pressure varying from 0-100 g/cm^2 and for sensor size from1-16 cm^2. In order to verify the validity of these empirical models, the performance of the sensor was tested at a new sensor size of 12.25 cm^2 and compared with the empirical models.

DECLARATION

I declare that no portion of the work referred to this thesis has been submitted in support of an application for another degree or qualification of this or any other university or other institute of learning.

25 January 2018

COPYRIGHT STATEMENT

i. The author of this thesis (including any appendices and/or schedules to this thesis) owns certain copyright or related rights in it (the "Copyright") and s/he has given The University of Manchester certain rights to use such Copyright, including for administrative purposes.

ii. Copies of this thesis, either in full or in extracts and whether in hard or electronic copy, may be made only in accordance with the Copyright, Designs and Patents Act 1988 (as amended) and regulations issued under it or, where appropriate, in accordance with licensing agreements which the University has from time to time. This page must form part of any such copies made.

iii. The ownership of certain Copyright, patents, designs, trademarks and other intellectual property (the "Intellectual Property") and any reproductions of copyright works in the thesis, for example graphs and tables "Reproductions"), which may be described in this thesis, may not be owned by the author and may be owned by third parties. Such Intellectual Property and Reproductions cannot and must not be made available for use without the prior written permission of the owner(s) of the relevant Intellectual Property and/or Reproductions.

iv. Further information on the conditions under which disclosure, publication and commercialisation of this thesis, the Copyright and any Intellectual Property and/or Reproductions described in it may take place is available in the University IP Policy (see http://documents.manchester.ac.uk/DocuInfo.aspx?DocID=2442 0), in any relevant Thesis restriction declarations deposited in the University Library, The University Library's regulations (see http://www.library.manchester.ac.uk/about/regulations/) and in The University's policy on Presentation of Theses

ACKNOWLEDGEMENT

I am thankful to all those people who helped me and provided their valuable time and advised me during the period of my research work.

I would like to express my most sincere gratitude to my supervisor, Dr Anura Fernando, and my co-supervisor, Dr Jayawan Wijekoon for spending their valuable time and effort in guiding and supporting me with great patience.

I am thankful to Dr Hugh Gong who provided me valuable information about nonwoven technology. I would also like to express my appreciation to Dr Syed Talha Ali Hamdani and Dr Arash M. Shahidi for giving me training and advises on the use of laboratory equipment, experimental setups and valuable advice. I am also very grateful to Mr Peter Moroz, Mr Edward Lay, Mr Phillip Cohen, and Mr David Kenyon for their supporting advice on chemicals, yarns and fabrics that helped me immensely to complete this work.

Additionally, I would like to give my sincere thanks to my supportive family for their continuous encouragement which gave me the strength to complete this work. Especially, I am thankful to my loving wife who gave me endless motivation to finish the research work. And I would like to take this opportunity to thank all my friends who were with me during my studies at the University of Manchester as well.

Chapter One: Introduction

1.1 Background

Due to the faster pace of modern life where higher pressure from work is experienced by humans, more and more people are found suffering issues related to mental/physical strain. These issues could cause disorders during people's work or life elsewhere, which could manifest as various physical conditions such as cardiorespiratory diseases, vascular system related deceases etc. Their time and place of occurrence are such that these conditions appear unexpectedly. Taking the case of cardiorespiratory diseases, reports show the cases that vehicle drivers were suffered from heart attacks while driving.[1, 2]

To prevent further damage caused by mental strain, one method is to carry out long-term cardiorespiratory monitoring on those who may have such conditions. Traditional instruments like electrocardiography (ECG) and ballistocardiography (BCG) machinery cannot meet the demands of portability and long-term usage. Most of the current research on portable cardiorespiratory monitoring systems is mainly focused on hard portable devices. The solid-state sensors that are used in these devices are then usually integrated into a belt or into a garment to achieve a portable monitoring system. However, these devices will lead to discomfort and possibly skin irritation to the wearer, thus causing non-compliance on their wearing. Therefore this dilemma has resulted in the birth of the research area, wearable electro/smart textiles, which primarily investigate the creation of flexible, electroconductive ink based sensors for use on electro-textile garments for weak bio-signal capturing applications.

Today there is an increasing demand for developing flexible and wearable sensing materials that are convenient to be processed by textile manufacturing machinery and processes. These flexible electro-textile materials provide the textile-based sensors with flexibility and the possibility of easy integration into everyday clothing. Therefore, the main focus of the current research is the creation and investigation of various electro-textile structures, based on fibres, yarns and fabrics, integrated with electroconductive ink or coatings, in order to engineer flexible electro-textile sensing materials with reliable and repeatable performance.

1.2 Problem definition

As the biggest threat to people's lives, cardiorespiratory related diseases are still increasing in the number of kills at an alarmingly fast speed. According to the statistics published by Heart UK, cardiovascular diseases (CVD) are responsible for 30% of deaths in the world, increased from 25% in 2008.[3, 4] CVDs account for 17.3 million deaths in a year, which value is expected to increase to 23.6 million by 2030.[5] Every year in the UK, altogether 45,000 new cases of angina and heart failure are diagnosed, not including those cases ignored by potential patients with minor symptoms. Other than the quality of living (even lives lost), a large amount of money has been spent on fighting against cardiorespiratory related diseases. The health expenditures and productivity lose cost by CVDs in the US have been raised from 108.9 billion dollars in 2010 to 320 billion dollars and 316 billion dollars in 2015 and 2017, respectively.[4–6] £19 billion has been spent on the direct health care, productivity losses and informal care due to CVDs in the UK. Globally, the estimated cost due to CVDs is estimated to increase from 863 billion dollars to 1044 billion dollars from 2010 to 2030.[5] All these figures represent the imminent need for more attention to cardiorespiratory related diseases.

Cardiorespiratory signal monitoring is one critical approach to help ease the threat of cardiorespiratory related diseases. To medical practitioners, the information obtained from cardiorespiratory signal monitoring not only can help the detection of early-stage heart attacks but also the valuable supportive information for correct diagnosis. Additionally, the cardiorespiratory signal is of the most importance in monitoring patient's health status after medical treatment. Current clinical and hospital cardiorespiratory signal monitoring system is ECG; however, due to the fact that the operation of ECG requires complex machinery and terminal connections, as well as the difficulties in the interpretation the ECG result by normal people, the usage of ECG is mostly limited to clinics and hospitals. Therefore, only the need for the clinical cardiorespiratory monitoring can be fulfilled by ECG; whereas the demand for daily, long-term and the ambulatory cardiorespiratory monitor is unmet. Electro-textile material based weak bio-signal sensor is considered as the best candidate to create applications that can be used for daily, long-term and ambulatory cardiorespiratory monitoring. The feasibility of easy integration into a garment make electro-textile material based sensor available for a large range of users. The flexibility of the electro-

textile material causes little interferences to people's normal life while capable of carrying out the task of weak bio-signal acquisition, such as cardiorespiratory monitoring.

Much attention and efforts have been put on the development of the electro-textile material based bio-signal sensors. Vivometrics, Inc. developed LifeShirt^{TM}, a multi-function system which was embedded in the garment, where several physiological signals can be monitored, recorded and analysed simultaneously.[7] Recently, a non-contact four-sensor array integrated into a shirt was developed in order to detect the cardiorespiratory signal of the wearer according to the change in the magnetic induction.[8] However, the directional requirement for the inductive sensors frequent calibration work is needed. Fibre optic sensors have also been investigated for acquiring respiratory signals, while their sensitivity requires improvement in order to detect cardiac signals.[9] Using capacitive sensor is another approach for monitoring cardiorespiratory signals.[10, 11] However, capacitive sensors were found more vulnerable to noise and motion artefacts.[12] Therefore, it can be concluded that there is a need for developing a piezo-resistive electro-textile sensor for the weak bio-signal monitoring system.

1.3 Research aim and objectives

As discussed previously, there is an urgent need for developing a weak bio-signal monitoring system, such as cardiorespiratory signals monitoring, which is designed for daily, long-term and ambulatory condition. The main aim of this research is to develop a non-invasive electro-textile material based piezo-resistive sensor suitable for garment integration and physiological signal monitoring.

The objectives of the current research can be summarised as follows:

- the investigation of the piezo-resistivity of the electroconductive ink impregnated nonwoven fabric materials;
- the design and engineering of the piezo-resistive nonwoven fabric based sensor;
- the investigation of the sensor performance for acquiring the weak bio-signals (cardiorespiratory signals);
- the development of empirical models in order to characterise the function of the sensor.

1.4 The scope of the research

Research of publications has revealed that there is a gap in the technology for creating a weak bio-signal monitoring system that can be used in daily, long-term and ambulatory conditions. Various electro-textile sensing materials have been investigated in order to create flexible cardiorespiratory sensors. In this research, piezo-resistive materials are selected to produce the sensor and the investigated in-depth. Due to the fact that nonwoven materials have the advantages of good solution absorption and the contact points that intensely respond to compression, they are chosen as the textile substrate to create the electro-textile materials. The nonwoven materials are granted with piezo-resistivity by dip-coating impregnation technology. The nanoscale silver particle ink impregnated piezo-resistive nonwoven sensing materials are characterised under quasi-static and dynamic situations in order to determine the performance of the materials. The responsivity and accuracy of the nonwoven sensing material fabricated cardiorespiratory sensor are also investigated. The empirical models of the conductance, sensitivity and piezo-resistivity of the piezo-resistive nonwoven sensor fabricated by laying directional monofilaments/yarns are calculated. The empirical models provide characteristics and predictions of the performance of the sensor over variable sensor areas and pressure levels, which are verified by an independent test setup.

1.5 The layout of this thesis

The first chapter focuses on introducing the background information of this thesis. The motivations and aims of this research are discussed, together with the scope of this research.

Chapter two focuses on the literature review, in which the detailed history and information of the bio-signals, the cardiorespiratory signals and their importance is introduced. Feasible monitoring methods are demonstrated. It also discusses the different types of smart textile materials that can be used for creating cardiorespiratory sensors. Additionally, existing portable/wearable cardiorespiratory sensor applications are studied. In this chapter, electroconductive ink made from different electroconductive materials are explained, together with the methods of integrating such inks into textile materials and possible approaches to curing them.

Chapter three explains the methodology of this research work. The operational principle of the piezo-resistive textile material is explained in detail. Also, the materials and methods used in order to create nanoscale silver particle based electroconductive ink, the impregnation procedure of such ink and the design and fabrication steps of the ink impregnated textile based sensor are described in this chapter. Additionally, the scope of the tests that are to be carried out is introduced together with their test setups and parameters.

The results and findings from microscopy analysis on the nanoscale silver particle ink impregnated materials are illustrated and discussed in chapter four. The morphology of the silver deposition and the effects of the properties of the silver particle based ink and fibre distribution and orientation in the nonwoven on the impregnation performance are discussed in detail.

The fifth chapter presents the experimental work carried out in order to characterise and optimise the nanoscale silver particle-based piezo-resistive sensor. The effects of the properties of the electroconductive textile materials on the piezo-resistive performance and cardiorespiratory sensor performance are studied. The nonwoven sensors fabricated with directional electroconductive monofilaments/yarns are developed in order to simulate the piezo-resistivity of the nonwoven fabric based sensors. The conductance, piezo-resistive sensitivity and resistivity of the directional monofilaments/yarns laid nonwoven sensor are empirically modelled.

Chapter six concludes the current research. The findings from this research are summarised and recommendations for future investigations are given in this chapter.

Chapter Two: Literature Review

2.1 Introduction

Monitoring weak bio-signals is becoming more and more important and essential in people's life. Not only the patients in a hospital require such services as cardiorespiratory signals monitoring, but also people who work under high stress or people with cardiorespiratory disease history would benefit from full-time access to such information.[13] In this chapter, the fundamental background of cardiorespiratory and available methods of monitoring cardiorespiratory signals is introduced. Further, existing knowledge of developing portable and wearable cardiorespiratory sensors is investigated. Additionally, the electroconductive inks which can be used to create cardiorespiratory sensors and methods used in the creation of electroconductive textile-based materials are discussed in detail. At the end of this chapter, a summary is given, demonstrating the discoveries and conclusions from the literature review.

2.2 Bio-signals and cardiorespiratory monitoring

A bio-signal is defined as a description of a physiological phenomenon.[14] Generally, bio-signals cover an extreme broad range of aspects: as simple as a visual appraisal from a physician, the action potential which is the electrical signals from the polarisation of a cell in order to perform mechanical contraction;[15] electrical signals generated by central nervous system which can be detected by electroneurogram (ENG); auditory brainstem response (ABR) from brainstem in reaction to audio signals.[16, 17] These examples are only a glance to the area of bio-signals. However, among numerous of bio-signals that are being investigated by researchers, the cardiorespiratory signals are the most studied.[18–22]

The cardiorespiratory system mainly consists of the heart and the circulatory system, together with numerous blood vessels that deliver the oxygenated blood to all parts of our body and pump away the de-oxygenated blood and metallic waste products.[23] An adult's heart circulates approximately 9,000 litres of blood over 100,000 beats each day. The health of the cardiorespiratory system is most critical to people's health.

Unfortunately, cardiovascular disease (CVD) is now the number one cause of death globally with an estimated 7.4 million due to coronary heart disease and 6.7 million due

to stroke.[13] In extreme conditions, people with such heart-related illnesses were found unconscious without the ability to contact any medical emergency services.[24–26] CVDs are not isolated to other body systems; as stated in literature, patients suffered from rheumatoid arthritis have a higher risk in CVDs;[27, 28] cardiorespiratory fitness was found related to type 2 diabetes, especially to those patients who were statin-treated;[29] reports also showed that the development of depression among the middle school students could be significantly prevented by improving cardiorespiratory fitness;[30] mental stress is also considered as related to cardiorespiratory status.[31] Therefore, cardiorespiratory monitoring is one important approach to reduce the risk level on those individuals with such cardiorespiratory conditions and to provide fundamental information which supports the medical diagnosis.

2.2.1 Methods of cardiorespiratory monitoring

The important signals generated by the cardiorespiratory system can be concluded as heart rate (HR), number of heartbeats per minute; heart rate variability (HRV), the variation of the interval between two heartbeats; respiratory rate (RR), number of respirations per minute; and oxygen saturation, the concentration of oxygenated hemoglobin.[23]

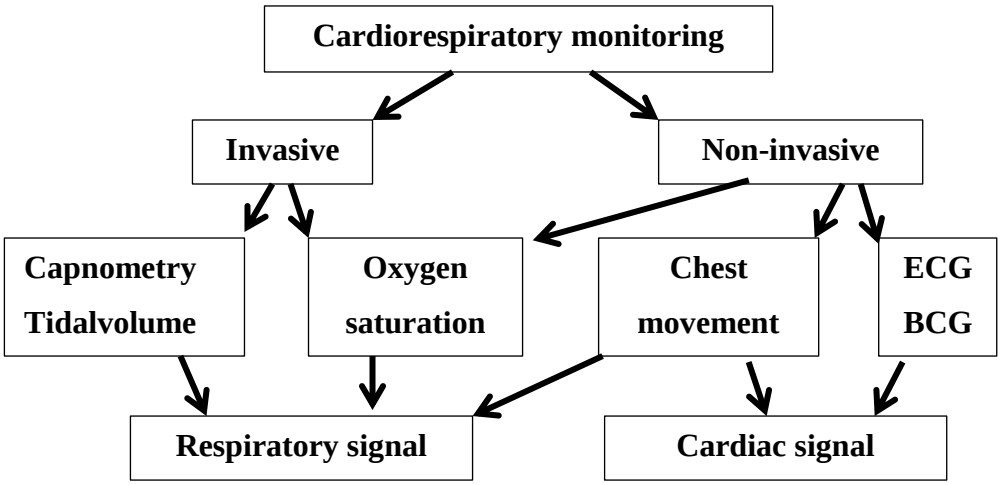

Figure 2-1. Possible cardiorespiratory monitoring methods.

Methods for monitoring cardiorespiratory signals has been summarised in **Figure 2-1** and can be classified into two categories: invasive and non-invasive methods. Tidalvolume and capnometry tests measure the volume of air inhaled/exhaled and the CO_2 exhaled with breathing. These tests require intubation which generates strong pain

and irritation to the patients.[32] Oxygen saturation can be measured using invasive methods with an arterial blood sample, and non-invasive methods if oxygen saturation is above 70%.[33] Monitoring the chest movement is feasible for not only respiratory signal but also for the cardiac signal. Additionally, ballistocardiography (BCG) and electrocardiography (ECG) are the two well-developed and widely-used technology nowadays.

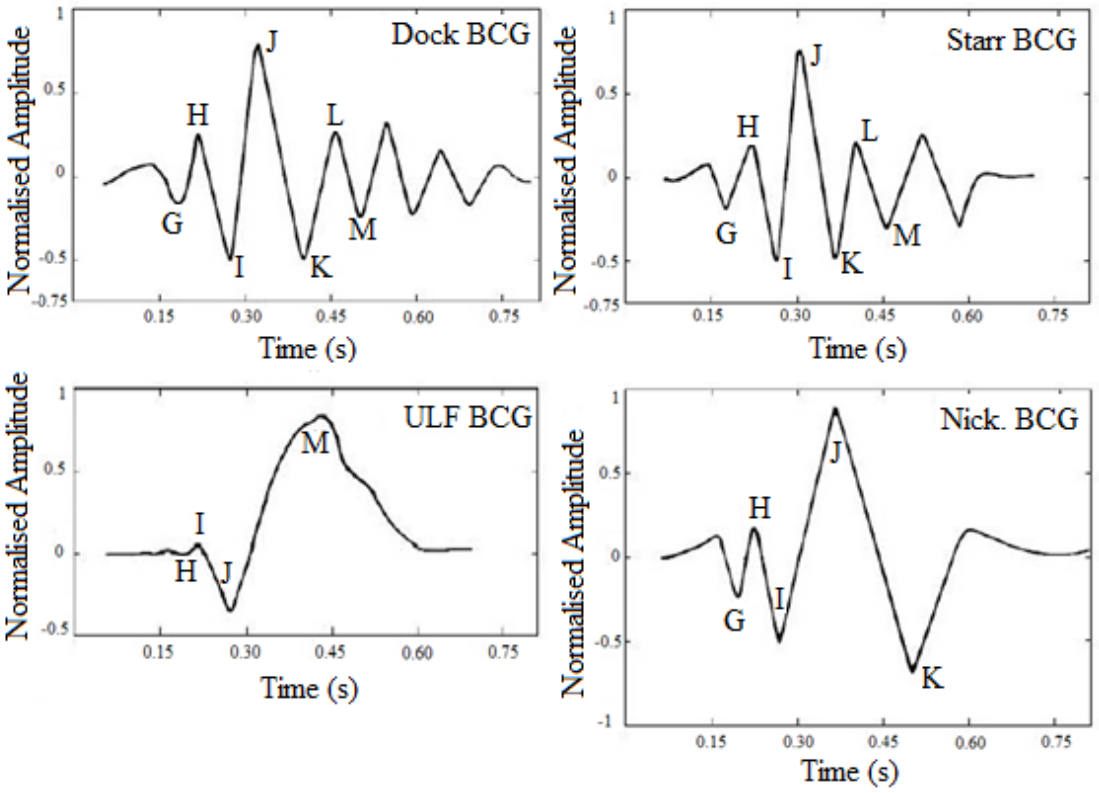

Figure 2-2. Differences and similarities in waveforms acquired from different BCG systems.[34]

Heartbeat causes noticeable body movements which can be used to identify and record the HR and HRV. This technology is called BCG. Since it was first seen and founded, BCG has been well studied and developed over a century.[35, 36] Literature show cases where different BCG systems were developed and compared, from which the waveforms of BCG were found with noticeable similarities and yet differences (as illustrated in **Figure 2-2**).[34]

Other than the ballistic force created by the heart movement, specific electrical signals depolarise the heart and control the activity of the heart during each beat. These electrical signals follow a specific order and can be detected non-invasively using ECG

technology. As shown in **Figure 2-3**, a typical ECG pattern consists of P wave (atrial depolarization), QRS wave complex (ventricular depolarization) and T wave (ventricular repolarization).[37] To a trained clinician, the intensity of the waves and intervals between the waves in an ECG pattern represents the healthiness of the heart.[38] Studies also found that in a single heart cycle, the largest wave in ECG (R wave) and BCG (J wave) have an interval of approximately 200 ms (as shown in **Figure 2-4**), which is due to the fact that there is a delay between the depolarisation signal (ECG) and the mechanical contraction of the heart (BCG).[39, 40] Compared with BCG, ECG has a specific pattern, which gives it advantages in the determination of HR and HRV. However, in order to acquire all the polarisation electrical signals and represent their intervals correctly, the standard ECG requires 10 cables to be connected to the skin using electroconductive gel covered terminals. Such complex setup and irritative connection limit the usage of ECG mostly to hospital and clinic.

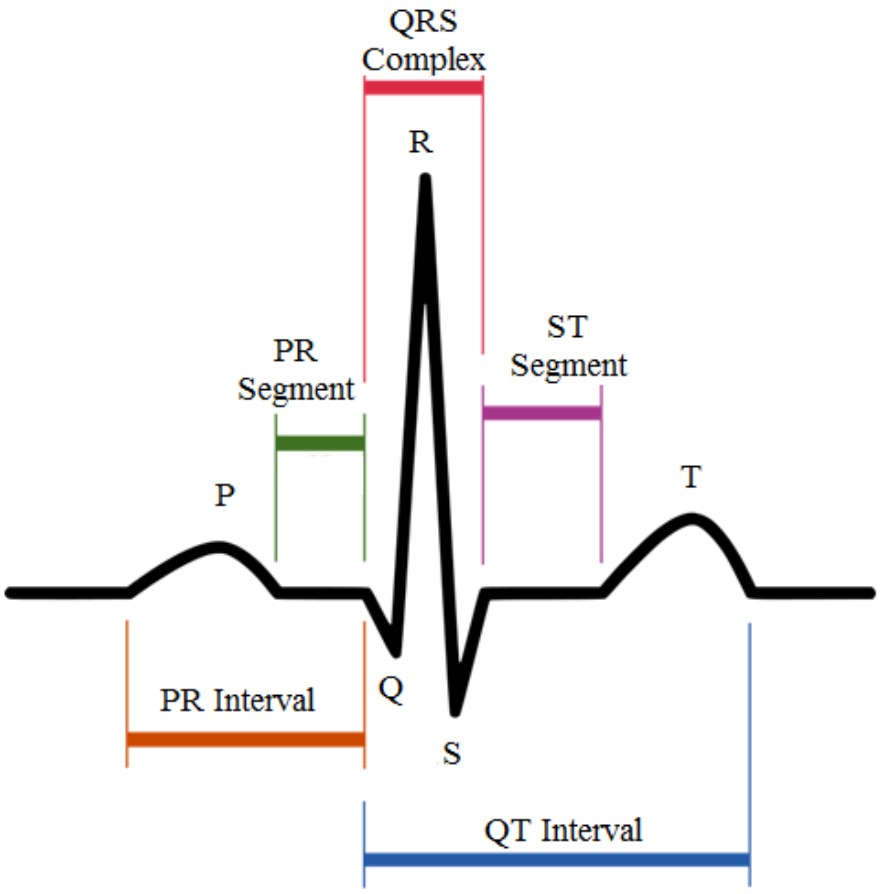

Figure 2-3. ECG of a heart in normal sinus rhythm.[41]

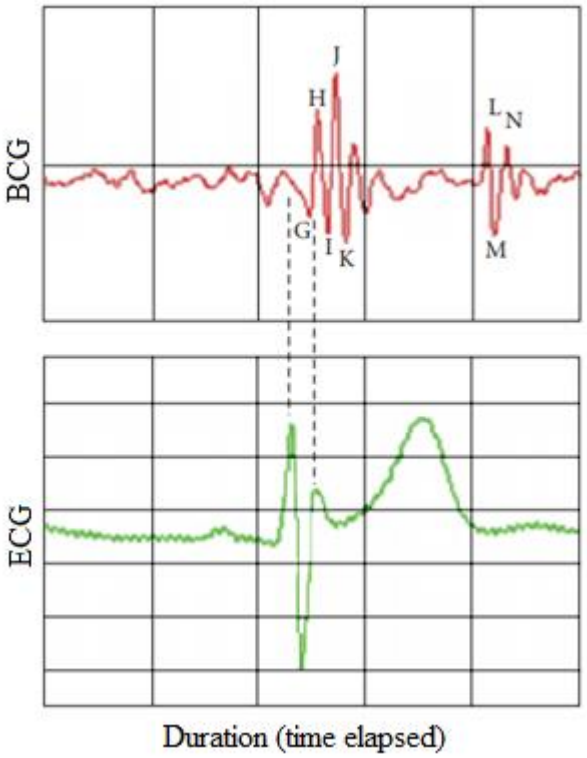

Figure 2-4. BCG and ECG signals of a single heart-cycle.[40]

2.2.2 Smart textile materials for sensory applications

The different methods discussed above all require complex preparation and setup. Intubation and blood sample acquiring are painful, and the results cannot be achieved immediately. BCG and ECG need professional machinery and results may be difficult to interpret for normal people. The phenomenon in clinic and hospital, as well as the connection to complex medical instruments, will cause irritation to the patient physically and mentally, which further influences the accuracy of the test results.[42] Therefore, developing non-invasive and portable cardiorespiratory monitoring suitable for daily, long-term and ambulatory conditions has gained more and more attention from the researchers from all kinds of fields. Due to the fact that textile materials have already been the most inseparable part in people's lives for thousands of years, electro-textile materials, further developed as smart textiles, are the best candidates to the non-invasive and portable cardiorespiratory monitoring applications. Smart textiles are products made from conventional textile materials. Such products can be the complete devices that are designed for interacting with the users or the environment, or parts that are used in such devices in order to grant such devices with the properties of textiles, like flexibility and feasibility of being integrated into textile garments.[43]

The textile materials used for creating smart textiles can vary from basic materials such as fibres/filaments/yarns to advanced concepts like electroconductive material coated thin films.[44–46] One of the approaches to creating the electroconductive yarns used in electro-textiles is combining fine metal wires with textile yarns. Some evidence was found in the literature: the copper cored electroconductive yarns with cotton sheath were developed for electroconductive fabric applications;[47, 48] a stainless steel based electroconductive yarn was used for electromagnetic shielding applications;[49] electroconductive woven fabric could be produced from stainless steel wrapped by polypropylene nonwoven ribbons as well.[50] Electroconductive yarns can also be created by coating yarns with electroconductive materials, such as carbon nanotubes (CNT) and polyaniline conductive polymer.[51, 52] In literatures, electroconductive yarn based applications are mostly used as strain sensors, which are suitable for detecting the mechanical signals generated by the respiratory cycle. However, due to the fact the BCG signals are much weaker than the respiratory signal, electroconductive yarn based strain sensors are found incapable of capturing such weak bio-signals.

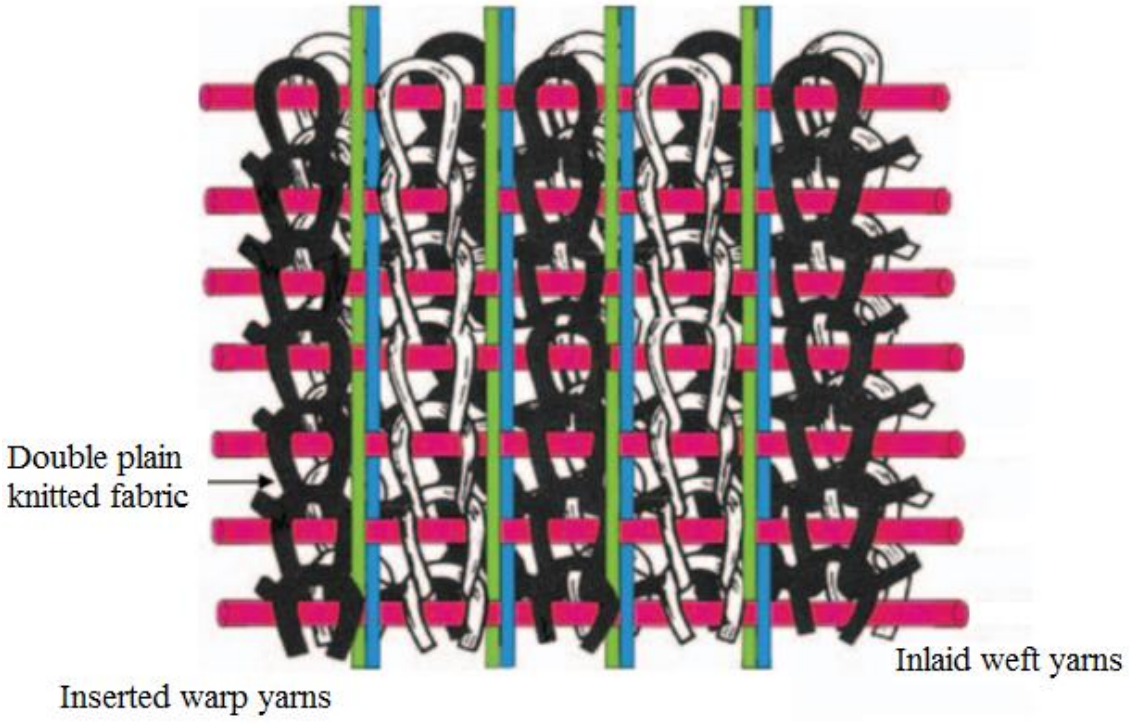

Figure 2-5. The diagram of co-woven-knitted fabric.[53]

Broadly, the electroconductive yarns were used together with weaving and knitting technologies to produce different electroconductive fabric based applications.[54–58]

Electroconductive yarn based woven or knitted structures are commonly used to reinforce electroconductive composites. A polypropylene composite reinforced by co-woven-knitted fabric was developed using copper, stainless steel and nylon hybrid yarns.[53] The co-woven-knitted structure (as shown in **Figure 2-5**) improved both the mechanical properties and the conductivity of the composite.[59, 60] The other examples showed that conductive yarns can be sewn into a textile material as well.[61, 62] In the aspect of nonwoven fabric based smart textiles, the electroconductive properties are granted in a more direct way. Spin coating technology can be used to create nonwoven fabric based electrode.[63] Evidence was discovered in the literature, where electroconductive CNTs were deposited on nonwoven fabrics by sonication in an aqueous bath.[64, 65] A limited amount of literature was found related to the nonwoven based piezo-resistive sensor. However, due to the wellness of the nonwoven materials that can thoroughly absorb electroconductive materials and induce resistive signal actively to pressure changing,[63] nonwoven fabrics were used throughout the current research.

2.3 Portable/wearable cardiorespiratory sensors

As discussed, monitoring the chest movement is one non-invasive approach that can acquire both cardiac and respiratory signals under the same principle, while keeping the patients away from complex clinical leads and setups. Therefore, it is necessary to develop portable/wearable respiratory sensors based on the chest movement and cardiac sensors based on the ballistic signals generated by the heart contraction.

2.3.1 Inductive cardiorespiratory sensor

The principle of the inductive sensor is Faraday's law of induction, which is that the variation of the magnetic flux through a closed circuit will generate electric current.[66] The working principle of a normal inductive sensor was illustrated in Bakhoum and Cheng's work.[67] They developed an inductive pressure sensor which had miniature size and high sensitivity. The design of the sensor is based on the change in the inductance between two coil materials, as shown in **Figure 2-6**. As under pressure, the soft iron core in the middle of the sensor could be displaced, thus, causing a change in the inductance between two parallel coil materials.

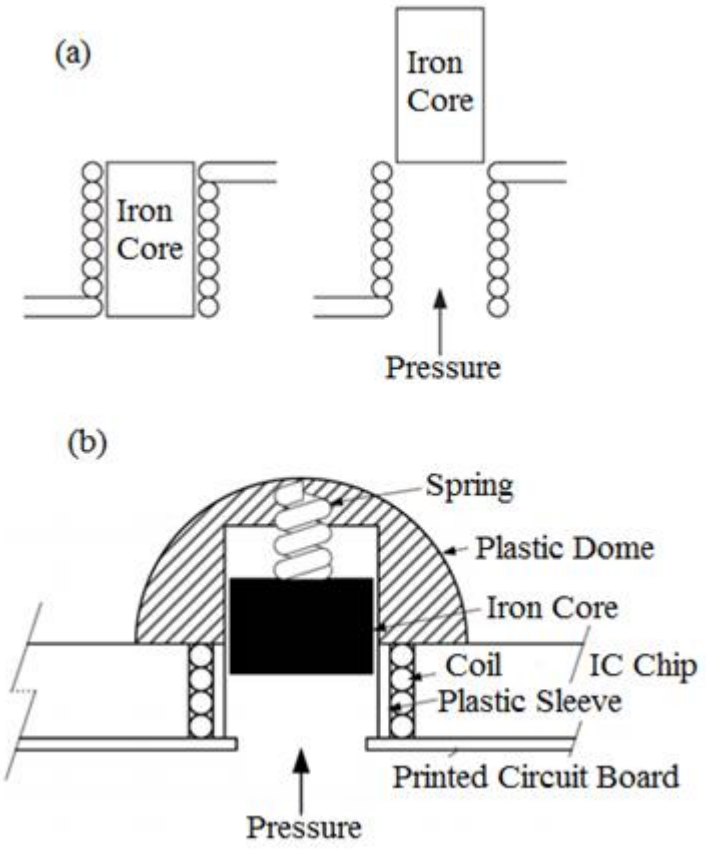

Figure 2-6. Schematic diagram (a) and mechanical sketch (b) of the inductive sensor.[67]

Literature shows numerous of applications based on inductive sensors: Pederson et al. patented an inductive sensor for measuring relative or absolute pressure, which used the resonant frequency and allowed the reading of the pressure/resonance frequency remotely;[68] Cos et al. developed an inductive pressure sensor, with an innovative circuit which minimised the hysteresis to a negligible level of 1.4% without sacrificing the high linearity.[69]

In order for the inductive sensor to be suitable for wearable cardiorespiratory monitoring, developing lightweight inductive sensors has been drawn more attention from researchers. Due to the nature of electromagnetic induction, the coil is the most important mechanism in inductive based sensors. The coil could either be simply integrated into the textile garment or remotely controlled by a cantilever, as shown in **Figure 2-7**.[70–72] A non-contact inductive cardiorespiratory sensor was developed and integrated into a shirt, named as magnetic induction (MAIN) shirt.[8] A bendable and wearable cardiorespiratory monitoring system was developed, based on two sensors, an

inductive sensor for respiratory signal and a photoplethysmography sensor for the cardiac signal.[73] The fabricated sensor was in the form of a circuit board, including a coil and other electronics, which could be fitted into a shirt pocket. It can be seen in **Figure 2-8**, that the complete system was established on a hard circuit board, and its flexibility remains uncertain. In the report conducted by Zhang et al., they investigated respiratory inductive plethysmography (RIP) module designed for processing multiple inductive sensors for respiratory monitoring.[74] Another portable RIP application was studied together with a position sensor for the calibration during daily activities.[71]

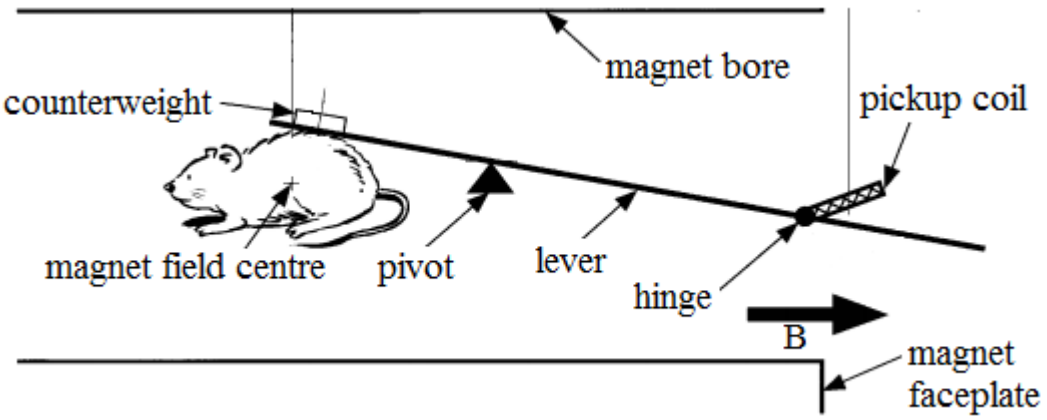

Figure 2-7. The sketch of a cantilever type inductive cardiorespiratory sensor.[72]

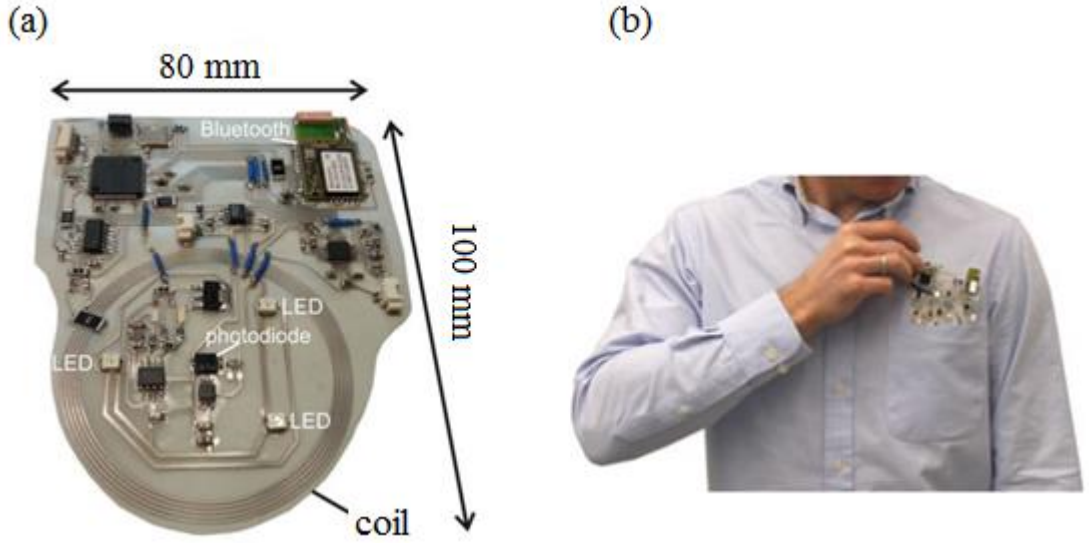

Figure 2-8. (a): Flexpock device. (b): Flexpock device fit into a shirt pocket.[73]

Through literature, it was found that inductive sensors have advantages of high linearity, high sensitivity and low-temperature hysteresis.[67] However, the necessity of a coil

and the electric circuit has a potential risk of burns to the user; and due to the importance of direction of magnetic flux and electric current, more work of calibration is inevitable.[72] Also, inductive sensor applications were not suitable for integration into a garment for long-term daily usage as to their poor bendability.

2.3.2 Fibre optic cardiorespiratory sensors

The idea of fibre optics was first established in the 1840s, based on the guided refraction of light, which was later developed into the theory of total internal reflection (TIR).[75–78] The TIR of light is a phenomenon that light strikes a medium boundary at a certain angle which results that the complete light is reflected without any being refracted through the boundary (as shown in **Figure 2-9**).

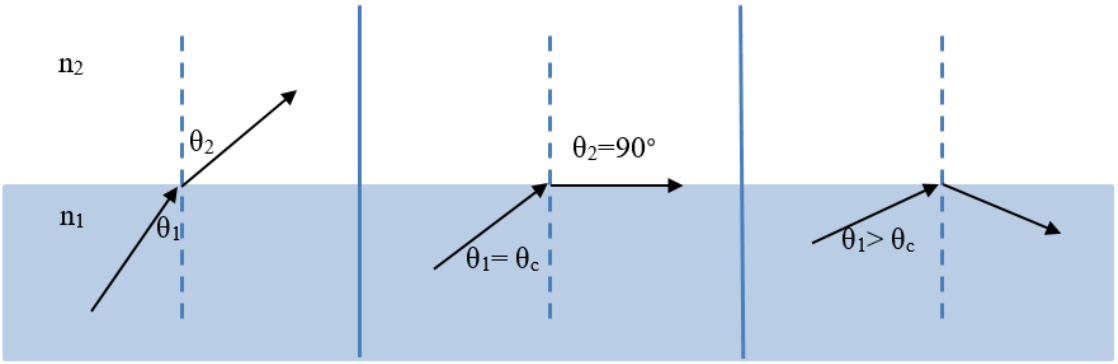

Figure 2-9. Refraction of light between two materials at different incident angles. Left: normal refraction of light. Middle: no refraction of light at a critical angle. Right: total internal reflection.

According to Snell's law:

$$n_1 \times \sin\theta_1 = n_2 \times \sin\theta_2 \qquad \textbf{Equation 2-1}$$

where: n_1 and n_2 are the refractive indices of the two materials; θ_1 and θ_2 are the angles of the incident ray and refracted ray, respectively.

Therefore, the critical angle θ_c (when $\theta_2 = 90°$ and $\sin\theta_2 = 1$) can be calculated as:

$$\theta_c = \arcsin\frac{n_2}{n_1} \qquad \textbf{Equation 2-2}$$

From **Equation 2-2**, it is obvious that TIR can only occur when n_2/n_1 is less than or equal to 1.

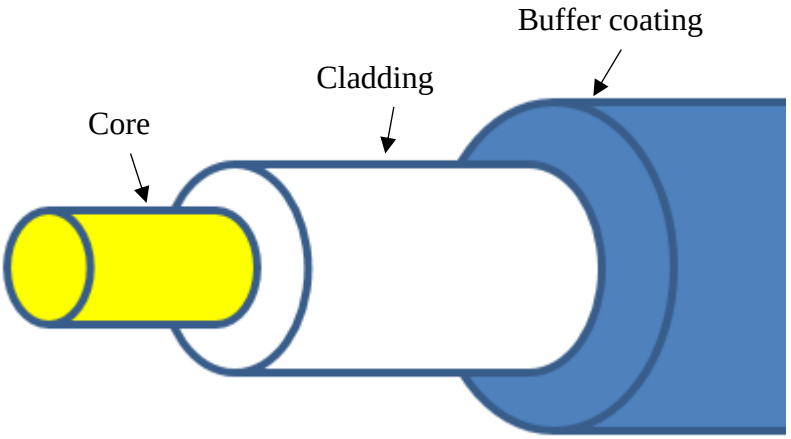

Figure 2-10. The cross-section of an optical fibre.

Optical fibres are made from extremely pure glass or plastic fibre and normally consist of three parts: core, cladding and buffer coating, as demonstrated in **Figure 2-10**. The core and the cladding material provides a medium boundary where TIR is possible, resulting in the guidance of the optical signal through the core. The buffer coating protects the fibre from outside.[79] The type of optical signal varies from ultraviolet, visible to infrared radiation, based on the choice of the core.[75] Depending on the number of the optical signals can be transmitted at the same time, the optical fibre can be categorised as (a) monomode, which normally fabricated with a fine core allowing the transmission of light with specific wavelength; (b) multimode, which allows multiple light signals to be transmitted at the same time, however, with a sacrifice in the core diameter (increased diameter for more optical signal feasibility), modal noise and the constancy of far-field radiation pattern.[80] The optical fibre can be used in two types of sensors: extrinsic sensors and intrinsic sensors. Extrinsic sensors use optical fibre as a cable, which transfers optical signal from another optical sensor to an optical transmitter. Intrinsic fibre optic sensor can be used to detect stress/strain by measuring the change in the intensity, phase, wavelength, polarisation and the transit time of the optical signal.[81, 82]

The optical fibre material is commonly used as an intrinsic sensor in cardiorespiratory monitoring applications. As early as in 1998, Gagnadre et al. reported their application for physiological signal using optical fibre materials.[83] Reports show that optical fibres can be integrated with textiles for respiratory monitoring.[32, 33] A respiratory

monitoring system was developed based on optical fibre material, named as the Fibre Optic Respiratory Plethysmograph (FORP).[84] The FORP is a non-invasive method for detecting cardiac and respiratory signal at the same time. Cardiac signal acquiring systems based on fibre optic sensors have also been investigated; however, the intensity and accuracy of the signals require improvement.[85, 86] The optical fibre has the advantages of lightweight, simple connection and high sensitivity.[87] However, due to the fact that optical fibre requires buffer coating to protect its core and cladding, its bending property is much worse compared with other electro-textile materials. Therefore, similar to the inductive sensor, it was found difficult to fully integrate fibre optic sensor into the garment. Additionally, these two types of sensors were found lack of capability in capturing cardiac signals due to the sensor sensitivity.

2.3.3 Capacitive/piezoelectric material based cardiorespiratory sensors

A capacitive sensor is another common type of pressure sensor. The simplest model of a capacitive sensor consists of two non-contact electrodes, the capacitance of which is determined by the size of the electrodes and the distance between them. Therefore, capacitive sensors are widely seen in the applications of touch screens.[88] Capacitive sensors have higher sensitivity and lower hysteresis than piezo-resistive sensors; however, the problem of the non-linearity of the measured result needs to be resolved.[67] The purity of the material (substrate or vacuum) between the two electrodes of the capacitor is critical to the behaviour of the capacitive sensor.

Generally, capacitive sensors are fabricated by laying different functional layers. A liquid crystal polymer (LCP) based capacitive sensor was designed by Palasagaram and Ramadoss.[89] The top and bottom layers of the sensor were made of the LCP substrate, the positions of which were patterned with metallised electrodes. These LCP substrate layers sandwiched another LCP substrate layer with spaced holes at the corresponding positions in the top and bottom layers. The fabrication of the sensor is shown in **Figure 2-11**. Radosavljevic et al. designed a resonant pressure sensor based on low-temperature co-fired ceramic (LTCC) technology, which was made by stacking seven layers of LTCC tapes with different dimensions and functions.[90] The evidence was reported in the literature, where a respiratory sensor was functioned by changing the overlapping area of the two electrode layers.[91] Vacuum seal technology was developed to create pure capacitive sensors, in order to increase the stability and accuracy. A vacuum sealed

capacitive pressure sensor which could be batch manufactured was developed by Chavan and Wise.[92] The sensor had a responsivity of 39 fF/torr. Another vacuum sealed capacitive sensor was created, achieving different gap thickness of 800 μm, 1000 μm, 1200 μm, and 1500 μm and responsivities of 0.08 pF/kPa, 0.12 pF/kPa, 0.15 pF/kPa and 0.2 pF/kPa, respectively.[93]

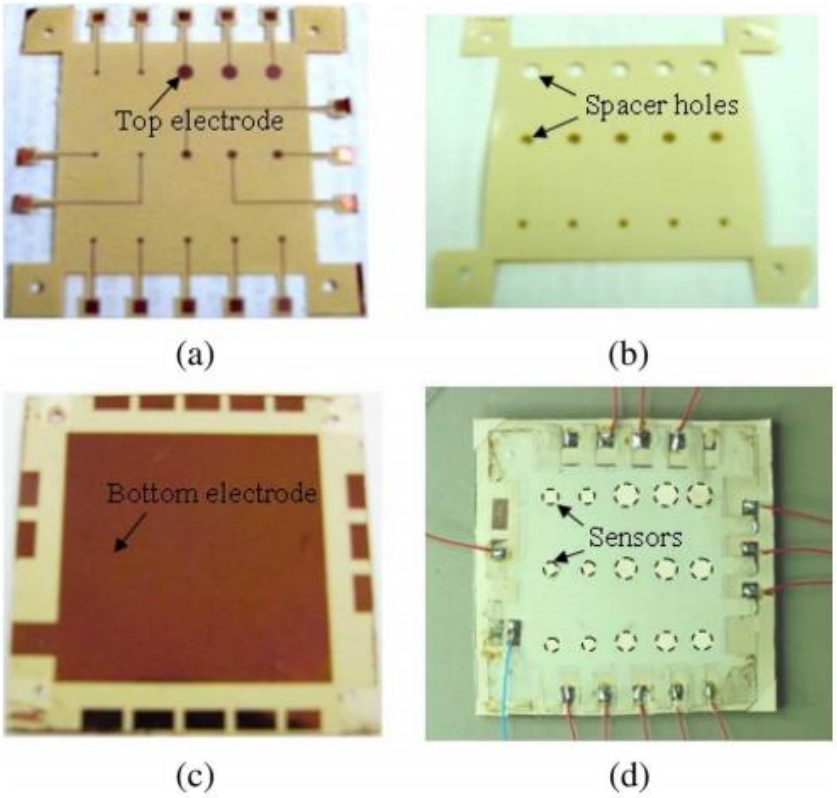

Figure 2-11. (a) top LCP layer with metallised patterns; (b) middle LCP layer with space holes;(c) bottom LCP layer with metallised patterns on the other side; (d) the fabricated sensor.[89]

Evidence shows that capacitive sensors are also used in the applications of cardiorespiratory monitoring. A flexible capacitive sensor was integrated into a mattress in order to monitor the user's sleep pattern.[94] Other capacitive-based sensors were created in order to detect the wearer's gait or cardiorespiratory signals during exercise.[95, 96] González-Sánchez et al. demonstrated in their research work report that the breathing and heart signals were able to be captured non-invasively and remotely on laboratory mice using capacitive-based sensors.[97]

The piezoelectric effect is that a crystalline material will generate electric charges while being subjected to force, which has similarity to the operational principle of the

capacitive sensors.[98] **Figure 2-12** shows the piezoelectric effect of a quartz crystal. Commonly known piezoelectric materials include piezoelectric ceramics (quartz, barium titanate, lead zirconate), electro Mechanical Film (a thin polypropylene with cellular structure) and polyvinylidenefluoride (PVDF).[98–100]

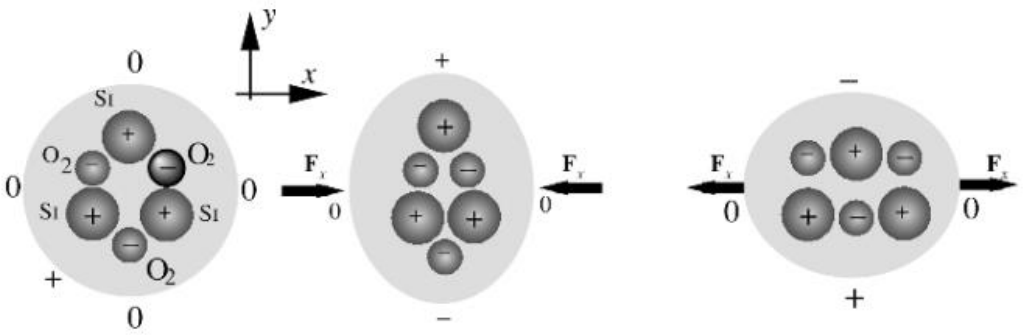

Figure 2-12. Piezoelectric effect in a quartz crystal.[98]

Due to the demand in the flexibility of the sensor materials used for portable/wearable cardiorespiratory monitoring applications, much attention has been put on PVDF. Pressing, stretching or bending the PVDF material will create noticeable voltage signal which can be measured for physiological activities. Evidence is found in the literature where PVDF based pressure sensors were widely investigated for in-sleep cardiorespiratory sensor applications;[42, 101, 102] Jiang et al. developed a PVDF based flexible sensor for cardiorespiratory sensing, which could be encapsulated in a flexible substrate pocket in order to eliminate the bending artefacts (as shown in **Figure 2-13**).[103] A potentially wearable PVDF sensor was developed, in the form of a fibre-type sensor with a metal core.[104] Other evidence shows that the cardiorespiratory signals can be obtained using PVDF material based on tensile stretching.[105] However, due to the fact that both PVDF and capacitive sensors are vulnerable to noise and motion artefacts, extra shielding processing or data filtering algorithm is essentially required for such sensors.[12]

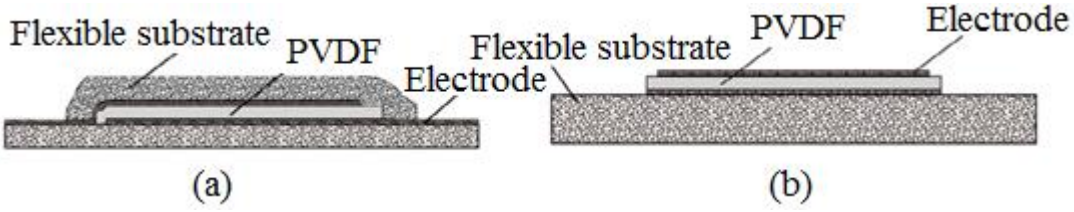

Figure 2-13. PVDF based flexible sensor. (a): bending in-sensitive. (b): bending sensitive.[103]

2.3.4 Piezo-resistive material based cardiorespiratory sensors

Because that chest movement is a ballistic force, the piezo-resistive material is widely studied and used in the application of cardiorespiratory sensing. The internal atom positions and their properties determine the resistivity of a material. If external force/strain changes the arrangement of the internal atoms, the electrical resistivity of the material changes accordingly. Therefore, piezo-resistivity is a material property that the electrical resistance of the material is dependent on strain.[106] The piezo-resistive material is naturally suitable for the cardiorespiratory monitoring application. The strong chest movement caused by respiration and even much smaller signals like pulses can generate resistance signal strong enough for detection and analysis.

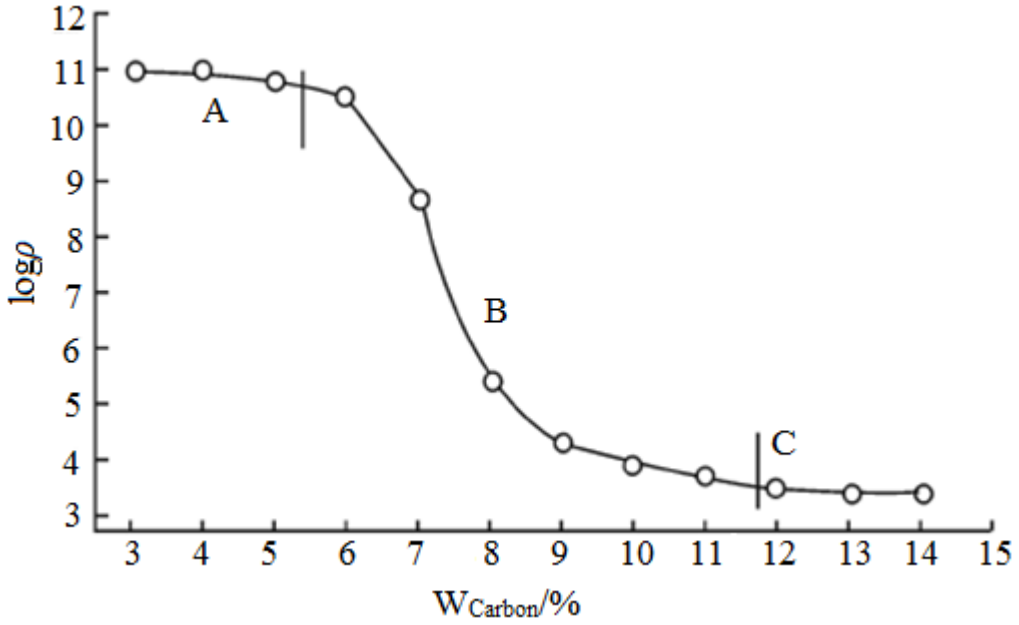

Figure 2-14. Relationship curve of carbon black content and resistivity of conductive rubber.[107] Zone A: Insulation zone. Zone B: Percolation zone. Zone C: Conductive zone.

Conductive rubber as a kind of piezo-resistive material has the advantages of easy acquisition of the signal, small thickness, and simple circuit design compared to capacitive and inductive sensors. Conductive rubber has been widely studied in the application of force or tactile sensors. Generally, the conductive rubbers are made from silicon rubber with an evenly distributed carbon black composition, which fulfils both the requirements of elasticity and electrical conductivity. The relationship between the content of carbon black composition and electrical resistivity of the conductive rubber

can be demonstrated in **Figure 2-14**. In the insulation zone (Zone A), where the carbon black particles are separated from each other, it is difficult to find a reliable electrical path. The conductive rubber shows a high resistivity. In the percolation zone (Zone B), with the increasing carbon black content, the conductivity of the conductive rubber material increases sharply. In the case of the conductive zone (Zone C), as the congeries links and electrical paths stabilise, the material maintains a high conductivity.[107]

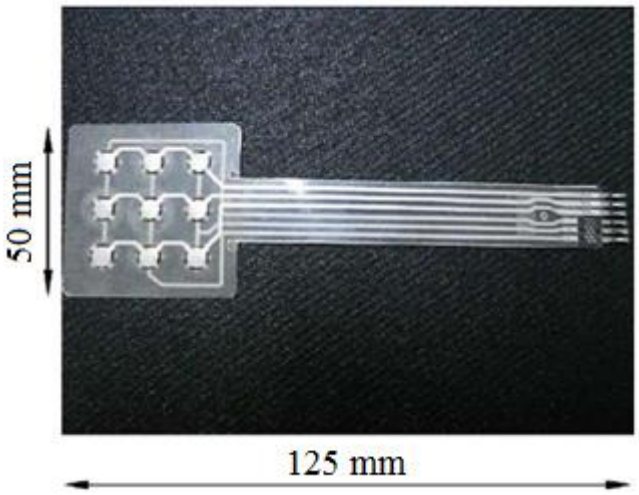

Figure 2-15. The fabricated sensor array.[108]

Zhang et al. developed a soft tactile sensor array based on silicon rubber.[108] The array design, as in **Figure 2-15**, was achieved by sandwiching the conductive silicon rubber with two layers of screen printed external layers, which reduced the complexity of the manufacturing process. The adhered multi-layer structure reduced the hysteresis in the sensing performance. Wettels et al. presented an individual electrode sensor based on silicone rubber in their report.[109] The silicon conductive rubber sensor simulated the function of human finger skin, which had a sensitive response to the force ranging from 0.1 to 30 N. A polyimide-based tactile sensor has been developed, of which the sensor array consisted of up to 32 by 32 unit cells.[110] The continuous pressure was able to be detected ranging from 0 to 1 N. Ohmukai et al. investigated several electrodes for conductive rubber piezo-resistive sensor.[111] They discovered that the tightness of the binding of the electrodes to the conductive rubber sheet determined the sensor performance. They concluded that among four types of electrodes (Al film, vacuum deposited Al rubber sheet, Cu film and silver pasted rubber sheet), the vacuum deposited Al rubber sheet provided the best potential in the application of a force sensor, due to the tightest binding. Huang et al. focused on the fitting of the sensor they

developed based on silicone rubber, carbon and nano-SiO_2.[107] What they concluded was that the piezo-resistive curve correlated better under a quadratic polynomial fitting. A novel 3D force tactile sensor was developed based on silicone rubber film added with carbon black, which can detect the size and direction of a 3D force.[112] Efforts have been made in order to reduce the thickness of the conductive rubber materials and thus improve their flexibility and drapability, such as developing an electrical-wire-stitched method (as illustrated in **Figure 2-16**) and using one-mask photolithographic process.[113, 114] As mentioned previously, conductive rubber has its advantages in sensitivity and linearity, while the flexibility requires improvement, which is one of the most critical parameters in portable and wearable cardiorespiratory applications. The hysteresis problem of the conductive rubber materials also result in the poor sensor reproducibility.[111] Therefore, the conductive rubber materials are more commonly used in the applications of force detection and robotic tactile sensors.

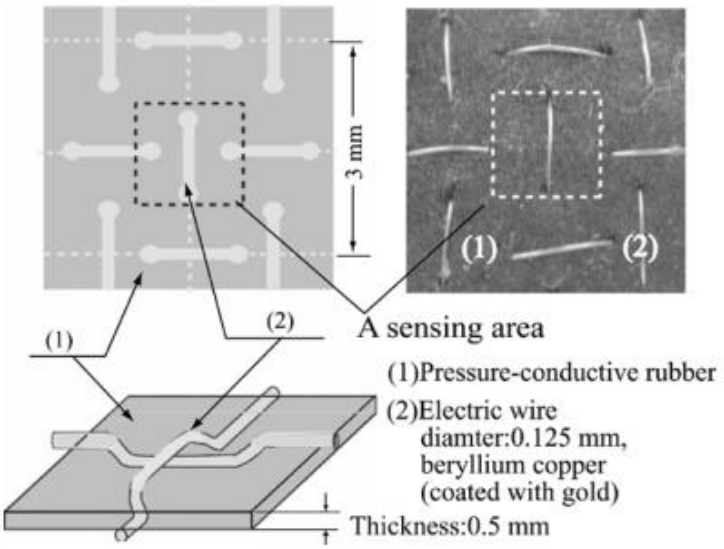

Figure 2-16. Electrical-wire-stitched technique.[113]

Piezo-resistive electro-textiles are natural electrodes with high structural flexibility, which are much more suitable for wearable cardiorespiratory monitoring systems than other non-flexible electrodes. They are widely used in the applications of monitoring sleeping positions, postures and cardiorespiratory signals. Evidence was found in literature where a piezo-resistive material based sensor was used to monitor respiration in sleep monitoring application.[115] The respiration sensor provided more accurate results while it was placed underneath the mattress than on top of it, which was due to

the fact that the sensor placed on top of the mattress did not have a firm contact to the subject at all time if the subject changed sleep position or posture. The weight of the mattress increased the stability of the sensor as well. It was also found that the biasing pressure was essential for the sensor to be functional. Another cardiorespiratory and motion sensor for sleep monitoring was developed based on piezo-resistive material, which was reported as 99% accurate in detecting sleep position.[116] The sensor was pressed on the left chest of the subject by a belt instead of being underneath the mattress so that the weak heart signal was able to be captured. Other than sleep monitoring, piezo-resistive electro-textile material based sensors can also be used for wearable monitoring applications. Evidence was found in literature where piezo-resistive fabric sensors were created using knitting or printing technology, in order to be integrated into the garment to capture the cardiorespiratory signals.[117] Another report showed that a textile-based piezo-resistive sensor was developed in order to acquire respiratory signal under clinical, exercise and gravitational conditions (as shown in **Figure 2-17**).[118, 119] Taylor and Chapin invented a flexible piezo-resistive and piezo-capacitive hybrid force and pressure sensor, which potentially can be used in cardiorespiratory applications.[120]

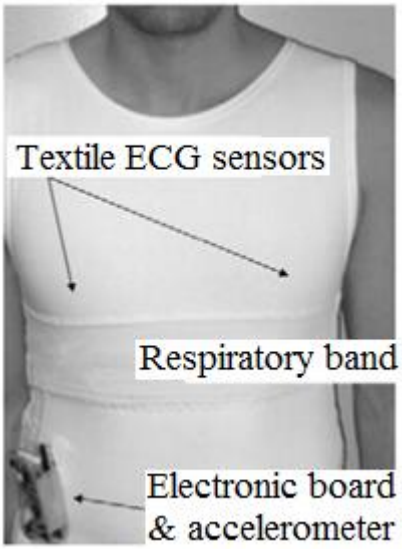

Figure 2-17. Sensor setup for clinical, exercise and gravitational conditions.[119]

Melnykowycz et al. conducted a report that vital signals such as systole and diastole blood pressures can be measured using the piezo-resistive material as well.[121] The developed wrist sensor was able to detect the motion artefacts of the wrist and finger

movements; however, the signal curves showed very similar in shape so that only the movements could be detected but not the gestures. A clear heartbeat pattern can be observed with a large amount of fluctuations which implied that noise filtering and data smoothing was required for piezo-resistive type of cardiorespiratory sensor. Hamdani and Fernando developed a piezo-resistive material based cardiorespiratory sensor used in car seat belt application.[122] The piezo-resistive cardio-respiratory sensor was pocketed in the car seat belt in order to ensure a firm and stable contact between the sensor and the subject. Other than the fabric-based sensors, Huang et al. conducted a yarn based piezo-resistive strain sensor, which showed superior linearity and sensitivity (as shown in **Figure 2-18**).[123] However, due to the fact of the strain sensor, it was not suitable for capturing BCG signal on the chest as the strain change of the BCG signal was too small.

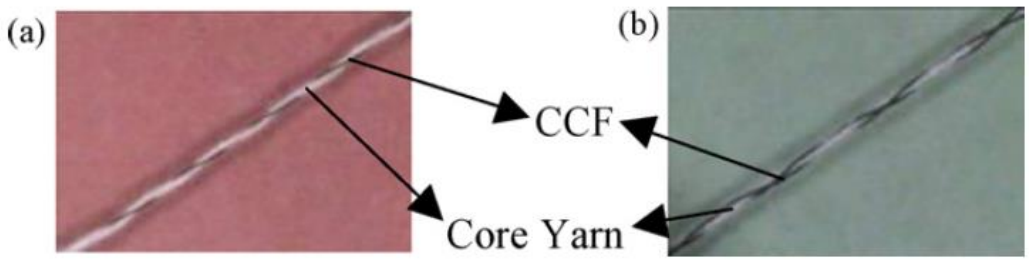

Figure 2-18. Carbon-coated fibre twisted yarn. (a): Single wrapped; (b) Double wrapped.[123]

2.4 Electroconductive inks

Electroconductive ink is an ink that consists of electroconductive particles which can be used for smart textile applications. Depending on the impregnation methods, electroconductive inks can be used to turn conventional textile materials to piezo-resistive materials for strain sensing or capacitive materials as pressure sensors.[124–126] The electroconductive ink used in electro-textile applications has three key features: low viscosity of the ink, highly dispersed solution, and high electrical conductivity.[127] The low viscosity of the ink allows the ink perform uniformly under all circumferences; in the aspect of inkjet printing application, this can also prevent the nozzle from the blockage.[128] The highly dispersed solution ensures the ink free from unnecessary agglomerations which may negatively influence the quality of the ink, and

further affect the performance of the applications based on such ink. The most commonly known applications using electroconductive inks include printed circuit boards, electrodes, electro-textile material based sensors, which require the high electrical conductivity of the ink. The three key features have an influential on each other; report shows that the viscosity of a silver particle ink with nanoscale particle size slowly increased by 0.4% per 20 days over 4 months, eventually resulting in agglomerates in the ink and poor performance of the sensor.[127] In order to obtain low viscosity and highly dispersed ink, it is essential to reduce the particle size in the ink.

Additionally, due to the strong π-π and Van der Waals forces, nanoscale particles tend to agglomerate to large particles.[129–131] Many efforts have been made to avoid agglomerations during the manufacturing process and/or prevent the fabricated ink from further agglomeration. Using stabiliser or protective coating during the manufacturing process is the most commonly used technology in order to prevent agglomeration in the fabrication of electroconductive inks.[132] Other technologies used in order to obtain agglomeration-free electroconductive ink involve mechanical dispersion, using surfactants and surface modification.[133–137]

2.4.1 Metallic electroconductive inks

The electroconductive inks mainly consist of different kinds of metallic-based inks, such as silver, copper, gold, and aluminium.[132] As mentioned previously, nanoparticle-based metallic conductive inks require an additional stabiliser, usually polymeric material, to ensure the reproducibility of the ink. Compared with silver based conductive inks, other metallic based inks either have the problem of rapid oxidisation (copper and aluminium based inks) or higher cost (gold-based inks).[138, 139]

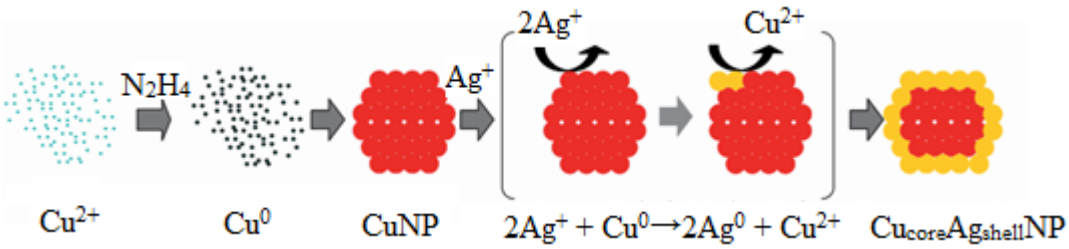

Figure 2-19. Schematic diagram of silver coating on a copper nanoparticle.[140]

A technology of coating copper nanoparticles with silver was developed to resolve the issue of oxidisation in copper-based nanoparticle inks.[140] With a silver coating of 2

nm, the encapsulated copper nanoparticles stabilised from oxidisation after being inkjet printed, as shown in **Figure 2-19**.

Gold nanoparticle ink can be synthesised using the following methods:

a) physical methods: photochemistry, radiolysis, sonochemistry;[141–143]
b) chemical methods: borohydride reduction and citrate reduction;[144–146]
c) biosynthesis methods;[147, 148]
d) seed growing methods.[141, 149]

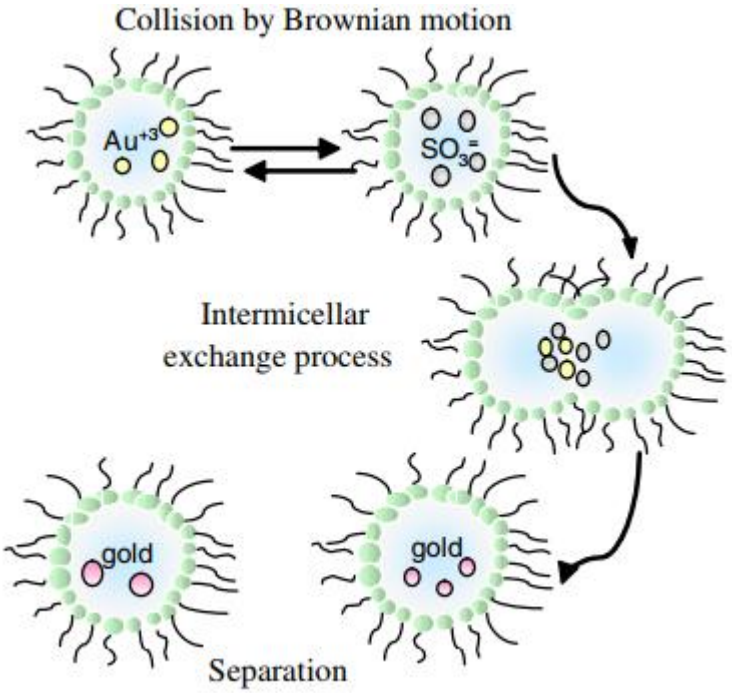

Figure 2-20. The concept of the separation of gold agglomerates.[150]

Physical methods generally synthesis gold nanoparticle in a short period of time which require extra and precise control.[151] Chemistry methods provide mild reaction process and aqueous results, which is more suitable for electroconductive ink applications. Biosynthesis methods use bacteria to reduce gold compound to nanoparticles, which have the advantages of the clean and nontoxic procedure. Seed growing methods use external energy source (electron-beam lithography) to stimulate the chemical reaction of gold compounds and other chemicals on a substrate. The agglomeration of gold nanoparticles can be prevented using nylon membranes or sodium bis-(2-ethylhexyl) sulfosuccinate based reverse micelles (as illustrated in **Figure 2-20**).[150, 152]

Silver elemental is the other popular metallic particle used for electroconductive ink. Silver has a very low electrical resistivity of approximately 15.87 nΩ·m.[153] Additionally silver also has a remarkable cost to performance ratio making it much more preferable in industrial applications. The literature describes a research in which a silver nanoparticle ink, synthesized for inkjet printing, with a particle size from 50 to 100 nm and 49% of the silver content.[154] Walker et al. described a synthesis method using silver acetate to create silver nanoparticle ink with a very low ink viscosity suitable for inkjet printing.[155] Polyvinylpyrrolidone (PVP) is commonly used as a stabiliser in the silver particle ink in order to avoid silver agglomerations.[154, 156, 157] Acid can be used as a stabiliser for silver nanoparticle electroconductive ink as well.[127] Literature also reported that acrylic resin was one candidate that can be used to prevent silver agglomeration, however, with a loss of resistivity of the silver ink.[158] A silver particle-based conductive ink was developed which was capable of self-healing from scratch damage of a gap up to 25 µm wide.[159] Such silver ink consists of encapsulated hexyl acetate solvent which was released due to scratching. If the printed surface was damaged, the released hexyl acetate would re-dissolve the silver particles near the scratching so that these silver particles could recover the printed surface after the hexyl acetate being evaporated (as illustrated in **Figure 2-21**).

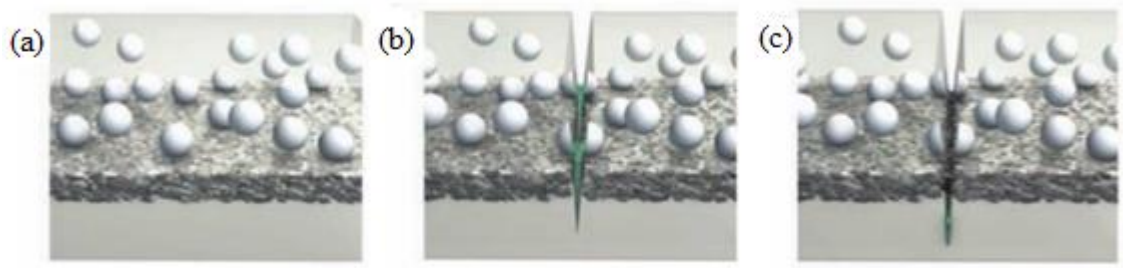

Figure 2-21. The concept of self-healing silver ink. (a): before scratching; (b): immediately after scratching; (c): after restoration.[159]

2.4.2 Carbon/graphene-based electroconductive ink

Carbon nanotube (CNT) and graphene materials are newly discovered as an excellent candidate for electroconductive inks. The superior electrical conductivity and mechanical properties make CNT and graphene the most popular material during the recent years. Evidence was found in the literature that inkjet printed film sensors using CNT were developed, which had high optical transmittance and excellent electrical

conductivity.[160, 161] Graphene is a two-dimensional sheet made of hexagonal lattice carbon atoms, which is the material with the lowest resistivity at room temperature.[162, 163] Currently, the reduction of graphene oxide (GO) is the most promising method to create graphene.[164] The reduction process requires at least 24 hours in order to achieve 90% weight percentage of carbon element. Reduced graphene oxide (RGO) is the most often used graphene material for the electroconductive ink-based applications. Similar to the CNT material, RGO is most preferred in the production of printed films for different applications, such as gas sensors, pressure sensors and humidity sensors.[165–167] Little work has been reported regarding the graphene ink impregnated/coated textile materials. Supercapacitor electrodes were developed by using controlled electrodeposition of MnO_2 on graphene coated fabrics.[168] Other reductive agents such as sodium dithionite, sodium hydrosulphite and hydrazine were investigated in order to create graphene modified textile materials.[169–171] However, due to the fact that if being deposited onto the randomly oriented substrates (fibre/fabric surface), the electroconductivity of CNT/RGO is significantly affected due to the non-uniform orientation.

2.4.3 Impregnation methods

As the core process in the ink based microelectronic technology, the impregnation methods have been widely investigated and well developed over decades. Screen printing and gravure printing are relatively old techniques, which have the advantages of low cost and simple principles. However, products based on these two methods are less precise than inkjet printed products, as the printing position of screen printing and gravure printing are generally controlled manually. Now the inkjet printing technology is highly researched worldwide. Also, some new approaches, such as omnidirectional printing which is used in tissue engineering, have placed more focus on the applications required for better bending capabilities. Additionally, dip-coating technology is the other method that can be used for producing not only electroconductive material coated thin film sensors but also electroconductive particle coated fabric materials.

2.4.3.1 Inkjet printing

Inkjet printing technology has been widely used in the area of printed circuits for electronic construction. The electronic circuits could be of use as computer components,

capacitors and transistors. As shown in **Figure 2-22**, inkjet printing technology simplifies the process of creating high-precision devices.[172]

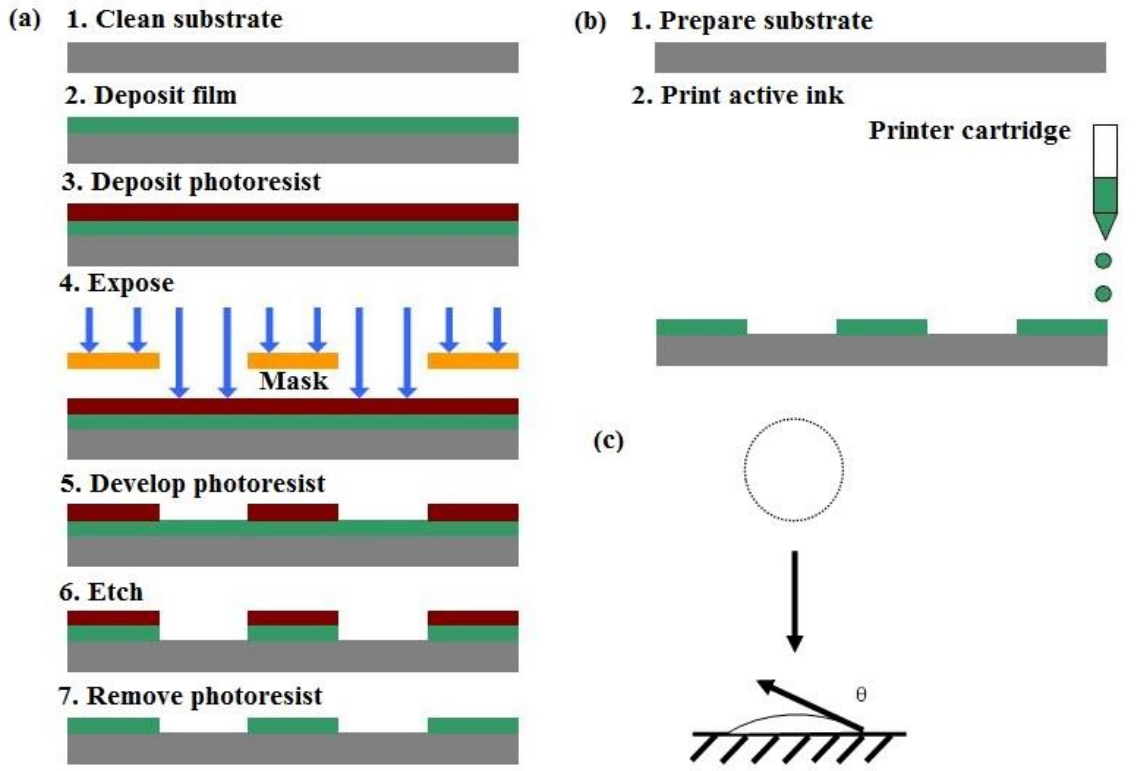

Figure 2-22. A comparison of the processing steps involved in subtractive microfabrication and additive direct write printing. (a): traditional microfabrication. (b): inkjet printing technique.[172] (c): a theoretical model of an ink droplet deposits on a solid substrate.

The factors that are critical to the quality of the ink used for inkjet printing are studied thoroughly. In fluid dynamics, there are three controlling quantities, the Weber number (*We*), the Ohnesorge number (*Oh*) and the Reynolds number (*Re*) which are used to determine the deposition and solidification of a droplet. '*We*' and '*Oh*' can be presented in the following equations:[173]

$$We = \frac{\rho V^2 a}{\sigma} \qquad \textbf{Equation 2-3}$$

$$Re = \frac{\rho V a}{\mu} \qquad \textbf{Equation 2-4}$$

$$Oh = \frac{\sqrt{We}}{Re} = \frac{\mu}{\sqrt{\rho a \sigma}} \qquad \textbf{Equation 2-5}$$

where: ρ is the density of the liquid; a is the diameter of the drop before impact; V is the impact velocity; σ is the surface tension; μ is the viscosity of the liquid.

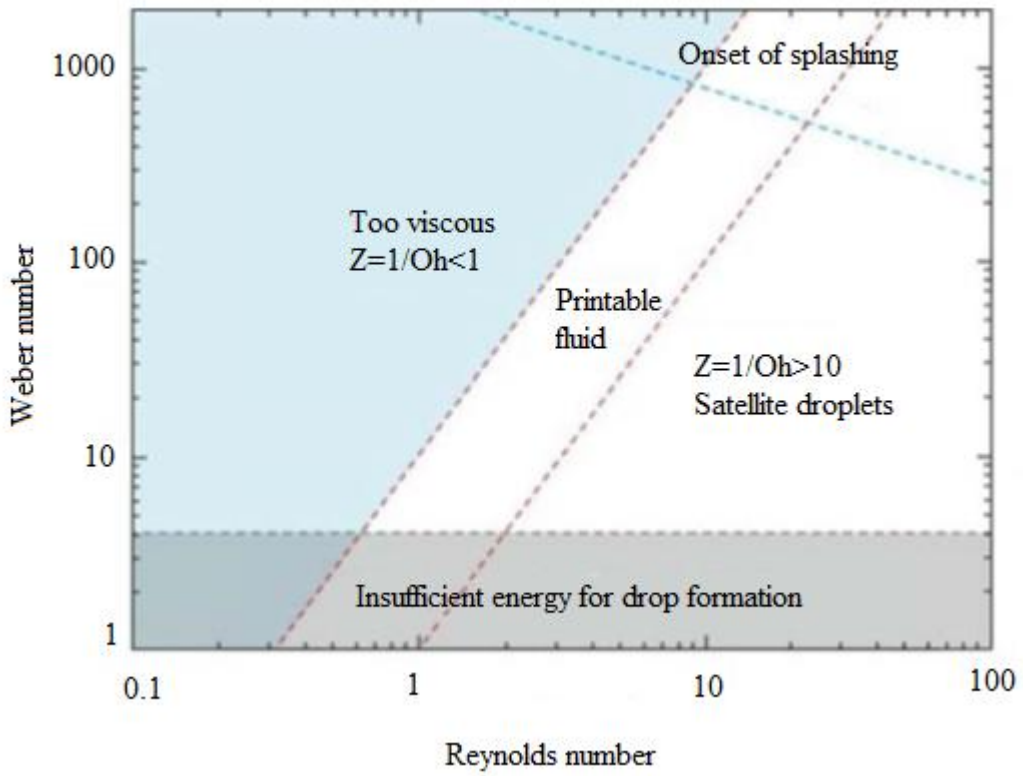

Figure 2-23. Ink suitability for printing using non-dimensional numbers.[173]

A droplet with a lower '*We'* value holds its shape independently of its impact velocity after deposition. '*Oh'* value relates the viscous forces to inertial and surface tension.[174] '*Re'* is the ratio of inertial forces to the viscous forces, as illustrated in **Figure 2-23**.[173] Schiaffino and Sonin classified the drop impact into four types:[174]

1) when '*We'*>>1 and '*Oh'*<<1, fluid behaves like an inviscid fluid;
2) when '*We'*<<1 and '*Oh'*<<1, the motion of the inviscid fluid depends on its capillarity;
3) when '*We'*<<1 and '*Oh'*>>1, the capillarity and viscosity of the fluid become more important;
4) when '*We'*>>1 and '*Oh'*>>1, the kinetic energy and viscosity of the fluid determine the deposition.

Through further investigations, the wettability of the solid substrate was another important factor which determined the performance of the deposited droplets.[175] It

was found out that compared with '*We'* and '*Oh'* values, the wettability of the solid substrate was more important in the droplet deposition. Smith et al. [176] and Doggart et al. [177] investigated the relationship between the width of the printed pattern, droplet diameter and the space between adjacent droplets. The dimensions of the printed pattern were found adjustable via changing the solvent composition or the viscosity of the ink (as shown in **Figure 2-24**).

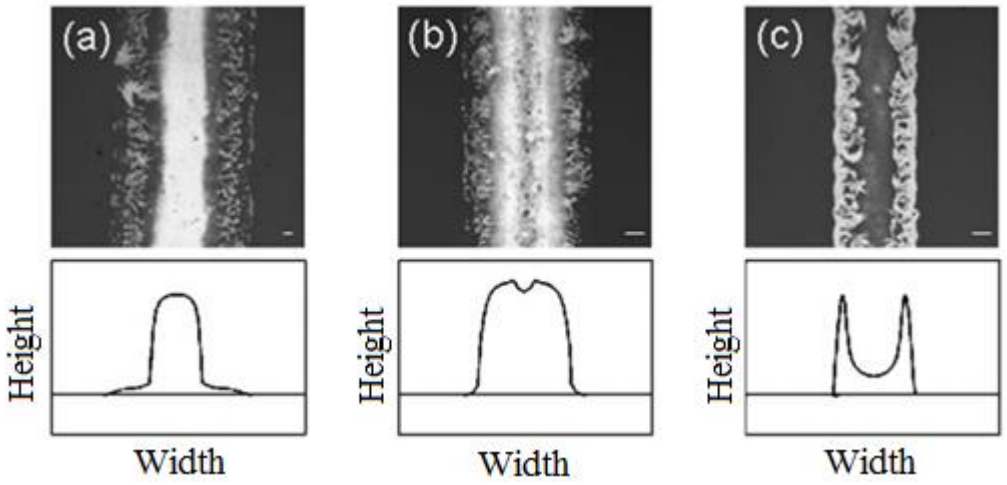

Figure 2-24. Optical image and typical cross-section sketch for annealed silver precursor lines printed at a dot-to-dot spacing of (a) 20 μm, (b) 40 μm, and (c) 80 μm.[177]

O¨hlund indicated in the thesis that the roughness of the substrate surface was the most important feature in terms of inkjet printed conductive materials.[178] A higher surface roughness would eventually result in a thicker coating, which would adversely affect the electrical conductivity of the conductive layer. Therefore, a sufficiently small value of surface roughness and porosity were beneficial for the printing and electrical performance of the material. However, reducing the surface roughness of the substrate would limit the range of electroconductive ink feasible, because the printing quality and electroconductivity of the coating rely on the matching of the surface energy of the substrate and surface tension of the electroconductive ink. In order to obtain a smooth surface of the printed sensor, hexamethyldisilazane (HMDS) treatment was found useful in reducing the surface energy of the substrate, thereby reducing the roughness of the printed film.[179–181] Using HMDS treatment, silver nanoparticles were deposited onto the cellulose film substrate in order to create an organic transistor.[182] Li introduced a flexible capacitor on a polyester substrate fabricated by inkjet printing

technology.[172] Another type of substrate, such as photo paper can also be used to print memory cards for cost-efficient applications.[183] The feasibility of hydrophobic substrate was studied.[184] They used ascorbic acid as a reducing agent and investigated copper salts, including copper sulphate and nitrate, and silver salts, such as silver nitrate, carbonate, acetate and chloride. Eventually, they found that among all metallic salts, copper sulphate and silver nitrate had the best water solubility, which was important in terms of inkjet useable ink. However, copper particles suffered from a more severe oxidisation problem than silver.

The electrical properties of a capacitor produced by inkjet printing were also investigated.[185] As demonstrated in the research reports, the relative permittivity and loss tangent of the inkjet printed Metal-Insulator-Metal capacitors were approximately 70 and 0.011 at 1 MHz, respectively.[186, 187] Low electrical resistance gold printed electrodes were able to be obtained using a cost-effective method of fabrication multi-layer electric components based on inkjet printing technology.[188]

2.4.3.2 Omnidirectional printing

Omnidirectional printing technology is established in 3D printing in the area of tissue engineering.[189] However, recently, it has been shown to offer a novel approach for printing electronics. Ahn succeeded in developing a technology for printing 3D microelectrodes using omnidirectional printing.[190, 191] The flexible and stretchable microelectrodes could withstand repeated bending and extension to a high level. This technology could be applied to a solar cell or light-emitting diode arrays.

2.4.3.3 Dip-coating

Dip-coating is a technology initially developed for mass production of coated fabrics; now it is also widely used for creating conductive thin films, conductive nanowires and conductive textiles, coated with different metallic or carbon-based colloid, which are integrated into applications including high transparency display electrodes, sensors, heating fabrics, solar cells and supercapacitors.[192–197] There is some evidence of dip-coated electro-textile materials found in literature: a three-dimensional silver nanowire sponge structure was created using dip-coating technology, which combined the high electrical conductivity with the sustainable mechanical properties of cotton;[194] other cotton based electroconductive fabrics were also developed using dip-coating technology;[198, 199] wool fabrics were treated with electroconductive

solvent as well in order to obtain electroconductivity.[200] Electro-textile based interconnectors can also be produced by dip-coating.[201]

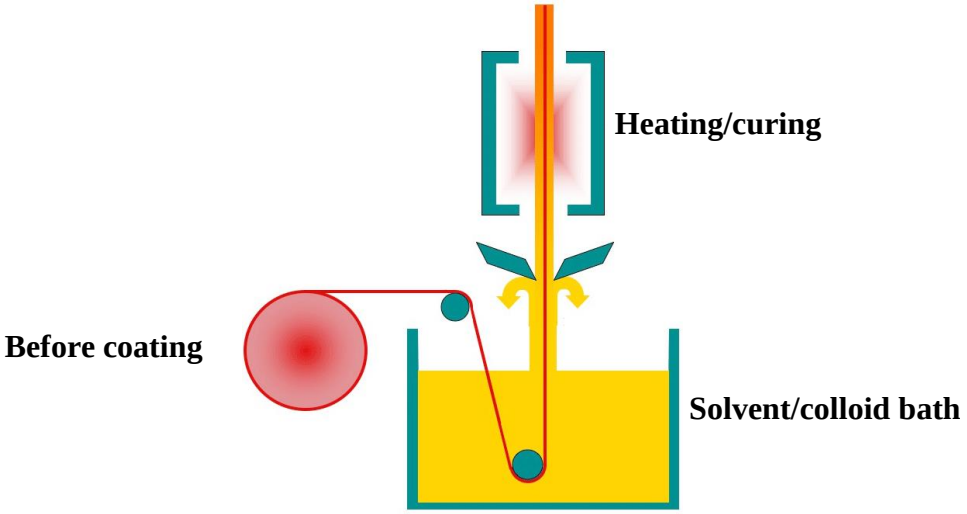

Figure 2-25. A schematic of the continuous dip coating process.

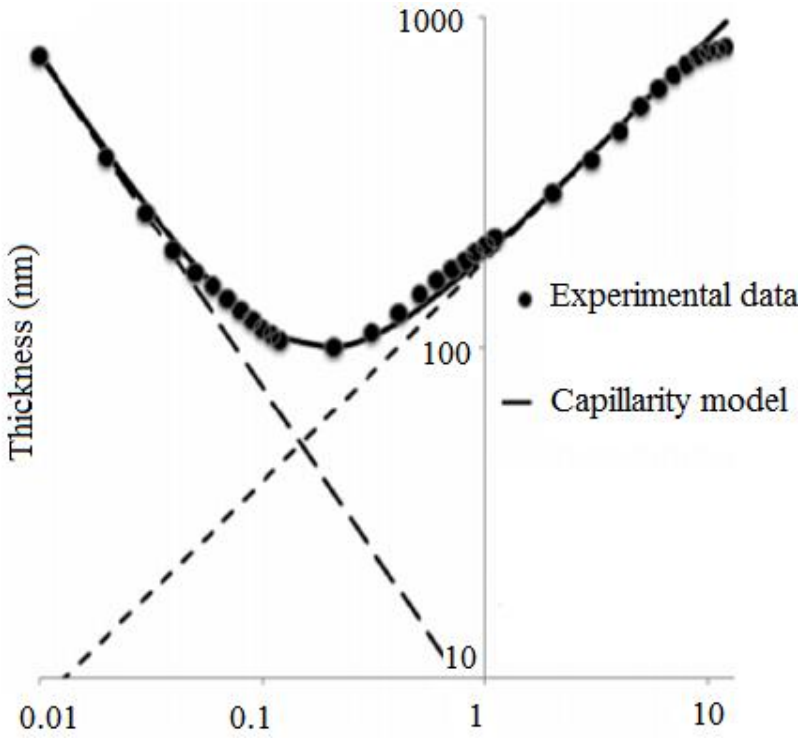

Figure 2-26. The relationship between dip coating thickness and speed.[202]

Figure 2-25 explains the procedure of dip coating process. The prepared material needs to be immersed in the solvent/colloid bath thoroughly and withdrawn from it at a specific speed in order to achieve required coating concentration and thickness. Depending on the type of solvent and substrate, the curing process is necessary. The

relationship between the coating thickness, curing condition and withdrawal speed has been studied. Faustini et al. demonstrated the relationship between dip coating thickness and speed in their work report.[202] It was shown in **Figure 2-26** that at different scales of speed, the thickness of the coating was depended on different factors. Generally speaking, the thick coating can be achieved at either high speed or low speed; however, higher speed will cause more fluctuation. In order to achieve ultrathin and uniform coating, an intermediate and uniform speed must be used. The withdrawal speed was also found critical to the interplanar spacing and pore size of the coating.[203]

2.4.3.4 Screen printing

Screen printing has been used for fabricating capacitive sensors since the middle of last century.[204, 205] Screen printing has the advantages of low-cost, simple principles and suitability for batch production.[205] Applications include capacitors, as a generator of energy harvesting systems, and electrodes for detection sensors.[204–206]

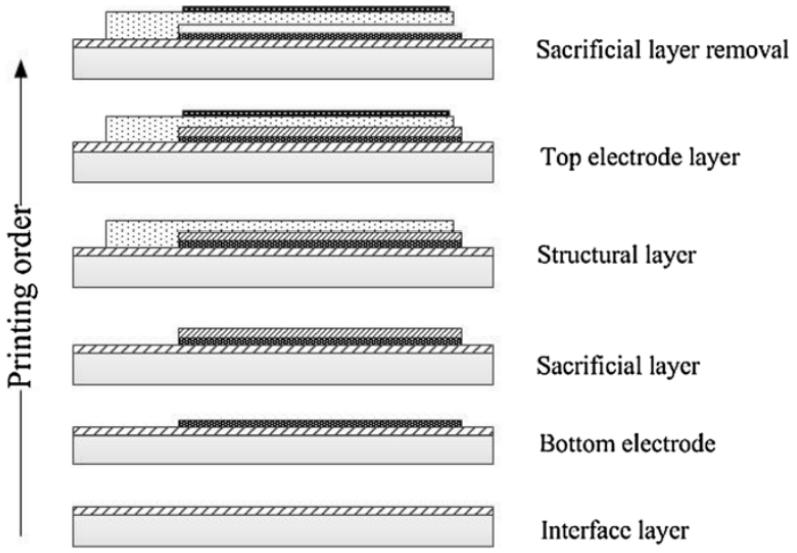

Figure 2-27. Printing sequence of a capacitive cantilever.[207]

A screen-printed capacitive motion sensor based on a novel cantilever has been developed.[207] A certain screen printing order was developed for the different function layers, including an innovative sacrificial layer (trimethylolethane TME) which was later removed to create the cantilever structure, as shown in **Figure 2-27**. An interface layer was used to reduce the fabric surface roughness and to achieve a smooth and flat

layer for subsequent layer printing. The motion sensor was able to detect human movement at low frequency.

2.4.3.5 Gravure printing

Gravure printing requires low temperature and less usage of resources while providing good quality throughout.[208] An organic thin film transistor sensor was fabricated by gravure printing.[209] The vapour polymerisation method was used to help form a thin conductive film to create a conductive polymer thin-film-transistor (TFT). However, this method is restricted to only a few materials, such as poly(3,4-ethylenedioxythiophene) (PEDOT) and polypyrrole (PPy), and does not have a good performance due to it not reproducing semiconductor capability.

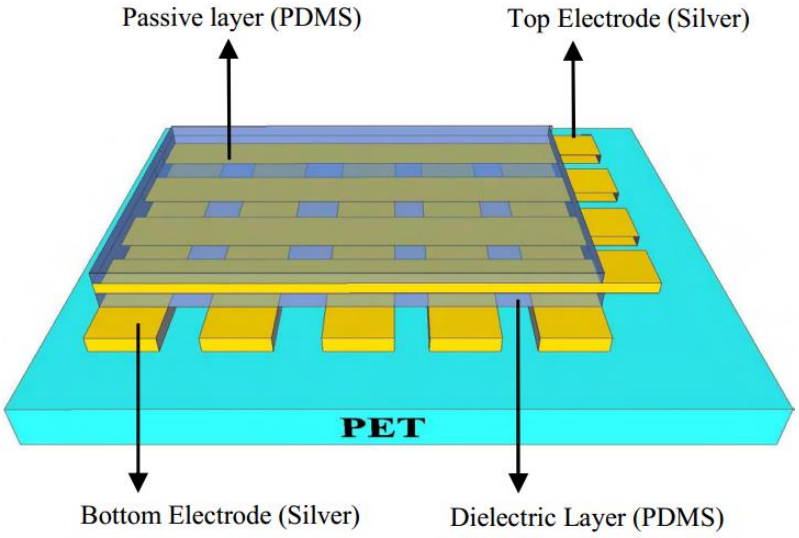

Figure 2-28. Schematic of the gravure and screen printed pressure sensor.[210]

Narakathu et al. developed a flexible gravure and screen printed capacitive pressure sensor which was capable of detecting pressures from 800 kPa to 18 Mpa.[210] The sensor was based on a polyethylene terephthalate substrate, on which firstly silver electrode bars were gravure printed. Then a polydimethylsiloxane (PDMS) layer was screen printed as a dielectric layer. With the combination of gravure and screen printing, the fabricated sensor was highly flexible and had a thickness of 200 µm (as shown in **Figure 2-28**).

Comparing with the different impregnation methods discussed above, it can be concluded that inkjet printing, screen printing and gravure printing technologies are more suitable for the applications either based on capacitance or for strain sensing if

using the piezo-resistivity of the sensor. Omnidirectional printing is able to produce the sensors directly from the electroconductive ink. However, the rigidity of the sensor material and unique professional machinery make omnidirectional printing technology difficult to be used in the current research. From literature, it was found that dip-coating method is more suitable for creating fabric based flexible sensing materials with uniform properties.

2.4.4 Sintering process

As mentioned previously, nanoscale particle ink requires the nanoparticle to be encapsulated in a protective coating to reduce the viscosity of the ink. Therefore, after being printed onto the film, it is necessary to remove the insulating protective coating to increase the conductivity of the printing. This process is called sintering. Approaches to sintering range from room temperature drying to using energy from a flashing light.[211] **Figure 2-29** visualises the typical thermal sintering process.

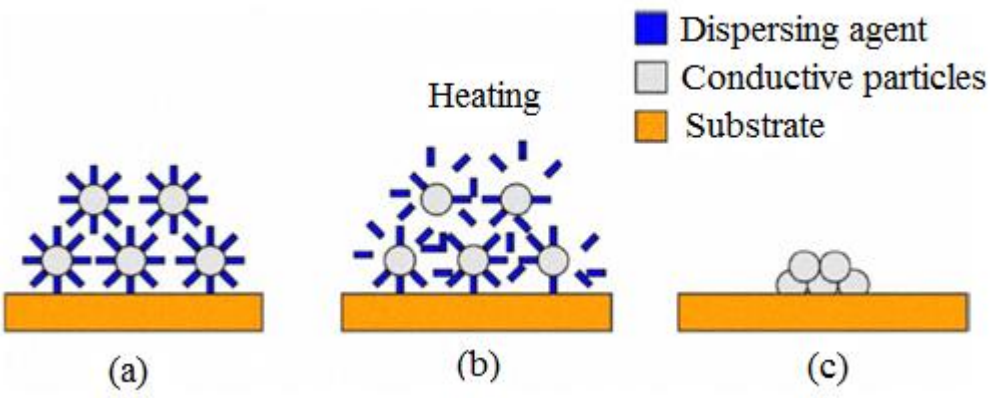

Figure 2-29. Thermal sintering process.[212]

2.4.4.1 Thermal sintering

The common way of sintering silver nanoscale ink is heating. Falat et al. studied the influence of sintering parameters on resistivity.[213] They found that at 250 °C sintering for 1 hour showed promising results even for low silver content samples. Also, they found that with lower silver content, the silver pattern might have a hairy fuzzy appearance. Mancosu and his colleagues discovered that a sintering temperature below 100 °C would cause the treatment to be incomplete therefore leading to a poor electrical conductivity.[212]

2.4.4.2 Laser and plasma sintering

Ma et al. carried out a study on argon (Ar) plasma sintering of silver nanoparticles.[214] However, the conductivity of the Ar plasma sintering was lower than that of thermal sintering. Tobjörk et al. used an IR lamp to sinter silver and gold particles.[215] They found IR-sintering could be used for different substrates, including paper, plastic and glass. The resistivity values of the samples were reduced to 10 μΩ cm and 25 μΩ cm, for Ag and Au samples respectively. However, the sintering time and intensity required extra consideration to avoid the coffee ring effect on the substrate.

UV light can also be used to sinter silver particles. **Figure 2-30** shows the results of the research on UV-sintering done by Polzinger.[216] It can be found that UV sintering gives a resistance value close to the thermal sintering process.

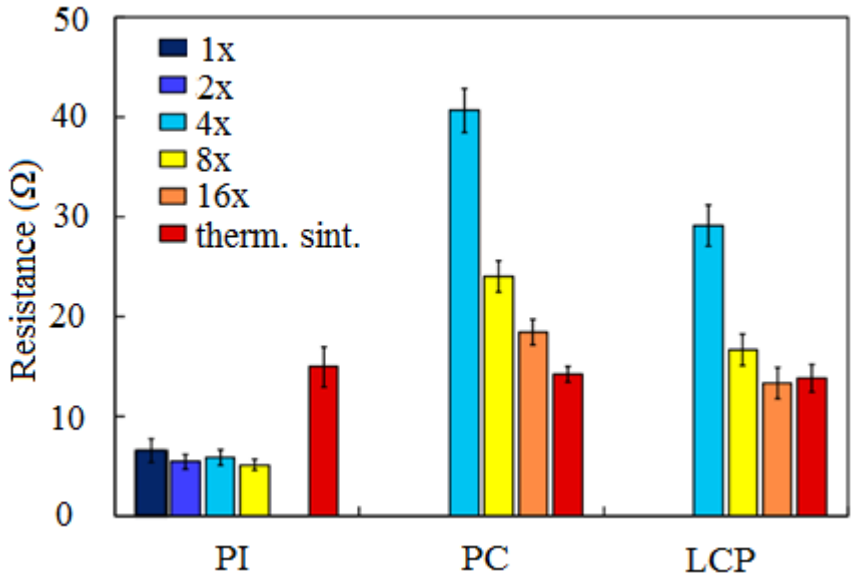

Figure 2-30. The resistance of UV-cured (1, 2, 4, 8 and 16 runs) and thermally sintered silver tracks on three different substrate materials (Polyimide, Polycarbonate, Liquid Crystal Polymer).[216]

Allen et al. discovered a sintering method based on temperature-sensitive photo paper.[217] The developed method was applied to sinter the silver nanoparticle arrays, the procedure of which was fast and required a lower temperature than the conventional thermal heating method. This method had the potential for sintering other materials, such as transparent indium tin oxide and semi-conductive materials.

2.4.4.3 Microwave sintering

Microwave sintering is also a useful approach for the creation of a conductive silver deposition on a polymer-based substrate. The absorbed power (P) per unit of the silver deposition and the depth (d_p) of the radiation can penetrate are calculated as below:[218]

$$P = 2\pi f \varepsilon'' E^2 \qquad \textbf{Equation 2-6}$$

$$d_p = \frac{1}{\sqrt{\pi f \mu \sigma}} \qquad \textbf{Equation 2-7}$$

where: f is the frequency of the microwave radiation; ε'' is the dielectric loss factor; E is the amplitude of the electromagnetic field; μ is the permeability of the material (substrate or silver layer); σ is the conductance.

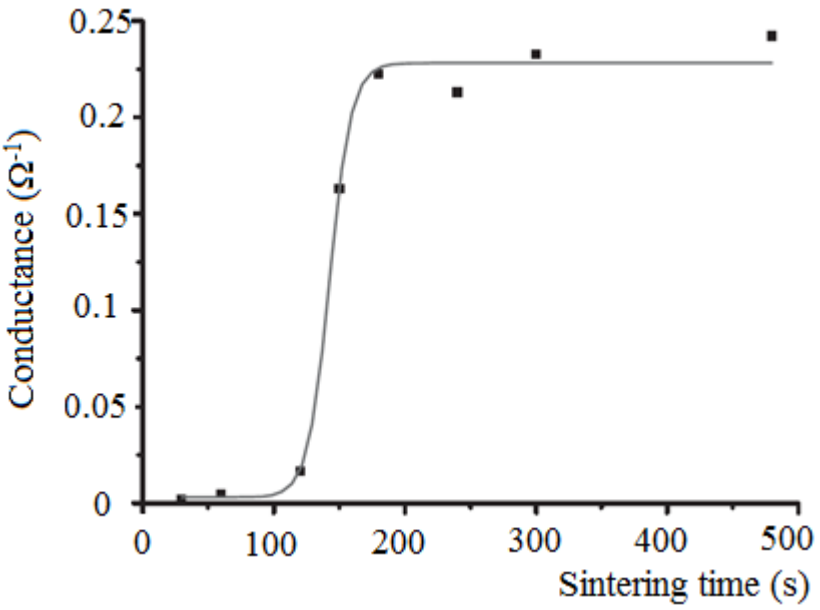

Figure 2-31. Microwave sintering on a silver paste printed Polyimide substrate.[218]

It can be seen in **Figure 2-31** that microwave sintering greatly reduces the treatment time required compared with thermal heating treatment. However, microwave radiation can just penetrate the conductive coating within a small depth.[219, 220]

2.4.4.4 Chemical sintering

The chemical soaking treatment had limited effect on silver particles. Magdassi et al. developed a new approach for sintering silver nanoparticles at room temperature with

the help of poly(diallydimethylammonium chloride) (PDAC).[221] This new approach allowed the sintering of paper or plastic substrates.

2.5 Summary

In this chapter, the fundamental background of bio-signals and cardiorespiratory monitoring has been introduced. Different types of portable and wearable cardiorespiratory sensors and the manufacturing methods in order to create such sensors were also discussed.

From the literature, it was learnt that BCG technology was found more suitable than ECG technology in the aspect of wearable and portable monitoring applications. Other than conventional electronics, electro-textiles based on knitted, woven and nonwoven fabrics have been widely investigated as the core materials used to create cardiorespiratory sensors, among which nonwoven fabrics have the advantages in the absorption of electroconductive inks and the response to pressure changing.

Depending on the operational principles, existing applications of wearable cardiorespiratory sensors can be classified into four categories: inductive sensor, fibre optic sensor, piezoelectric/capacitive sensor and piezo-resistive sensor. In order to acquire the cardiorespiratory signals under ambulatory conditions, piezo-resistive pressure sensors were discovered as the best candidate due to its high sensitivity to the weak BCG signals and better resistibility to noise and motion artefacts.

Electroconductive inks are the key to turning the normal textiles into electro-textile materials. During the literature survey, it was found that silver, copper, gold and carbon black particle based electroconductive inks were commonly used to create electro-textile materials. In order to obtain the electroconductive ink that is suitable for cardiorespiratory sensing, the electroconductive particles require coating to prevent the ink from agglomerations and sintering to improve the electroconductivity after impregnation.

Chapter Three: Methodology

3.1 Introduction

Construction and characterisation of nanoscale silver particle-based ink impregnated nonwoven piezo-resistive sensors have been selected as the focus of the current research. The justification for this decision was discussed within the literature survey in Chapter Two and summarised in section 2.5.

In this chapter, the working principle of a nonwoven fabric material as a piezo-resistive pressure sensor and the methodology of constructing and testing the sensor are described in detail, including the preparation of the nanoscale silver particle-based electroconductive ink, ink impregnation procedure and sensor design and fabrication, together with a summary of the samples that have been investigated in this research.

Additionally, this chapter introduces the test procedures that have been used in this research for the characterisation of the piezo-resistive nonwoven sensor materials and investigations of the sensor performance in capturing cardiorespiratory signals.

3.2 The operational principle of nonwoven fabric based piezo-resistive pressure sensor

As mentioned in section 2.3.4 the electrical resistance of a piezo-resistive material is manufactured in such a way that it responds to the change of external force. Therefore, the operational principle of a fabric-based piezo-resistive pressure-sensitive material can be illustrated in **Figure 3-1**.

1) In the beginning, the un-impregnated nonwoven fabric remains electrical insulated.
2) By applying electroconductive particles, the nonwoven fabric becomes a piezo-resistive material. The electroconductive particles are expected to be deposited evenly throughout the fabric. At this stage, a limited amount of electrical paths are created from the top surface to the bottom, resulting in a relatedly high electrical resistance.
3) On the application of a mechanical pressure, the thickness of the fabric will reduce and cause the electroconductive particles to become closer. Eventually, more electrical paths connecting the top and bottom surfaces of the piezo-

resistive material are created. At this stage, the electrical resistance between top and bottom surface decreases.

4) By investigating the level of the reduction in the electrical resistance, the level of corresponding mechanical pressure can be measured.

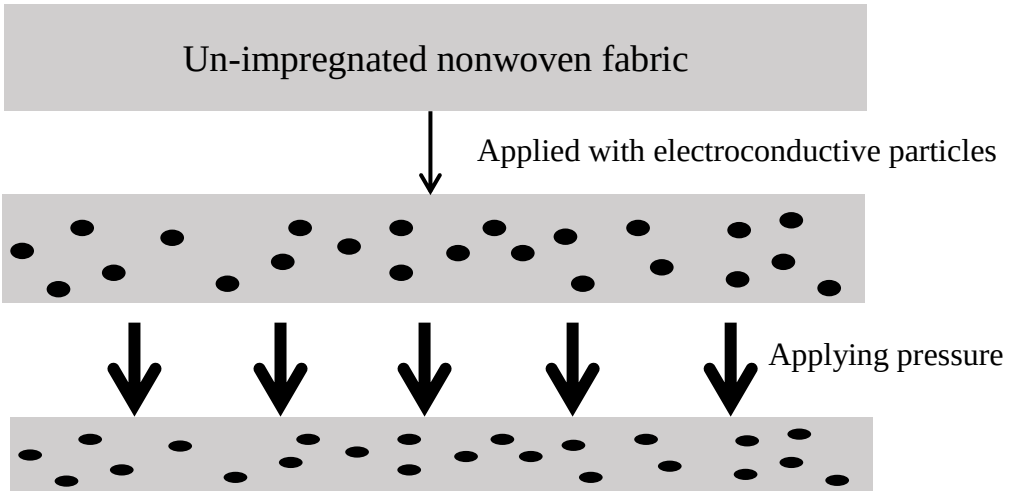

Figure 3-1. A schematic diagram of the operational principle of the nonwoven fabric based piezo-resistive material.

In obtaining a uniform electrical-resistance signal over the whole area of the sensor fabric, the nonwoven has an edge over other two types of textile materials (woven and knitted fabrics). The randomly oriented fibres in the nonwoven material are prepared to provide a uniform thickness over the sensing area. Due to the fineness of the fibres used to create nonwoven fabrics, they react to much weaker mechanical signals, and therefore more sensitive than yarns used to produce woven or knitted fabrics. The relatively loose structure allows the electroconductive particles to be delivered more uniformly in a deeper range. Due to these positive features, the cardiorespiratory sensors studied throughout this research are based on nonwoven fabric materials.

3.3 Materials and sample preparation

3.3.1 List of the fabric materials

Table 3-1 lists the functional fabrics used in the fabrication of the piezo-resistive nonwoven sensors. The silver knitted fabrics were used as electrodes that connected the piezo-resistive nonwoven sensor to a circuit for the measurement of electrical resistance. The silver knitted fabrics had a very low electrical resistance which could be considered

as a conductor during testing. Compared with nonwoven fabrics, the fibres in the knitted structure were more stable and closely connected so that the electrical resistance change of the silver knitted fabrics during compressive testing could be neglected. Also, the fluffy surface created extra connections between the silver knitted fabric and the nonwoven fabric layer. These reasons made the silver knitted fabric an ideal electrode material which provided reliable connection while affected little to the sensor performance. The webbing fabrics acted as adhesives to improve the connections between nonwoven fabrics and electrode fabrics. The webbing fabrics consisted of low density polyethylene (LDPE) which melted under a temperature of 60 °C applied by a hot iron. The function of the webbing fabrics was to firmly secure the position of the nonwoven fabric and electrode fabrics so that relative movement between sensor layers would be eliminated during testing, especially for cardiorespiratory signal acquisition as motion artefacts might change the layer position significantly. The usage of the webbing fabric also reduced the effect of the elasticity of the knitted fabric along the planar directions as the sensor was designed as a pressure sensor. The test results of the effectiveness of the webbing fabrics are to be discussed in Chapter Five.

Table 3-1. The functional fabrics.

Fabric name	Thickness (mm)	Function	Properties
Silver knitted fabric	0.38	Electrode	Surface electrical resistance: <100 Ohms/m^2
Webbing fabric	0.13	Adhesive material	Melting temperature: 60 °C

As the electroconductive ink impregnation process is to apply the electroconductive particles onto the surface of the fibres rather than to let the fibres absorb the particles, the type of the fibre in the nonwoven fabric does not affect the impregnation or the sensor performance, as long as the selected fibres are chemically stable during and after ink impregnation. Therefore, polyester fibres were selected as the main material of the nonwoven fabrics, due to the fact that polyester fibres are widely used in nonwovens. And the wellness in chemical stability makes the polyester fibres suitable for

electroconductive ink impregnation. However, due to the limitations in sourcing nonwoven materials, polypropylene (PP) and viscose blended fibres were also used.

In the aspect of the bonding technologies for the nonwoven materials, there are four main bonding methods, hydro entanglement, mechanical bonding, chemical bonding and thermal bonding. Apparently, the chemical bonding method is the least suitable for the present research as the electroconductive impregnation process would either be affected by the chemical adhesives in the nonwoven material or damage the chemical bonding of the nonwovens; therefore the sensor performance may be affected by the extra chemicals existing in the nonwovens. The hydro entanglement and mechanical bonding technologies share a similar working principle that is to mechanically entanglement the fibres in order to bond the fibres together. This process can be carried out either by water jet (hydro entanglement) or mechanical needle punching (mechanical bonding). Both of the two technologies will create fibres that are vertical to the fabric plane which naturally connect the top and bottom surfaces of the fabric. These connections will create electrical shorting during testing and therefore reduce the change in resistance. Thermally bonded nonwoven fabrics are produced by heating the fibres to their melting temperature by hot calendars. This method does not require extra chemical adhesives and has a much smaller chance of creating vertical fibres in the nonwoven material. Additionally, by adjusting the surface of the calendars, the surface structure of the nonwoven fabric can be modified. Therefore, thermally bonded nonwoven fabrics were mainly selected for the present research with different fabric thicknesses, area densities and surface structures in order to investigate how these parameters would affect the performance of the piezo-resistive sensors.

During the research, various types of nonwoven materials with different parameters were sourced. As summarised in **Table 3-2**, altogether 7 nonwoven materials were investigated, among which, fabrics 1 to 5 were purchased. The fabrics 6 and 7 were the knitted and woven fabric materials used in order to compare their piezo-resistivity with nonwoven materials. It is worth noting that fabric 4 was made of PP/viscose with a surface structure embossed with a dot pattern. The relatively low melting temperature of PP fibres made it feasible for creating the special embossed surface structure. Fabric 5 was the commercially available carbon-based electroconductive nonwoven piezo-resistive material made by spunlace technology, which was used in its original form as a core piezo-resistive layer.

Table 3-2. The purchased fabric materials.

Fabric	Fibre type	Average fibre diameter (micron)	Bonding method	Fabric thickness (mm)	Area density (g/m^2)	Remarks
1	Polyester	19	Thermal bonding	0.07	17	N/A
2	Polyester	14	Thermal bonding	0.10	60	N/A
3	Polyester	14	Thermal bonding	0.65	80	N/A
4	PP/viscose 1:1	20	Thermal bonding	0.61	60	Embossed dot surface
5	Polyester	12	Spunlace	0.43	84	Electro-conductive
6	Polyester	21*	Interlock knitted	0.92	N/A	*: measurement of a single fibre in the yarn
7	Polyester	18*	Plain weave	0.36	N/A	

3.3.2 Thermally bonded nonwoven materials

In order to investigate the effect of thickness and the area density of the nonwoven fabric on the piezo-resistive property on the fabricated sensors, nonwoven fabrics with different thicknesses and area densities were sourced from industry. However, due to the limit types of nonwoven materials obtained, the carding machine (**Figure 3-2(a)**) and air-through thermal bonding machine (**Figure 3-2(b)**) available in the university were used to produce more nonwoven materials with various thicknesses and area densities. Because that the limited maximum bonding temperature (130 °C) achievable by the air-through thermal bonding machine, using PET fibres alone was not feasible for thermal bonding. PP fibres were blended with PET fibres in order to fulfil the bonding process. PP/PET (1:1 blend ratio) staple fibres were selected. Thermal bonding time was set for 40 seconds for thorough and sufficient bonding of the PP/PET blended fibres. A flat

surface mould (as illustrated in **Figure 3-3**) was designed and constructed in order to produce flat thermally bonded nonwoven fabrics.

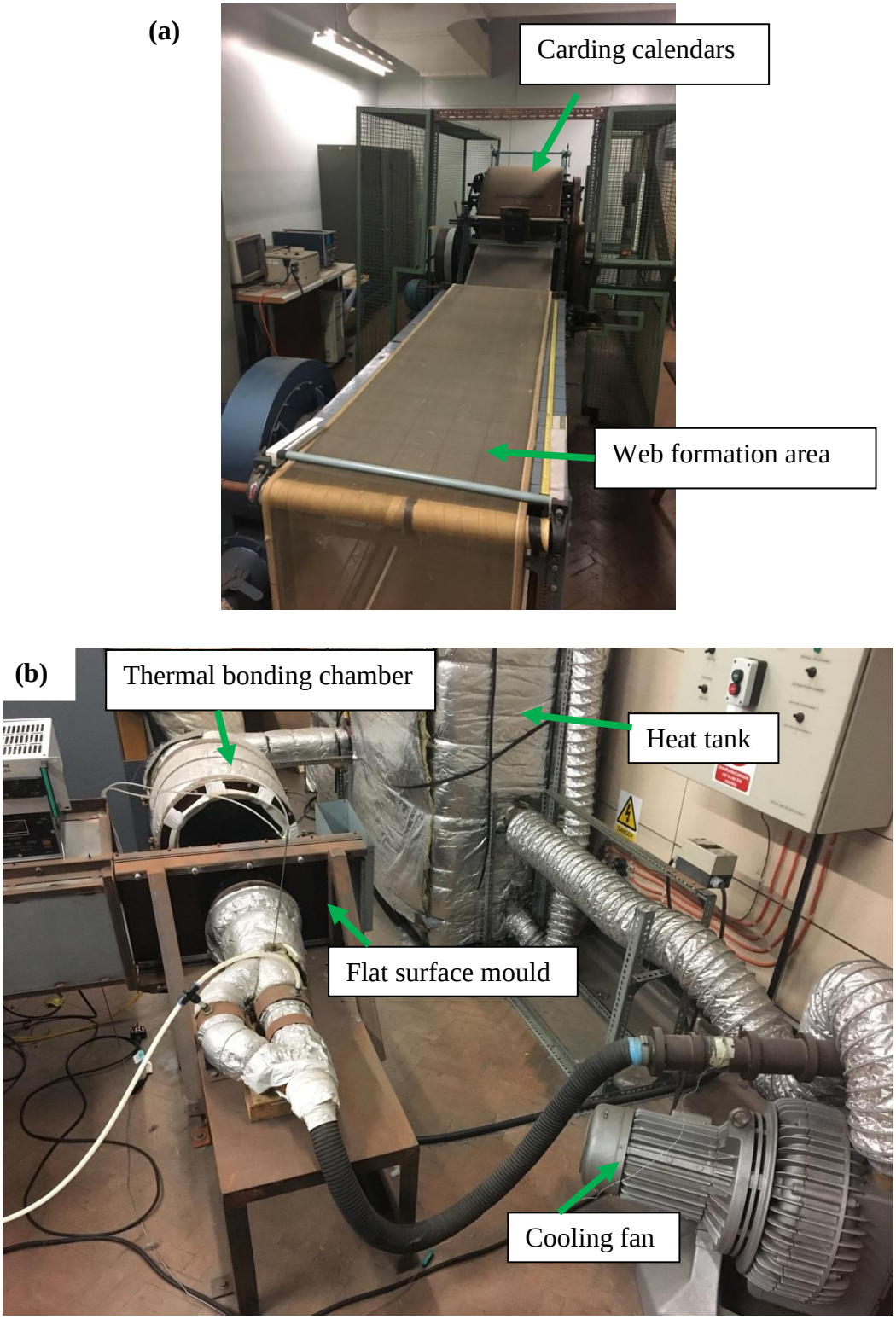

Figure 3-2. The (a) carding machine and (b) thermal bonding machine.

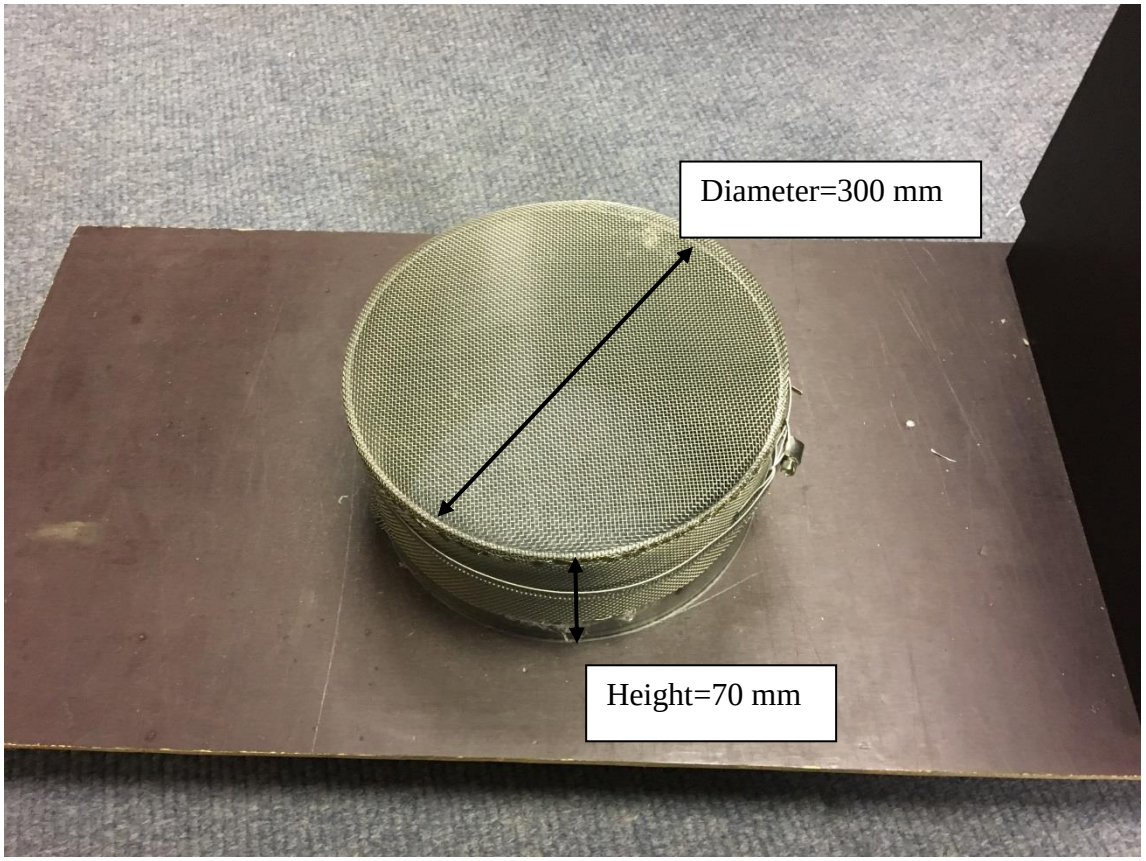

Figure 3-3. The flat surface mould used to create flat thermally bonded nonwoven fabric.

The procedure of producing thermally bonded nonwoven fabrics is listed as follows:

1) in order to achieve different area densities, four different weights of PP/PET staple fibres were measured, 15 g, 20 g, 25 g, and 30 g; the weighted PP/PET fibre bundle was primarily opened by hand and laid evenly on a belt at the rear of the carding machine; then, the belt was driven to feed the opened fibre bundles into the carding machine;
2) upon carding, the staple fibres were sufficiently opened by the complex mechanisms in the carding machine;[222] after carding, a fragile web about 600 mm in width and 1500 mm in length was created and sent to the front of the carding machine;
3) the starting and ending parts of the web that came out the carding machine were discarded due to non-uniformed web formation; an appropriate length (approximately 200 mm to 250 mm) of web cut from the middle part was placed carefully into the mould;

4) the web was then thermally bonded with the mould in the thermal bonding machine at 130 °C for 40 seconds in order to achieve the best bonding performance;
5) thereafter, the thermally bonded web was removed from the mould immediately after thermal bonding. The middle area of the web was used as the thermally bonded nonwoven fabric.

The thicknesses and the area densities of the thermally bonded nonwoven fabrics produced from four different weights of raw materials are measured and listed in **Table 3-3**.

Table 3-3. Laboratory-made thermally bonded nonwoven fabrics with different thickness and area densities.

Fabric	Weight of PP/PET (g)	Thickness (mm)	Area density (g/m^2)
8	15	0.16	33
9	20	0.17	36
10	25	0.19	38
11	30	0.28	60

3.3.3 Preparation of the nanoscale silver particle-based electroconductive ink

As discussed in section 3.2, the uniform distribution of the electroconductive particles throughout the nonwoven material is essential for the sensor to function well. The high dispersion of the nanoscale particle based electroconductive ink ensures the uniform absorption by the nonwoven material.

In this research, the nanoscale silver particle electroconductive ink was produced using the method developed by Walker and Lewis, [155] combined with the approach explained in the research report conducted by Zielińska and his colleagues.[223] This nanoscale silver particle ink was synthesised by reducing silver acetate directly to diamminesilver (I) complex by ammonia without the help of a silver oxide intermedia which reduced the complexity of the synthetisation. Formic acid was added to neutralise the excessed reducing agent. This method used silver acetate instead of commonly used

silver nitrate, which created the silver particle ink that was more stable, non-explosive and less harmful to the textile materials.[223, 224] The main reaction can be visualised as the following equation:

$$NH_4OH/H_2O + AgC_2H_3O_2 + CH_2O_2 \rightarrow [Ag(NH_3]^+[C_2H_3O_2]^- \rightarrow Ag \quad \textbf{Equation 3-1}$$

As discussed in section 2.4, it is necessary to add stabiliser to prevent the nanoscale silver particles from agglomerations. Polyvinylpyrrolidone (PVP) was selected as the stabiliser in the present research because of its low sintering temperature (120 °C), which was suitable for sintering PP fibre based nonwoven fabrics.[154] PVP, as a stabiliser, is not shown in **Equation 3-1**, as it only caps the silver particles for the necessary separation to avoid silver agglomerations. The following chemicals, as listed in **Table 3-4**, were used to produce the nanoscale silver particle-based ink.

Table 3-4. Chemicals used in the preparation of nanoscale silver particle ink.

Item	Description	Source
Silver acetate	≥99.0%, powder	Sigma Aldrich
Ammonia	33%, liquid, ammonium hydroxide	Sigma Aldrich
Formic Acid	≥98%, liquid	Sigma Aldrich
Polyvinylpyrrolidone	Average molecular weight 40,000	Sigma Aldrich

The following steps were carried out in order to obtain one portion (approximately 3 ml) of nanoscale silver particle ink. Due to the strong smell of ammonia solution, the synthesis was carried out in a ventilated condition, such as in a fume cupboard.

1) 10 g of PVP was added to 2.5 ml of ammonia; mild stirring was performed until PVP powder was fully dissolved;
2) 1 g of silver acetate was added into PVP solution with the help of a magnetic stirrer at an appropriate rotation speed;
3) after the silver acetate was thoroughly dissolved, the solution turned completely transparent and clear;
4) in the next step, 0.2 ml of formic acid was dripped into the solution slowly; the neutral reaction between ammonia and formic acid could be violent, where a

white fog was formed above the liquid; meanwhile, the solution turned black, in which black particles were observed as in **Figure 3-4(a)**;

5) then the solution was removed from the magnetic stirrer, capped, moved to a cool place and kept for 24 hours;
6) after 24 hours of standing, the black pre-matured silver agglomerations sank to the bottom (as shown in **Figure 3-4 (b)**); the upper solution showed complete transparent and clear; the upper solution was carefully transferred to a syringe filter with 0.2 μm pore size without disturbing the bottom agglomerated silver particles (as shown in **Figure 3-4 (c)**);
7) the filtered solution (the nanoscale silver particle electroconductive ink) was used to create the piezo-resistive nonwovens (as shown in **Figure 3-4 (d)**).

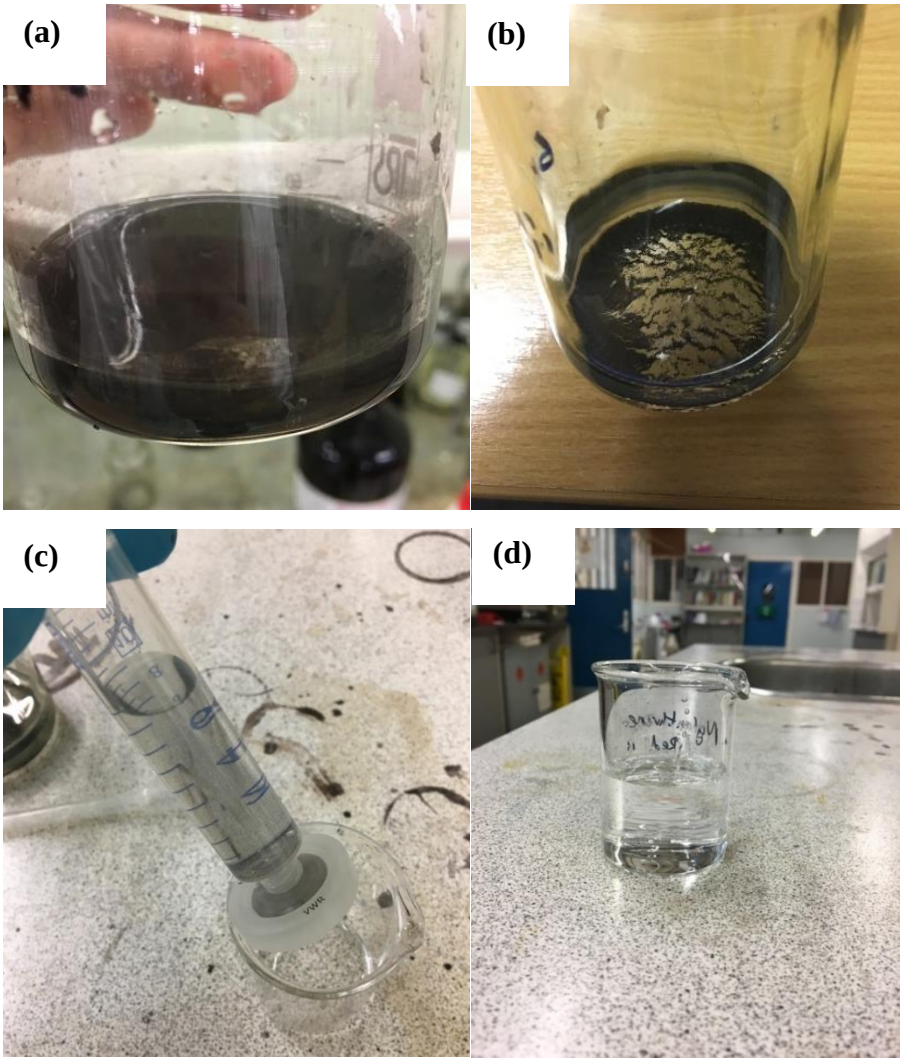

Figure 3-4. The photos of the preparation procedure of nanoscale silver particle ink; (a): before 24-hour standing; (b): after 24-hours standing; (c): syringe filtering. (d): filtered nanoscale silver particle ink.

3.3.4 Dip-coating impregnation and thermal sintering

Dip-coating has been proven to be the most suitable impregnation method to create electroconductive fabric based piezo-resistive sensor in section 2.4.3. Due to the fact that PVP was used as a stabiliser, nanoscale silver particles were covered with PVP. The removal of PVP was necessary for the high electrical conductivity of the impregnated fabric and was achieved by thermal sintering at 120 °C.[154] Through the literature survey, it was found that the time required for thermal sintering could be reduced by increasing the sintering temperature.[212, 213] However, due to the PP fibre used to produce the nonwoven fabrics, the maximum sintering temperature was limited to 130 °C. Therefore, the following sintering setup was decided: 120 °C for 30 minutes, for sufficient thermal sintering without damaging the PP fibre based nonwoven fabrics.

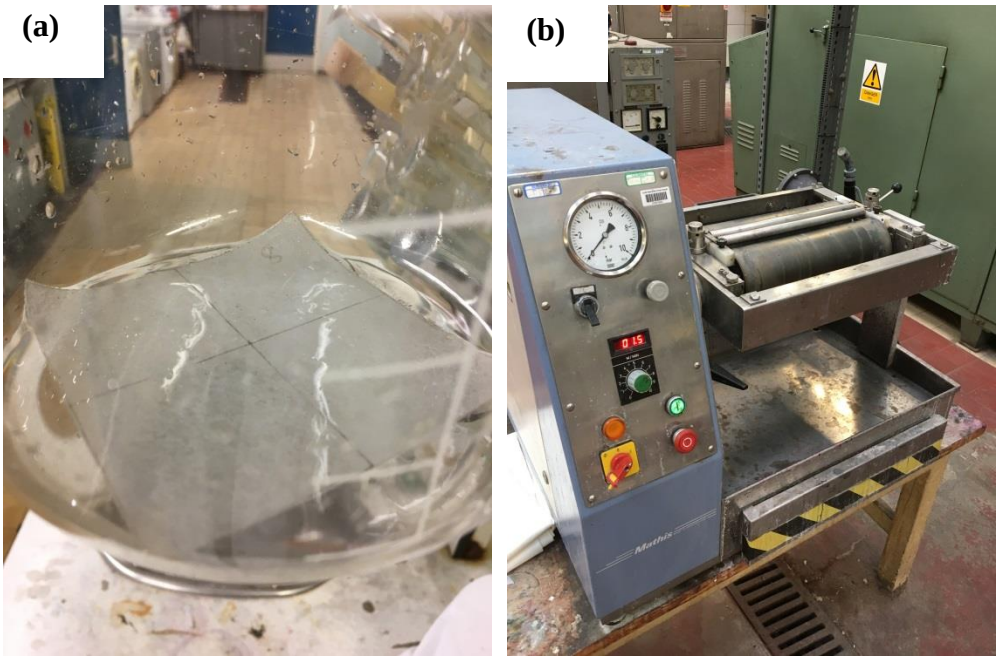

Figure 3-5. (a): the nonwoven fabric immersed in the nanoscale silver particle-based ink; (b): Werner Mathis CH-8155 Pad Mangle.

Generally, for every 90 mm by 90 mm area of the fabric, four portions (approximately 12 ml) of nanoscale silver particle electroconductive ink were required for thorough and uniform impregnation performance. However, in order to ensure that there was a sufficient amount of ink for thorough impregnation and the uniform result, 15 ml of nanoscale silver particle ink was used in the impregnation process for each piece of 90

mm by 90 mm fabric. The following steps were carried out to create the piezo-resistive nonwoven fabric material:

1) the nonwoven fabric was measured and cut into a 90 mm by 90 mm square;
2) the cut nonwoven fabric piece was fully immersed in the 15 ml of prepared nanoscale silver particle-based ink for 5 minutes; mild shaking of the container, the beaker in most of the cases, was performed from time to time, in order to obtain the result of thorough and uniform impregnation (as illustrated in **Figure 3-5(a)**);
3) then, the fully wet nonwoven fabric was transferred to a Werner Mathis CH-8155 Pad Mangle in order to remove the excessed ink solution; the surface rolling speed and the compressing pressure of the mangle was set at 1.5 m/min and 1 bar, respectively (as illustrated in **Figure 3-5(b)**);
4) the fabric was mangled once and immediately removed from the mangle, after which the sintering process was carried out on a preheated hotplate for 30 minutes; the temperature of the hotplate was set at 120 °C;[154]
5) the thermal sintered 90 mm by 90 mm nonwoven fabric was then cut into four 45 mm by 45 mm pieces for later usage in creating piezo-resistive sensors; as these four pieces were dip-coated in the same process, they were considered as identical in the silver concentration.

During the sintering process, the change of the nonwoven fabric could be clearly observed. Before sintering, the nonwoven fabric showed its natural white colour (as shown in **Figure 3-6(a)**). It can be seen in **Figure 3-6(b)** that during the thermal sintering process, the nonwoven fabric turned to black first, then, gradually turned to a silver colour, which represented the completion of the thermal sintering process (as shown in **Figure 3-6(c)**).

The amount of silver content that has been absorbed by the nonwoven material can be quantified by the take-up percentage value, as shown in **Equation 3-2**:

$$Take\text{-}up = \frac{W_1 - W_0}{W_0} \times 100\% \qquad \textbf{Equation 3-2}$$

where: W_0 is the weight of nonwoven fabric before impregnation; W_1 is the weight of the nonwoven fabric after impregnation with silver ink and sintering. Generally, the

nonwoven fabric with a higher silver take-up is expected to be with higher electrical conductivity.

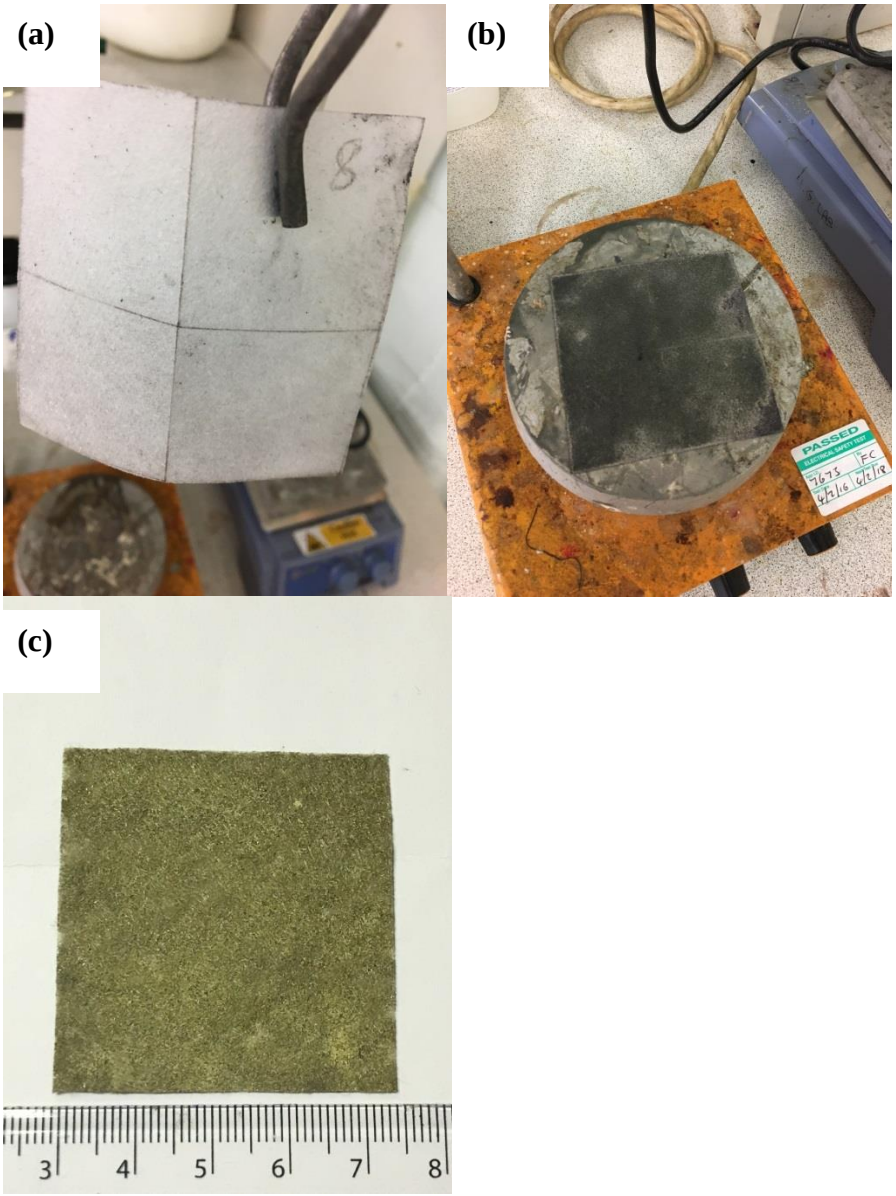

Figure 3-6. The nanoscale silver ink impregnated nonwoven fabric, (a) before thermal sintering; (b): during thermal sintering; (c): thermal sintered and cut into a smaller size designed for sensor fabrication.

3.3.5 Piezo-resistive sensor design and fabrication

The size of the cardiorespiratory sensor is an important factor of the sensor performances, especially for those sensors based on textile materials, which potentially will be integrated into garments. From the literature, it was found that most of the electro-textile material based cardiorespiratory sensors were tested under the condition

of being integrated into a pocket on a shirt, fabricated onto a belt type sensor which had a width of approximately 40 to 50 mm, or directly sewn/embroidered into a garment covering a square area of 40 to 50 mm.[8, 73, 225–227] The working area of the cardiorespiratory sensors designed and investigated in the current research was 40 mm by 40 mm, inspired by Hamdani and his colleagues.[228] The complete design and fabrication of the piezo-resistive nonwoven material based cardiorespiratory sensor are described in detail.

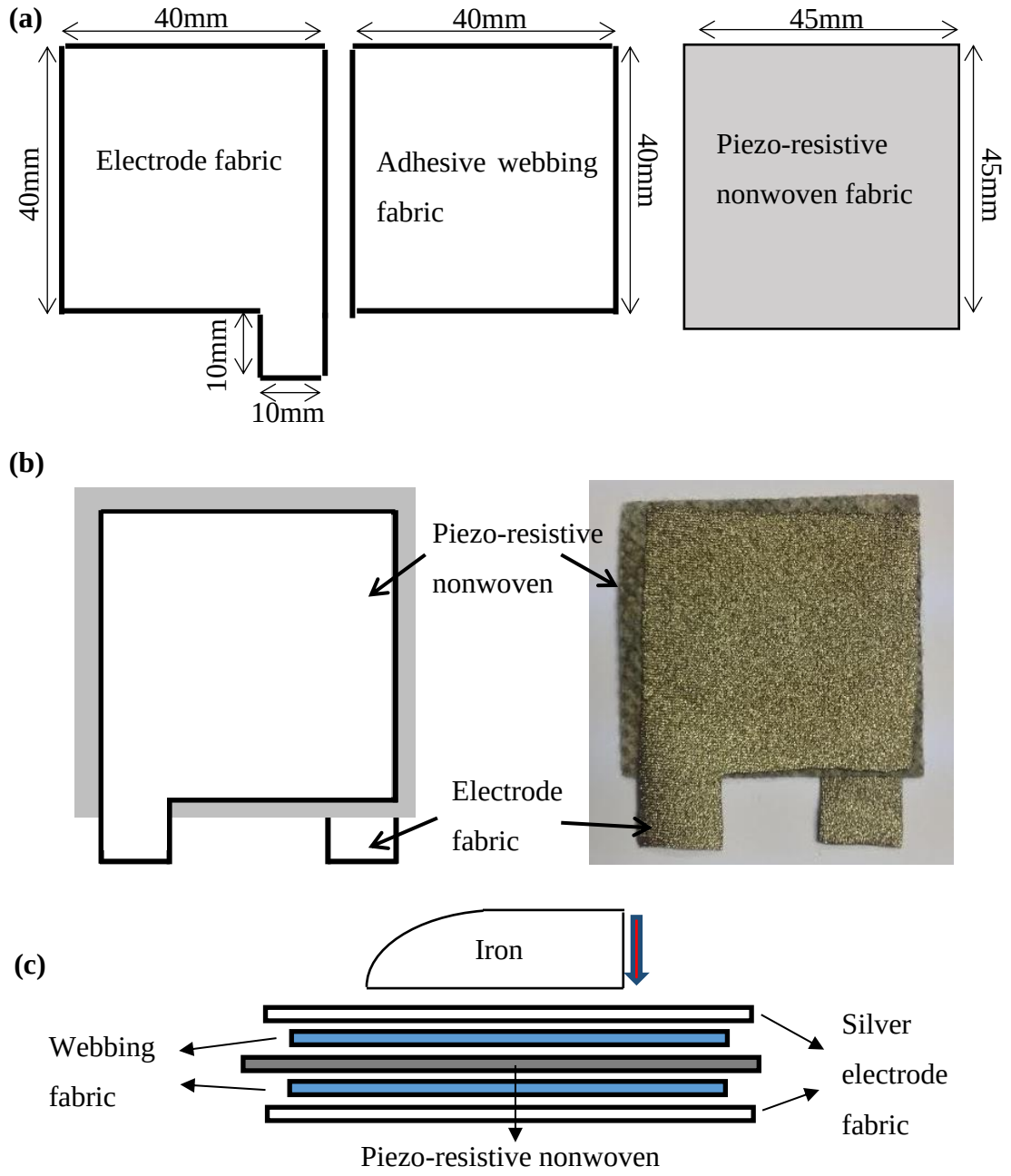

Figure 3-7. (a) The dimensions of designed sensor layers; (b) and (c): the layer schematic of the nonwoven piezo-resistive sensor.

The piezo-resistive sensor consists of five layers, one core piezo-resistive nonwoven fabric layer, two electrode layers made from silver coated nylon for the top and bottom surfaces, and two adhesive webbing fabric layers. The adhesive webbing fabrics were also dip-coated with the nanoscale silver particle-based ink using the method described in section 3.3.3 and 3.3.4; however, due to the low melting temperature (60 °C) of the webbing fabric, the sintering process was performed at 45 °C for 1 hour. The dimensions and layer schematic of the five layers are shown in **Figure 3-7**. After properly aligning the each of the layers, a steam iron was used to apply a heat level of 70 °C for 30 seconds, in order to melt the webbing fabric layer to provide adhesion. The two electrode fabric layers were connected to form a Wheatstone half-bridge circuit in order to acquire of the electrical resistance of the fabricated sensor along the thickness direction. Therefore, as shown in **Figure 3-7**, the core piezo-resistive nonwoven fabric layer was designed to be slightly bigger than the working area, as it can help to avoid the electrical shorting between the top and bottom electrode fabric layers.

3.3.6 Piezo-resistive nonwoven fabric based sensors

All these 11 types of sensors (as listed in **Table 3-5**) were investigated via microscopy analysis, electromechanical characterisations and the investigation of the performance of these materials in cardiorespiratory sensing applications, the procedures and results are presented in the later chapters.

Table 3-5. The piezo-resistive nonwoven fabric based sensors.

Sample	Fabric No.	Sensor thickness (mm)	Silver take-up (%)	Remarks
A	1	0.96	25.2	N/A
B	2	1.04	13.3	N/A
C	3	1.29	68.0	N/A
D	4	1.24	65.2	Embossed dot surface
E	5	1.16	60.0% carbon	Electroconductive
F	8	1.13	98.1	15 g of PP/PET
G	9	1.14	82.3	20 g of PP/PET
H	10	1.16	111.2	25 g of PP/PET
I	11	1.23	78.6	30 g of PP/PET
J	6	2.19	49.0	Interlock knitted fabric
K	7	1.22	32.2	Plain woven fabric

3.4 Test procedures

In this section, the methodology of the characterisation of nanoscale silver particle-based piezo-resistive nonwoven materials and the evaluation methods of such nonwoven materials used in a cardiorespiratory sensor are introduced.

3.4.1 Measurement of electrical resistance

The methods of measuring the electrical resistance commonly include two-wire resistance measurement, four-wire resistance measurement and Wheatstone bridge circuit.[229, 230] The two-wire resistance measurement (as illustrated in **Figure 3-8**) has the simplest principle based on Ohm's law:

$$R_{Subject} + 2 \times R_{wire} = \frac{V_{Voltmeter}}{I_{Ammeter}} \qquad \textbf{Equation 3-3}$$

When the R_{wire} value is negligible, $R_{subject} = V_{Voltmeter}/I_{Ammeter}$. However, the $R_{subject}$ may be far away from the Ammeter and the Voltmeter, in which case that the R_{wire} is not negligible. The actual $R_{subject}$ value will be lower than the measurement (calculated from $V_{Voltmeter}/I_{Ammeter}$).

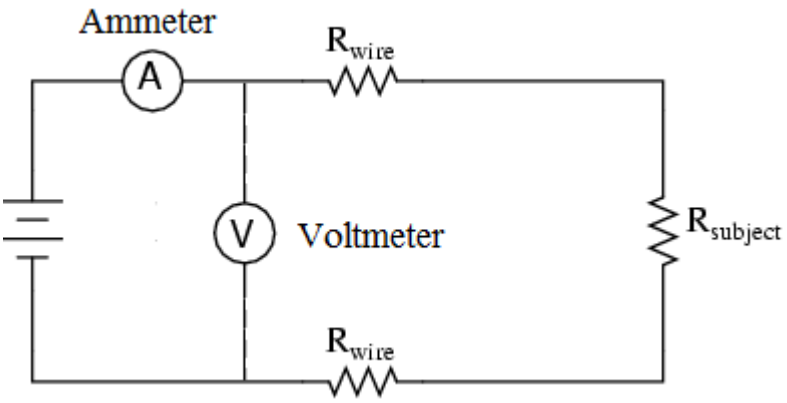

Figure 3-8. A schematic of two-wire resistance measurement.[229]

Therefore, a four-wire resistance measurement method (as shown in **Figure 3-9**) is used in the case that R_{wire} has to be taken into account. Because the current on the voltmeter is negligible, $V_{Volmeter}=V_{Rsubject}$; therefore, $R_{subject} = V_{Voltmeter}/I_{Ammeter}$. Though the four-wire measurement setup is able to overcome the issue raised by the extra electrical resistance of the long connections, which is helpful in this research as there is a distance between the tensile tester and the computer, it is still not good enough for capture the

resistance change accurately for the nonwoven piezo-resistive sensors. This is due to the fact that the measurement range and accuracy of the four-wire setup are limited by the power supply.

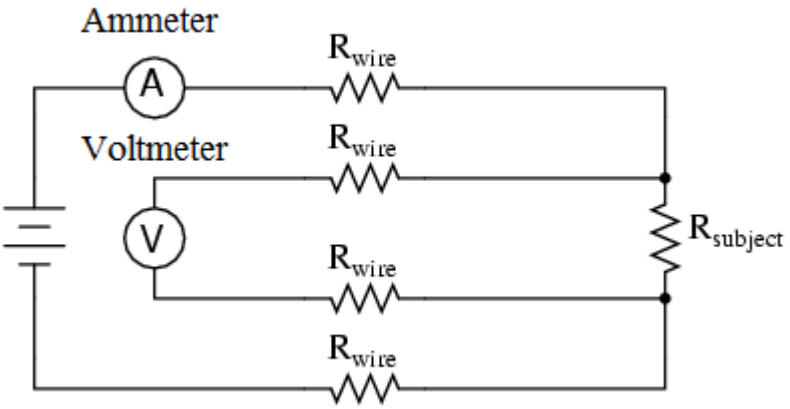

Figure 3-9. A schematic of four-wire resistance measurement.[229]

Therefore, the Wheatstone bridge circuit was used in this research for electrical resistance measurement. The circuit diagram of a Wheatstone bridge is shown in **Figure 3-10**.

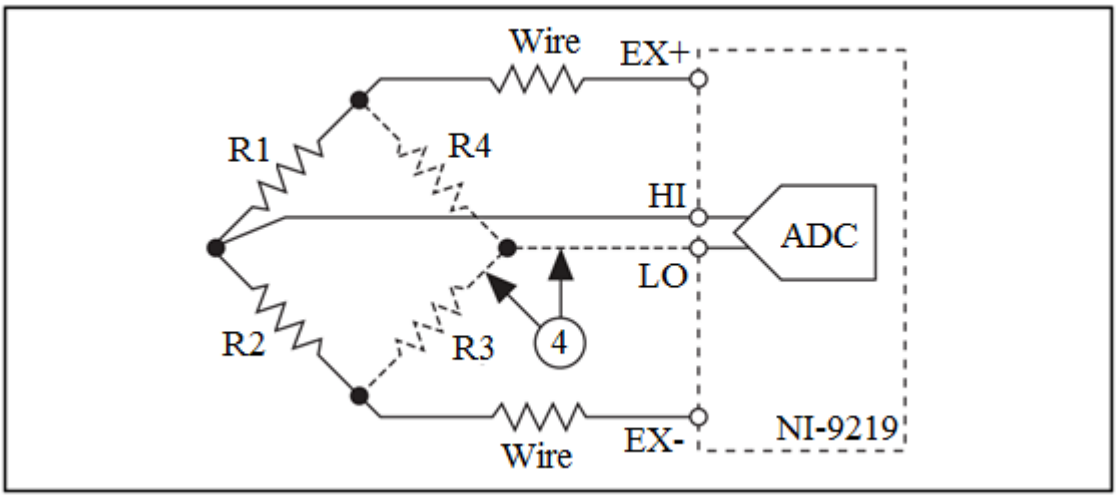

Figure 3-10. The Wheatstone half bridge circuit diagram for the NI 9219. The dotted lines are the circuit built into the data acquisition card.[231]

Generally, when the bridge is balanced, the voltage at HI and LO will be equal, which means no current will flow through analogue-to-digital converter (ADC). According to Ohm's law:

$$U_{HI} = U_{EX} \times \frac{R_1}{R_1+R_2}$$ **Equation 3-4**

$$U_{LO} = U_{EX} \times \frac{R_4}{R_3+R_4}$$ **Equation 3-5**

Therefore, when the bridge is balanced,

$$U_{HI} = U_{LO}$$ **Equation 3-6**

$$U_{EX} \times \frac{R_1}{R_1+R_2} = U_{EX} \times \frac{R_4}{R_3+R_4}$$ **Equation 3-7**

By simplifying,

$$\frac{R_1}{R_1+R_2} = \frac{R_4}{R_3+R_4}$$ **Equation 3-8**

The Wheatstone bridge circuit can be classified into full-bridge, half-bridge and quarter-bridge circuit. As their names informed, the full bridge circuit involves four variable resistors; half bridge circuit involves only two variable resistors (usually R_1 and R_2), while the other two stay constant and equal; the quarter bridge circuit has only one variable resistor, while the rest three stay constant and equal. The full bridge circuit is suitable for complex setups, in which multiple variable resistors exist and require measurement. The half bridge circuit is for the application of accurately measuring the electrical resistance that changes in a relatively big range. The quarter bridge circuit is used in the resistance measurement of an unknown but constant resistor.

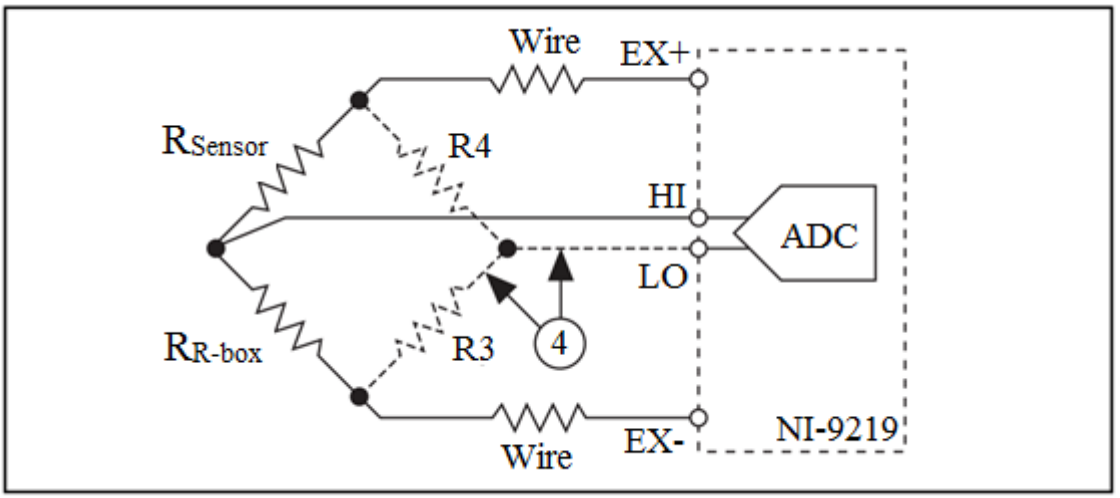

Figure 3-11. The Wheatstone half bridge circuit diagram used to measure the resistance of the piezo-resistive sensor in this research.

In this research, due to the fact that the piezo-resistivity of the sensor material was investigated mainly by measuring the change in the electrical resistance, the half-bridge circuit was used throughout all types of tests involving electrical resistance measurement and recording. The piezo-resistive sensor and a resistance box ($R_{R\text{-}box}$) was connected to form the half-bridge circuit, as illustrated in **Figure 3-11**.

In the static conditions, the resistance box ($R_{R\text{-}box}$) was used in order to balance the half bridge circuit; therefore,

$$\frac{R_{Sensor}}{R_{Sensor}+R_{R-box}} = \frac{R_4}{R_3+R_4} = \frac{1}{2} \qquad \textbf{Equation 3-9}$$

By simplifying,

$$R_{Sensor} = R_{R-box} \qquad \textbf{Equation 3-10}$$

In the dynamic conditions, while the electrical resistance of the sensor was continuously changing because of the changing pressure applied on the sensor, the balance of the bridge was broken; therefore, there was a voltage difference between node HI and LO.

$$U_{HI-LO} = U_{HI} - U_{LO} \qquad \textbf{Equation 3-11}$$

$$U_{HI-LO} = U_{EX} \times \frac{R_{Sensor}}{R_{Sensor}+R_{R-box}} - U_{EX} \times \frac{R_4}{R_3+R_4} \qquad \textbf{Equation 3-12}$$

$$U_{HI-LO} = U_{EX} \times \frac{R_{Sensor}}{R_{Sensor}+R_{R-box}} - U_{EX} \times \frac{1}{2} \qquad \textbf{Equation 3-13}$$

$$\frac{U_{HI-LO}}{U_{EX}} = \frac{R_{Sensor}}{R_{Sensor}+R_{R-box}} - \frac{1}{2} \qquad \textbf{Equation 3-14}$$

$$R_{Sensor} = R_{R-box} \times \frac{1-2\times\frac{U_{HI-LO}}{U_{EX}}}{1+2\times\frac{U_{HI-LO}}{U_{EX}}} \qquad \textbf{Equation 3-15}$$

The NI-9219 data acquisition card (as shown in **Figure 3-12**) was able to measure and record the $\frac{U_{HI-LO}}{U_{EX}}$ reading during the tests. In order to acquire a continuous resistance signal under dynamic conditions, the following method was conducted.

1) The bridge was balanced using the resistance box before starting the tests and the reading of the resistance box was noted.

2) The test was carried out while the $\frac{U_{HI-LO}}{U_{EX}}$ readings were recorded by NI-9219 data acquisition card.
3) **Equation 3-15** was applied in order to calculate the dynamic electrical resistance of the sensor.

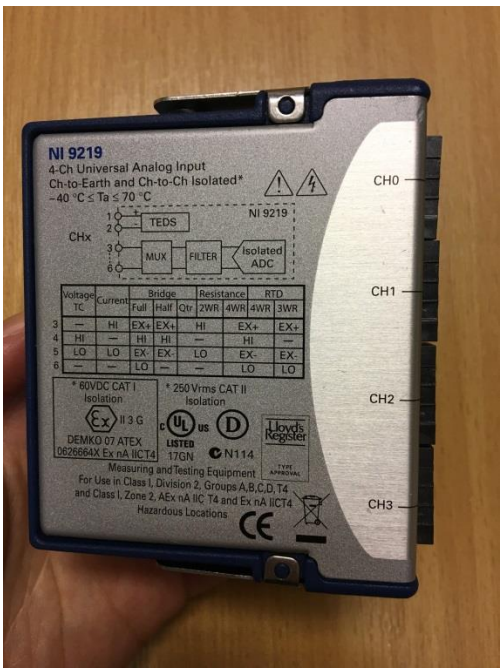

Figure 3-12. NI-9219 data acquisition card.

Two different timing options of the NI-9219 data acquisition card were used to record the signal of the changing resistance: high resolution mode and high speed mode.[231] The high resolution mode provided the best noise filtering of 50 Hz and 60 Hz, with an expense of sampling rate. The maximum sampling rate under this mode was 1.95 Hz. The high speed mode increased the sampling rate up to 100 Hz, however, with the scarification of noise filtering.

According to Nyquist Theorem,[232, 233] the sampling rate needs to be at least twice as the value of the signal frequency. Thus, the high resolution mode was sufficient for acquiring signals up to 0.975 Hz. Therefore, the high resolution mode was mainly used to record the electrical signal in the quasi-static compressive and cyclic tests for the characterisation of the piezo-resistive nonwoven materials. The high resolution mode was also used to obtain the respiratory signals, the frequency of which normally varied from 0.1 to 0.5 Hz.[234] However, the frequency of the cardiac signal under normal condition ranges from 1 to 1.67 Hz.[234] It is essential to use the high speed mode in

order to properly sample the cardiac signals. Additionally, a bandpass filter was applied to remove the noise and motion artefacts. The detailed setups of the tests are to be described in later sections.

3.4.2 Characterisation of nanoscale silver particle-based piezo-resistive nonwoven materials

Generally speaking, the characterisation of the nanoscale silver particle-based piezo-resistive nonwoven materials is based on the investigation of the piezo-resistive performance of the materials. Therefore, the electromechanical tests, including quasi-static compression test, cyclic loading test and resistance time drift (RTD) analysis test were carried out. Additionally, the selected sensors, which were found with excellent piezo-resistivity and high sensitivity, were then used to capture the cardiorespiratory signals. The performance of the selected sensors in the cardiorespiratory signal capturing was evaluated by the comparison against a commercially available bio-signal monitoring system (Plux bio-signal system).

3.4.2.1 Preliminary tests

- Textile conditioning

The test fabric materials were conditioned under the standard textile conditioning environment a 21 °C ± 2 °C and 65% ± 5% relative humidity for at least 24 hours based on ISO 139:2005.

- Compressive strength tests

The compressive strength tests were carried out in order to determine the elastic regions of the piezo-resistive sensors, based on which a suitable pressure region was calculated and used in later tests. The compressive strength tests on the fabricated sensors were performed using Zwick 050 tensile tester (as shown in **Figure 3-13**), under a compressive area of 40 mm by 40 mm and a deformation speed at 1 mm/min, up to 100 N. Five tests were carried out for each type of sample.

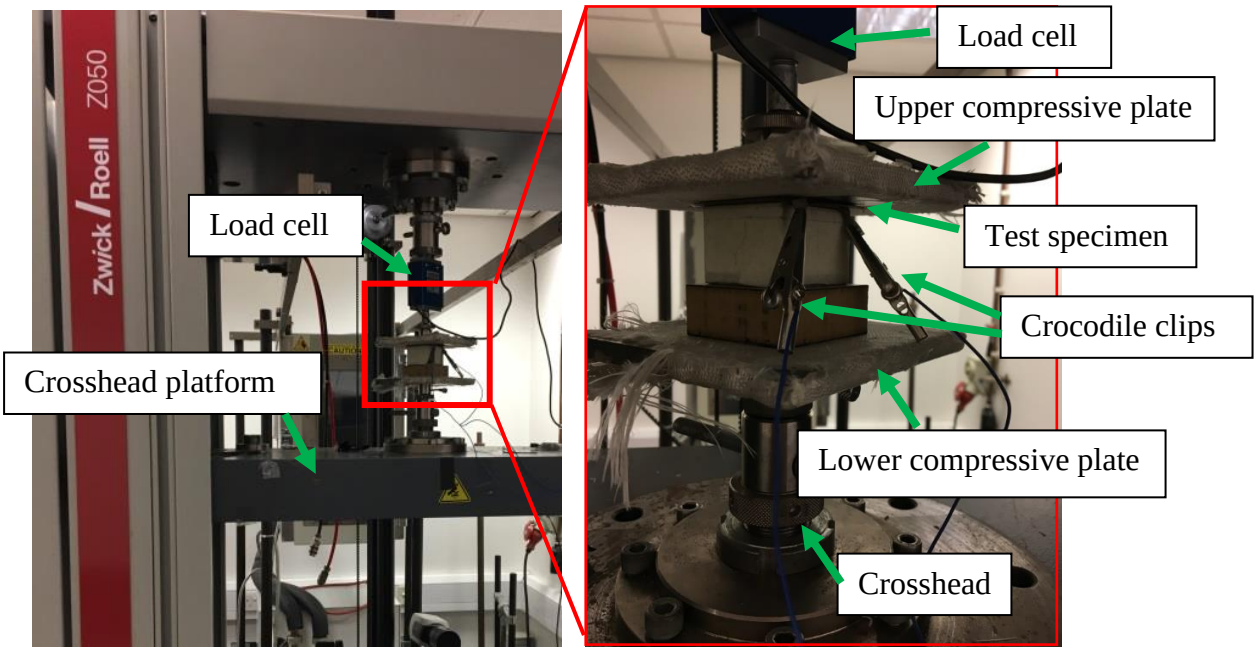

Figure 3-13. Zwick 050 tensile tester under compression test settings.

- Effect of the webbing fabric

Effect of the webbing fabric was investigated by comparing piezo-resistive properties of the piezo-resistive nonwoven sensor fabricated with and without webbing fabrics. Quasi-static electromechanical compressive tests were carried out on these samples. The testing parameters are introduced in detail in section 3.4.2.2.

- Effect of silver take-up percentage on the piezo-resistive property

The amount of silver content that has been deposited on the nonwoven fabric had a significant effect on the resistance, the piezo-resistivity and the sensitivity of the nonwoven material. In order to achieve different levels of silver take up percentage, the nonwoven materials were mangled once, twice and three times, at a pressure of 2 bars. Then, electromechanical quasi-static compressive tests were performed on the sensors fabricated by these nonwoven fabrics. The testing parameters are introduced in detail in section 3.4.2.2.

3.4.2.2 Electromechanical characterisation

- Quasi-static electromechanical compressive test

Quasi-static electromechanical compressive tests were performed, in order to investigate the piezo-resistivity of the fabricated sensor under pressure sensing conditions. The tests

were performed using Zwick 050 tensile tester, under a compressive area of 40 mm by 40 mm and deformation speed at 0.1 mm/min, up to 100 g/cm^2. A preload of 0.1 N was applied in order to achieve firm connections between the electrode fabrics and the piezo-resistive nonwoven layer. In the meantime, the electrical resistance signals of the piezo-resistive nonwoven sensors were recorded and calculated by the NI-9219 data acquisition card using the high resolution mode (sampling rate: 1.95 Hz) and visualised in SignalExpress 2012 software. Five tests were carried out for each type of sample.

- Cyclic compressive loading

The reproducibility of the piezo-resistive nonwoven sensor was investigated by carrying out cyclic compressive load tests. With the help of Zwick 050 tensile tester, the piezo-resistive nonwoven sensor samples were compressed from 0 to 100 g/cm^2 for 20 cycles, at a deformation speed of 0.5 mm/min for both loading and unloading cyclic. The electrical resistance was recorded simultaneously using the same settings as the quasi-static electromechanical compressive test.

- Resistance time drift (RTD) analysis

RTD is a phenomenon that can be commonly observed in semiconductors, which is that the electrical resistance of the materials will change as time elapses under low mobility states.[235–238] In the tests for the investigation of RTD on the piezo-resistive nonwoven sensors under compressive application, the sensor samples were compressed at a deformation speed of 0.5 mm/min, to different pressure levels of every 10 g/cm^2 interval, from 10 g/cm^2 to 90 g/cm^2. The pressure levels were maintained for 60 seconds and the electrical resistance drifts were recorded under the high resolution mode of the NI-9219 data acquisition card at a sampling rate of 1.95 Hz.

3.4.3 Cardiorespiratory signal capturing

In order to acquire the best signal acquisition performance, the fabricated sensor samples were placed on the left chest of the user, under a biasing pressure level of 25 g/cm^2.[239] A thin flat block was used to ensure the biasing pressure was evenly applied over a 40 mm by 40 mm area on the nonwoven piezo-resistive sensor. During the tests, other than recording the electrical resistance signals from the piezo-resistive nonwoven sensors, validation cardiorespiratory signals were also recorded at the same time, with

the help of a commercially available bio-signal monitoring system from Plux Wireless Bio-signals S.A.. The respiratory signals were captured using a belt-type strain sensor and the cardiac signals were detected using a finger pulse oximeter both provided from the Plux. The full setup for capturing cardiorespiratory signals is illustrated in **Figure 3-14**, **Figure 3-15** and **Figure 3-16**.

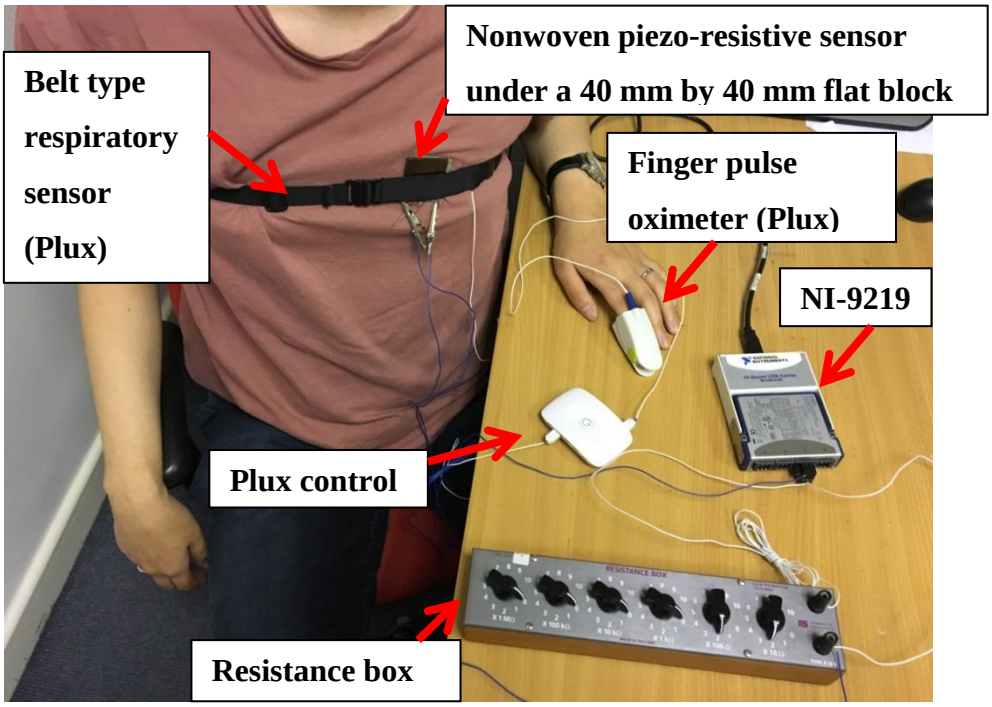

Figure 3-14. Sensor setups for cardiorespiratory signal capturing.

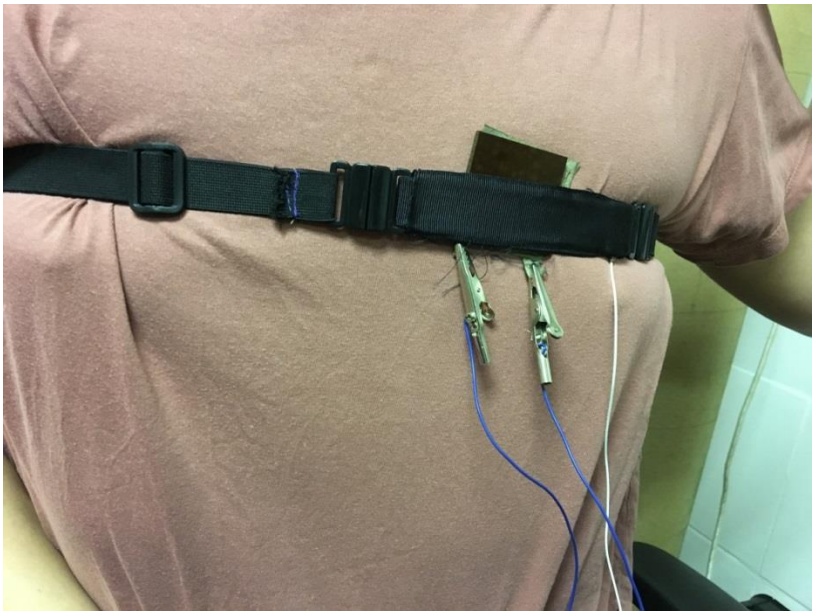

Figure 3-15. On-body setup of the nonwoven sensor.

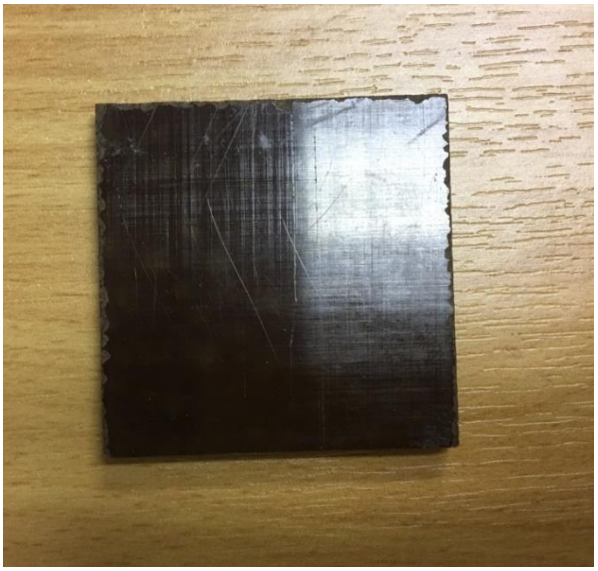

Figure 3-16. The 40 mm by 40 mm thin flat block.

3.4.3.1 Respiratory signal capturing

The test procedure used for acquiring the respiratory signal consisted of four repeats of normal breathing followed by holding the breath (each repeat has 30 seconds of normal breathing followed by 30 seconds of holding the breath). These 4 repeats were followed by rapid breathing for 60 seconds and normal breathing for 30 seconds. In order to observe the capacity of the sensor to capture the respiratory signal during body movement, further testing was carried out while the test subject was lifting and lowering the right arm three times, and the left arm three times. The electrical resistance signal from NI-9219 data acquisition card (high resolution mode of sampling rate at 1.95 Hz) and the respiratory signal from the Plux belt sensor were recorded simultaneously.

3.4.3.2 Cardiac signal capturing

The cardiac signal was acquired while the subject held his breath for 90 seconds. During this period, as the breathing was suppressed, a much weaker heartbeat signal was expected to be captured. As discussed in section 3.4.1, the frequency of the cardiac signal could be up to 1.67 Hz under the normal condition, thus resulting in that the sampling rate of the NI-9219 data acquisition card has to be at least 3.34 Hz. Therefore, during the tests for obtaining the cardiac signal, the timing option in the NI-9219 data acquisition card was selected to the high speed mode with a sample rate of 3.5 Hz.

3.4.4 Investigation of the reliability and accuracy of the nonwoven piezo-resistive sensor

The reliability and accuracy of the nonwoven piezo-resistive sensor were investigated by matching the location and number of the peaks, which represented as cardiorespiratory signals, with the peaks in the curve generated by the Plux wireless bio-signal system. The identification of the peaks and their locations were carried out by a Matlab program under the criteria that the minimum distance between every two adjacent peaks needs to be at least 0.35 second and 3 seconds interval for heartbeat signals and breathing signals, respectively.

3.4.5 Response and recovery time of the piezo-resistive nonwoven sensor

The response and recovery time of the piezo-resistive nonwoven sensor was measured during the cardiorespiratory signal acquiring. The time that the piezo-resistive nonwoven sensor required to respond functionally was noted and averaged in order to calculate the sensor response time. The recovery time of the sensor was calculated by noting the time required by the sensor to fully recover from motion artefacts.

3.5 Summary

In this chapter, the operational principle of the nonwoven fabric material based piezo-resistive pressure sensor was demonstrated and discussed. The methodology of constructing the nanoscale silver particle electroconductive ink impregnated nonwoven piezo-resistive sensor, including ink preparation, fabric impregnation process and sensor fabrication, was explained in detail. Also, the method used to create thermally bonded nonwoven materials with different parameters was introduced as well. Additionally, the key parameters that will have an effect on the piezo-resistivity of the sensor material have been listed together with the introduction of the fabric materials used throughout this research. The test procedures that carried out in this research in order to characterise and evaluate the fabricated sensors were explained in detail.

Chapter Four: Microscopy analysis of the nanoscale silver particle-based piezo-resistive nonwoven materials

4.1 Introduction

The impregnation performance of the nanoscale silver particle-based ink on the nonwoven materials was investigated using Scanning Electron Microscopy (SEM) together with Energy-dispersive X-ray Spectroscopy (EDX) technology. SEM analysis allowed a clear and high-resolution observation of the surface morphology of the nonwoven materials. The backscattered electrons (BSE) detected in SEM showed a different colour for different elements; the atom nuclei with a larger size (higher atomic number) were detected with more BSEs, therefore resulting in a stronger signal and brighter image. By detecting the BSEs from the sample, a preliminary idea of the distribution of the silver particles could be obtained. However, due to the fact of the tiny size of the nanoscale silver particles, EDX spectrum imaging technology was used for the in-depth investigation of the distribution and elemental amount of the nanoscale silver particles in the impregnated nonwoven samples.

4.2 Nonwoven materials with a smooth surface structure

The nonwoven materials with a smooth surface structure used in this research consist of sample A, B, C, E, F, G, H and I, as concluded in **Table 3-5**.

4.2.1 Thin nonwoven materials (sample A and B)

Among all samples, sample A and B are with relatively small thicknesses which are 0.07 mm and 0.1 mm, respectively. The images of sample A and B, captured from SEM test are shown in **Figure 4-1** and **Figure 4-2**. As mentioned previously, the silver element which has a higher atomic number will show bright in the BSE SEM image, whereas the fibres which mainly consist of carbon will show in a darker colour.

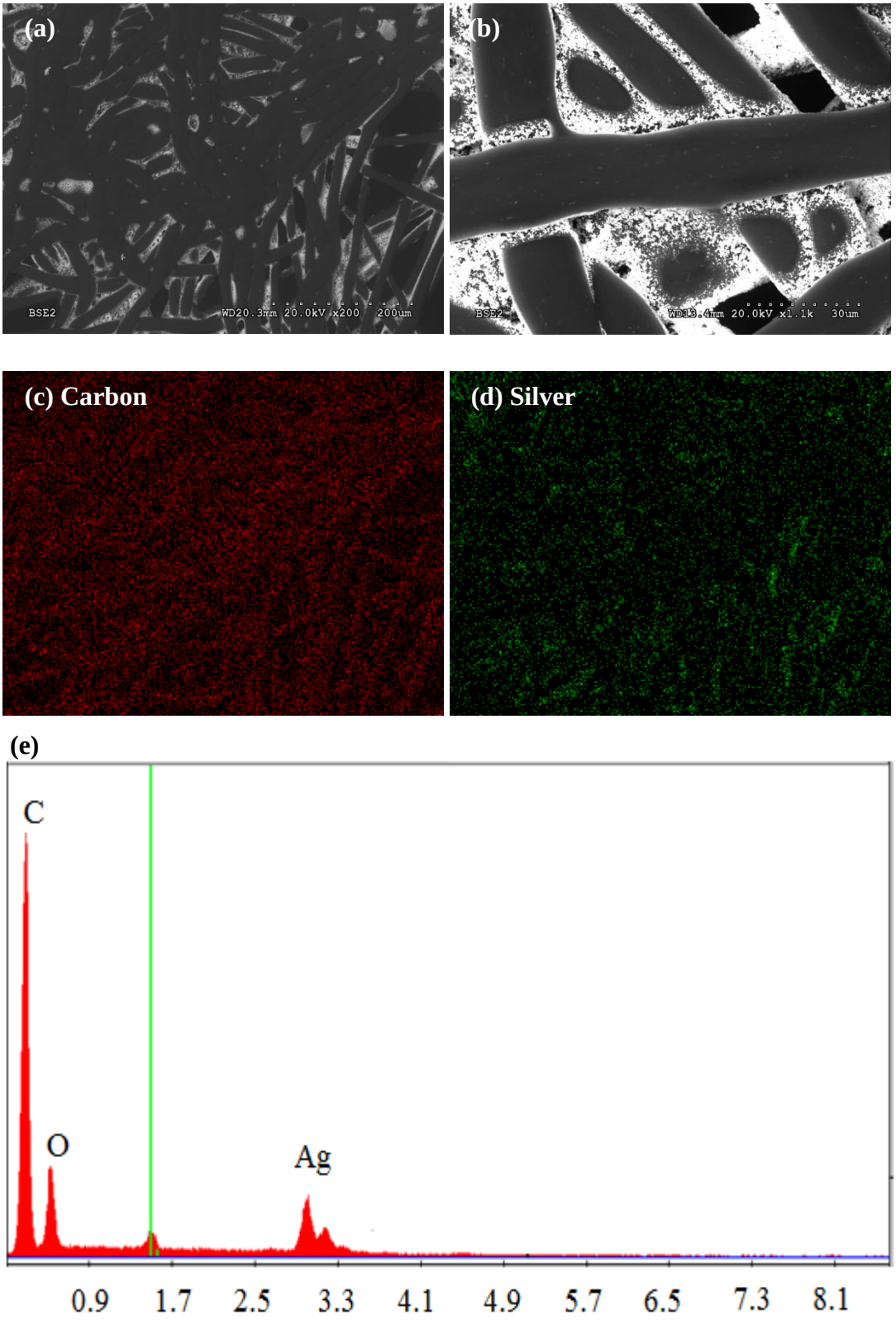

Figure 4-1. (a) and (b): The SEM images of sample A with different magnifications; (c) and (d): the EDX elemental mapping of (a); (e): the EDX elemental spectrum.

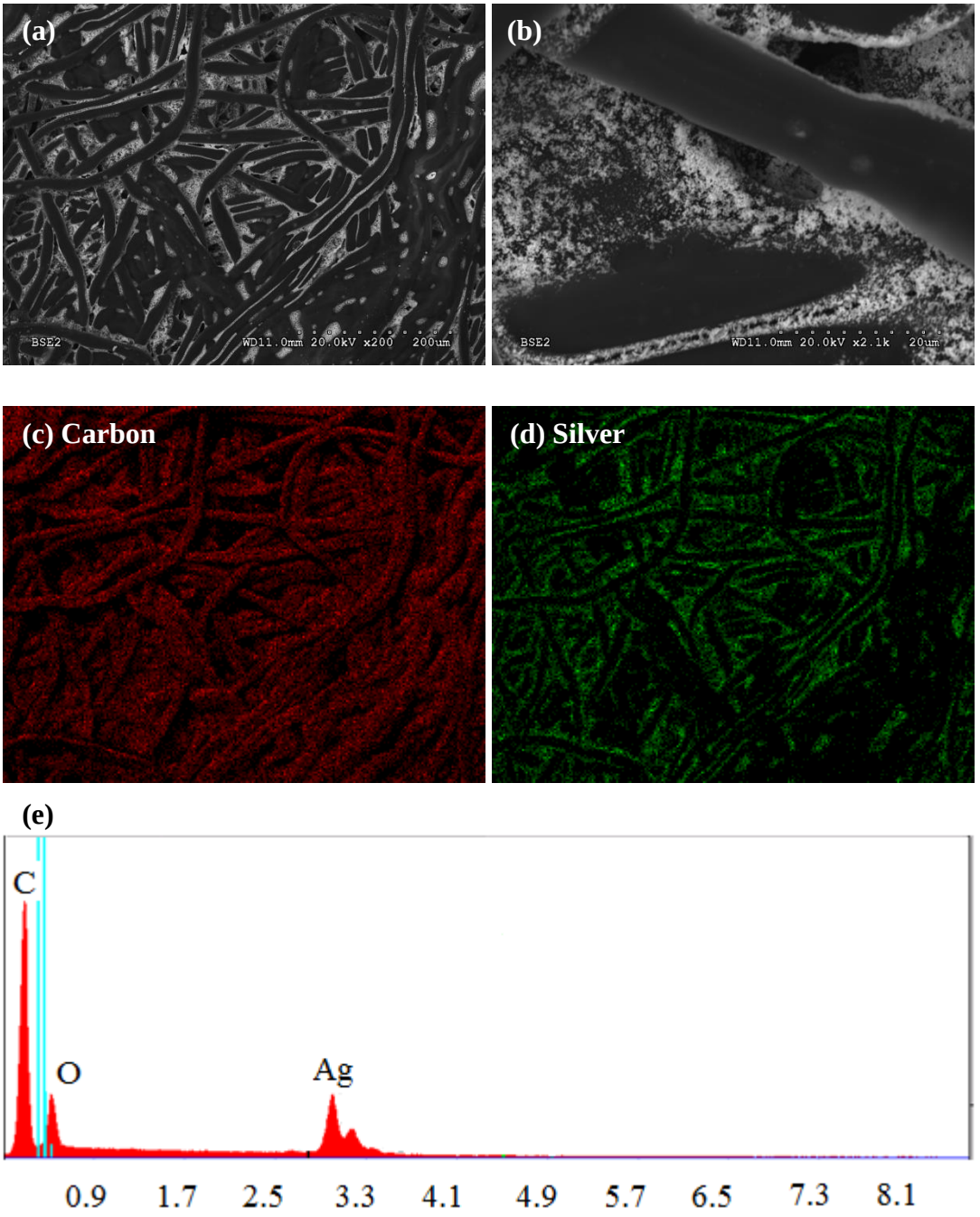

Figure 4-2. (a) and (b): The SEM images of sample B with different magnifications; (c) and (d): the EDX elemental mapping of (a); (e): the EDX elemental spectrum.

Clearly, it can be seen in **Figure 4-1(a)** and **(b)** that the silver particles are gathered in the spaces in between the fibres, whereas much fewer bright spots can be identified on the surface of the fibres, only under higher magnification. However, from the EDX mapping and spectrum results **Figure 4-1(c)**, **(d)** and **(e)**, the silver particles (shown in green colour) are evenly distributed over the whole area, proving the uniform dip-coating result. Regarding sample B, similar conclusions can be made from the SEM

images, other than more silver contents can be observed. While the EDX analysis results show a much clearer orientation of the fibres, in both carbon and silver elemental mappings. However, in the silver elemental mapping, most of the silver elements are detected only in the pore area of the nonwoven material, which is considered as a less uniform distribution than sample A. Comparing the microscopy results of sample A and B, it is found that sample A is a more 2D structure. This is because that in order to create a thin thermally bonded nonwoven, during the thermal bonding process, a high pressure is applied and due to reaching the melting point, the fibres are pressed flat. Therefore, there is a higher chance of the disposition of the nanoscale silver particles on the more flat material (sample A), resulting in a more uniform performance. And as a result of high area density, the fibres on the surface of sample B become even closer due to the high level of pressure, which further prevents the silver particles from going into the fabric.

Table 4-1. The weight percentages of carbon, hydrogen, oxygen and silver elements in the piezo-resistive nonwoven fabric A and B.

Element	Nominal weight percentage (%)	
	Sample A	Sample B
C/H/O	86.29	79.62
Ag	13.71	20.38

4.2.2 Thick nonwoven materials (sample C and E)

Sample C and E are the purchased samples which are thicker than sample A and B. The SEM images and results of EDX analysis of sample C are shown in **Table 4-2**, **Figure 4-3**, **Figure 4-4** and **Figure 4-5**. It is obvious that sample C shows a multi-layer structure, compared with sample A and B. The inner layer of the nonwoven fabric structure is observed by capturing SEM images through a pore on the surface under a higher magnification. As shown in **Table 4-2**, more silver element appears inside the nonwoven fabric. It is believed that the nanoscale silver particles can be trapped more easily in the pores within the fabric structure, rather than within the pores on the surface

(areas for agglomeration is higher within a volume than on a surface). This can be observed in the cross-section image as well, as shown in **Figure 4-3(c)**.

Table 4-2. The weight percentages of carbon, hydrogen, oxygen and silver elements in the piezo-resistive nonwoven fabric C, on the surface and inner layer.

Element	Nominal weight percentage (%)	
	Surface	Inner layer
C/H/O	75.93	62.05
Ag	24.07	37.95

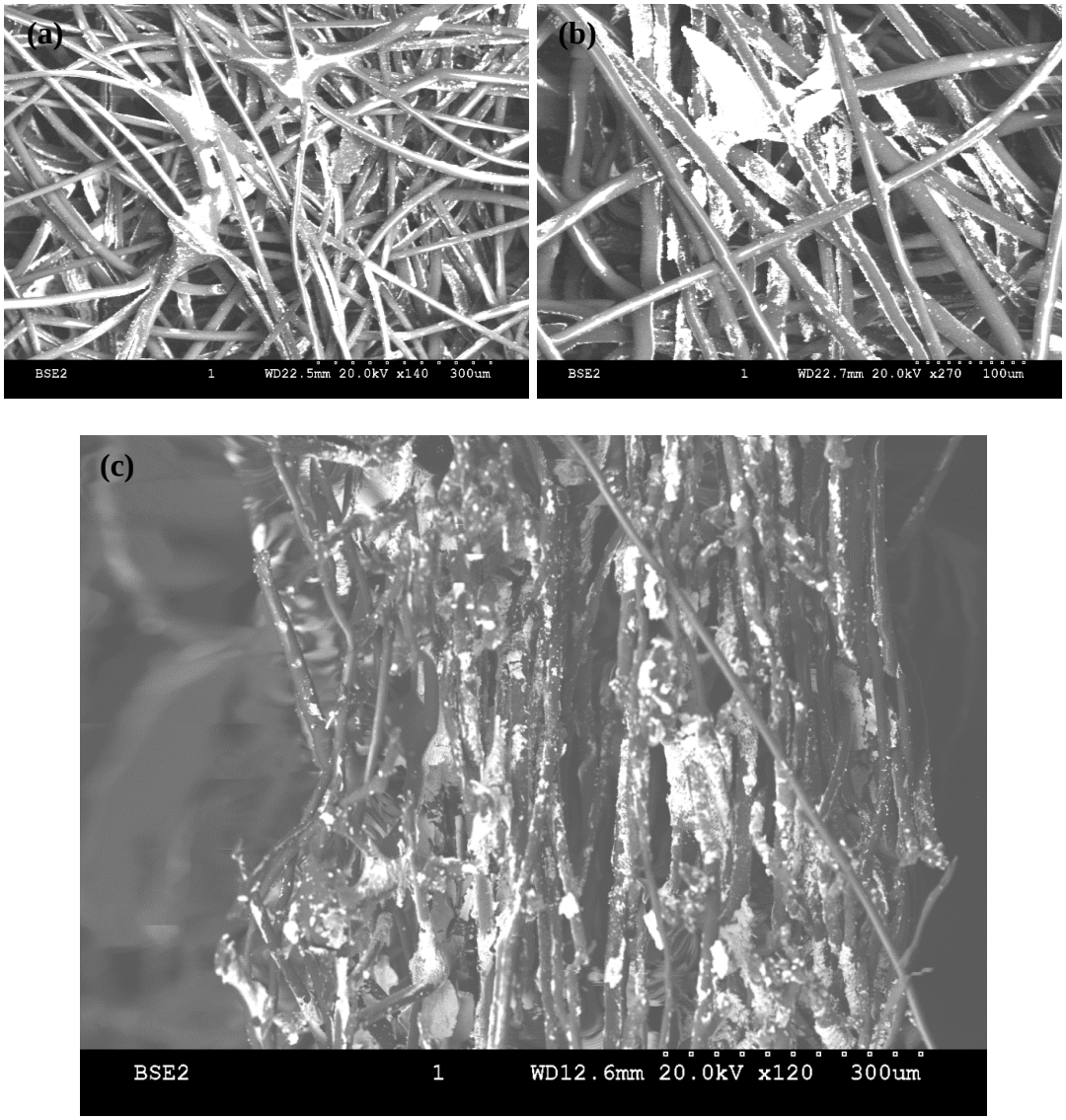

Figure 4-3. The SEM images of sample C with different magnifications. (a): surface SEM image; (b): inner layer SEM image; (c): cross-section SEM image.

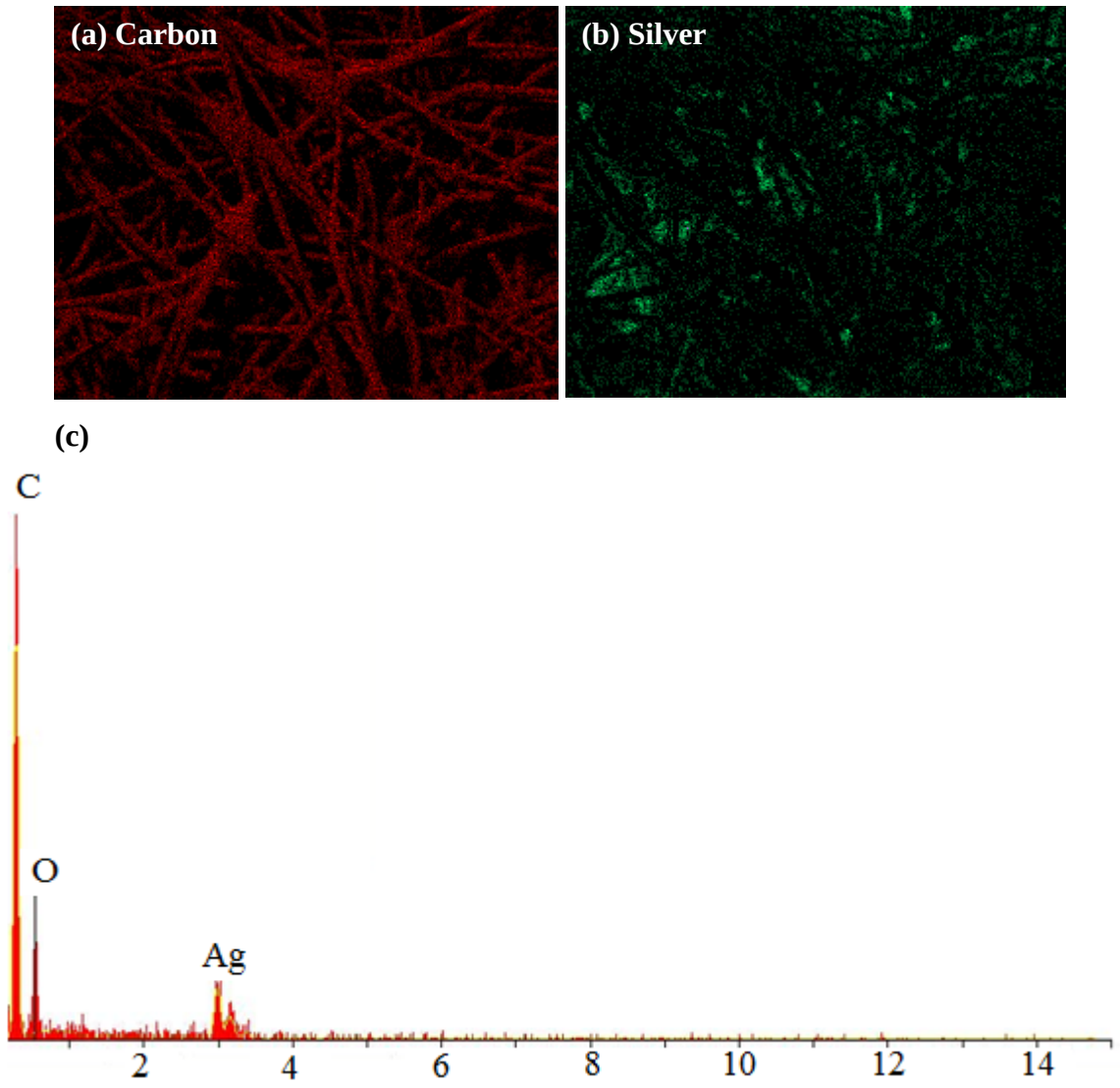

Figure 4-4. (a) and (b): the EDX elemental mapping of the surface on sample C; (c): the EDX elemental spectrum.

The EDX element mappings for both the surface and inner layer of the nonwoven material can be found in **Figure 4-4** and **Figure 4-5**. The fibre orientation for both these areas can be clearly seen through the carbon element mapping. However, in the silver element mapping, the silver particles are less evenly distributed than sample A and B; the silver particles either fill some pores completely or do not appear at some pores at all. From the spectrum analysis carried out for the internal structure, a higher intensity of silver element is visible due to the large area of the silver covering in the upper part of the image seen in **Figure 4-5(b)**. Other than that large agglomerate of silver, the rest of the area has less silver element.

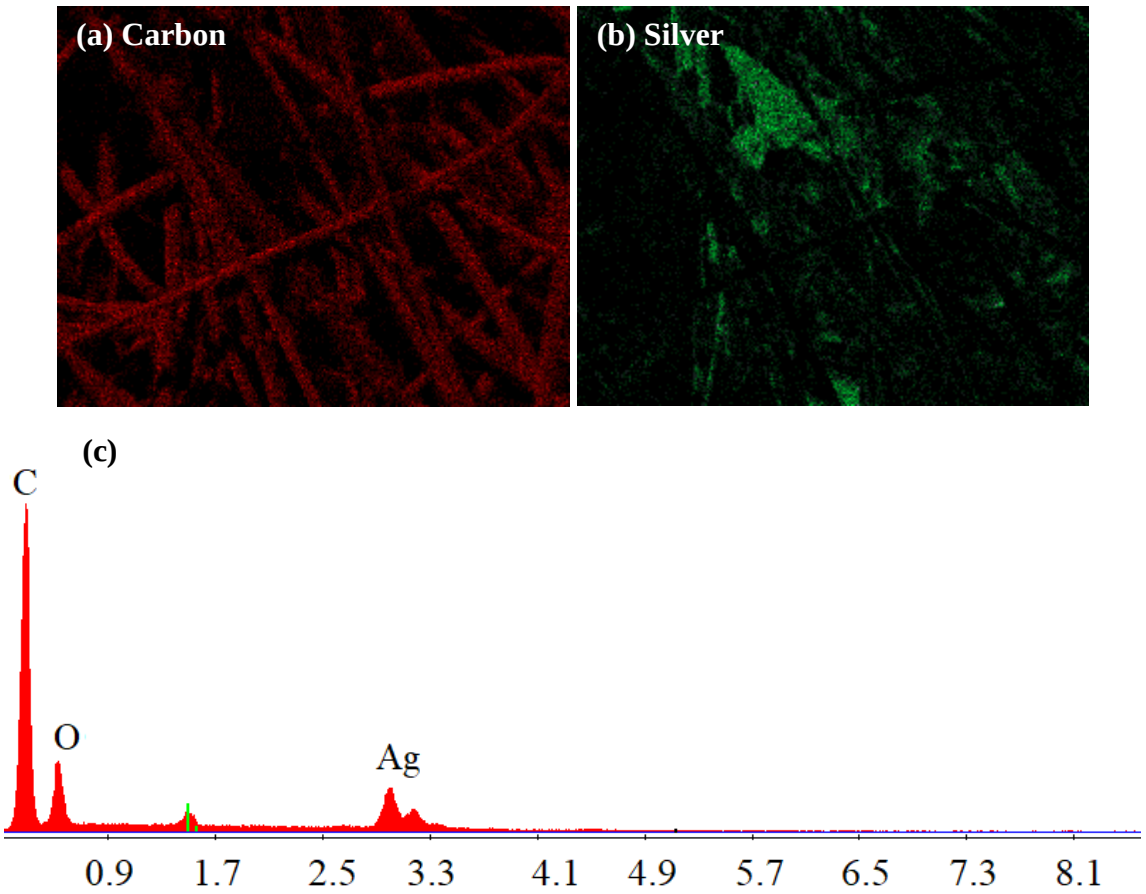

Figure 4-5. (a) and (b): the EDX elemental mapping of the inner layer of sample C; (c): the EDX elemental spectrum.

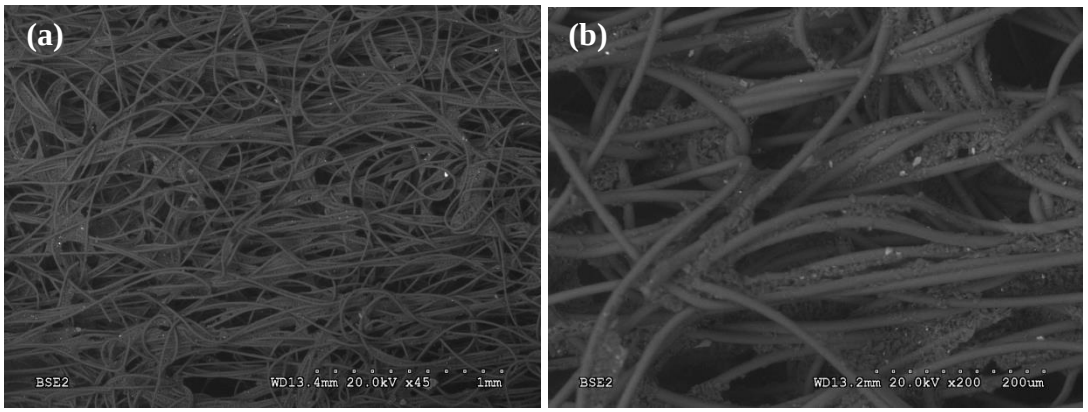

Figure 4-6. The SEM images of sample E under different magnifications.

Sample E is produced via spunlace bonding technology, which as expected will show a difference in the appearance of the nonwoven fabric. This can be clearly observed from the SEM images (**Figure 4-6**). The carbon particles have a coarse appearance on the nonwoven fabric, covering the pore area, where only very little can be found on the

fibres. Instead of being deposited onto the fibres, the carbon particles are acting more like an adhesion that turning many fine fibres into heavier fibre bundles.

A noticeable difference between the nonwoven materials with small and big thickness is that the porous structures in the thicker nonwoven are found free from clogging. Even in the example of sample E where carbon particles practically glue the single fibres into fibre bundles, still, most of the pores are not clogged. However, in the event of the thinner nonwoven materials, the troughs between fibres are found full of silver agglomerates. This further enhances the thinner nonwoven materials as single layer structure, which means in the piezo-resistive based application, the change in resistance mostly can be obtained from the deformation, whereas the thicker nonwoven materials may show better piezo-resistivity due to the creation of extra contact points between layers apart from between fibres.

4.2.3 Laboratory-made thermally bonded nonwoven fabrics (sample F to I)

The nonwoven fabrics produced from university available facilities were examined under SEM and EDX as well. From the SEM images shown in **Figure 4-7**, **Figure 4-8**, **Figure 4-9** and **Figure 4-10**, it can be discovered that the silver morphology and distribution in these samples are very similar to each other. Due to the fact that during the dip-coating process, the aqueous ink will create thin membranes at the pore areas based on its surface tension; the smaller the pore size, the easier for the thin membranes to form. While being thermal sintered, the aqueous solution is being evaporated quickly, leaving the silver agglomerations along the pore area. Therefore, the following deposition situations can be concluded.

1) Deposition on the surface of the fibres: this is observed from **Figure 4-9(b)** that silver particles evenly covered the whole fibre structure showing a white shiny appearance.
2) Complete coverage over the pore: this happens when the membrane is thick enough to maintain its form throughout the thermal sintering process, where the maximum amount of silver is left as shown in **Figure 4-8(a)** and **Figure 4-10(b)**.
3) Partial coverage over the pore: during the thermal sintering process, the membrane breaks due to heat or surface tension of the ink; however, a lot of silver particles remain at the pore, as can be seen in **Figure 4-9(a)** and **Figure 4-10(b)**.

4) Deposition along the pore: as illustrated in **Figure 4-7(a)**, silver particles are deposited on the inner ring of a pore (marked in a red circle).

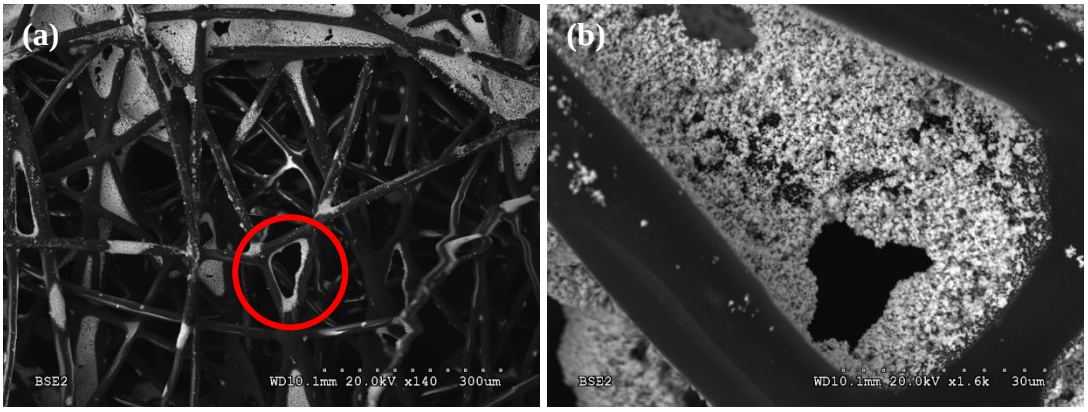

Figure 4-7. The SEM images of sample F; (a) and (b): under 140x and 1600x magnification.

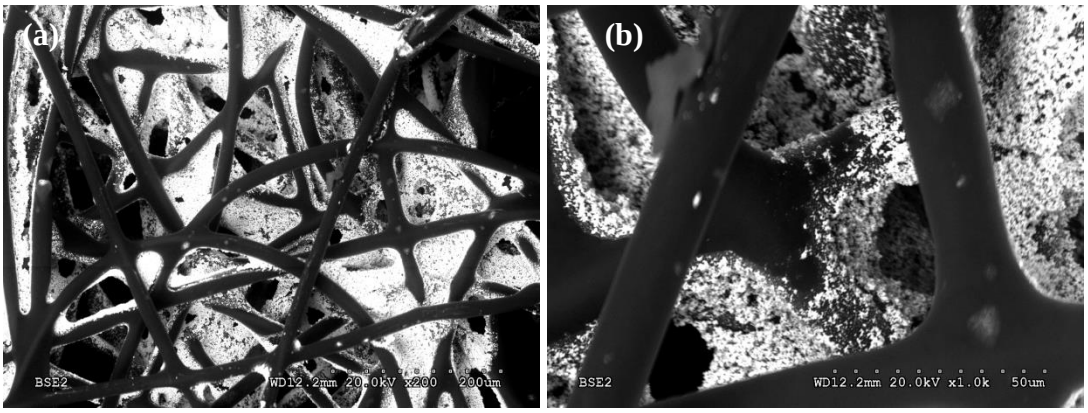

Figure 4-8. The SEM images of the sample G; (a) and (b): under 200x and 1000x magnification.

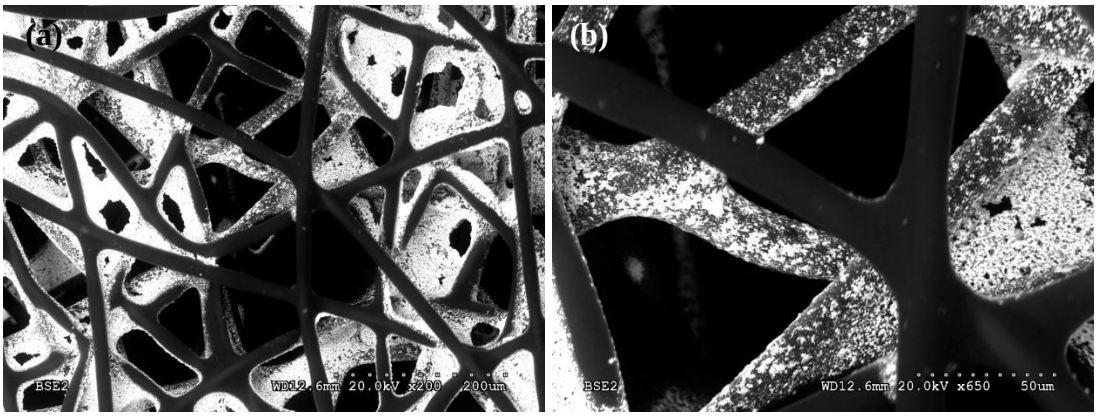

Figure 4-9. The SEM images of the sample H; (a) and (b): under 200x and 650x magnifications.

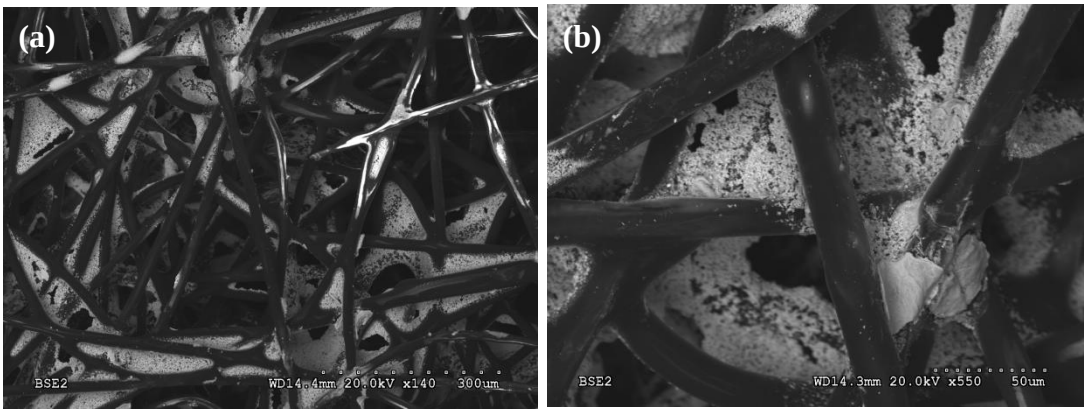

Figure 4-10. The SEM images of sample I; (a) and (b): under 140x and 550x magnifications.

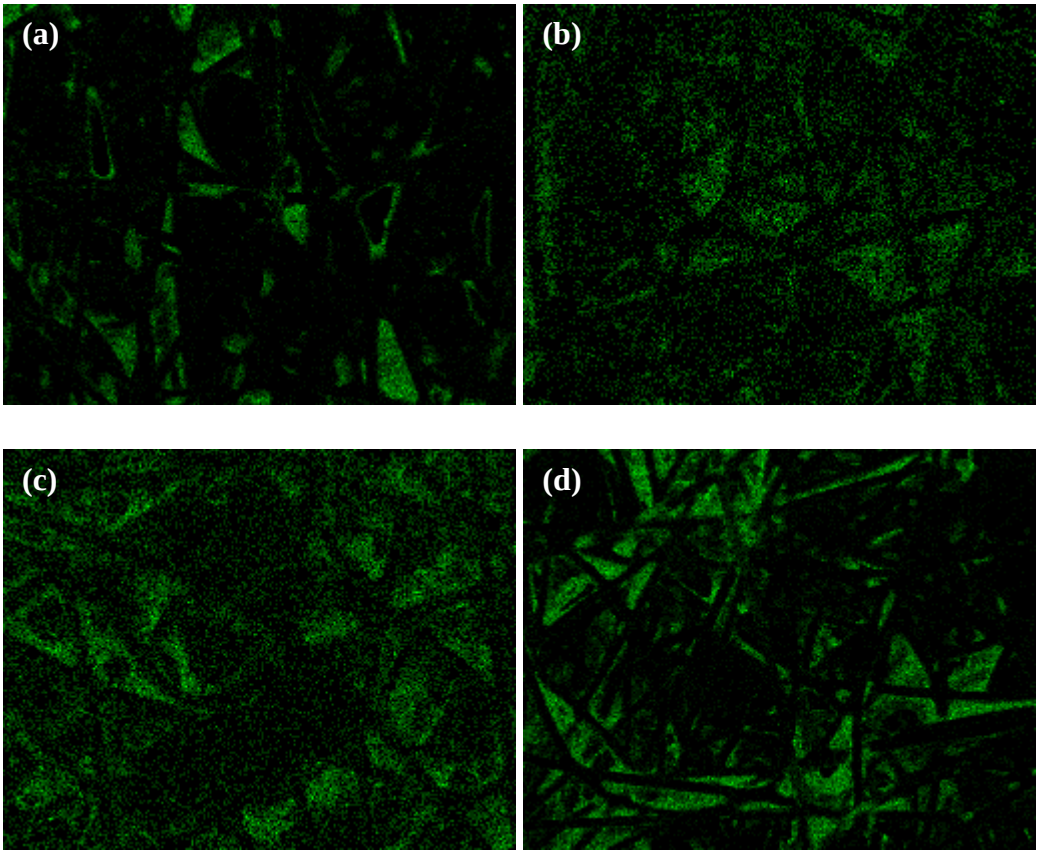

Figure 4-11. The EDX elemental mappings of (a): sample F, (b): sample G, (c): sample H and (d): sample I.

Figure 4-11 and **Table 4-3** show the results of EDX analysis on these samples. Uniform silver particle distribution can be observed from the elemental mappings of sample G and H; other than some pores covered completely by silver particles, other areas were distributed with silver particles evenly. However, in the aspect of sample F and I, the

silver particles gathered mostly at some pore areas. This corresponds to the relatively low silver weight percentages of sample F and I.

Table 4-3. Silver element weight% of sample F, G, H and I.

Sample	Silver element weight percentage (%)
F	13.68
G	22.64
H	25.10
I	19.52

It can be concluded that the evenness of the nanoscale silver particle distribution relies on following two conditions:

(1) whether or not the silver particles can be deposited on the surface of the fibre instead of just forming membranes between fibres;
(2) whether or not the silver particles can enter the inner structure of the fabric.

One approach to achieving these two conditions is to reduce the thickness of the nonwoven fabric which turns the fabric to a planar structure. However, this limits the area density of the nonwoven fabric, as increasing the area density will decrease the distance between fibres, which eventually causes the formation of silver membranes and clog the porous area. Also, the thinner nonwoven fabrics were found less capable of taking-up silver contents (as shown in **Table 3-5**), which would increase the electrical resistance of the sensor and affect the sensor performance.

The other method is to reduce the diameter of the silver particles. With finer silver particles, it will be more difficult for the silver particles to form strong membranes between fibres; therefore, most of the silver particles will be deposited on the surface of the fibres. This method is also helpful for the silver particle distribution in the inner fabric structure.

4.3 Nonwoven material with an embossed dot pattern (sample D)

The dot pattern embossed nonwoven fabric can be produced using thermal point bonding by passing the batt web through a pair of engraved hot calendars. The batt web

will only be bonded at the engraved points. Therefore, there are two different surface structures in the dot pattern embossed nonwoven fabrics.

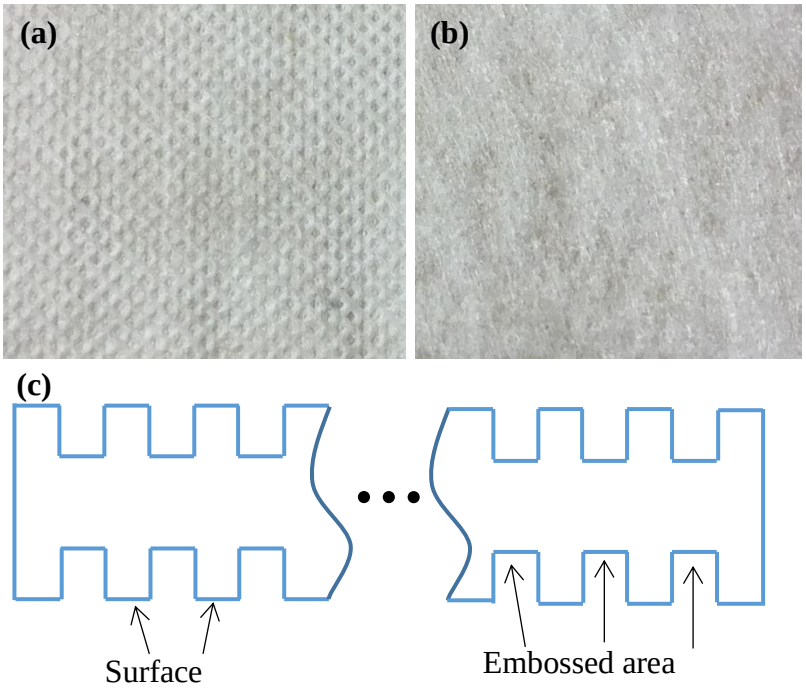

Figure 4-12. Photos of (a) dot embossed nonwoven fabric and (b) smooth surface nonwoven. (c): a schematic of dot embossed nonwoven fabric.

The differences between the dot pattern embossed nonwoven fabric and the smooth surface nonwoven fabric are illustrated in **Figure 4-12**. The nanoscale silver particle ink impregnation performance on both the surface and the embossed area is analysed.

It can be seen in **Figure 4-13** that the surface SEM picture clearly shows the fibre orientation and the larger number of silver particles. In the SEM image taken inside the surface depression created due to embossing, there is a lower amount of silver ink visible which is to be expected due to the depth of vision inside the embossing. As illustrated in **Figure 4-13(a)**, it is apparent that the silver particle ink is more or less evenly distributed onto almost every fibre on the surface, while not covering them completely. Additionally, as the figure shows, the ink particles do not clog the pores in the nonwoven structure, which was not observed in any other nonwoven materials. This is because that the fibres in the surface structure were not thermally bonded, which resulted that the porous structure was not fixed as thermally bonded structures. Due to the pressure applied during mangle process, the thin silver ink membrane existed in the

porous structure was broken, which provided the results of silver disposition on the fibre surface or along the inner ring of the pore structures as discussed in section 4.2.3.

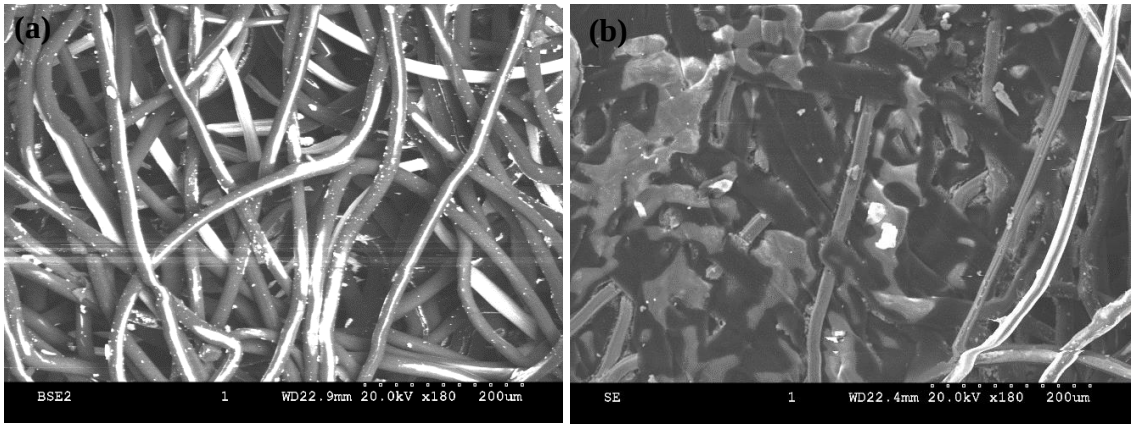

Figure 4-13. SEM images of the dotted pattern nonwoven (sample D); (a): surface SEM image; (b): embossed area SEM image.

In the EDX spectrum analysis, the weight percentage and atomic percentage of the silver element on the surface of the fabric and inside of the fabric are close (as shown in **Table 4-4**). This can be considered as evidence that the nanoscale silver particles are evenly distributed in the electroconductive nonwoven fabric both on the surface structure and embossed area.

Table 4-4. Silver element weight% of sample D.

Element	Nominal weight percentage (%)	
	Surface	Embossed area
C/H/O	88.71	87.1
Ag	11.29	12.9

Figure 4-14 clearly illustrates the fibre orientation and the distribution of the carbon and silver elements on the surface structure of the dot pattern embossed nonwoven fabric, which shows the uniform distribution of nanoscale silver particles.

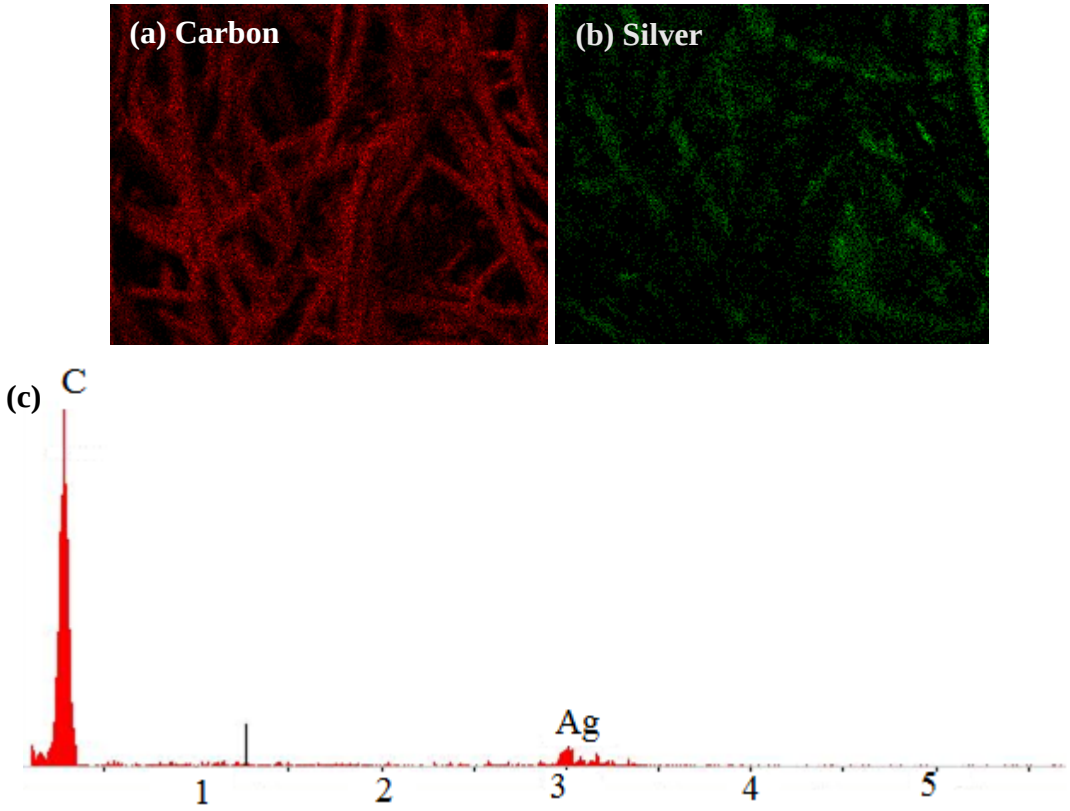

Figure 4-14. (a) and (b): the EDX elemental mapping of the surface structure of sample D; (c): the EDX elemental spectrum.

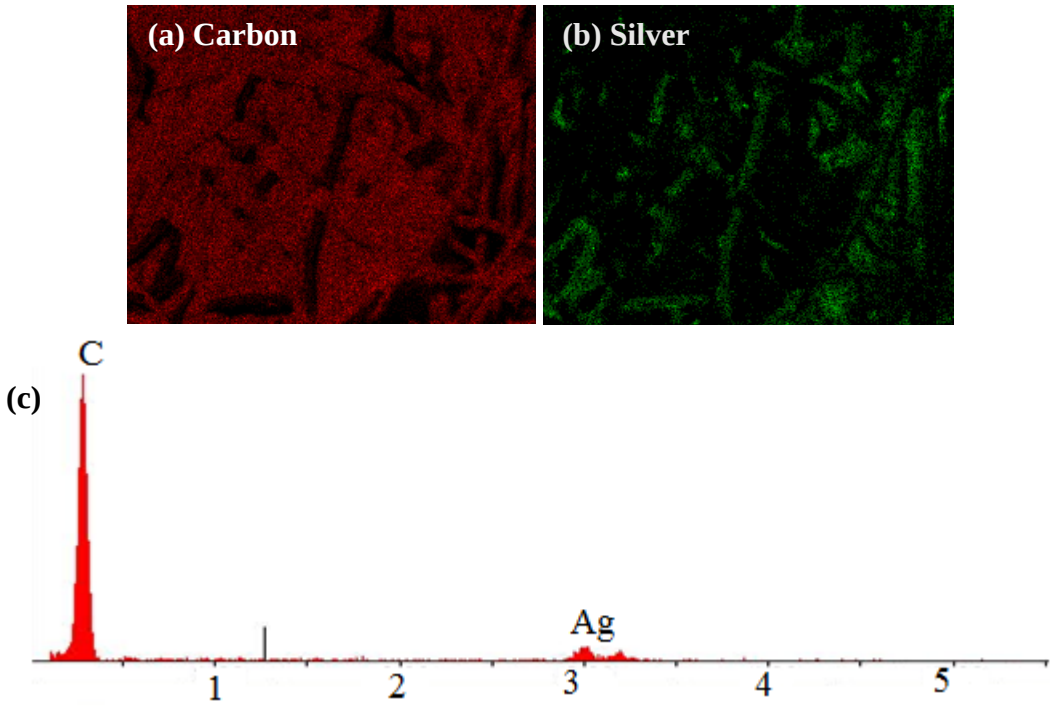

Figure 4-15. (a) and (b): the EDX elemental mapping of the embossed area of sample D; (c): the EDX elemental spectrum.

Figure 4-15 shows the EDX analysis on the embossed area of the dot pattern embossed nonwoven fabric. In the spectrum analysis, the intensity of the silver peak is similar to

that in the surface spectrum, which is identical to the findings from **Table 4-4**. As seen in **Figure 4-15(a)**, due to the larger density of the fibres produced by the point bonding during the embossing, the image shows a larger amount of carbon elements, where the orientation of the fibres cannot be clearly identified. However, from the silver element mapping (illustrated in **Figure 4-15(b)**), nanoscale silver particles are still visible as evenly distributed.

Comparing with the SEM and EDX results from the nonwoven fabrics with a smooth surface and the nonwoven fabrics with a dot embossed pattern, it can be concluded that the dot pattern embossed nonwovens gains a more uniform impregnation performance. One reason for this is that the partially bonded surface makes the silver particle enter the inner fabric structure more easily, which has been discussed above. The other reason for the better impregnation performance can be that the embossed area allows the silver particle ink be impregnated through not only the surface but also the wall of the embossed area.

4.4 Knitted fabric and woven fabric

The impregnation performance of the nanoscale silver particle-based ink on the knitted fabric and the woven fabric was investigated by SEM and EDX as well, in order to provide comparisons against nonwoven materials.

The knitted fabric sample was an interlock structure fabric, which was created with 10 gauge Shima Seiki electronic flatbed knitting machine, using two ends of 167/34 polyester yarns. The woven fabric was a plain weave. The closely twisted polyester filaments and the tight fabric structure provided a very dense performance, which can be clearly seen in the SEM images in **Figure 4-16**. Different from the nonwoven fabric samples, it is difficult to observe silver particles on the surface of the yarns, whereas the yarns capture a lot of silver particles within them. This is under expectation as the microstructures of fibres were able to absorb the nanoscale particle-based ink better than the yarn structure. From the results of EDX analysis (as shown in **Figure 4-17**), the silver particles are found evenly distributed within the yarns.

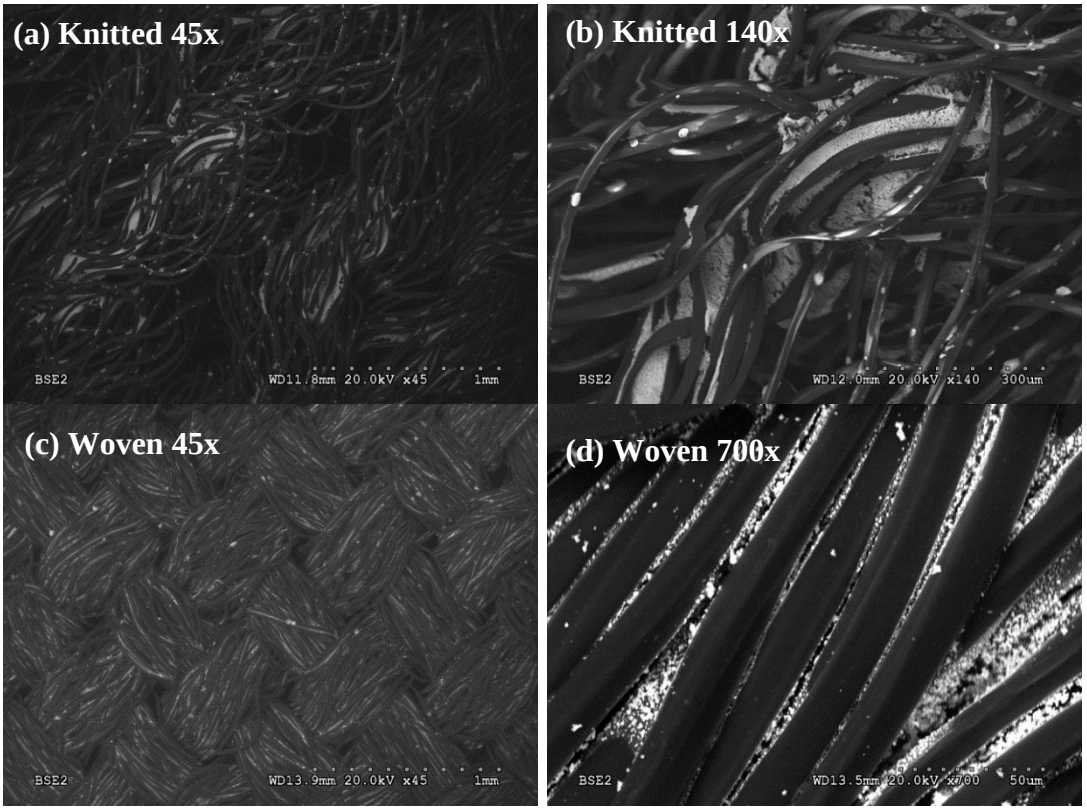

Figure 4-16. The SEM images of knitted fabric sample J and woven fabric sample K, under different magnifications: (a) 45x; (b) 140x; (c): 45x; (d): 700x.

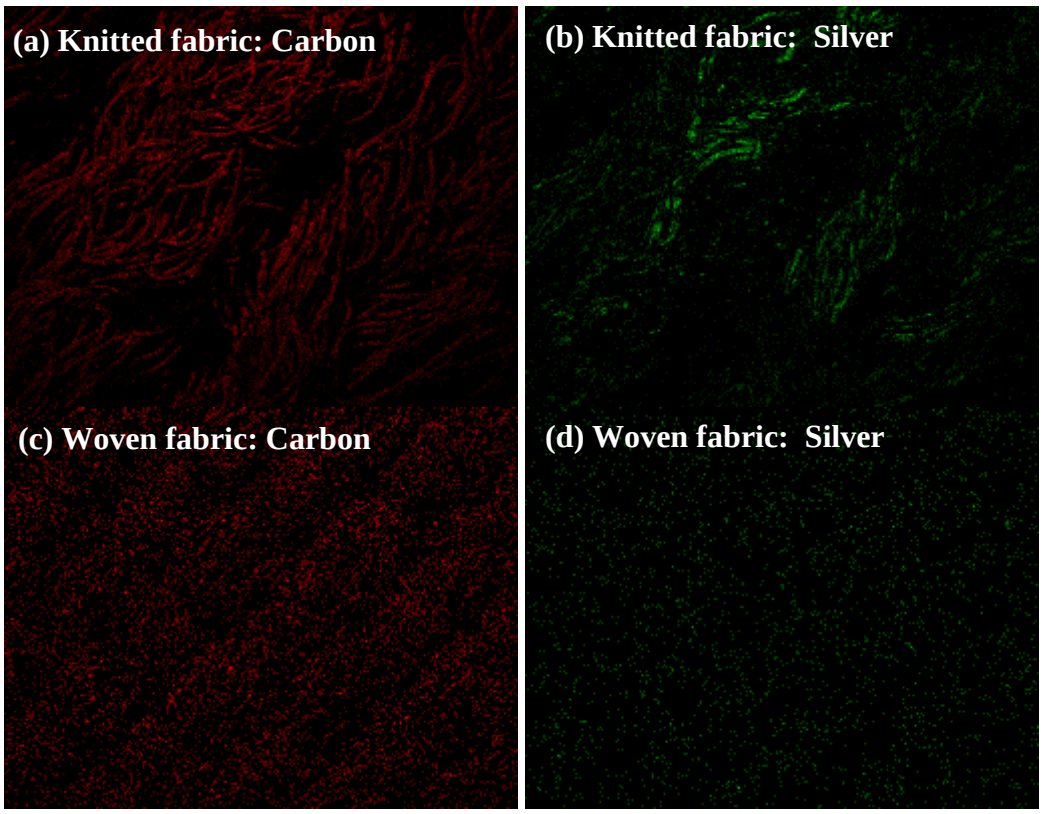

Figure 4-17. The EDX elemental mapping of knitted fabric sample J and woven fabric sample K.

4.5 Summary

In this chapter, SEM and EDX analysis were carried out on the nanoscale silver particle-based electroconductive ink impregnated nonwoven fabrics, together with a knitted fabric sample and a woven fabric sample, in order to understand the morphology of the silver particle distribution and the impregnation performance. It was found that the morphology of the silver particle distributions can be classified into four types, depending on whether or not the silver particles were deposited on the fibre surface and the coverage over the pore area.

The thinner nonwoven fabric samples (sample A and B) were found in a 2D planar form, due to the high pressure applied by the calendars during the thermal bonding process. The fibres were compressed close to each other, especially for sample B which had a higher area density. With a close fibre distance, the silver particles might clog the areas between fibres, which further prevented the silver particles from being deposited into the fabric. Therefore, the thinner nonwoven fabric samples had a higher chance of uneven particle distribution on the surface and the inside of the fabric than the thicker nonwoven fabric samples (sample C and E).

It was also found that the dot pattern embossed nonwoven fabric (sample D) achieved a better impregnation result than smooth surface nonwoven fabrics (sample A, B and C), thanks to the unique embossed surface structure that provided more surface area for the nanoscale silver particles to enter the inner fabric. The partially bonded surface structure also contributed to the even particle distribution.

Additionally, from the SEM and EDX analysis results of the knitted fabric (sample J) and woven fabric (sample K), it was discovered that upon impregnation, the nanoscale silver particles were absorbed by the yarns, instead of staying on the surface of the yarns. This gave the knitted and woven fabric samples a uniform nanoscale silver distribution under EDX analysis.

Chapter Five: Characterisation and optimisation of the nanoscale silver particle-based piezo-resistive sensor

5.1 Introduction

In this chapter, the experiments and results of the characterisation of the nanoscale silver particle-based ink impregnated nonwoven piezo-resistive sensor were reported. Also, the cardiorespiratory signals were captured using the designed sensor and their evaluations were carried out by comparison against a commercially available bio-signal monitoring system (Plux bio-signal system). Additionally, the empirical models of the conductance, piezo-resistive sensitivity and resistivity of a nonwoven sensor fabricated with directional silver coated polyester yarns were calculated.

5.2 Characterisation of nanoscale silver particle-based piezo-resistive nonwoven materials

Generally, the characterisation of the nanoscale silver particle-based piezo-resistive nonwoven materials is based on the investigation of the piezo-resistive performance of the materials. Therefore, the electromechanical tests, including quasi-static compression tests, cyclic loading tests and resistance time drift (RTD) analysis tests were carried out. The piezo-resistive sensors investigated are summarised in **Table 5-1**.

Table 5-1. The piezo-resistive nonwoven fabric based sensors.

Sensor	Sensor thickness (mm)	Silver take-up (%)	Remarks
A	0.96	25.2	N/A
B	1.04	13.3	N/A
C	1.29	68.0	N/A
D	1.24	65.2	Embossed dot surface
E	1.16	60.0% carbon	Electroconductive
F	1.13	98.1	15 g of PP/PET
G	1.14	82.3	20 g of PP/PET
H	1.16	111.2	25 g of PP/PET
I	1.23	78.6	30 g of PP/PET
J	2.19	49.0	Interlock knitted fabric
K	1.22	32.2	Plain woven fabric

5.2.1 Preliminary tests

The preliminary tests include the compression tests on the piezo-resistive nonwoven fabric based sensors fabricated using the method introduced in Chapter Three in order to determine the elastic regions of the fabric sensors. Also, the effectiveness of the webbing fabrics was investigated. In addition, the effect of the silver take-up percentage on the nonwoven fabrics was studied.

5.2.1.1 Compressive strength tests

Figure 5-1 shows the results of compressive strength tests on all 11 samples, from which it can be found that the nonwoven fabric-based sensor samples behaved similarly. Considering the application of the investigated sensors was aimed at weak bio-signals, such as cardiorespiratory signals, the compressive range used in further testing was selected as 0 to 100 g/cm^2 (up to 0.981 N/cm^2), which was within the elastic region of all samples.

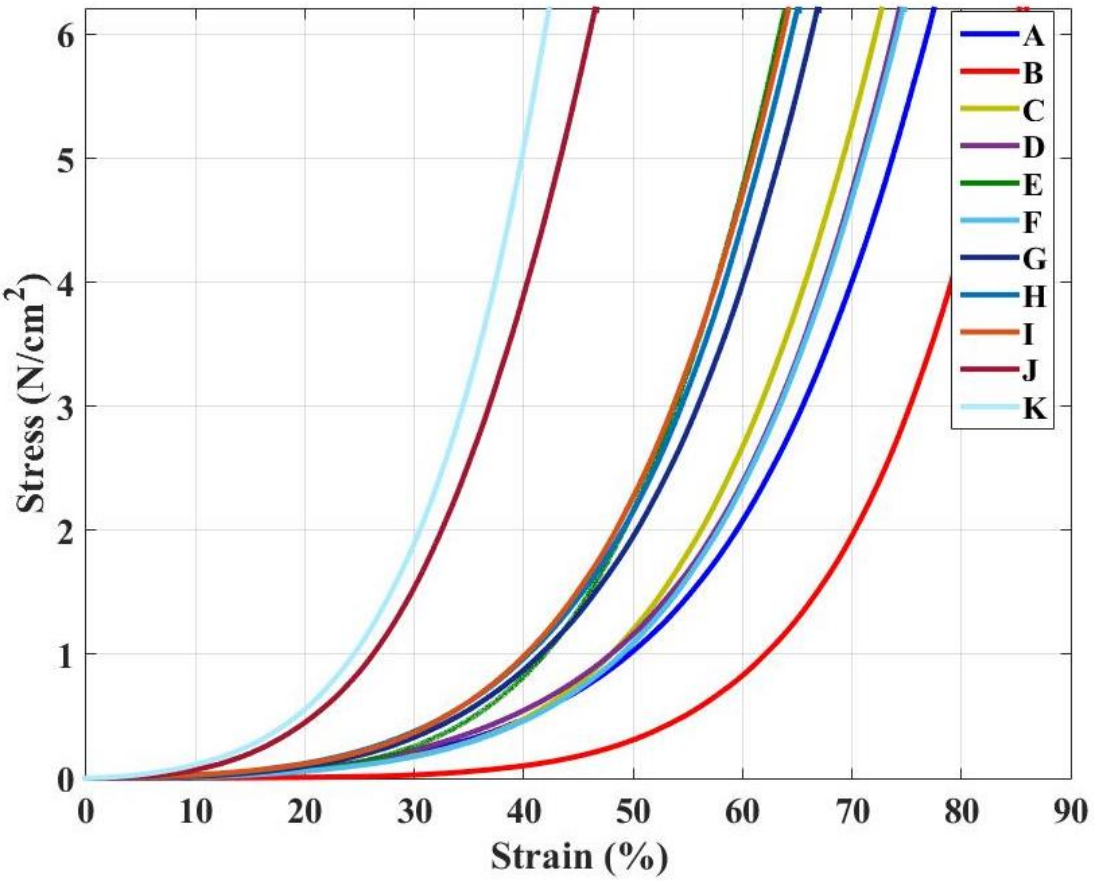

Figure 5-1. Compressive strength test results.

5.2.1.2 Effect of the webbing fabric

In order to find out the effect of the webbing fabric as adhesive to improve the connection, sample C and D were selected as they had similar area density and thickness, while with distinct surface structures. The effectiveness of the webbing fabric was evaluated by comparing the standard error of the resistance change according to pressure and the sensitivity of the sensor, which can be calculated using the following equation:

$$Piezoresistance\ sensitivity = \frac{\Delta R}{\Delta P} \qquad \textbf{Equation 5-1}$$

where: ΔR and ΔP are the change in electrical resistance and pressure, respectively.

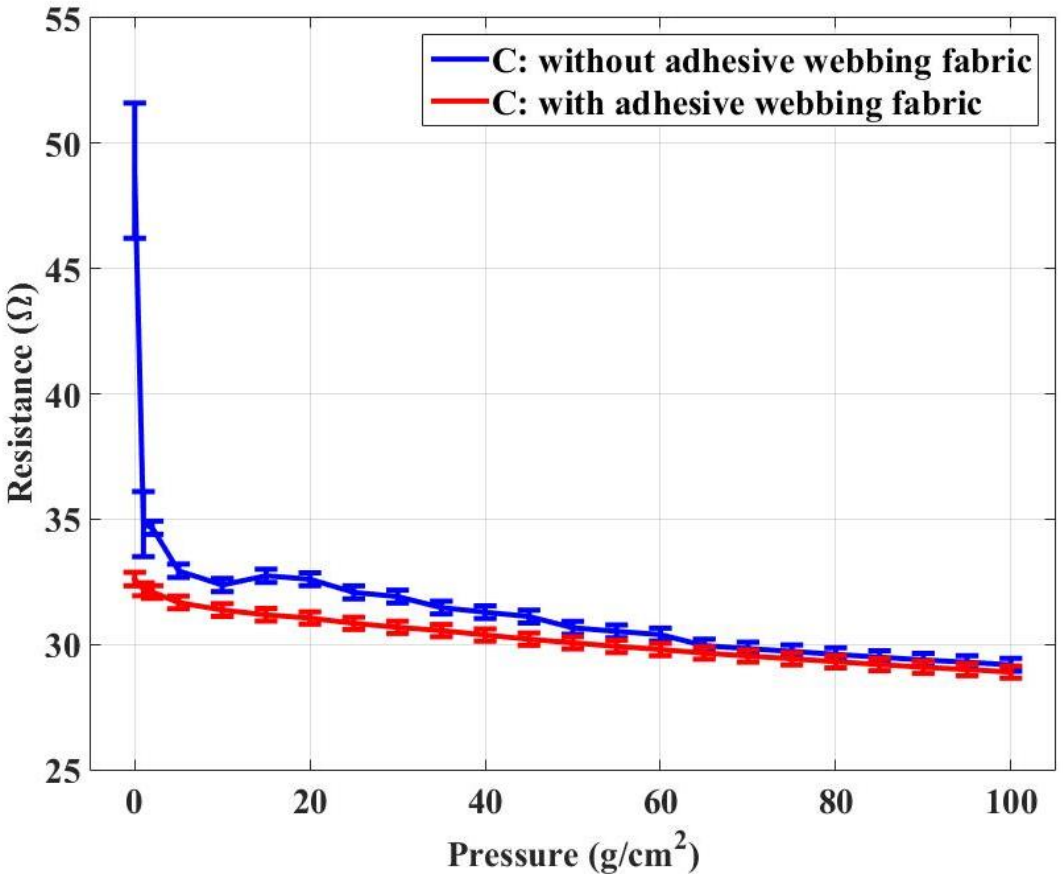

Figure 5-2. The quasi-static resistance-pressure curves of Sample C with a smooth surface structure.

It can be clearly observed in **Figure 5-2** that without the adhesive webbing fabric, sample C starts with large error bars at lower pressures, which is due to the insufficient pressure on the sensor. At a very low compressive force on the sensor (near-zero

pressure in this case), the fibre arrangement tends to have a large variation in the fibre to fibre distance in each test, which eventually causes resultant large variation in the initial resistance. As the pressure increased, the error bars (standard error) immediately decreased considerably. The adhesive webbing fabric layers were used to bind the knitted electrode and electroconductive nonwoven layers in the sensor to stabilize the sensor performance. As the experiments showed, this had an immediate result in reducing the error bars in the characteristic curve. By adding the additional webbing fabric layers, the overall resistance of the sensor was decreased.

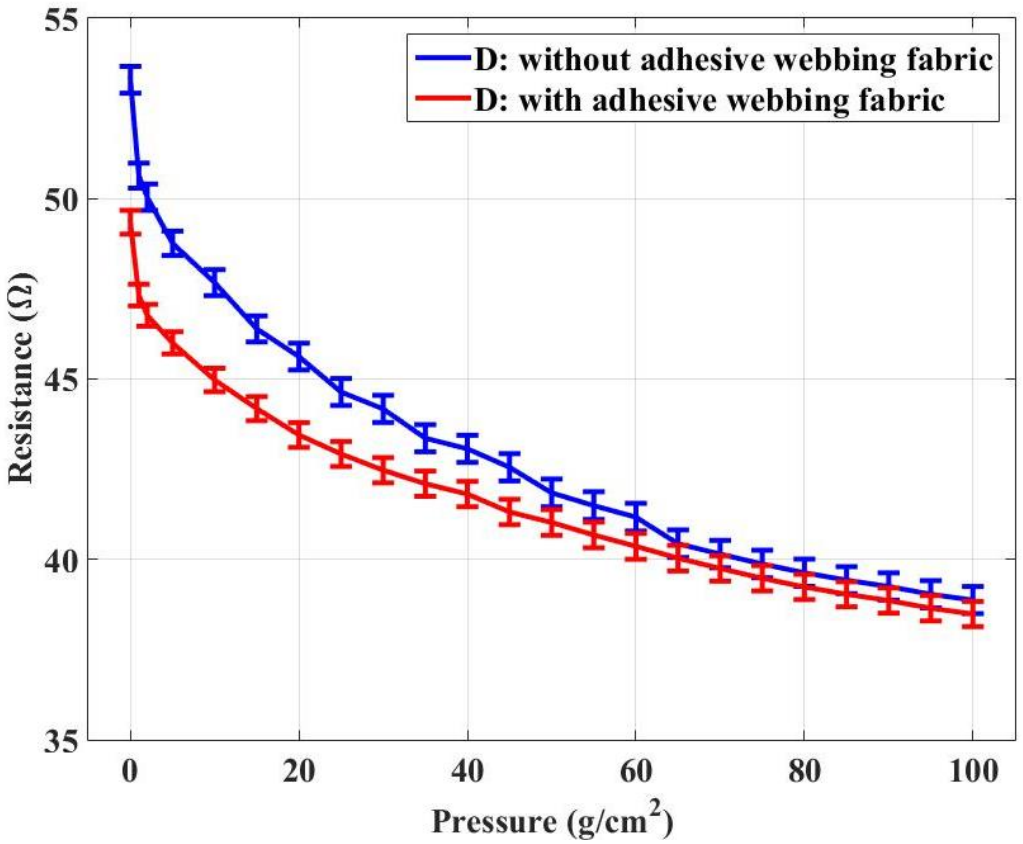

Figure 5-3. The quasi-static resistance-pressure curves of Sample D with a dot embossed surface structure.

While in **Figure 5-3**, the effect of the adhesive webbing in sample D is not as significant as in sample C. The error bars of sample D are considerable small without adhesive webbing fabrics, which means that sample D is already a more stable material than sample C in the aspect of the piezo-resistive sensor. By using adhesive webbing fabric, the fluctuations between 40 g/cm^2 to 70 g/cm^2 are eliminated.

In the aspect of the piezo-resistive sensitivity of the sensors, the webbing fabrics did not improve the sensitivity of the piezo-resistive sensor significantly as shown in **Figure**

5-4 and **Figure 5-5**, where the sensitivity of the piezo-resistive nonwoven sensor is seen to reduce as the pressure increases. As the nonwoven material gets closer to the fully compressed state, it has a reduced chance of creating additional electrical paths within the silver impregnated nonwoven material. The highest sensitivity points for both types of the nonwoven sensors are seen at 1 g/cm^2 (not shown in **Figure 5-4)** for sample C without webbing fabric, as the relatively large change in resistance causes a sensitivity value of 14.11 Ω/(g/cm^2), which is not shown in the graph). However, considering the inaccuracy caused by the large error bars, it is not suitable to use the sensor at such low-pressure levels. Generally, the piezo-resistive sensitivity of the samples without adhesive webbing fabrics is higher than those with webbing fabrics. This is due to the fact that the samples without adhesive webbing have a bigger change in the resistance overall. However, this may be caused by the large variation. Therefore, in order to obtain the accuracy and reliable resistance signal, it is necessary to construct sensors with the help of the adhesive webbing fabrics.

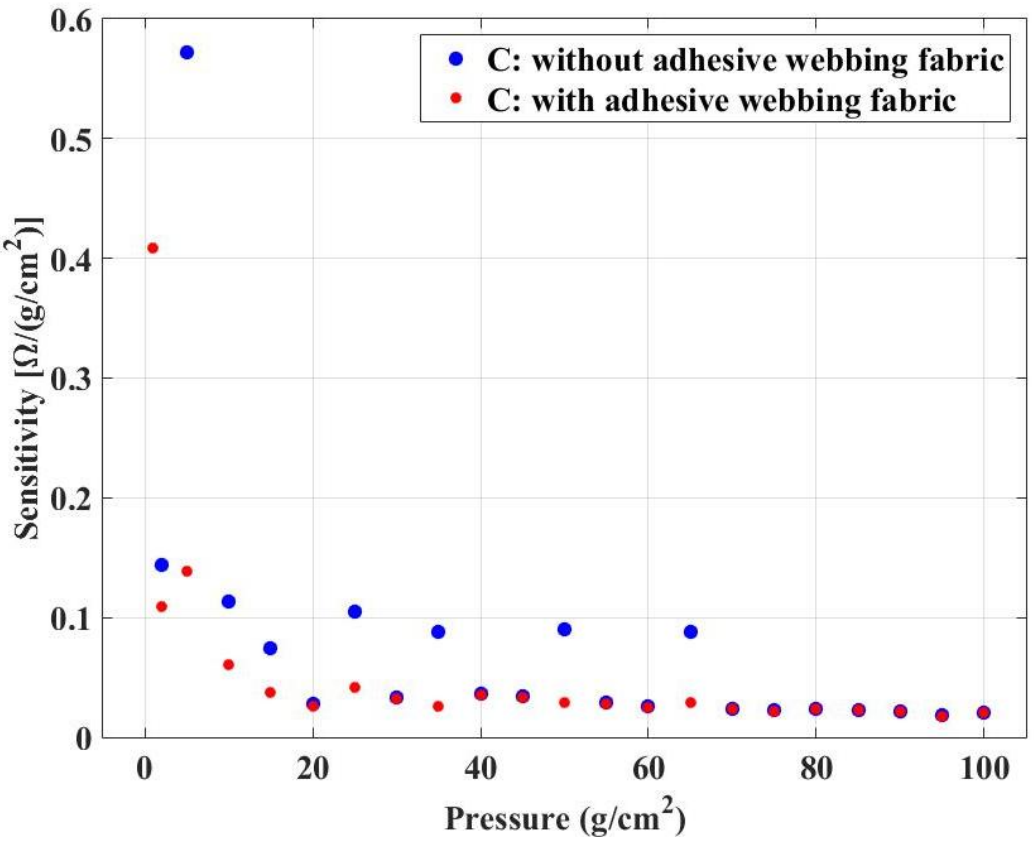

Figure 5-4. The piezo-resistive sensitivity of Sample C with a smooth surface structure.

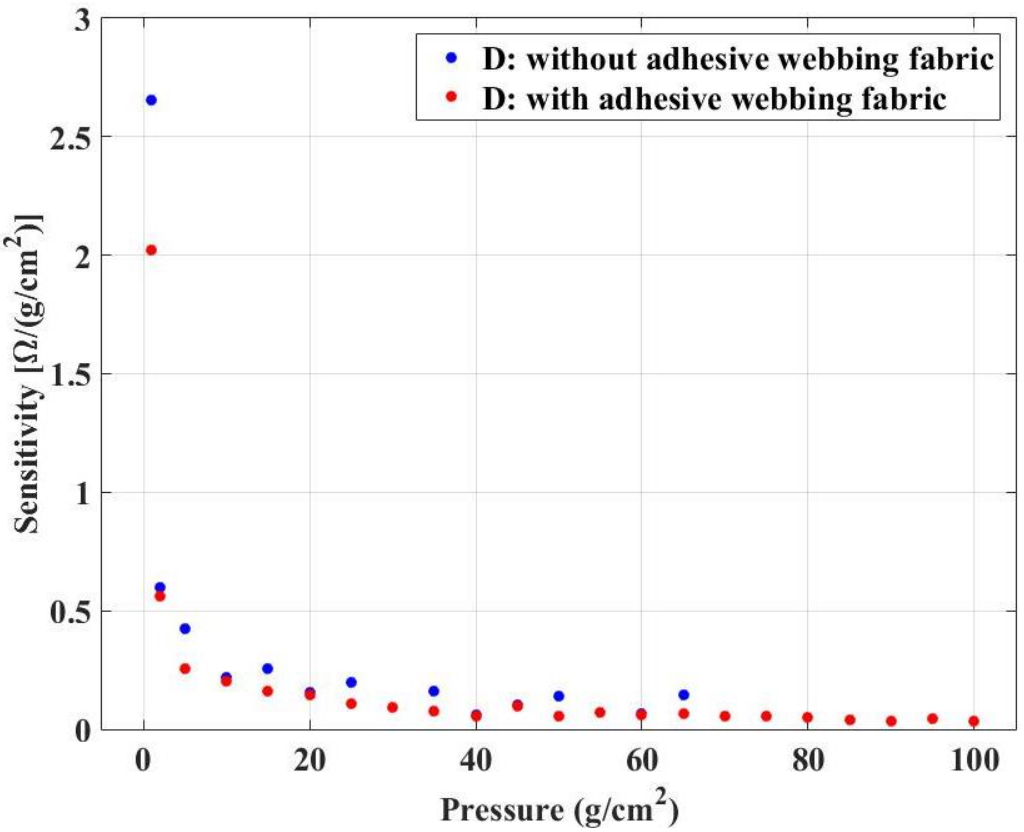

Figure 5-5. The piezo-resistive sensitivity of Sample D with a dot embossed surface structure.

Both types of the nonwoven sensor's sensitivity show a relatively flat curve after exceeding 20 g/cm^2. However, within the pressure range between 10 and 20 g/cm^2, the nonwoven sensors show a good piezo-resistive sensitivity (an average sensitivity of 0.0415 Ω/(g/cm^2) and 0.170 Ω/(g/cm^2) for the sample C and D, respectively). The sensor constructed with the dot pattern embossed nonwoven (sample C) layer showed a higher piezo-resistive sensitivity than the sensor constructed with a smooth surface nonwoven (sample D).

Therefore, it can be concluded that the adhesive webbing fabric can greatly improve the stability and reliability of the piezo-resistive nonwoven sensors, especially to the sensor materials with higher variation in resistance. The adhesive webbing fabric also has effect in stabilising the relative movements between the material layers in the nonwoven piezo-resistive sensor, while maintaining an overall low sensor electrical resistance, and high piezo-resistive sensitivity. In addition, usage of the adhesive webbing fabrics can reduce the level of biasing pressure required for the sensor to function properly and

reliably, thereby achieving a broader range of working pressure. The rest of the samples are all fabricated and tested with adhesive webbing fabric layers.

5.2.1.3 Effect of silver take-up percentage on the piezo-resistive property

Table 5-2. The times of sensor C being mangled and the corresponding silver take-up %.

Number of times of mangling process at 2 bar	1	2	2	3	3
Silver take-up (%)	32	14	12	9	7

Nonwoven fabric C was selected to investigate the effect of the silver take-up percentage on the piezo-resistive property of the sensor. **Table 5-2** summarises the different silver take-up percentage achieved on sensor C. As expected, the more times the fabric had been mangled, the less silver would be left within the fabric as was expected. However, it was difficult to control the exact amount of silver content in the nonwoven materials. The quasi-static electromechanical characterisation results are illustrated in **Figure 5-6** and **Figure 5-7**, from which it can be clearly observed that with the increase in the silver take-up percentage, the overall electrical resistance of the nonwoven fabric based piezo-resistive sensor reduces. The sensor samples with similar silver take-up percentage behaved in a very similar way. The nonwoven fabric samples with low silver take-up percentage (7% and 9%) started with a high resistance which dropped sharply with little increase in the pressure. Though the sharp decrease in the resistance at low-pressure region provides the sensors with a high sensitivity, the variation in the resistance also increases. With the increasing pressure on the nonwoven fabric based sensor, the resistance curves gradually flatten. Eventually, it can be seen that all the sensors end with a resistance value and piezo-resistive sensitivity very close to each other at a pressure of 100 g/cm^2, disregarding the sensitivity and the piezo-resistive performance at the beginning. Therefore, it can be concluded that the silver take-up percentage has a significant effect on the absolute electrical resistance of the piezo-resistive nonwoven materials. The high silver take-up results in low electrical resistance. The low silver take-up also can cause the resistance of the sensor reduces in a more rapid way with pressure increasing, which results in a high sensitivity at the low-pressure region. However, this will also increase the variation in the sensor, which leads to unstable and unreliable readings. More importantly, it is not worth increasing the

sensitivity by this approach, as the 'improved' sensitivity will very soon drop down to normal level when the pressure reaches 20 g/cm^2 to 30 g/cm^2.

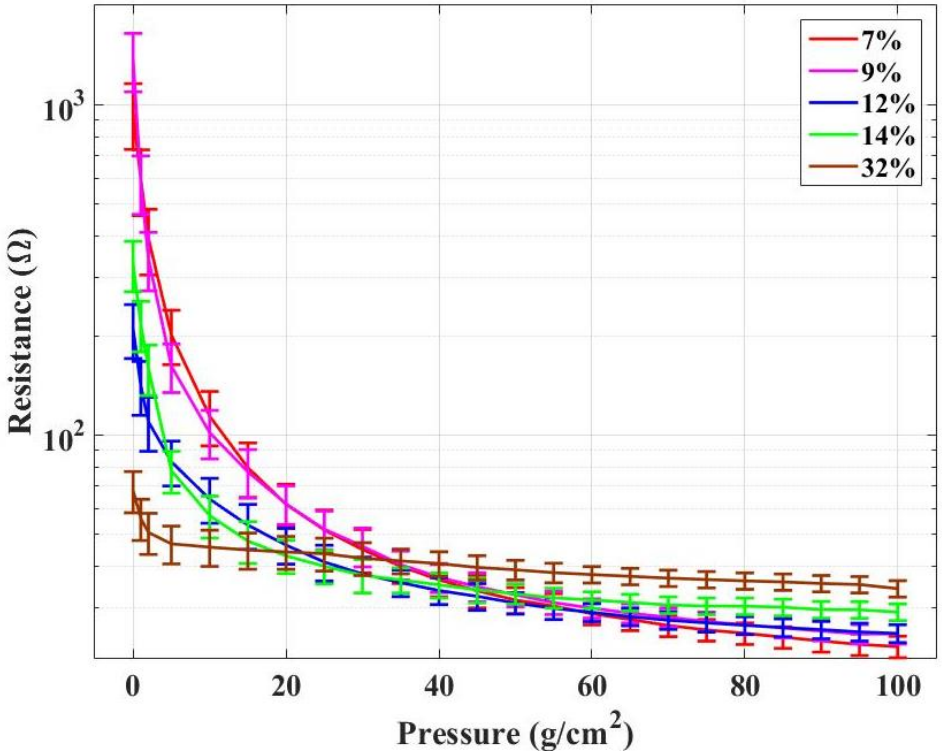

Figure 5-6. Sensor C with different silver take-up percentages.

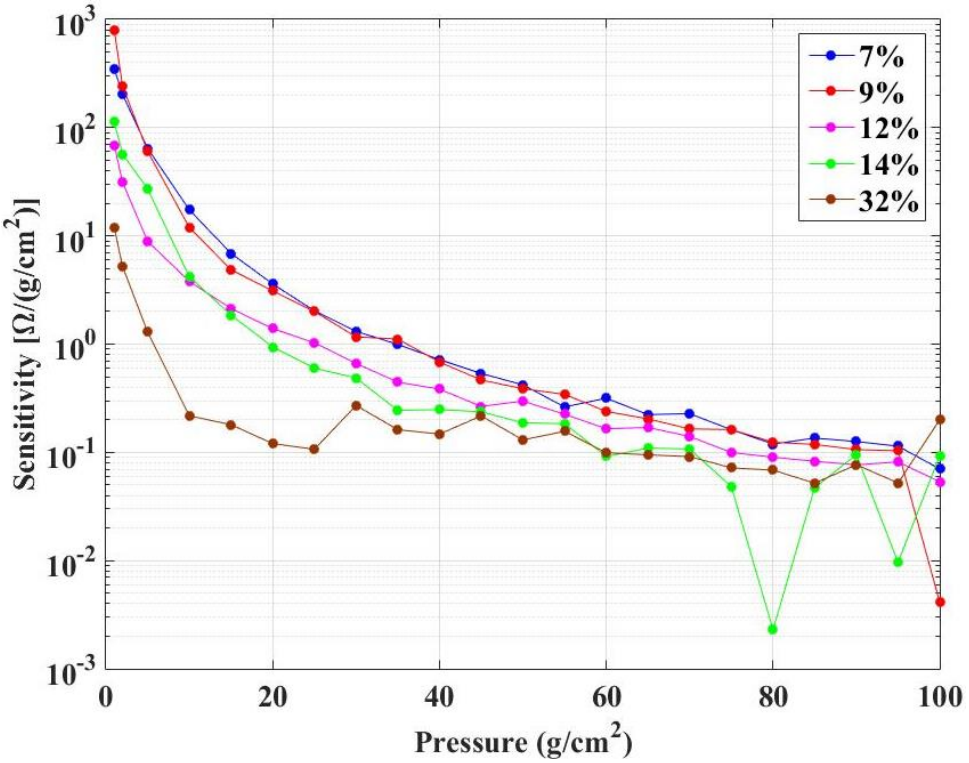

Figure 5-7. Sensitivity of sensor C with different silver take-up percentages.

5.2.2 Electromechanical characterisations

From the preliminary tests, it was found that the adhesive webbing fabrics are critical in the production of reliable piezo-resistive nonwoven fabric based pressure sensors. And in the aspect of silver take-up percentage, it can be engineered to control the electrical resistance of the sensor; however, a low silver take-up percentage will cause unstable performance of the sensor. Therefore, for the electromechanical characterisations and cardiorespiratory signal investigation, the sensors were all fabricated with the adhesive webbing fabrics; the mangling process was altered from the one used in section 5.2.1.3; during the impregnation process, all samples were mangled only once at a low pressure of 1 bar, in order to obtain a high silver take-up percentage for reliable sensor performance. The materials used in the creation of piezo-resistive pressure sensors were impregnated with silver particles to appropriate levels so that they had a similar electrical resistance range. In this way, the differences in the piezo-resistivity of the nonwoven fabric based pressure sensors are considered the only dependant to the fabric structures and impregnation performance.

5.2.2.1 Quasi-static electromechanical compressive test

The quasi-static electromechanical compressive test curves of the small thickness sample A and B are shown in **Figure 5-8**. Clearly, it can be observed that sample A produces a more promising and reliable curve; its resistance drops from 34 ohms to 29 ohms in a smooth trend. While the resistance change of sample B is much smaller and more fluctuations occur. This is due to the fact that there is less silver take-up percentage in sample B (13.3%) than sample A (25.2%). Considering the area density of sample B (60 g/m^2) and sample A (17 g/m^2), sample B is supposed to be capable of absorbing more silver content. Such low silver take-up percentage is due to the fact that in order to achieve the small thickness during the thermal bonding process, a high pressure was applied on the web. While sample B had a higher area density, the fibres became much closer to each other due to the high pressure, causing the distance between the fibres on the surface to be very small. Thus, during the dip-coating process, the thin ink membranes were formed on the surface more easily, preventing from thorough and even impregnation. The more uniform silver particle distribution in sample A also results in a better piezo-resistive property.

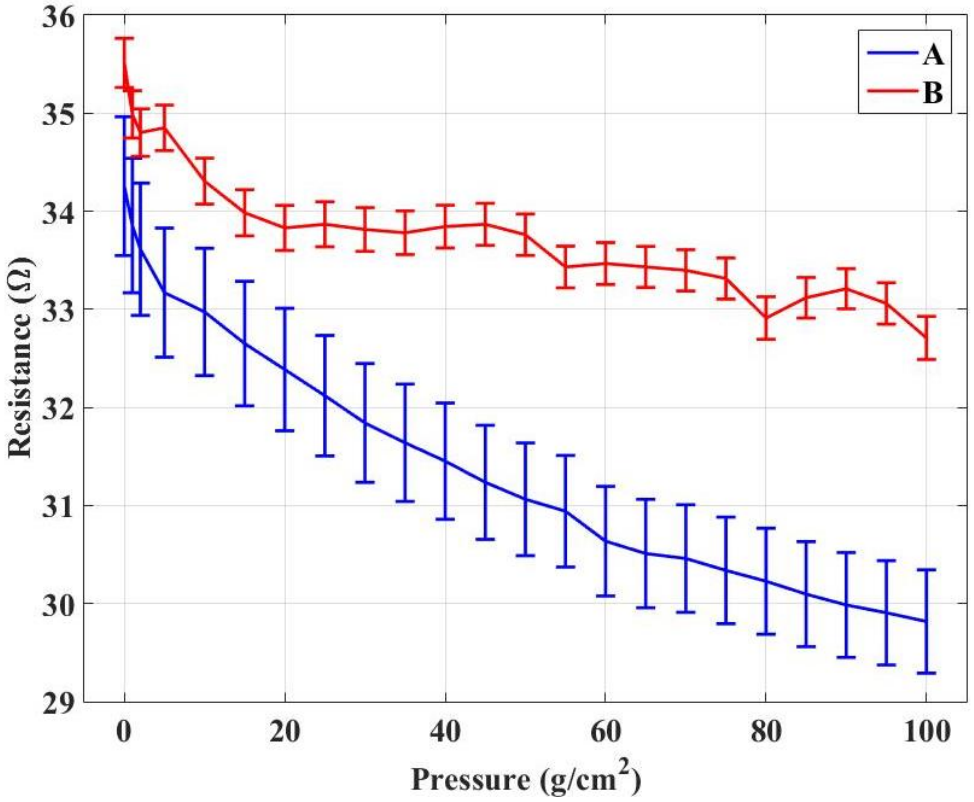

Figure 5-8. Resistance vs. pressure of sample A and B.

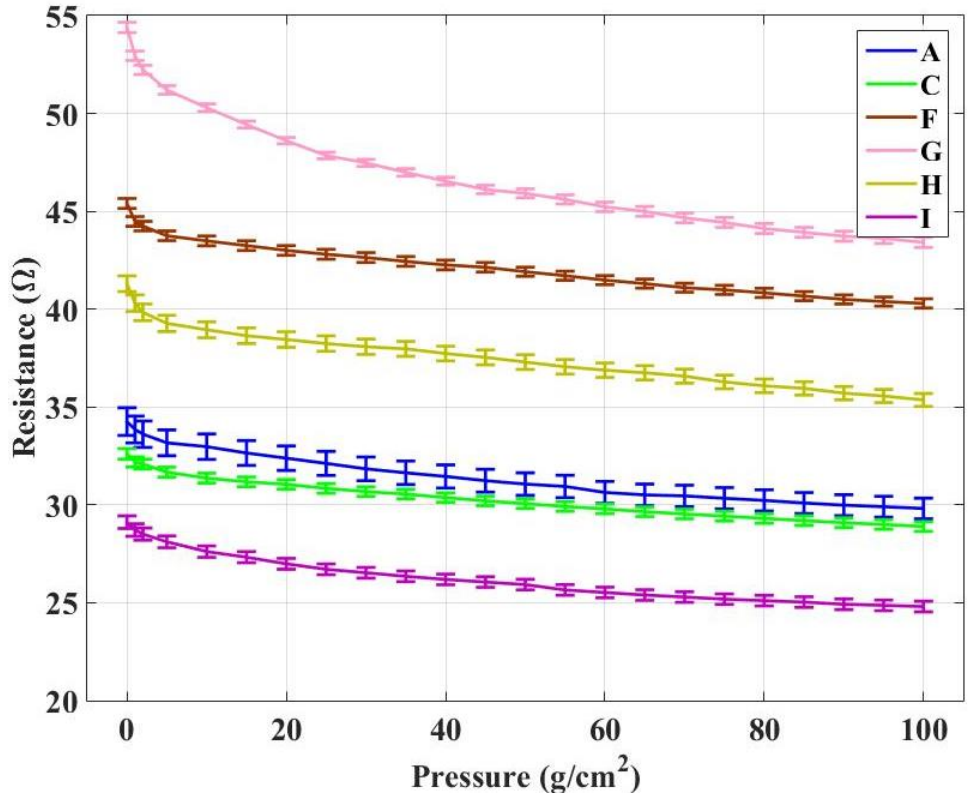

Figure 5-9. Resistance vs. pressure of sensor samples with different thicknesses.

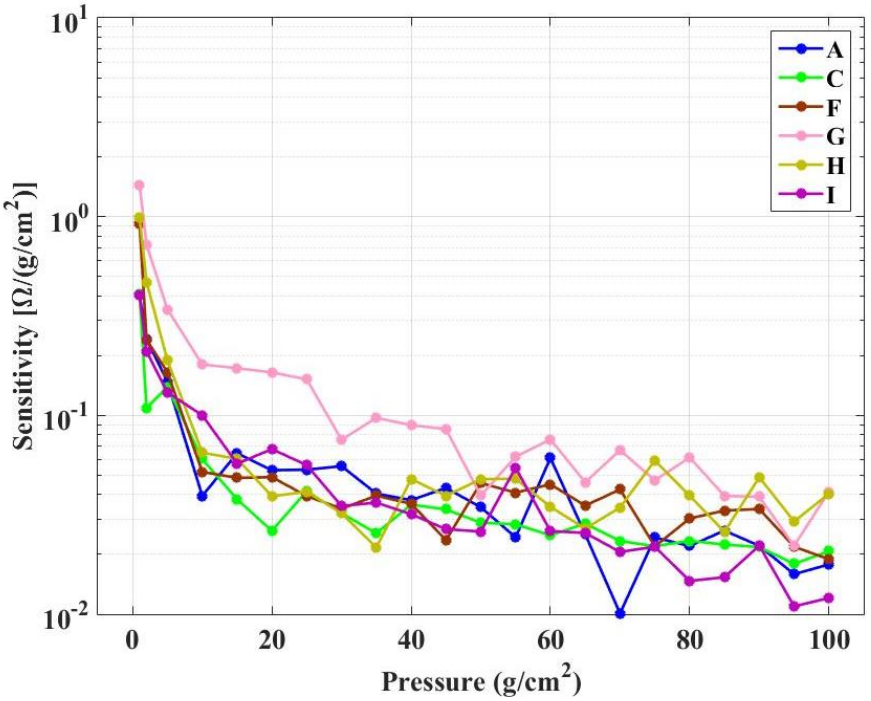

Figure 5-10. Sensitivity of smooth surface nonwoven material fabricated sensors.

Comparing the quasi-static electromechanical characterisation curves of sample A and with other sensors made from smooth surface nonwoven fabrics with a big thickness (sample C, F, G, H and I), it can be found that sensors with a bigger thickness have a better performance. The slopes of these samples are very similar, where fewer fluctuations and small error bars are found in samples with bigger thicknesses (as shown in **Figure 5-9**). Among them, sample G shows the best piezo-resistivity, which has a high piezo-resistive sensitivity up to 45 g/cm^2 (as illustrated in **Figure 5-10**). By comparing the sensitivity of these sensors, sample G is found with the least fluctuations generally. In the aspect of nanoscale silver particle-based electroconductive ink impregnated piezo-resistive nonwoven sensor that was fabricated from smooth surface nonwoven materials, sample G is considered with the best piezo-resistive property.

Comparing the piezo-resistive sensors made from a smooth surface nonwoven material, dot pattern embossed nonwoven material, knitted fabric material and woven fabric material, it can be found in **Figure 5-11** and **Figure 5-12** that other than the commercially available material (sample E), the rest four sensors behaved in a very similar way that the resistance curves have the same trend. They all have a high sensitivity near zero pressure, while the sensitivity reduces at 5 to 10 g/cm^2, and keeps on reducing gradually. Some fluctuations in sensitivity are observed at high-pressure region (above 50 g/cm^2), which indicates that the chance of creating a new electrical

path within the sensor structure has become minimal. The commercially available electroconductive nonwoven material (sample E) has the biggest resistance change upon compressing, which results in a relatively but not significantly high sensitivity among these five samples across the complete pressure range. However, it has much lower sensitivity at the low-pressure levels, which is a critical disadvantage to capture the weak bio-signals.

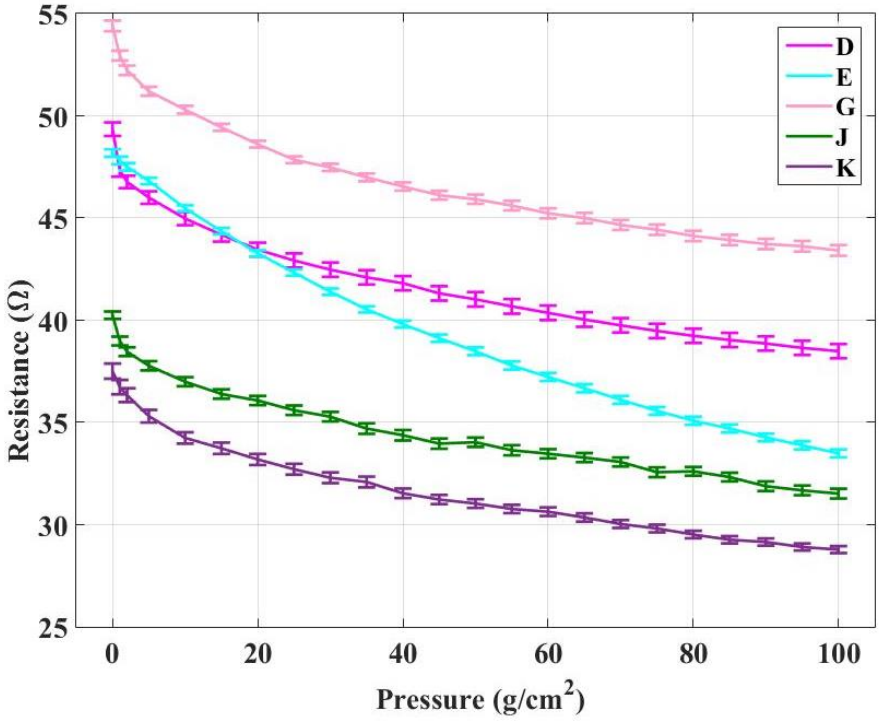

Figure 5-11. Resistance vs. pressure curves of sample D, E, G, J and K.

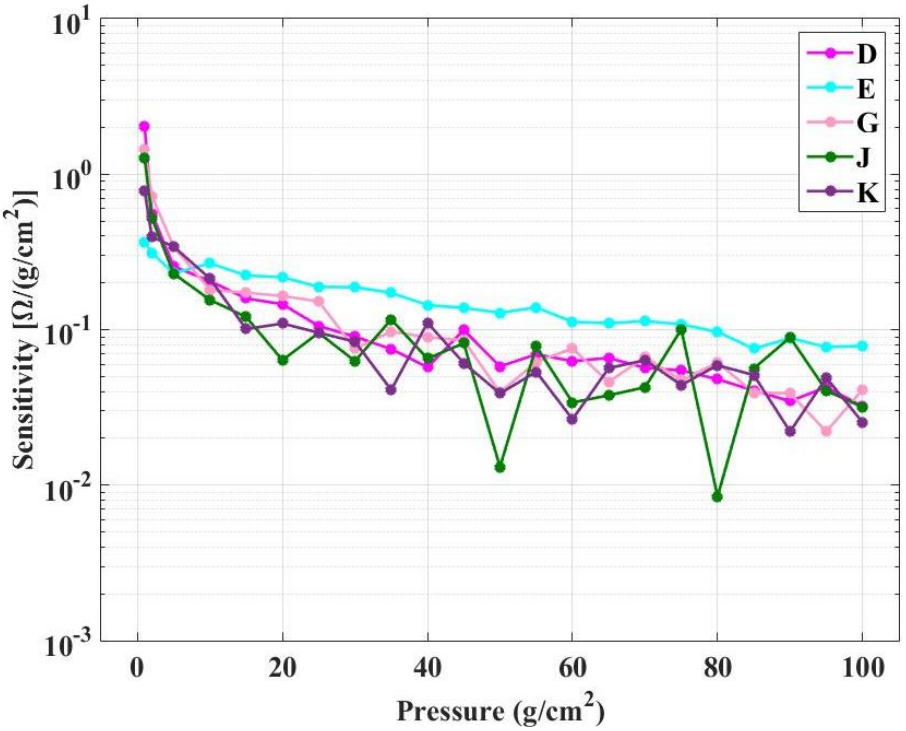

Figure 5-12. Sensitivity of sample D, E, G, J and K.

Throughout the quasi-static electromechanical compressive tests, the piezo-resistivity of the electroconductive ink impregnated nonwoven material based pressure sensor was studied. By characterising the piezo-resistive sensors with different parameters, the following findings can be summarised:

1) the nonwoven materials impregnated with a higher silver take-up percentage performs better; due to the random fibre orientation and distribution of the nonwoven materials, the contact points of the fibre within the nonwoven fabric can change significantly with pressure applying; therefore, with a high amount of silver particles, either coated on the fibre surface or gathered at the pore areas which are made from joints, the chance of creating new electrical paths through the two surfaces of the nonwoven fabric is improved;
2) nonwoven material based pressure sensors with a bigger thickness show better piezo-resistivity and sensitivity, as well as stability and reliability; basically this is due to the fact that the big thickness allows multiple layers exist within the nonwoven fabric, compared with thin nonwoven fabrics; therefore, providing the multi-layered structure has been sufficiently nanoscale silver particle impregnated, upon pressure, not only the joints of fibres will create new electrical paths, but also the contact between inner layers may show piezo-resistivity as well.

5.2.2.2 Cyclic compressive loading

Cyclic compressive load tests were carried out in order to investigate the repeatability of the sensor. Sample D, E, G, J and K were selected to be discussed in detail as they were proven to show reliable and good piezo-resistivity from the previous results; the cyclic loading results of the rest of samples are available in Appendix A. The results of the cyclic compressive loading tests were shown in **Figure 5-13** to **Figure 5-17**. It can be seen that generally all five samples induce a hysteresis in the resistance-pressure curves and show satisfactory repeatability after 20 cycles of continuous loading and relaxing. It takes nonwoven material based sensors (sample D, E and G) two or three cycles to show a repeatable resistance curve; however, the knitted fabric based piezo-resistive sensor (sample J) requires 8 cycles. Though the woven structure based sensor (sample K) was able to perform excellent repeatability since the sixth cycle, the hysteresis effect of the first loading cycle and the loading cycles thereafter was so big that the sensitivity and

piezo-resistivity of the sensor would be compromised. It is noticeable that at the bottom right part of **Figure 5-16** that the knitted fabric based sensor performs differently in the last four cycles. During the compressive loading procedure, the electrical resistance values of the last four cycles dropped to an extra low value of 34.1 Ω at the pressure around 90 g/cm^2, which is believed due to the fact the at this point, some extra electrical paths were established, resulting in the extra reduction in the resistance. While during the unloading procedure, the newly established electrical paths disappeared as the pressure decreased to a certain level and the resistance value returned to normal. This certain pressure level gradually reduced from 90 g/cm^2 to 60 g/cm^2. This is due to the fact that upon cyclic compression, the newly established electrical paths over 90 g/cm^2 became stronger and stronger, which were able to persist under a lower pressure. It is believed that after 16 cycles, the knitted structure turned relatively unstable under the high biasing pressure (90 g/cm^2) during unloading procedure, which affected the piezo-resistive property of the sensor.

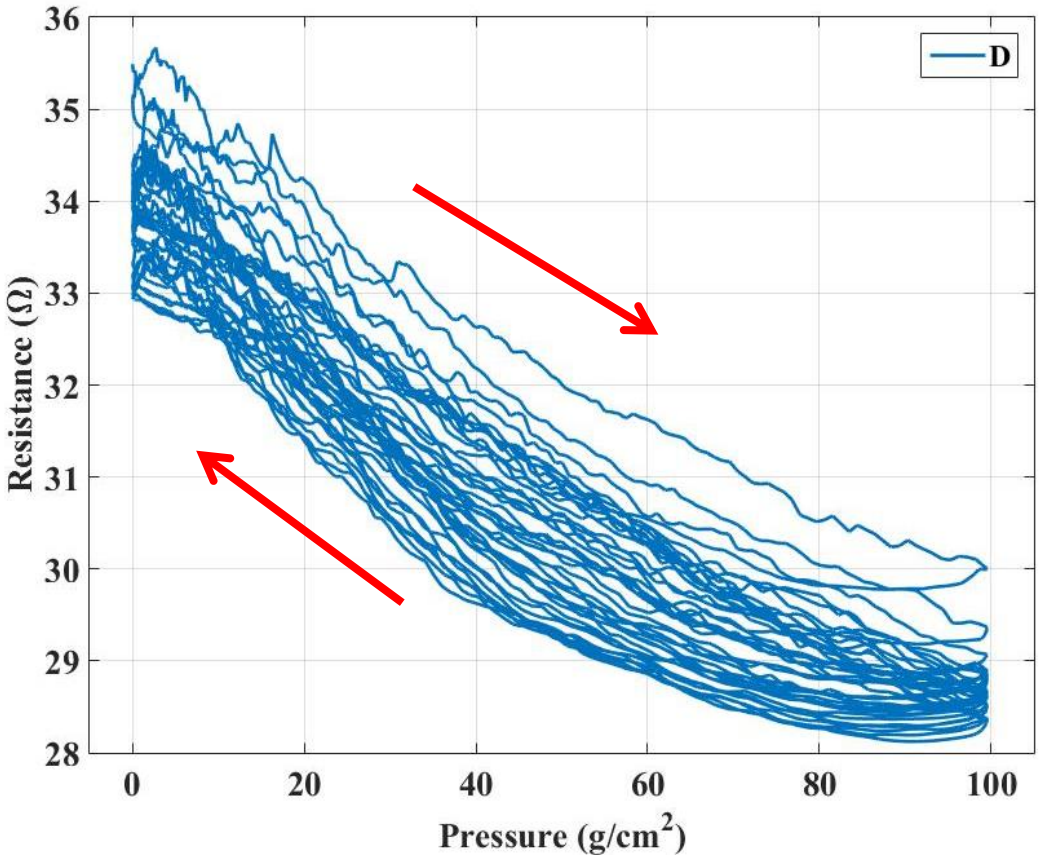

Figure 5-13. Cyclic compressive load resistance vs. pressure curve of sample D.

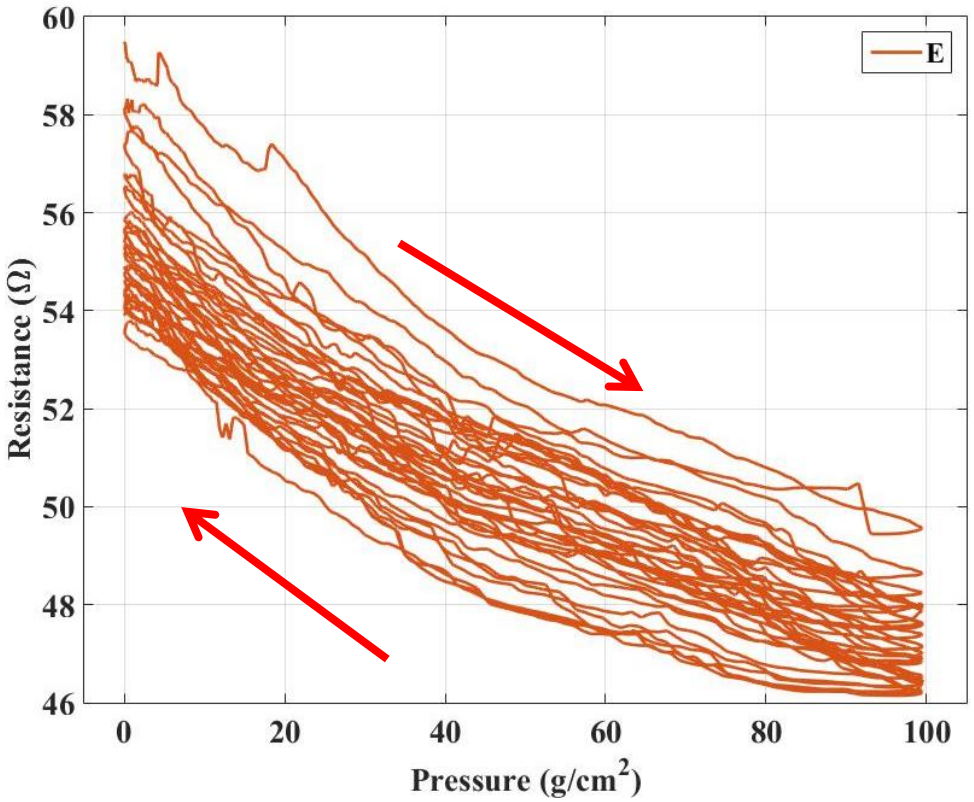

Figure 5-14. Cyclic compressive load resistance vs. pressure curve of sample E.

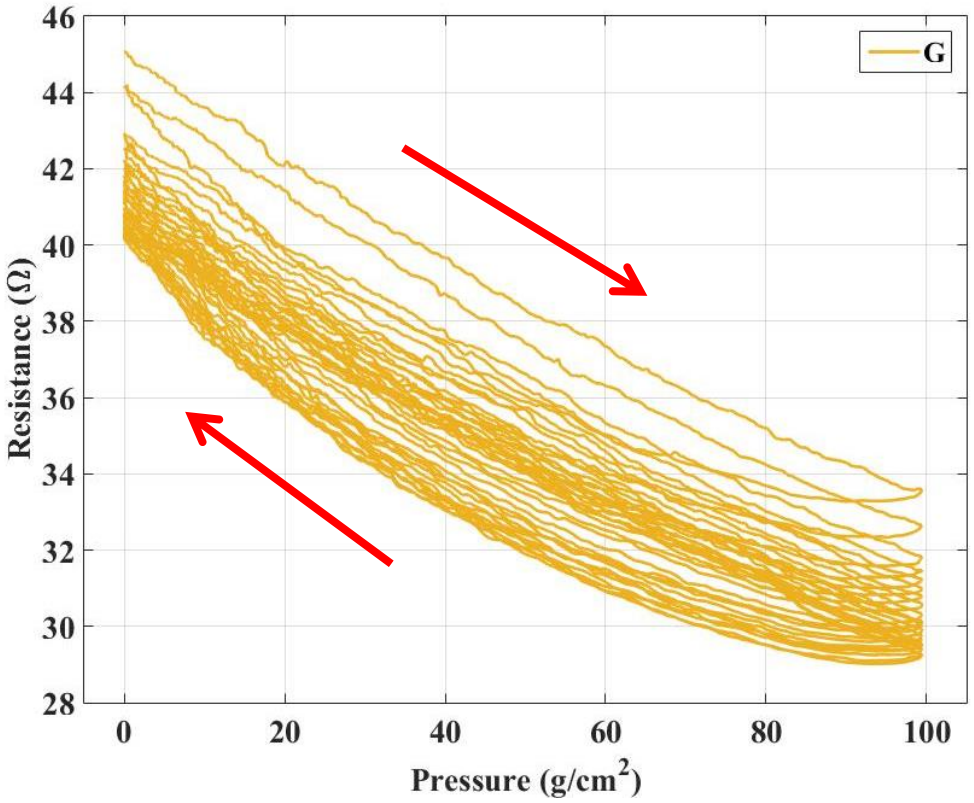

Figure 5-15. Cyclic compressive load resistance vs. pressure curve of sample G.

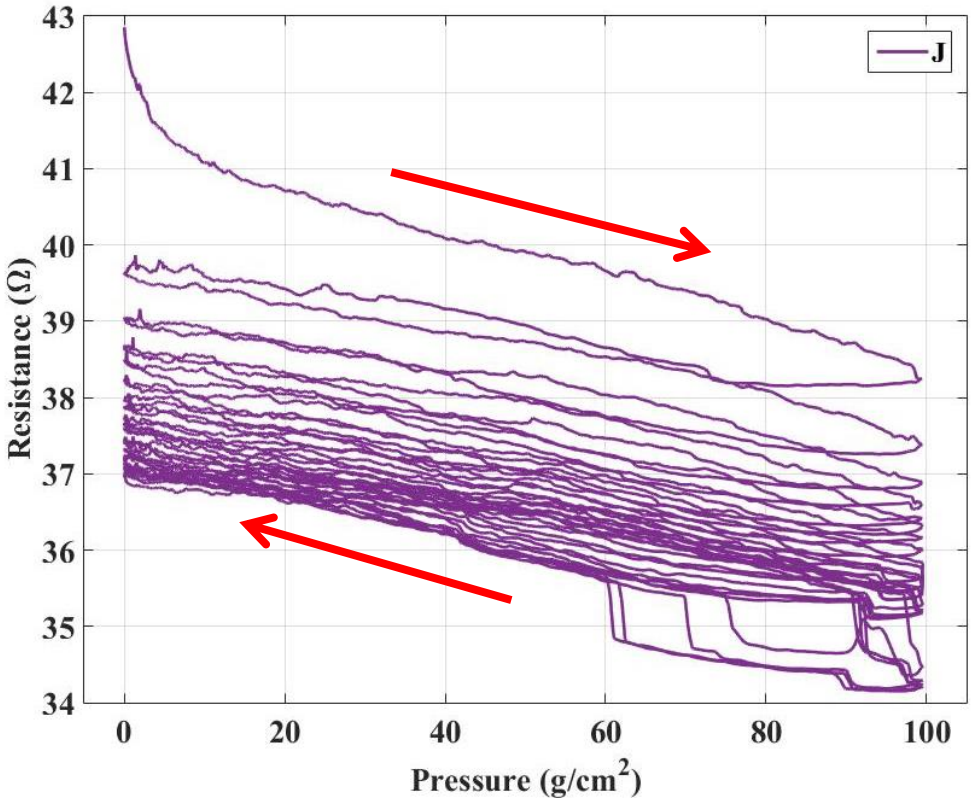

Figure 5-16. Cyclic compressive load resistance vs. pressure curve of sample J.

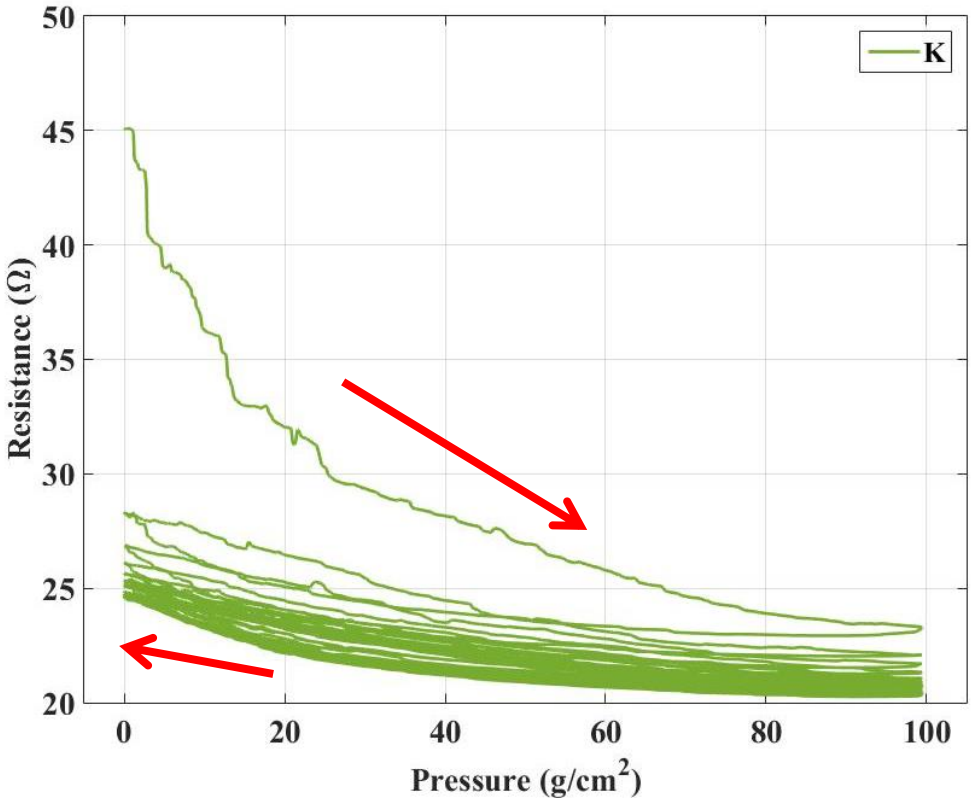

Figure 5-17. Cyclic compressive load resistance vs. pressure curve of sample K.

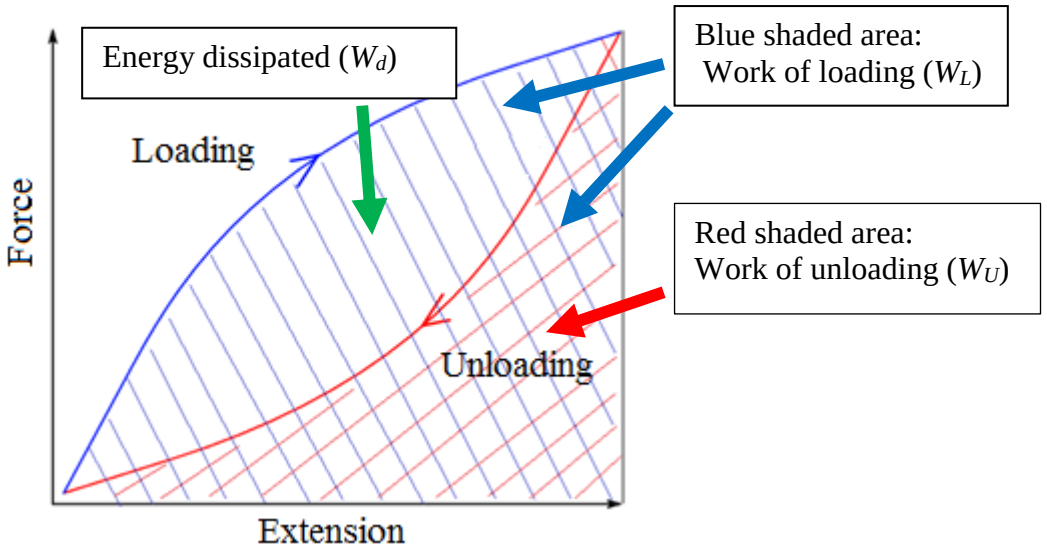

Figure 5-18. Diagram of a typical cyclic force-extension curve of a textile material.

In the tensile cyclic test for textile materials, the hysteresis can be measured by calculating the dissipated energy (W_d) and the percentage of energy dissipation (A) between the loading and unloading cycle of the material.[240–242] As illustrated in **Figure 5-18**, during one cycle of loading and unloading, a certain amount of energy will be dissipated due to the internal friction of the material. The dissipated energy (W_d) and the percentage of energy dissipation (A) can be calculated as:

$$W_d = W_L - W_U \qquad \textbf{Equation 5-2}$$

$$A = \frac{W_d}{W_L} \times 100\% \qquad \textbf{Equation 5-3}$$

where: W_L is the work of loading or the energy stored due to extension; W_U is the working of unloading or the energy released due to relaxing the material.

In order to evaluate the hysteresis effect of the electrical resistance of the nonwoven-based pressure sensor, the resistance hysteresis loss (R_{HL}) and the percentage of the resistance hysteresis loss were calculated based on the principle of **Equation 5-2** and **Equation 5-3**.

$$Resistance\ hysteresis\ loss\ (R_{HL}) = RP_L - RP_U \qquad \textbf{Equation 5-4}$$

$$Resistance\ loss\ percentage = \frac{R_{HL}}{RP_L} \times 100\% \qquad \textbf{Equation 5-5}$$

where: RP_L and RP_U are the designated area surround by pressure axis and the resistance curves during loading and unloading procedure, respectively.

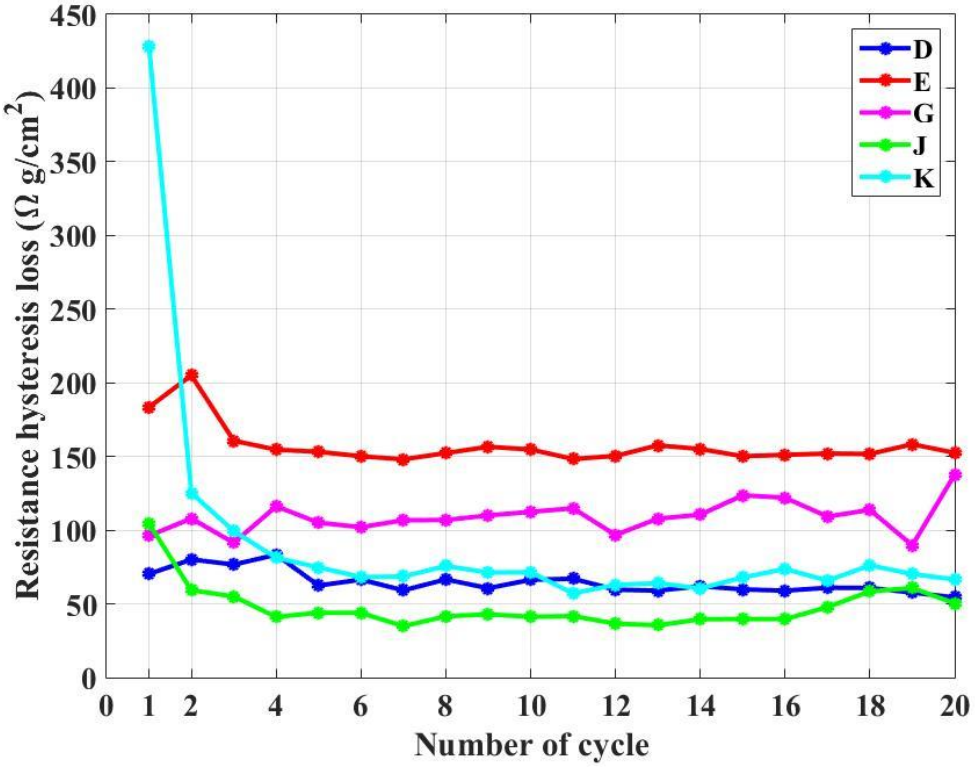

Figure 5-19. The resistance hysteresis loss of sample D, E, G, J and K of each cycle of the cyclic compressive loading test.

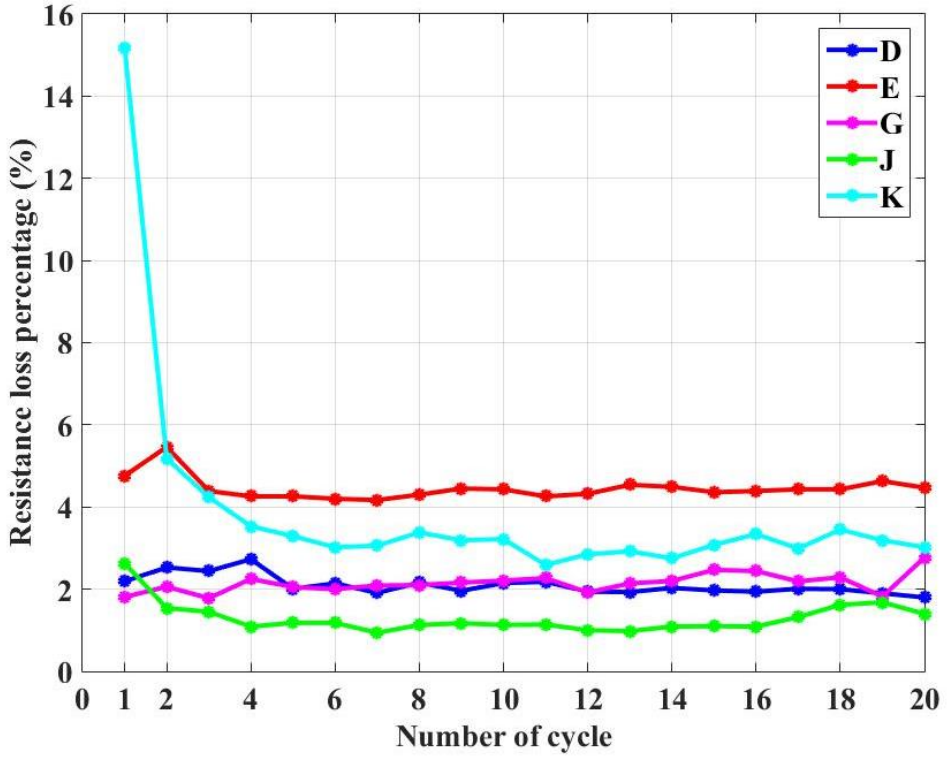

Figure 5-20. The resistance loss percentage of sample D, E, G, J and K of each cycle of the cyclic compressive loading test.

The results of the resistance hysteresis loss analysis are shown in **Figure 5-19** and **Figure 5-20**. The data points of the hysteresis loss can be found in Appendix B. It can be clearly observed that the woven fabric based piezo-resistive sensor has the biggest difference in the resistance hysteresis loss between the first cycle and the cycles thereafter, as was seen in **Figure 5-17**. This is due to the fact of the poor recoverability of the woven structure from compression. The rest of the four samples show quite stable hysteresis effect, among which the knitted fabric based sensor (sample J) has the smallest hysteresis effect in both the hysteresis loss value and hysteresis loss percentage, which is as expected due to the fact the interlooped structure of the knitted fabric provides the sensor with the best compressibility and elasticity. The two thermally bonded nonwoven fabric sensors (sample D and G) perform very similarly in the hysteresis effect; they both have stable hysteresis loss percentages of 2.10% and 2.15% in average, for sample D and G respectively (see Appendix B). The difference in the hysteresis loss value is due to the difference in the sensor resistance which is an inevitable result from the different silver take-up percentage due to different fabric properties. However, in the aspect of sample E, which was produced by the spunlace bonding technology, it is believed that the vertically entangled fibres within the structure and the highly adhered fibre bundles (as discussed in section 4.2.2) cause the sensor behaves poorly in the recovery from the compression. Disregarding the first cycle of the woven fabric based sensor, sample E shows the worst overall hysteresis effect over the cyclic compressive loading test, providing the average hysteresis loss percentage of 4.45%. Therefore, it can be summarised at this stage that the resistance hysteresis effect of the fabric based piezo-resistive pressure sensor relies on the recoverability of the fabric from the compressive force. A relatively loose structure, such as thermally bonded nonwovens and knitted structure, can be helpful for the sensor to show less hysteresis over cyclic loading tests.

Other than the hysteresis phenomenon, the resistance of the sensor gradually reduces as the cyclic compressive test carrying on. This phenomenon is studied by normalising the resistance at the peak (R_{peak}) and the trough (R_{trough}) in each compressive loading cycle to the resistance at the first peak (R_{peak0}) and trough ($R_{trough0}$) (as shown in **Figure 5-21** and **Figure 5-22**). It can be observed that with the increase in the number of cycles, the peak resistance in each cycle reduces by 8.5% in average for nonwoven fabric based sensors and 14% for knitted fabric based piezo-resistive sensor; whereas to the woven

structure based sensor, there is a significant resistance reduction since the first cycle. Again, this is mainly due to the poor recoverability of the woven structure. Sample D shows the best adaptability to the cyclic compressive load that it is able to provide reliable and repeatable reading since the third cycle, which is a result of the partially bonded structure. The dot pattern embossed surface structure allows the nonwoven fabric absorb more energy from pressure without deforming significantly. Once the pressure is removed, the surface structure which is not thermally bonded is able to recover sooner than other thermally bonded nonwoven fabrics. This also applies to the knitted fabric based sensor. Though the knitted structure is much denser than nonwoven fabric, the large thickness and curved stitches allow fast recovery compared with the woven structure which is made from fully straightened yarns under a much higher yarn tension. In the aspect of the change in the trough resistance, sample D and E show the most stable performance in the loading cycles. The drop percentages of the resistance of the five samples are all within an acceptable range.

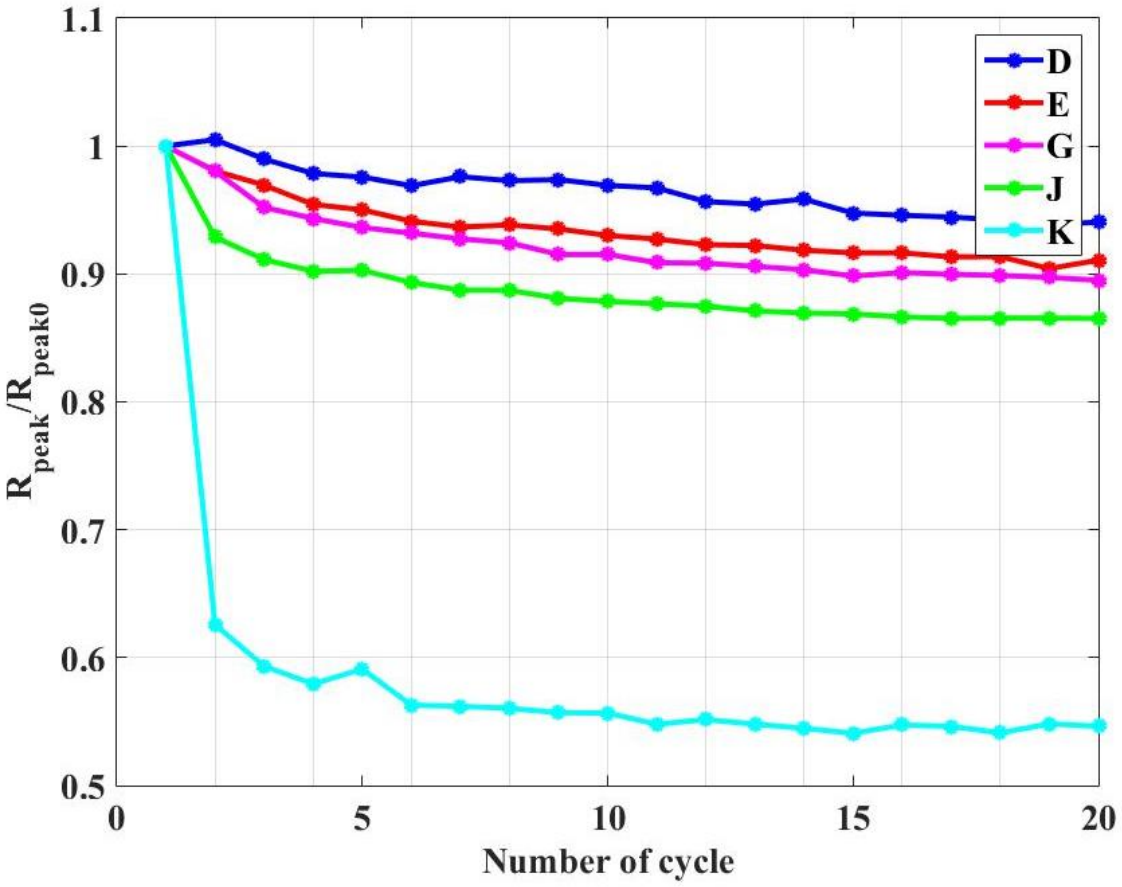

Figure 5-21. The change of peak resistance in each cycle.

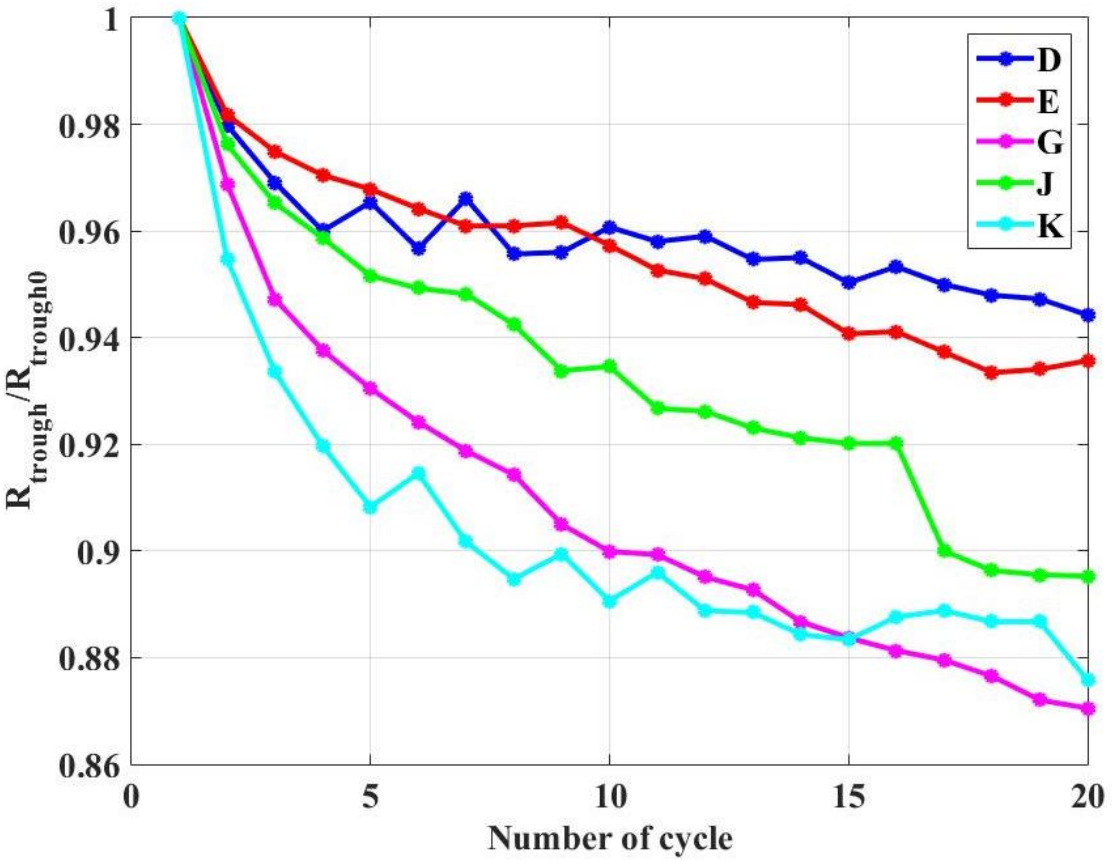

Figure 5-22. The change of trough resistance in each cycle.

From the cyclic compressive loading tests, it was discovered that nonwoven fabric based piezo-resistive sensors behaved better than knitted and woven fabric based sensor in the application where repeatable dynamic pressure signals were applied and reliable readings were needed. It was also found that the recoverability of the sensor from compression was critical to the reproducible piezo-resistive perform. Therefore, the nonwoven materials themselves already have an edge over other textile materials, where improvements can be made in respect of partial bonding in order to obtain better compressive recoverability.

5.2.2.3 Resistance time drift (RTD) analysis

Figure 5-23 illustrates the results of RTD analysis tests for sample D, E, G, J and K. It can be seen that at every 10 g/cm^2 interval, there is an obvious resistance drift (reduction) over 60 seconds. As expected, due to the poor compressive property of the woven structure based piezo-resistive sensor, sample K shows the strongest RTD effect among five samples; whereas minute resistance drifts were observed in sample D and J. It is also found that generally the piezo-resistive sensors suffered from more resistance

drift under the condition of the high-pressure level. With the increasing biasing pressure, the RTD effect weakens. This could be due to the sensor sample becomes less variable after being more compressed. RTD also reveals the fact that the piezo-resistive sensors are not suitable to measure the absolute pressure reading, while can be used in the detection of continuously pulsed BCG signals. The test results of rest of the sensor samples are in Appendix C, from which the same conclusion can be deduced.

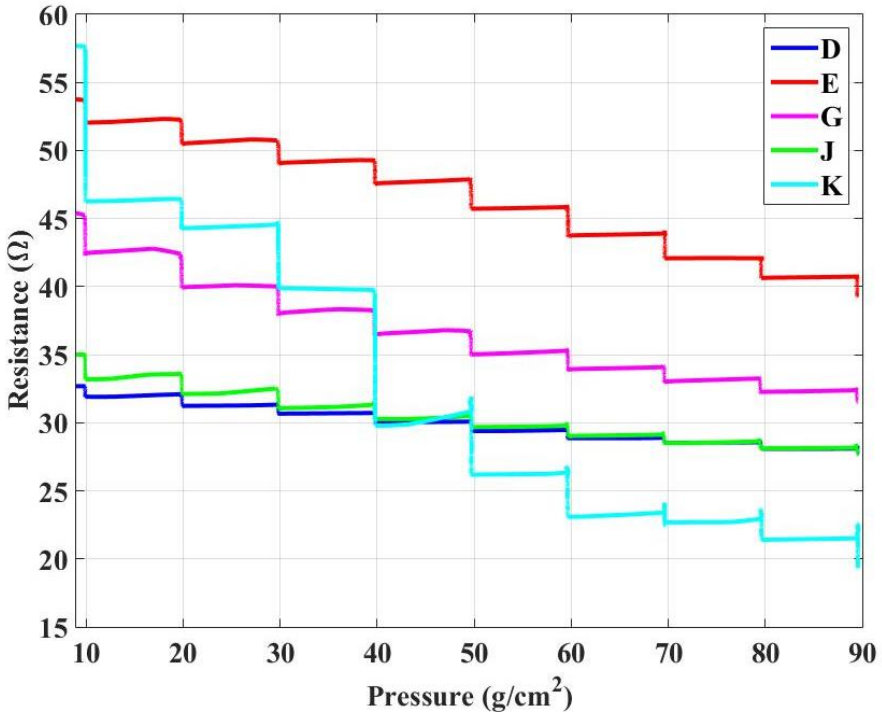

Figure 5-23. RTD of sample D, E, G, J and K.

5.3 Cardiorespiratory signals capturing

The selected sensors (sample D, E, G and J), which were found with excellent piezo-resistivity and high sensitivity, were then used to capture the cardiorespiratory signals. The performance of the selected sensors in the cardiorespiratory signal capturing was evaluated by the comparison against a commercially available bio-signal monitoring system. The cardiorespiratory signals captured by other sensor samples are shown in Appendix D and E.

5.3.1 Respiratory signal capturing

It can be seen clearly in **Figure 5-24** to **Figure 5-27** that the peaks in the signal of the piezo-resistive nonwoven sensor made from dot pattern embossed nonwoven fabric

sample D match well with those of the commercially available breathing belt-sensor. During the time the subject held his breath, the piezo-resistive nonwoven sensor was seen to capture less noise than the commercially available sensor.

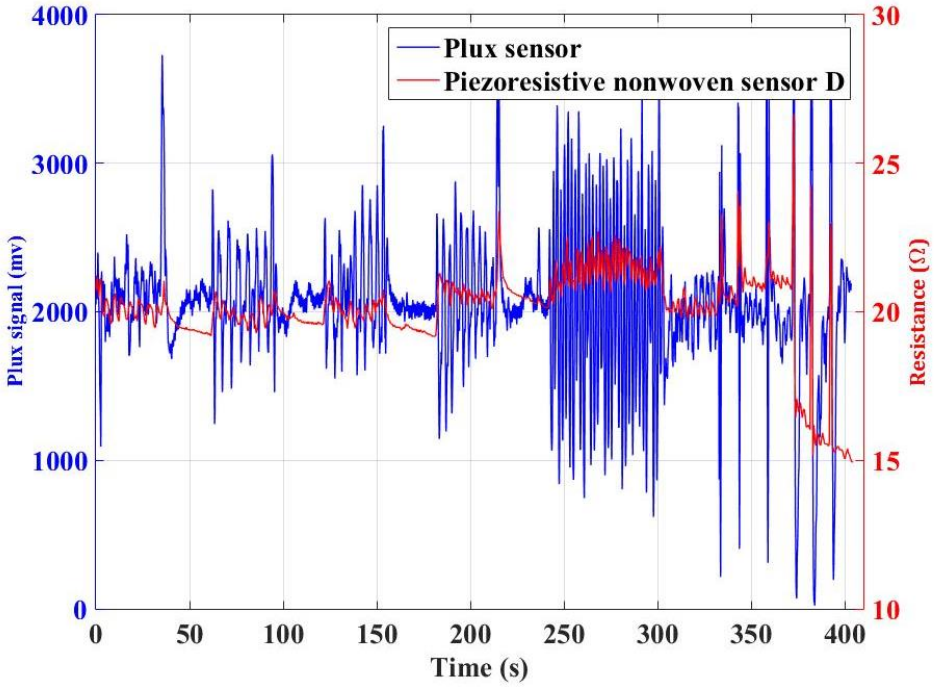

Figure 5-24. Breathing signal curve from the commercially available breathing belt sensor and the piezo-resistive nonwoven sensor D (dot pattern embossed nonwoven fabric based).

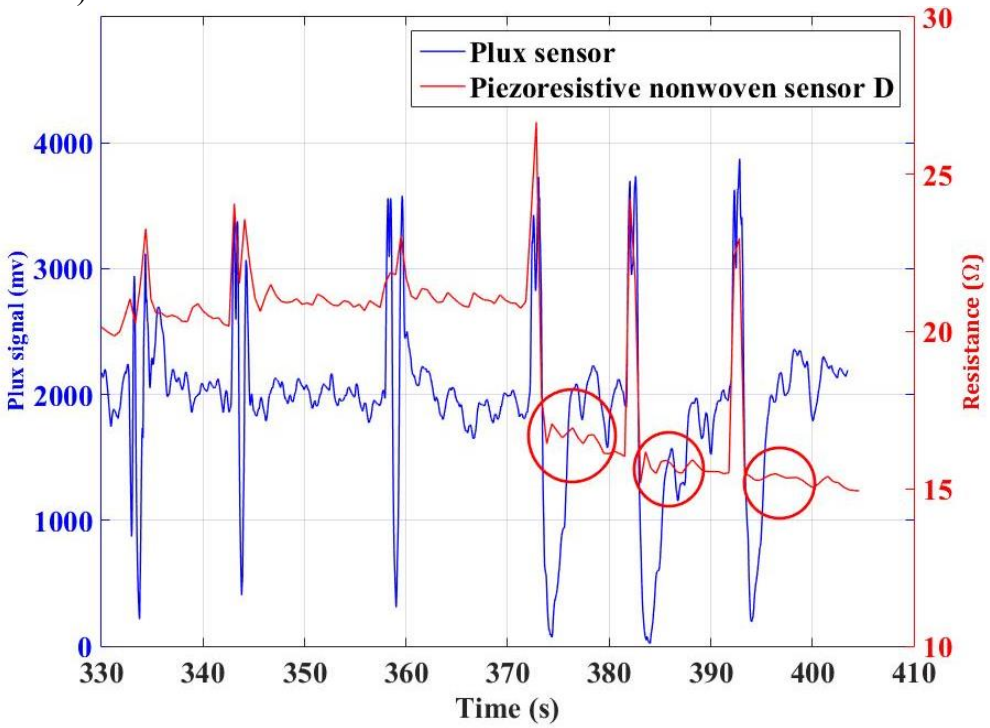

Figure 5-25. Arm movements during respiratory signal capturing (sample D). Red circles: the breathing signals captured by the piezo-resistive nonwoven sensor but

missed by the Plux sensor.

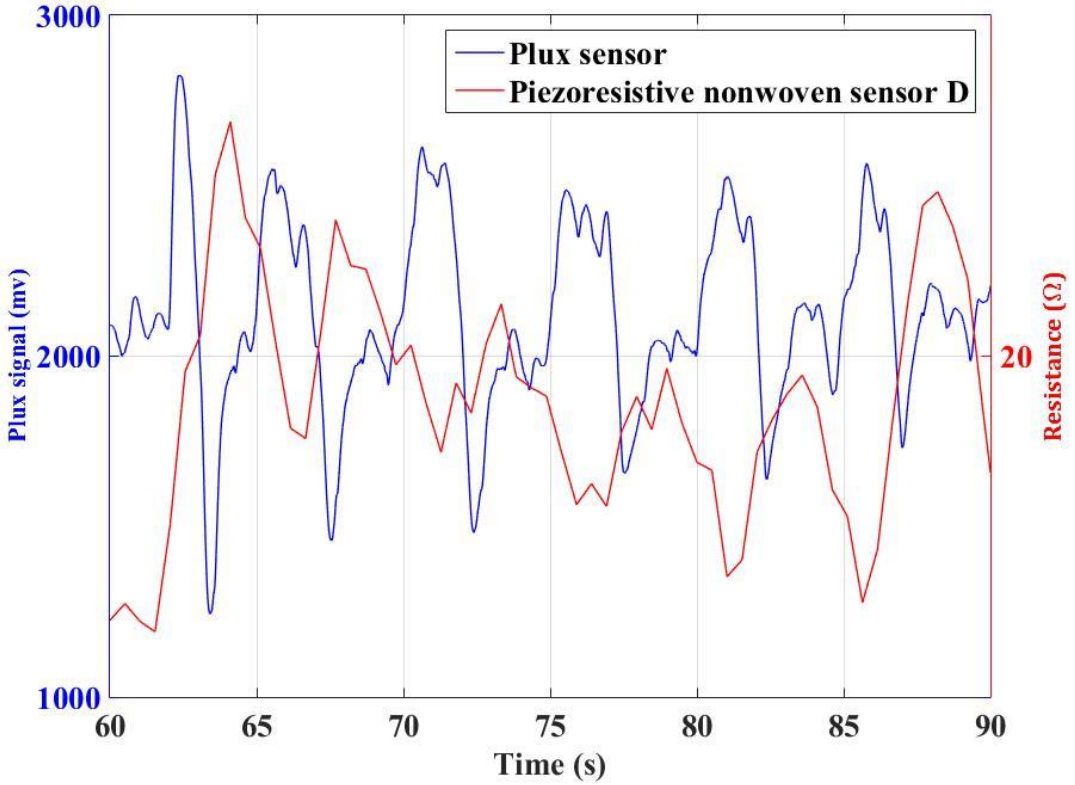

Figure 5-26. Scaled peaks during normal breathing (sample D).

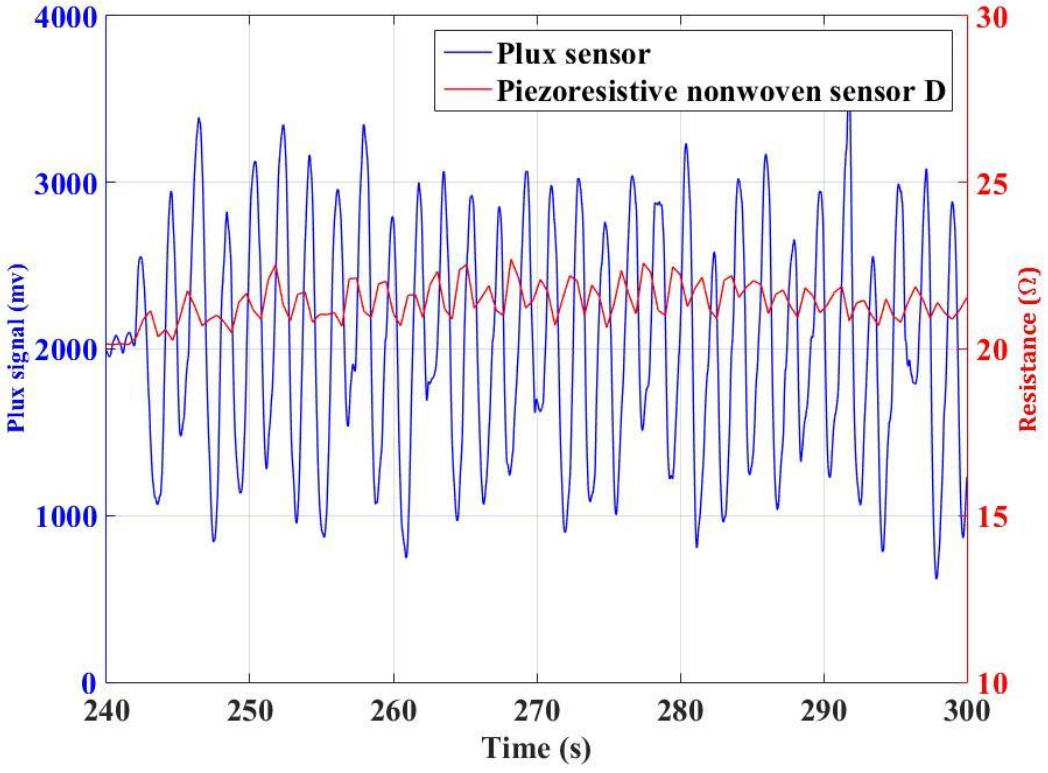

Figure 5-27. Rapid breathing signal capturing (sample D).

As described in section 3.4.3.1, the subject performed four repeats of normal breathing and breathe holding, followed by a period of rapid breathing; then he moved his right arm for three times and his left arm for three times. In **Figure 5-25**, it can be seen that the left arm movements affect the signal more than the right arm movements, as there is a noticeable reduction in sensor resistance and much bigger spikes due to arm movements. This is because that the sensor patch was attached on the left side of the subject's chest. It can also be observed that after the arm movements, the piezo-resistive nonwoven sensor captured the breathing signals almost immediately while the commercially available sensor failed to do so. The close agreement of peaks between the nonwoven sensor and the commercially available sensor verifies the accuracy of the nonwoven sensor. As marked in the red circle in **Figure 5-25**, every time when the left arm was lowered, the commercially available sensor missed a breathing peak; however, the nonwoven sensor was able to capture the complete breathing signal. This shows the nonwoven sensor has better reliability than the commercially available sensor in this situation. This may be due to the fact that the commercially available belt sensor was a tensile sensor which works on the principle of extension in length due to the increase in the girth of the chest while breathing. In the case of strong body movements, for example, the arm lifting in this case, the girth could keep unchanged, resulting in the missing peaks of the commercially available breathing sensor. In the case of the piezo-resistive nonwoven sensor, the arm lifting had less interference to the sensor functionality.

As observed in **Figure 5-26** while capturing the normal breathing signals, both of the nonwoven sensor and the commercially available sensor performed equally well. Since the commercially available sensor is based on a stretchable belt, and the nonwoven sensor is a multi-layer fabric pressed against the chest, the signals acquired from each tends to be in the opposite sense. In spite of the difference in the sensor technology between the commercially available sensor and the piezo-resistive nonwoven sensor, the results still show that the piezo-resistive nonwoven sensor has the full capability of acquiring the correct breathing signals. Similarly to the normal breathing signals, the sensor was capable of capturing the rapid breathing signals accurately, as may be seen in **Figure 5-27**.

Similar results were observed when using the smooth surface piezo-resistive nonwoven sensor (sample G) where each test period corresponding to the movements of the subject

can be clearly identified from the breathing signals (as shown in **Figure 5-28** to **Figure 5-31**). **Figure 5-29** illustrates that although the arm lifting movements were successfully captured, both the piezo-resistive nonwoven sensor G and the Plux sensor respond poorly in capturing the breathing signals following strong arm movement. The rapid breathing result in **Figure 5-28** shows that the piezo-resistive nonwoven sensor G failed to perform reliably during the rapid breathing period. The signals recorded consist of a large amount of fluctuation and a limited amount of peaks that could be matched with the control signal. The reason for such could be the strong chest movement during the rapid breathing, causing a higher pressure to be applied on the sensor fabric. As the pressure increased, the sensitivity and the change in resistance of the sensor decreased; resulting in a poor quality in the captured breathing signal.

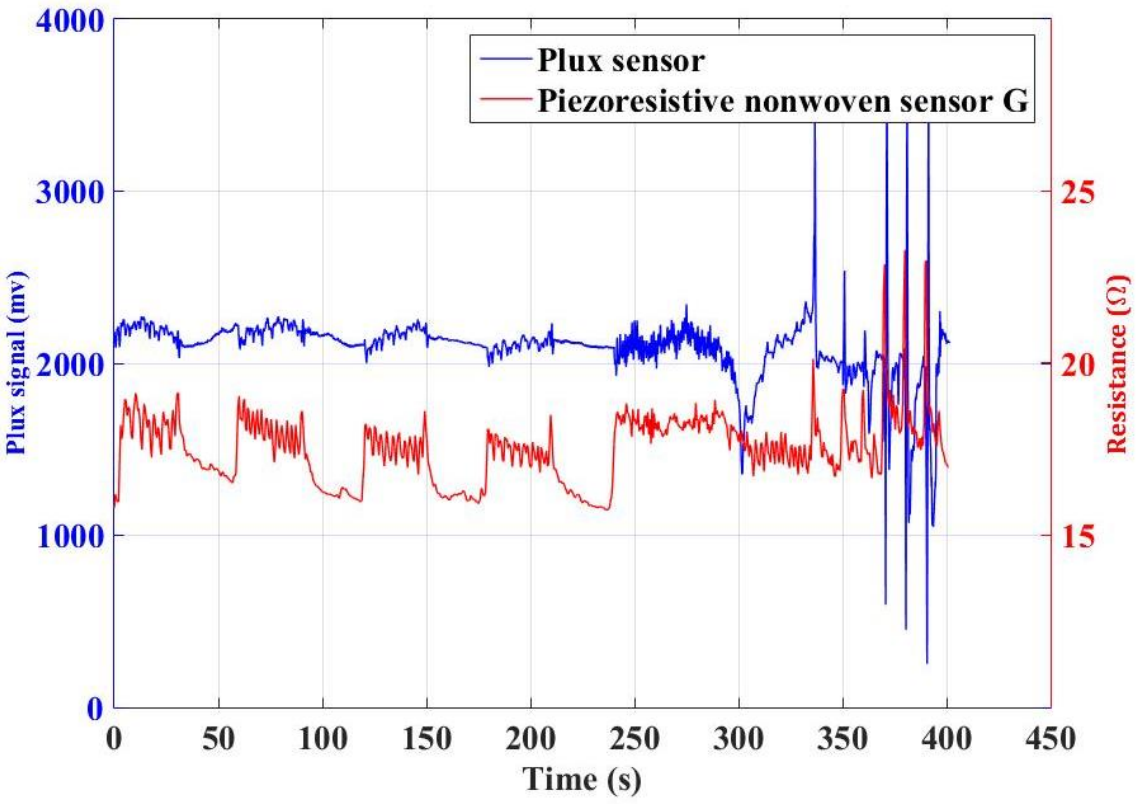

Figure 5-28. Breathing signal curve from the commercially available breathing belt sensor and the piezo-resistive nonwoven sensor G (smooth surface nonwoven fabric based).

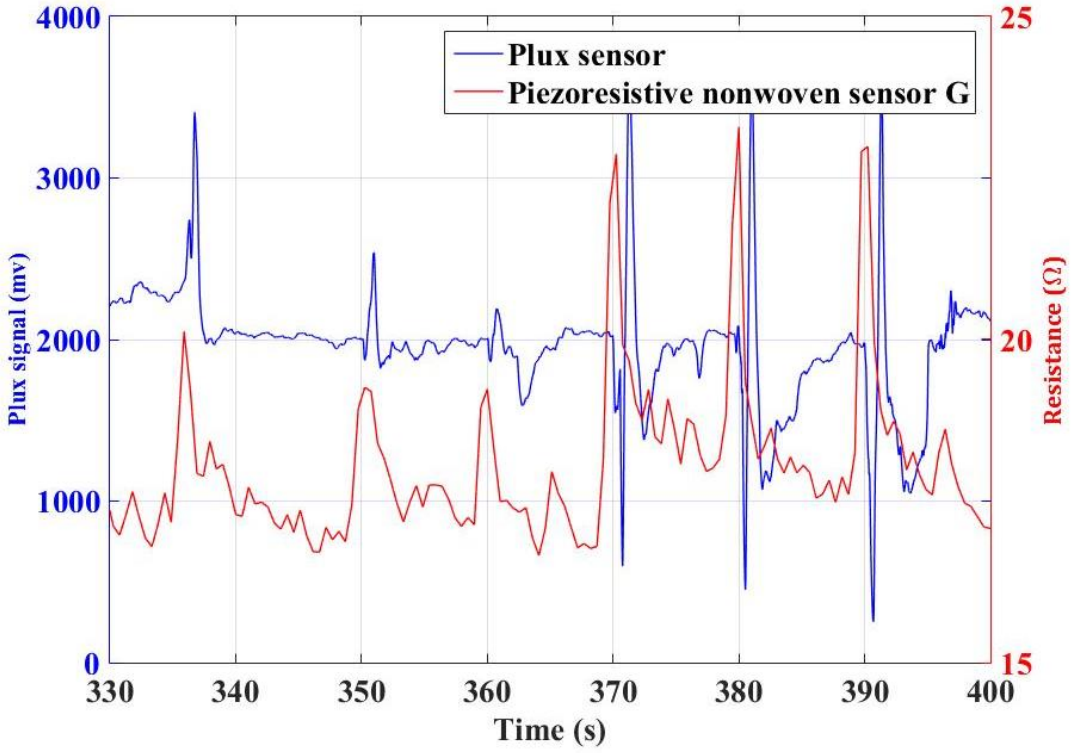

Figure 5-29. Arm movements during respiratory signal capturing (sample G).

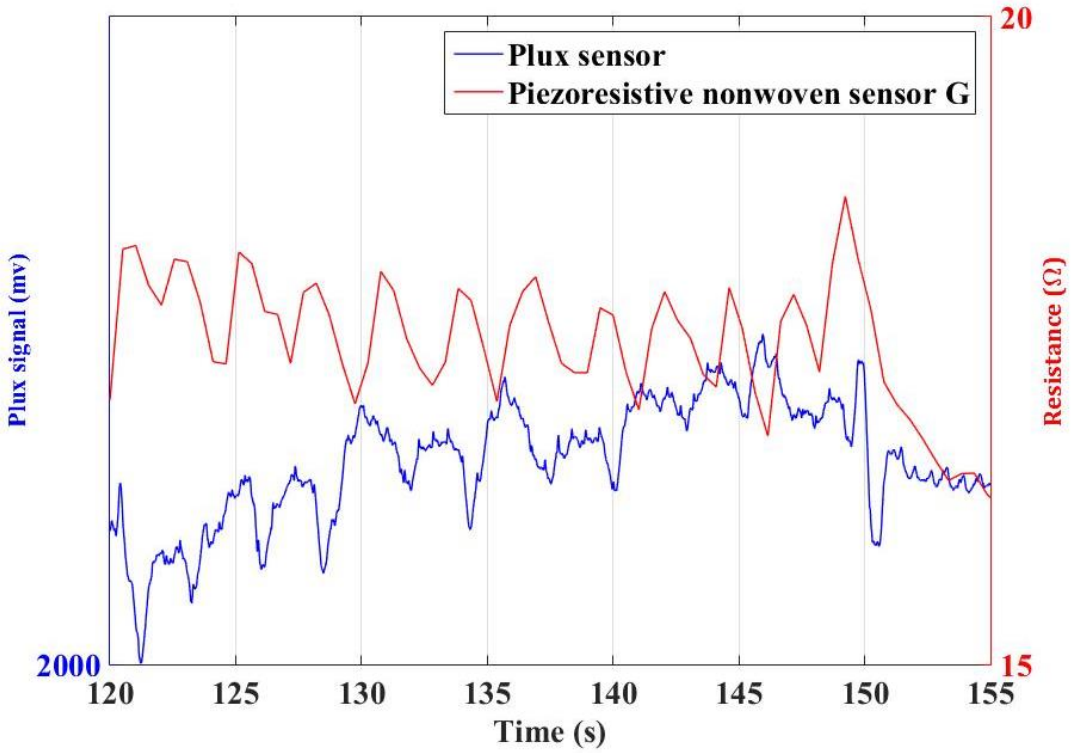

Figure 5-30. Scaled peaks during normal breathing (sample G).

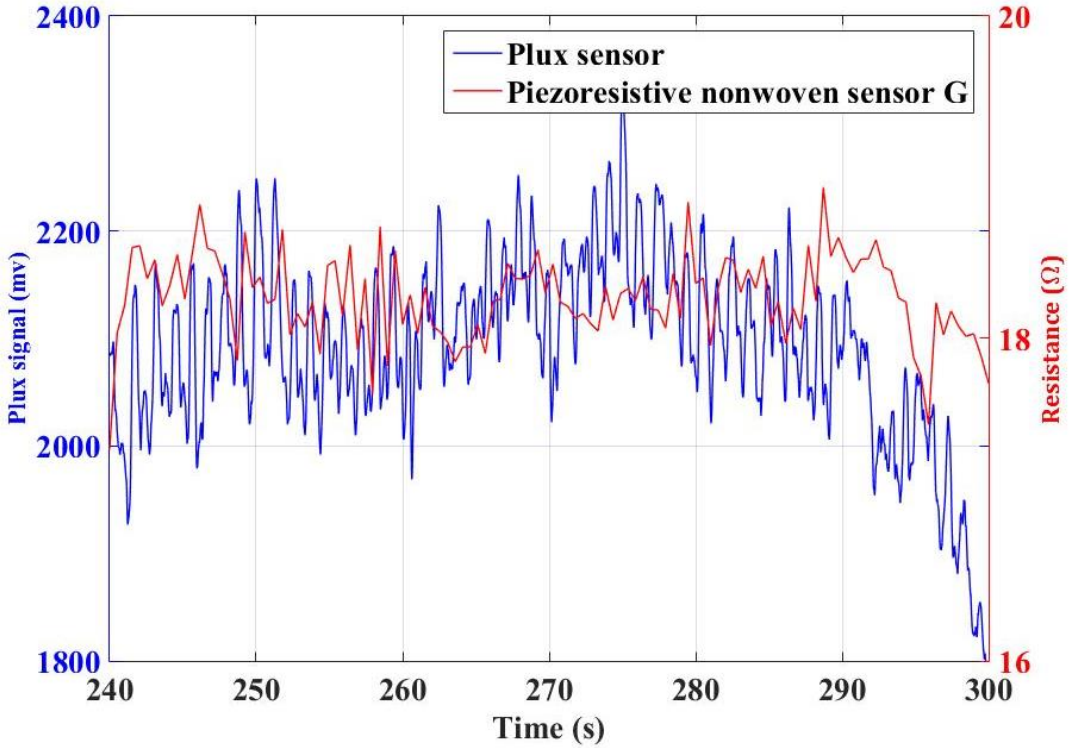

Figure 5-31. Rapid breathing signal capturing (sample G). The signal from the piezo-resistive nonwoven sensor is full of fluctuations.

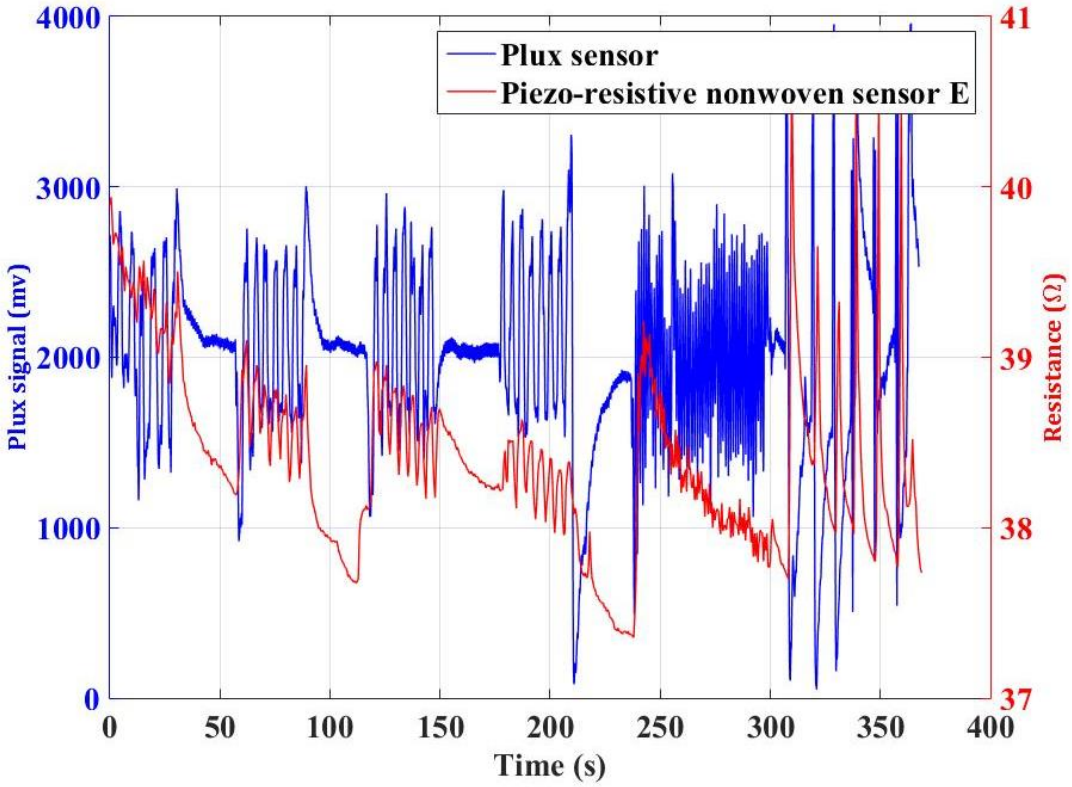

Figure 5-32. Breathing signal curve from the commercially available breathing belt sensor and the piezo-resistive nonwoven sensor E (commercial conductive nonwoven fabric based).

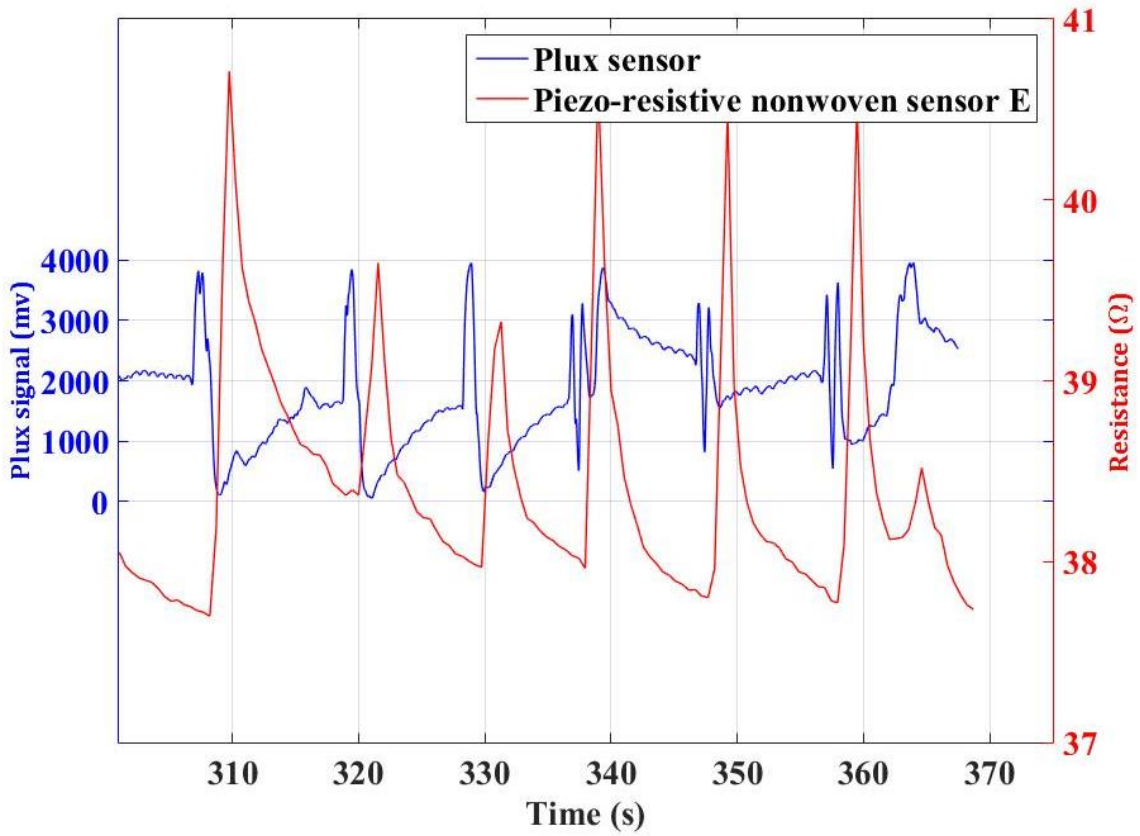

Figure 5-33. Arm movements during respiratory signal capturing (sample E).

Though the commercially available electroconductive nonwoven fabric sensor (sample E) showed excellent piezo-resistivity and reliability in the previous study, in the aspect of respiratory signal capturing, improvements are needed. The nonwoven sensor fabricated from sample E was able to capture the respiratory signal during normal and rapid breathing; however, it only responded the arm movements with large spikes, where no breathing signals could be identified (as shown in **Figure 5-32** and **Figure 5-33**).

The results of the respiratory signal captured by knitted fabric based piezo-resistive sensor (sensor J) are illustrated in **Figure 5-34** and **Figure 5-35**. Generally, the knitted fabric based sensor shows a lot of fluctuations, even in the period where the breathing was suppressed. Sensor J also performed poorly on capturing the respiratory signals under motion artefacts. The peaks caused by the arm lifting are much smaller and more difficult to identify than other piezo-resistive sensors. However, the knitted fabric based sensor still has the capability of capturing the respiratory signals. During the rapid breathing period, properly scale the graphs, it is found that the small peaks on the signal curve of sensor J correspond with the breathing signal captured by the commercially

available device (as shown in **Figure 5-35**). Therefore, it can be summarised that the knitted fabric based sensor has the potential to be in use of cardiorespiratory signal acquiring; however, proper improvements in reducing the noise level and increasing the stability are necessary and essential.

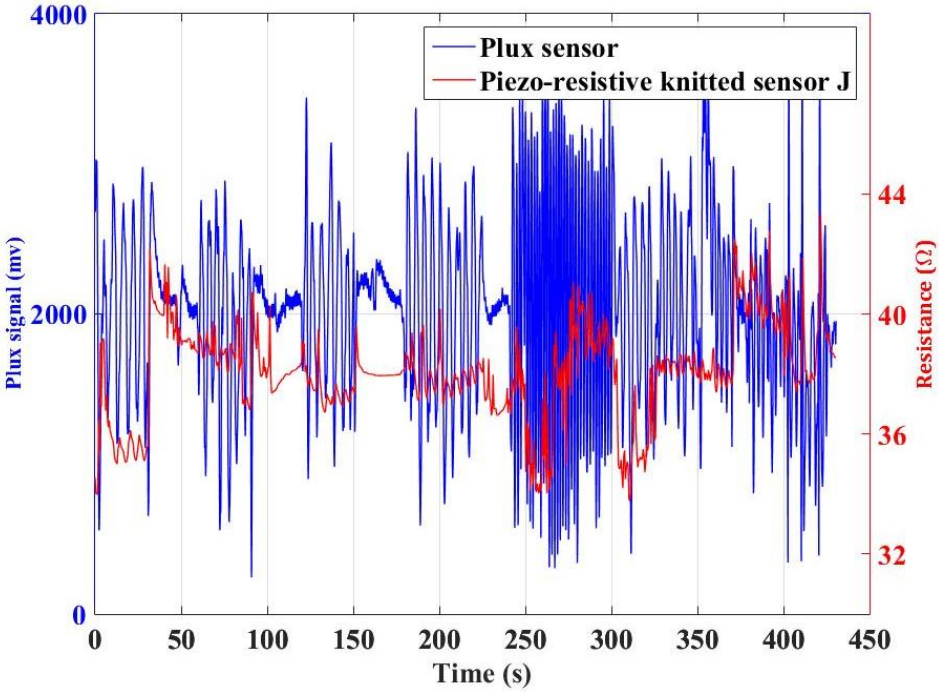

Figure 5-34. Breathing signal curve from the commercially available breathing belt sensor and the piezo-resistive sensor J (knitted fabric based).

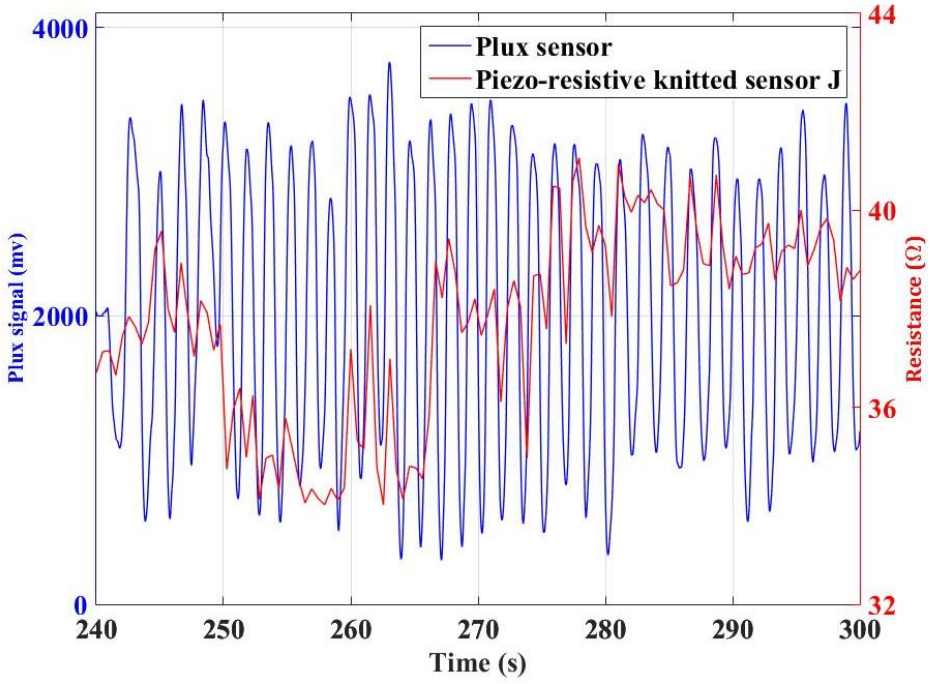

Figure 5-35. Rapid breathing signal capturing (sample J).

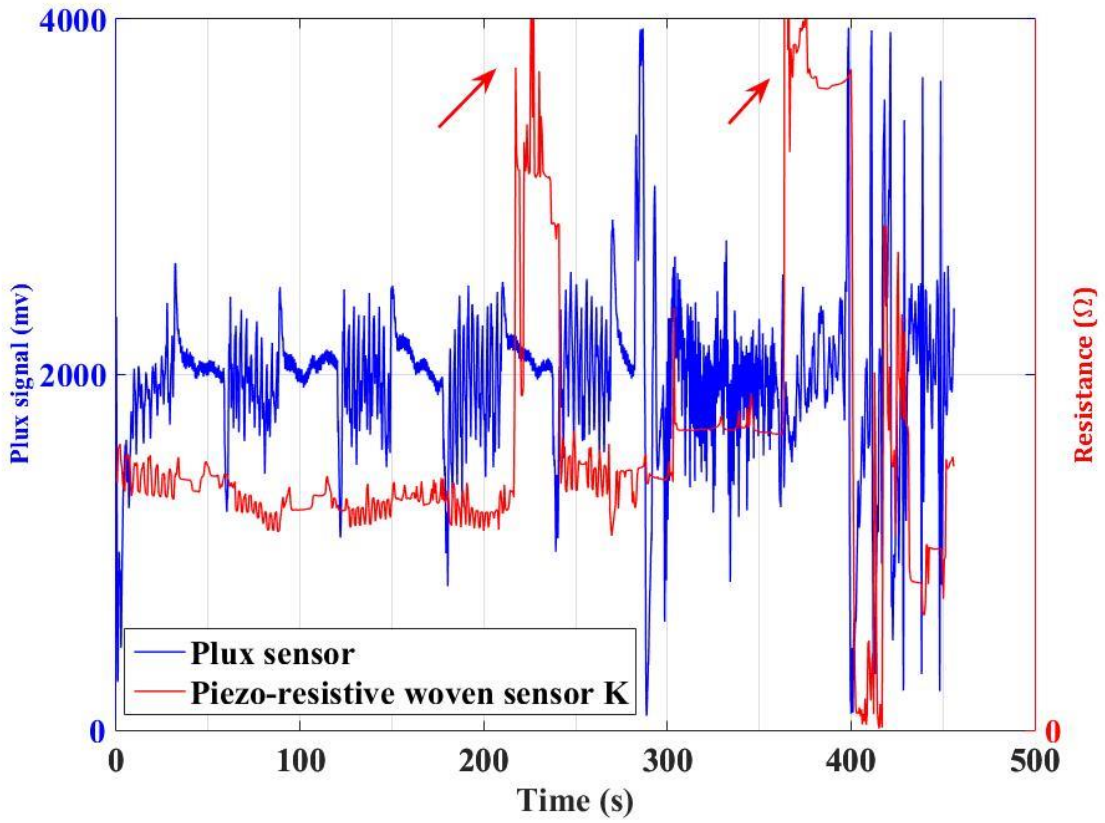

Figure 5-36. Breathing signal curve from the commercially available breathing belt sensor and the piezo-resistive sensor K (woven fabric based).

Figure 5-36 shows the results from woven fabric based sensor, which, as expected, performed poorly. Strong fluctuations appear throughout the test, especially during rapid breathing and arm lift periods. The huge spikes (marked by the red arrows) also indicate that the woven fabric based piezo-resistive sensor failed to perform functionally during the period that the subject held his breath. Due to the poor response to the rapid pressure signal, it is believed impossible to use woven fabric based piezo-resistive sensor in the application of acquiring weak bio-signals.

Comparing the piezo-resistive fabric based sensors fabricated from dot pattern embossed nonwoven (sample D), smooth surface nonwoven (sample G), commercially available electroconductive nonwoven (sample E) and knitted and woven fabrics, it is evident that in capturing the breathing signal, sample D based sensor performed better. Such sensor was able to respond correctly and accurately to the rapid breathing signal and successfully bypassed the interferences caused by the arm movements.

5.3.2 Cardiac signal capturing

In **Figure 5-37** and **Figure 5-38**, the results of the piezo-resistive nonwoven sensor show significant fluctuations in the general trend of the signal, yet heartbeats are still captured by the nonwoven sensor D. It can be observed that in the 'Drift Period' the resistance of the sensor reduces, which is due to the subject having to hold his chest non-moving to accommodate the long duration of breath holding. The green arrow shows the starting point when the subject was forced to move because of the breath holding; therefore, compared to the rest of this signal curve, 'Drift Period' provides a better clarity of the heartbeat signal. The tall peaks observed in the 'Drift Period' were caused by the body of the subject trying to avoid inhaling air. **Figure 5-38** illustrates the correct and accurate heart signal captured by the piezo-resistive nonwoven sensor. The signal has less amplitude, but the peaks are clear enough to identify the cardiac signal. Piezo-resistive nonwoven sensor D achieved an accuracy of 90.0% in acquiring the cardiac signal (18 heartbeats picked by sensor D compared with 20 picks from the Plux sensor).

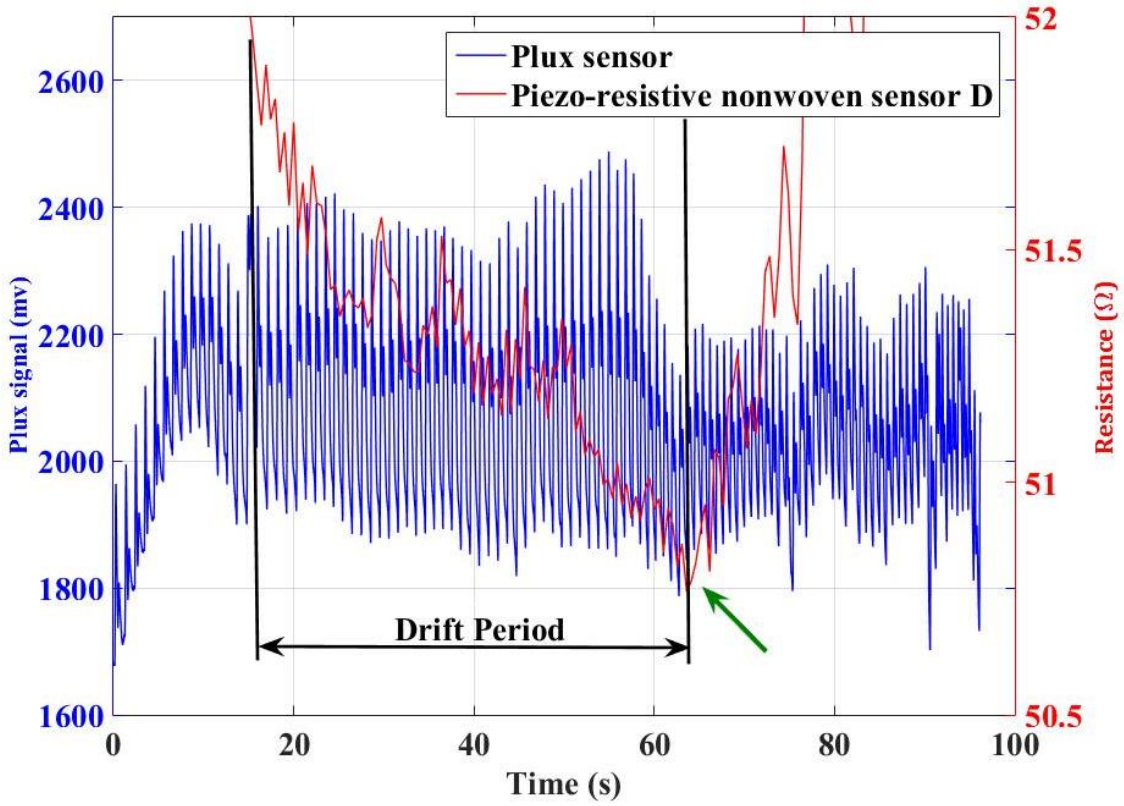

Figure 5-37. Heartbeat signal curve from the commercially available BCG sensor and the piezo-resistive nonwoven sensor D (dot pattern embossed surface).

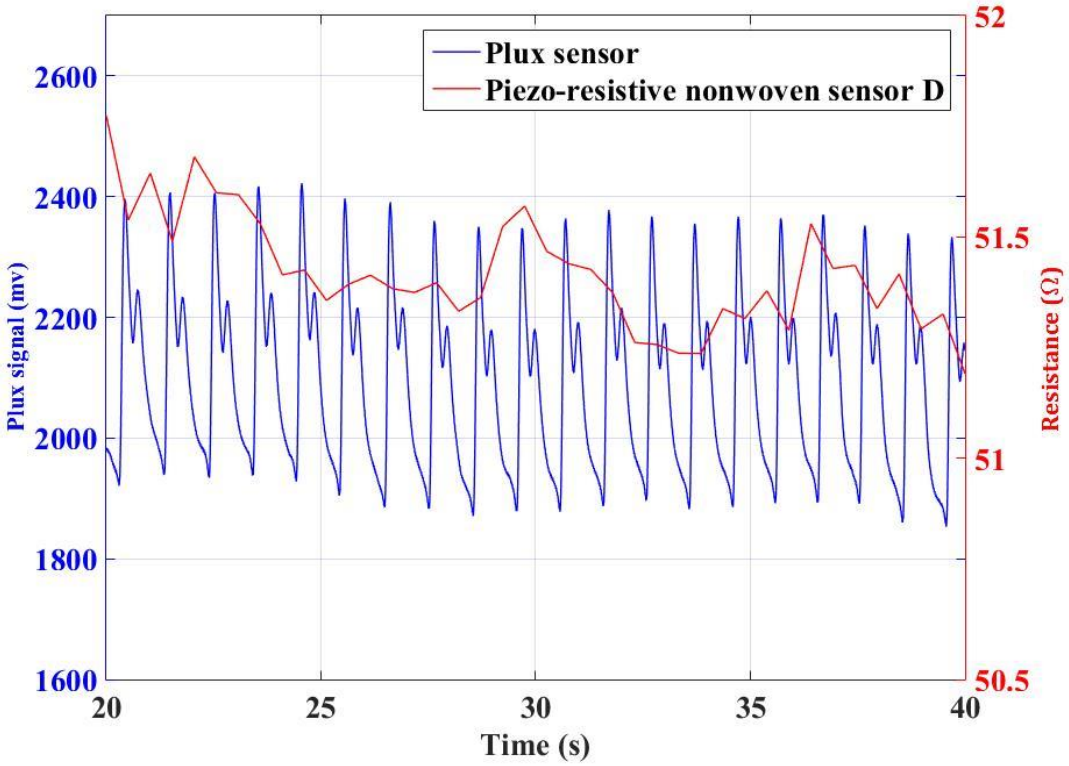

Figure 5-38. The successful cardiac signal acquisition using sensor D.

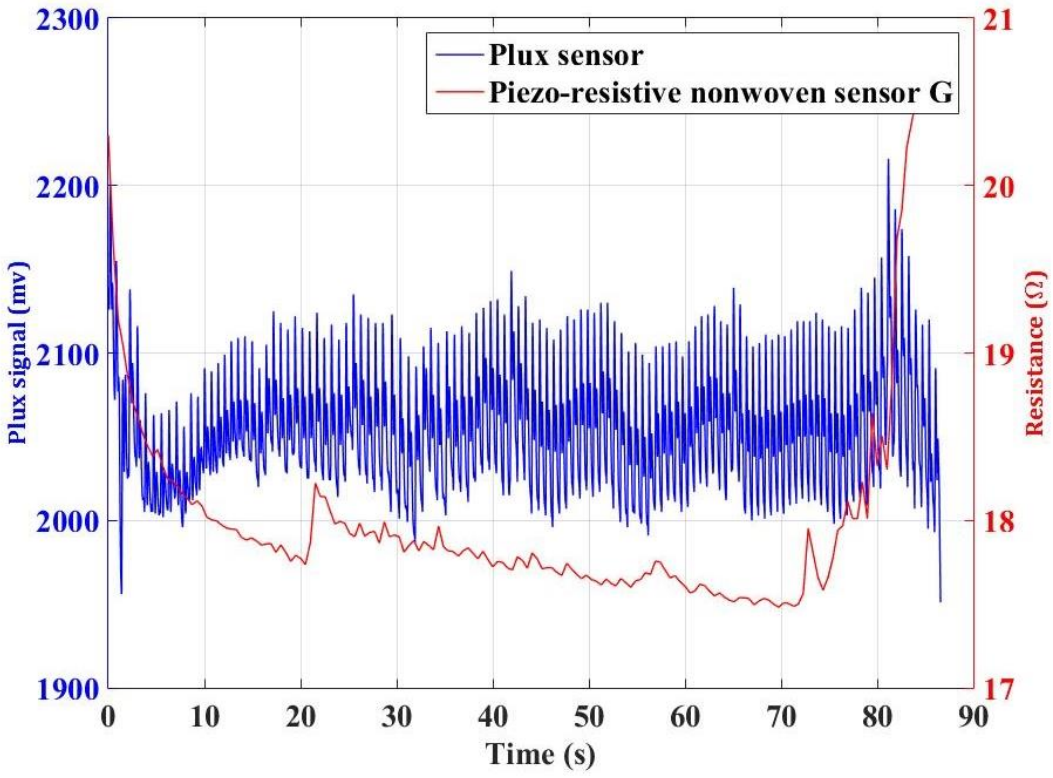

Figure 5-39. Heartbeat signal curve from the commercially available BCG sensor and the piezo-resistive nonwoven sensor G (smooth surface nonwoven based).

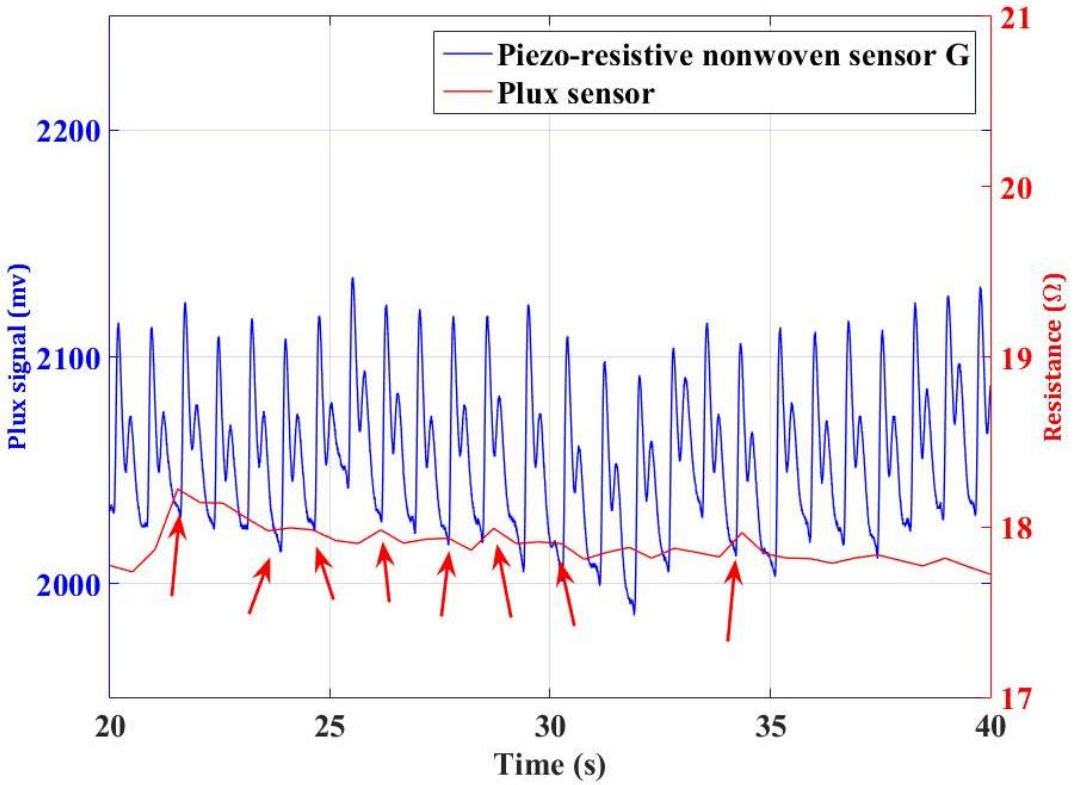

Figure 5-40. The peaks that correspond to the correct heartbeat from piezo-resistive sensor G.

The results of using the piezo-resistive nonwoven sensor G for capturing the heartbeat signals are shown in **Figure 5-39**. Compared with the Sensor D, the result of the Sensor G shows more fluctuation. As illustrated in **Figure 5-40**, at the selected period of time, only 8 potential heartbeats were detected out of 26 heartbeats as marked out by the red arrows in the figure. Though most of the curve shows irrelevance to the heart signal, every peak that appears in the curve correlated correctly to a peak in the curve from the Plux sensor. This shows that the piezo-resistive nonwoven sensor G has the potential to capture the cardiac signal; however, at this stage, the signal captured lack of intensity and is greatly affected by noises; and whether or not the peaks captured by the piezo-resistive nonwoven sensor G are actually the heartbeats remains unknown.

The cardiac signals acquired from commercially available conductive nonwoven, knitted and woven fabric based sensors show a lot of fluctuations, in which no cardiac signals can be found. The reason of their failure in capturing cardiac signals using such sensors is believed that as the intensity of the BCG is much weaker than breathing signals, the fabric sensor must not too dense, like knitted or woven structure, in order to prevent the weak signals from being damped. This concludes the reason why knitted or

woven structures are not suitable for use of piezo-resistive pressure sensor for weak signal acquiring applications. As a nonwoven material, which was constructed using much finer fibres (compared with yarns) and with an open structure, sample E initially showed high sensitivity, stability and reproducibility in sensing. However, as shown in the SEM analysis, it was found that the carbon dispositions in sample E adhere the fibres into heavier fibre bundles, which eventually prevented the weak BCG signals from transmitting through the fabric. Comparing the two relatively successful sensors, the dot pattern embossed nonwoven fabric sensor (D) and the smooth surface nonwoven fabric sensor (G), the dotted nonwoven fabric sensor showed a better performance in capturing the heartbeat signal. This is due to the fact that within the operating range of 10-20 g/cm^2, the sensitivity of the dot pattern embossed nonwoven fabric is higher than the smooth nonwoven fabric. It can also be concluded that in order to improve the intensity of the captured signals and reduce the influence from noises, it is necessary to apply further filtering methods.

5.4 Investigation of the reliability and accuracy of the nonwoven piezo-resistive sensor

In section 5.3, the feasibility of the nanoscale silver particle-based electroconductive ink impregnated nonwoven fabric-based sensor has been studied and proven. The reliability and accuracy of the piezo-resistive sensor are discussed in this section. Due to the fact that the dot pattern embossed nonwoven is most suitable for capturing the cardiorespiratory signals, the tests were carried out using the dot pattern embossed nonwoven fabric based sensor.

In order to improve the reliability of the electrical resistance signal generated by the sensor, a bandpass filter was applied. The frequency of the cardiorespiratory signals varies according to the situation of the subject. The respiratory signal normally is within the range of 0.1 to 0.5 Hz; whereas the cardiac signal has a frequency from 1 to 1.67 Hz.[234] Considering the extreme conditions, the bandpass filter was set from 0.1 to 1 Hz for respiratory signal and 0.8 to 2 Hz for cardiac signals. The sampling rate of the NI-9219 data acquisition card is set to the maximum value of 100 Hz for the best signal acquisition.

Figure 5-41 shows the result of using the bandpass filter on piezo-resistive nonwoven sensor D. In it can be seen that with the help of the bandpass filter, the cardiac signal

curve acquired from the piezo-resistive nonwoven sensor becomes considerably smoother than the signal obtained from the commercial available Plux sensor. The peaks of the cardiac signal curve match well with heart signal from Plux sensor, indicating that the bandpass filter not only reduces the noise level but also improves the accuracy of the sensor. The piezo-resistive nonwoven sensor picked 39 signals out of 40 signals from the Plux sensor, which gave an improved accuracy of 97.5% over the period of 30 seconds, compared with the accuracy of 90.0% without using the bandpass filter.

The bandpass filter was then used together with the commercially available electroconductive nonwoven fabric based sensor E, in order to find out whether or not sensor E was capable of capture the heart signal after filtering the noise. **Figure 5-42** illustrates the cardiac result of a selected period from sensor E, where a stable signal can be observed. The signal intensity of sensor E is much smaller than sensor D, which makes it very difficult to identify the cardiac signal from the peaks. The intensity of the signals remains constant, which is believed that no BCG signal is captured at all; while all the peaks may still be due to noise.

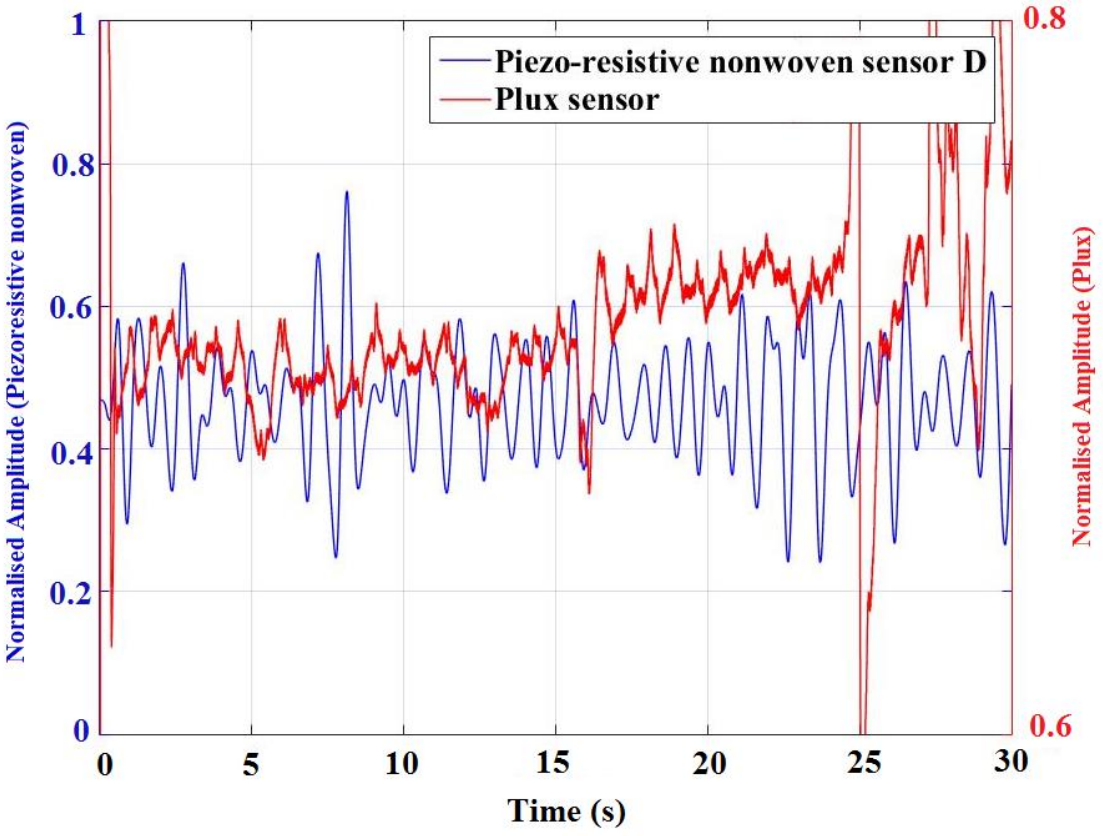

Figure 5-41. The bandpass filtered cardiac signal from piezo-resistive nonwoven sensor D.

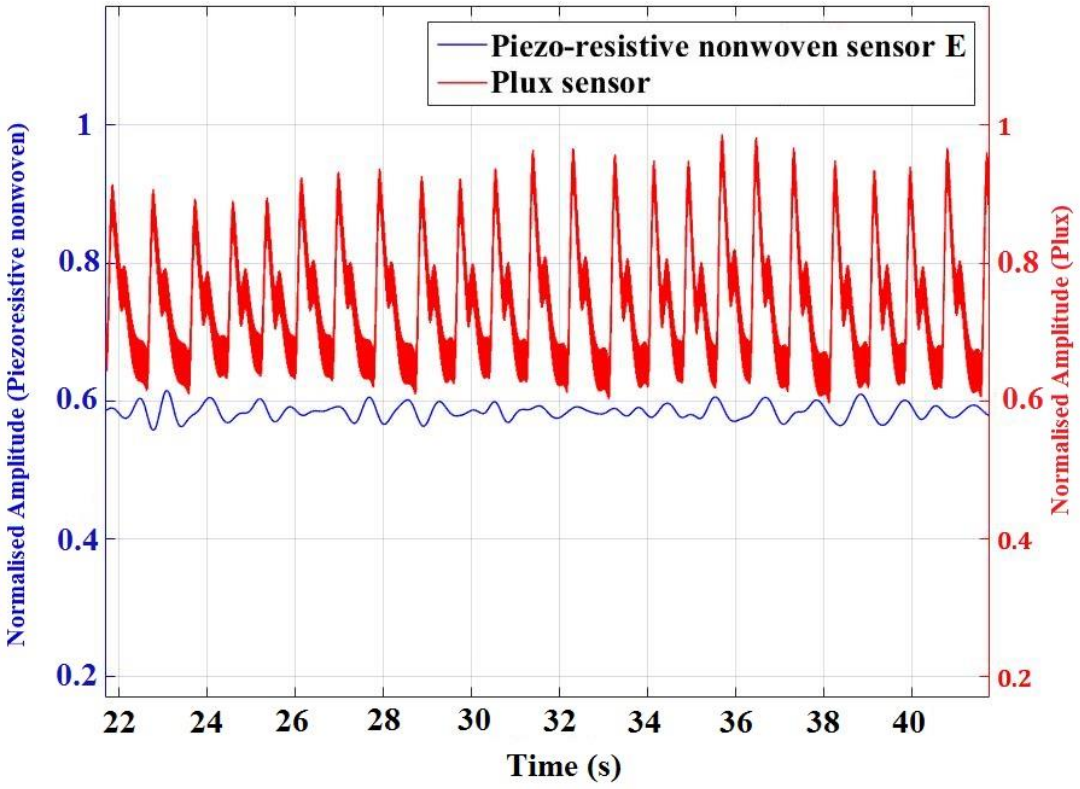

Figure 5-42. Bandpass filtered cardiac signal from commercially available piezo-resistive nonwoven sensor E.

The accuracy of the nanoscale silver ink impregnated piezo-resistive nonwoven sensor for capturing cardiorespiratory signals was investigated further by matching the number and the locations of the peaks detected in a period of time with the commercially available device. The number and the locations of the resistance peaks were detected and determined using a Matlab programme that considers the criteria that the minimum distance between every two adjacent peaks needs to be 0.35 second and 3 seconds for heartbeat signals and breathing signals, respectively. The amplitude of the peaks is normalised as the fraction of the difference between the maximum and minimum amplitude.

$$Normalised\ amplitude = \frac{R - R_{min}}{R_{max} - R_{min}} \qquad \textbf{Equation 5-6}$$

Five male and five female volunteers contributed their help for cardiorespiratory data collection. The cardiorespiratory data of a five-minute period of each volunteer were

recorded with the control cardiorespiratory data (captured by the commercially available bio-signal sensing system).

Table 5-3 and **Table 5-4** show the statistical data of the ten volunteers' cardiorespiratory signals, from which it can be concluded that the nonwoven piezo-resistive sensor performed reliably (the justification Matlab programme is available in Appendix G). Compared with the control data group, it acquired the cardiorespiratory signals with less variation. The discussions in the following sections are based on one volunteer's results, which were representative and typical. The accuracy of the respiration rate (*RR*) and heart rate (*HR*) of the piezo-resistive sensor is calculated as the following equations:

$$A_{RR} = \left(1 - \frac{|\overline{RR_{Belt}} - \overline{RR_{NS}}|}{\overline{RR_{Belt}}}\right) \times 100\% \qquad \textbf{Equation 5-7}$$

where: A_{RR} is the accuracy of the *RR*; $\overline{RR_{Belt}}$ and $\overline{RR_{NS}}$ are the average *RR* of the belt sensor and the nonwoven sensor, respectively.

$$A_{HR} = \left(1 - \frac{|\overline{HR_{BCG}} - \overline{HR_{NS}}|}{\overline{HR_{BCG}}}\right) \times 100\% \qquad \textbf{Equation 5-8}$$

where: A_{HR} is the accuracy of the *HR*; $\overline{HR_{BCG}}$ and $\overline{HR_{NS}}$ are the average *HR* of the BCG sensor and the nonwoven sensor, respectively.

Table 5-3. Cardiorespiratory data of the male subjects.

Male	No. of breathing/minute			No. of heartbeat/minute		
	Belt sensor	Nonwoven sensor	Absolute difference	BCG sensor	Nonwoven sensor	Absolute difference
1	13.93	12.96	0.97	70.04	72.17	2.13
2	15.08	13.30	1.78	74.83	74.43	0.40
3	15.07	12.69	2.38	57.52	69.82	12.30
4	14.74	13.17	1.57	79.42	72.35	7.07
5	11.87	12.19	0.32	70.53	75.59	5.06
Average	14.14	12.86	1.28	70.47	72.87	2.4
Standard error	0.60	0.20		3.65	1.00	
Accuracy		90.95%			96.59%	

Table 5-4. Cardiorespiratory data of the female subjects.

Female	No. of breathing/minute			No. of heartbeat/minute		
	Belt sensor	Nonwoven sensor	Absolute difference	BCG sensor	Nonwoven sensor	Absolute difference
1	14.47	12.32	2.15	67.06	66.86	0.20
2	15.16	13.43	1.73	71.38	71.38	0.00
3	14.41	11.10	3.31	71.28	64.56	6.72
4	15.02	12.45	2.57	75.30	70.95	4.35
5	14.79	12.42	2.37	79.66	67.83	11.83
Average	14.77	12.34	2.43	72.94	68.32	4.62
Standard error	0.15	0.37		2.13	1.28	
Accuracy		83.55%			93.67%	

5.4.1 Heartbeat signal matching

As mentioned above, the reprehensive cardiorespiratory signals captured by the piezo-resistive nonwoven sensor D are compared and discussed with the signals acquired by the Plux sensor in this section. The plotted data of the rest of the test subjects are available in Appendix F.

In the result of the peak detection and matching investigation (as shown in **Figure 5-43**), it is clear that the signal amplitude variation of the nonwoven piezo-resistive sensor is much smaller than that of Plux BCG sensor. Most of the peaks of the piezo-resistive nonwoven sensor are strong and clearly identifiable. In the peak location matching graph, minor shift between two sets of peaks can be observed due to the natural difference between the working principles of the Plux BCG sensor and the piezo-resistive nonwoven sensor which is that the Plux BCG sensor picks up the pulse on the finger which will cause a delay in the signal.

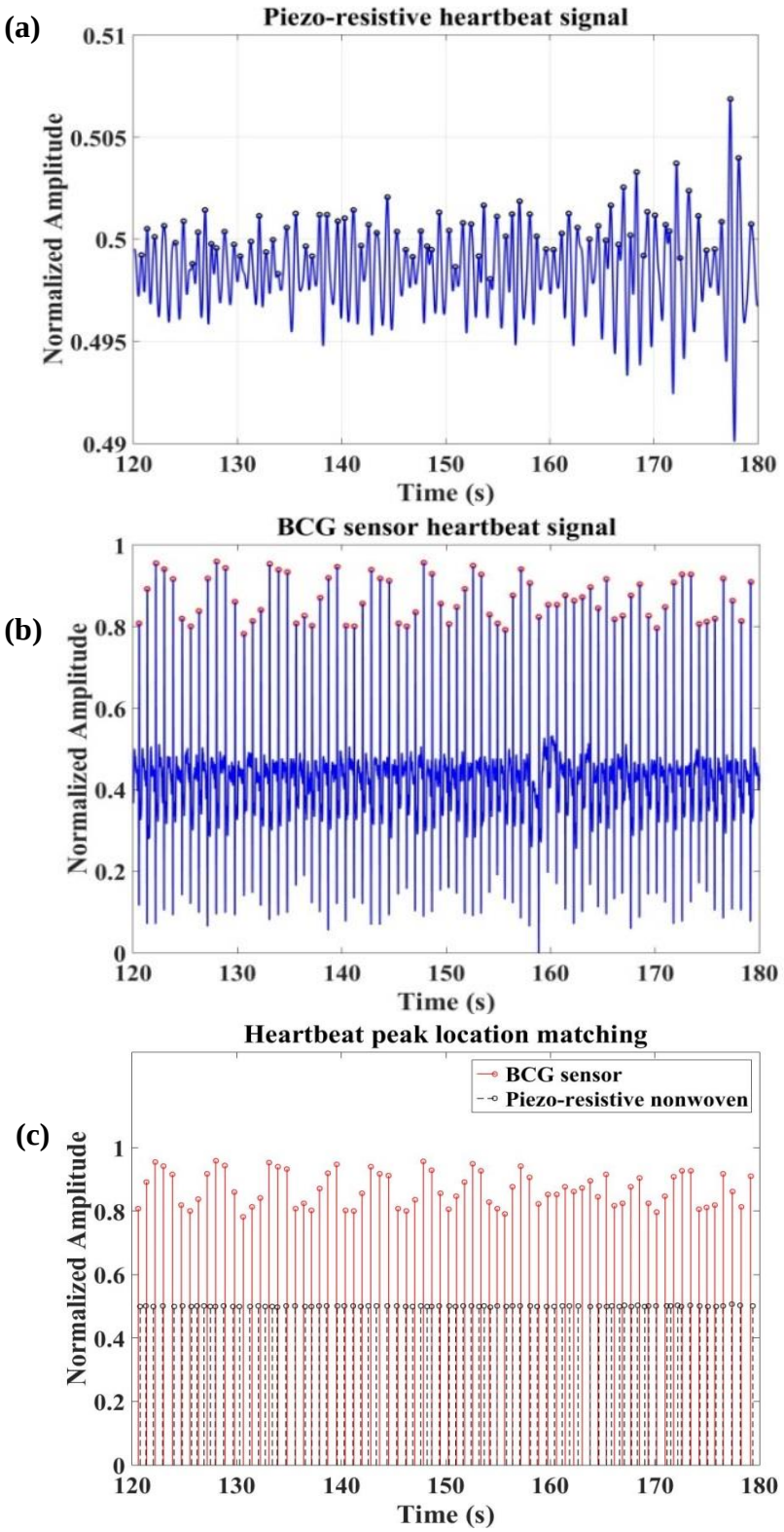

Figure 5-43. Heart signal peak detection and location matching between the nonwoven piezo-resistive sensor and commercially available BCG sensor.

The reproducibility of the electroconductive nonwoven fabric based sensor in the application of the capturing the cardiorespiratory signal was studied. The cardiorespiratory signals were acquired from the nonwoven sensor and commercially

available sensor (Plux bio-signal system) on the same subject for 10 times. Each test lasted at least 5 minutes. The heartbeat count of these tests, from the piezo-resistive nonwoven sensor and the commercially available BCG sensor, normalised to the number of beats in one minute. Among ten tests, one of the test results was found unusual that the piezo-resistive nonwoven sensor obtained a heart rate of 91.98 beats/minute where the Plux BCG sensor had only 72.92 beats/minute. The sensor performed normally in other nine tests. This unusual result could be due to the unexpected noise that affected the performance of the sensor. This issue should be able to be resolved if a better filtering system is applied. Due to the fact that the same subject was not available for more testing, the results of the other nine tests are illustrated in **Table 5-5**.

Table 5-5. Heart rate (number of beats per minute) comparison

Test	Plux BCG sensor	Piezo-resistive nonwoven sensor	Difference
1	71.88	64.63	7.25
2	71.88	73.93	2.05
3	71.43	77.71	6.28
4	70.34	72.34	2.00
5	72.05	79.64	7.59
6	66.73	72.86	6.13
7	73.39	70.86	2.53
8	68.90	75.02	6.12
9	65.82	76.88	11.06
Average	70.27	73.76	3.49
Standard error	0.86	1.47	
Accuracy			95.03%

It can be seen that the heart rate of the Plux BCG sensor and the nonwoven piezo-resistive sensor are comparable. The piezo-resistive nonwoven sensor achieved a

reliable performance with a standard deviation of 1.47 beats per minute and 95.03% of accuracy in detecting the cardiac signal.

5.4.2 Breathing signal matching

Table 5-6. Breathing rate (number of breaths per minute) comparison

Test	Breathing belt sensor	Piezo-resistive nonwoven sensor	Difference
1	11.31	11.68	0.37
2	11.35	11.35	0.00
3	12.77	14.06	1.29
4	11.14	14.00	2.86
5	11.62	11.42	0.20
6	13.17	12.37	0.80
7	11.89	10.96	0.93
8	12.44	11.81	0.63
9	10.85	13.03	2.18
10	12.21	11.25	0.96
Average	11.88	12.19	0.31
Standard error	0.24	0.36	
Accuracy			97.39%

Same as the tests in capturing heartbeats, ten tests were performed with the piezo-resistive nonwoven sensor and the breathing counts over one minute were determined. The statistical data in **Table 5-6** show that there are only negligible differences between the two types of sensors in the aspect of capturing the breathing signals and a high accuracy of 97.39% was achieved.

Figure 5-44 indicates the performance of the piezo-resistive nonwoven sensor while capturing the breathing signal, compared with the commercially available breathing belt sensor. The peaks of the signal captured by the nonwoven piezo-resistive sensor are clearer than that of the commercially available sensor system. However, there is a false peak detected in using the developed Matlab coding (marked in **Figure 5-44(a)**).

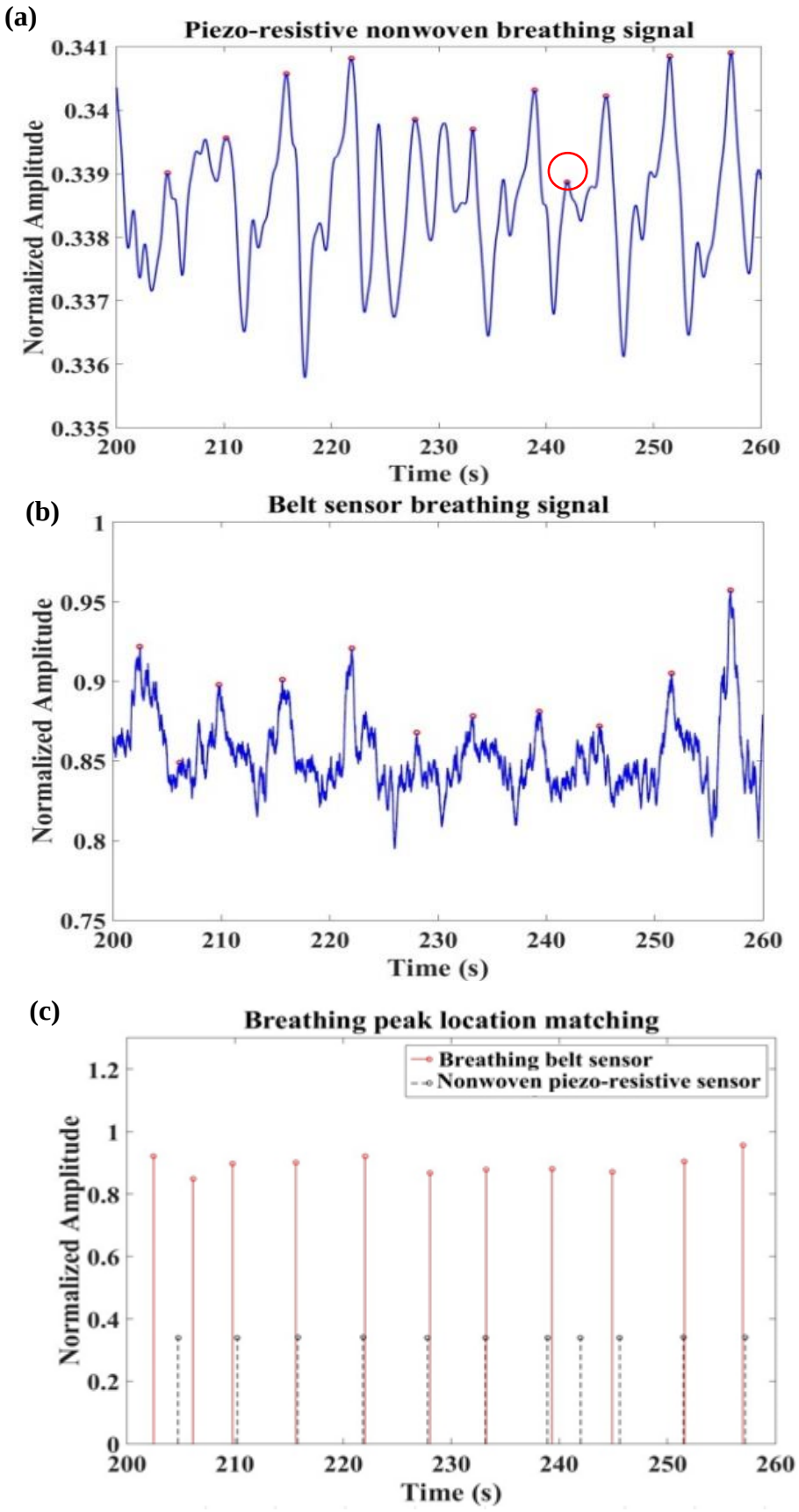

Figure 5-44. Breathing signal peak detection and location matching between the nonwoven piezo-resistive sensor and commercially available breathing belt sensor. (Marked: false peaks detected)

5.4.3 Response and recovery time of the piezo-resistive nonwoven sensor

A phenomenon was found throughout the tests that a short but varying period time is required at the beginning of the test, in order for the signals to be stabilised and capable of showing a reliable resistance reading.[243] Also, another similar phenomenon was observed when a sudden movement was carried out. The time for the sensor to respond the cardiorespiratory signals and recovery time from interferences was studied. It is discovered that the response time of the piezo-resistive nonwoven sensor is 12.65 seconds for heart signal capturing and 17.24 seconds for breathing signal.

The recovery time of the sensor was measured by calculating the average elapsed time before the signal fully recovered from strong movement spikes. In the cardiorespiratory signal acquisition test, the subject moved his body intentionally, at random intervals as long as the sensor had already recovered from the last interference. The typical cardiorespiratory signal acquired from this test is shown in **Figure 5-45**. It can be seen that the cardiac signal requires less recovery time, which is 10.37 second, while respiratory signal needs 25.83 seconds to be fully recovered from motion artefacts.

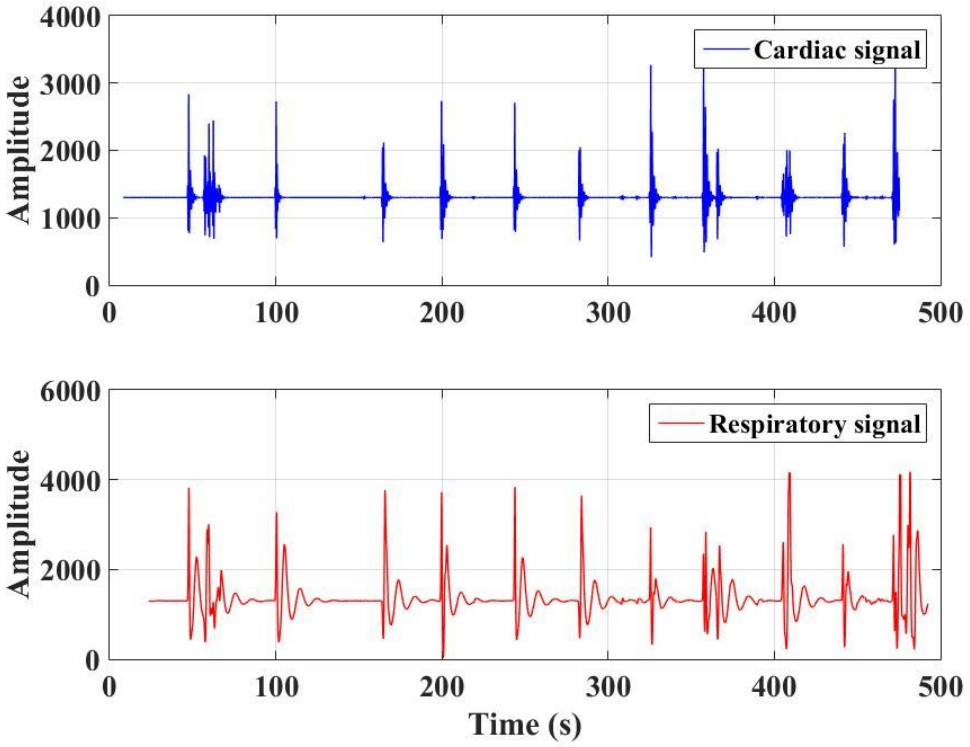

Figure 5-45. Recovery time of the piezo-resistive nonwoven sensor.

5.5 Development of a nonwoven sensor with directional electroconductive monofilament/yarns and its empirical modelling

As has been discussed in chapter two, nonwoven materials have advantages of excellent ink/particle absorbency and high resistance change with pressure applying; the nonwoven materials have been widely studied in use of piezo-resistive pressure sensing applications. It is necessary to develop a model for the piezo-resistive nonwoven material used in this research in order to characterise its function. However, due to the random nature of the nonwoven materials, it is almost impossible to create a precise model that can represent every part of the nonwoven structure. In the aspect of nanoscale electroconductive ink impregnation, the exact information of the substrate is critical to its piezo-resistivity. Many factors are related to the piezo-resistivity of the nonwoven material, such as location, morphology, quantity and the relationships with other joints or potential contacting points.

In order to overcome these issues, a nonwoven sensor with directional monofilaments/yarns laid at 0-degree and 90-degree angles multi-layer structure is introduced. Similar to nonwoven fabrics, the monofilaments/yarns in the structure are not interlooped or interlaced as knitted or woven fabrics, which provides this structure with an advantage that the weak signals will not damp as in knitted or woven structures. Also, the relatively loose structure allows the electroconductive ink to be thoroughly impregnated through the structure. The piezo-resistivity of such structure has similarity to the nonwoven fabrics: upon compressing, the change in the contact points results in the change of the resistivity of the material. Therefore, it is believed that this structure has a similar behaviour to the piezo-resistive nonwoven material. As the structure is fabricated under a less random condition, the details of the structure are controlled. This allows the modelling of such structure become possible.

5.5.1 Design and fabrication of the nonwoven piezo-resistive sensor with directional monofilaments/yarns

The design of the nonwoven sensor with directional monofilaments is illustrated in **Figure 5-46**. The structure was constructed as follows:

- as can be seen in **Figure 5-46**, on each layer, the monofilaments remain parallel with an interval of 0.5 mm between each other; the monofilaments in the

neighbouring layers are crossed at a 90-degree angle, creating a set of crossing points; in order to maintain straight, the ends of the monofilaments were taped firmly on a plastic frame;

- while creating the third layer, the monofilaments will be parallel with the first layer; however, the third layer is not stacked directly at the location of the first layer, but with a 0.25 mm shift; thus, the sets of the crossing points between layer 1 and 2, layer 2 and 3 are separate; this prevent joints from connecting to each other at zero pressure; also the dangling structure increases the thickness of the structure under the same area density; upon compressive, this can increase the chance of creating new contacting point via bending as well;
- the crossed area is 45 mm by 45 mm, which was suitable for a compressive area of 40 mm by 40 mm; the diameter of the monofilaments is 0.2 mm; altogether 8 layers of monofilaments were placed, in order to simulate the performance of the nonwoven materials used throughout the current research; the photos of the structure during construction and finished construction were shown in **Figure 5-47**.

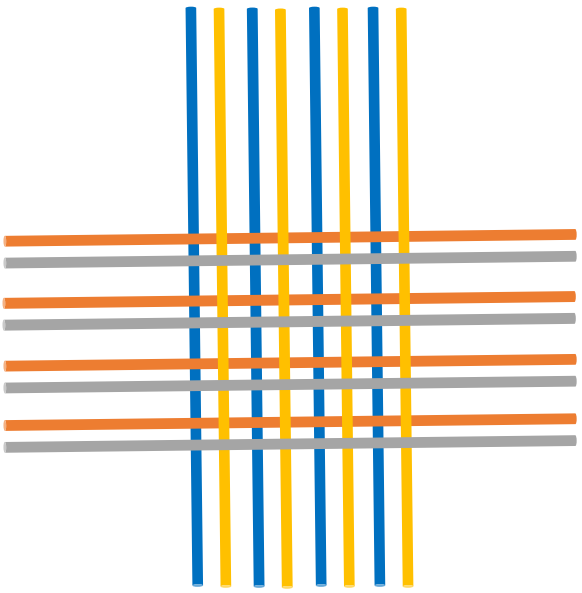

Figure 5-46. A schematic of the monofilament layered structure.

The monofilament used in the construction of this structure was high-density polyethylene (HDPE), which initially was designed for thermal bonding. However, due to the nature of HDPE and the high tension kept applied on the monofilament, shrinkage appeared during the thermal bonding process. As the mould used for creating thermally

bonded nonwoven materials could only apply pressure on the air-through direction, the shrinkage was inevitable and maintaining of the structure was impossible. Therefore, this structure was then investigated and tested without thermal bonding.

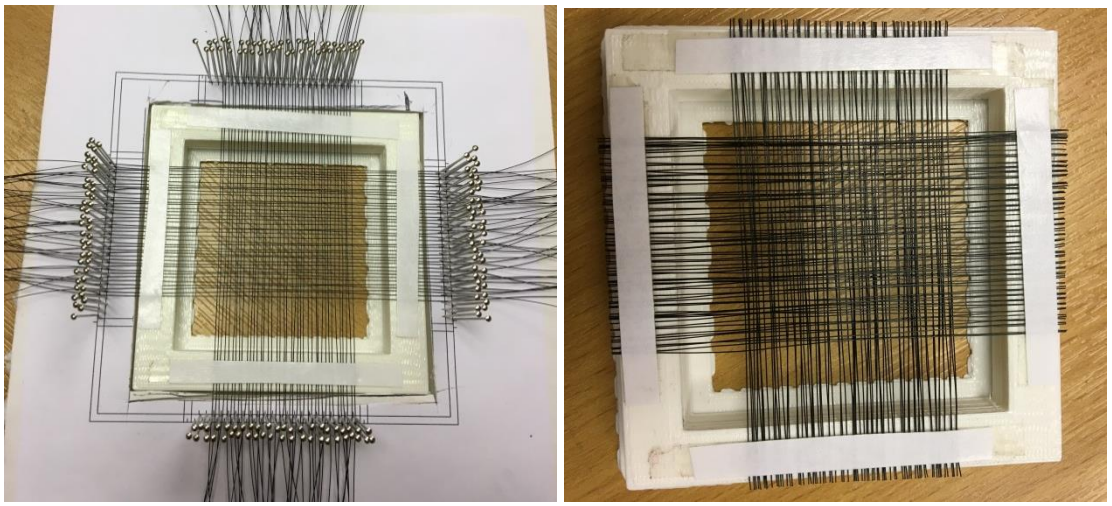

Figure 5-47. Photos of the monofilament layered structure. Left: during construction; right: finished nonwoven sensor with directional monofilaments.

5.5.2 Nanoscale silver particle-based electroconductive ink impregnation

In order to grant HDPE based structure piezo-resistivity, the structure was dip-coated with nanoscale silver ink. Due to the fact that the mangling and the thermal sintering process were not able to be carried out, the coated structure was left in a ventilated environment for at least 24 hours to ensure the silver ink was fully dried and naturally sintered.

The morphology of the silver deposition on the HDPE can be seen in **Figure 5-48**. Similar to the nonwoven materials, the coating of silver along the monofilament is observed. The silver particles were also found deposited on the structure in a form of a water drop. Due to a large amount of aqueous silver ink, the surface tension of the ink dragged the nearby monofilaments together, and eventually weakly bonded them together, as can be observed in **Figure 5-48(c)**. The results of EDX analysis reveal that though some silver agglomerates are found, generally, the nanoscale silver particle impregnation was uniform on the monofilaments, as illustrated in **Figure 5-49**.

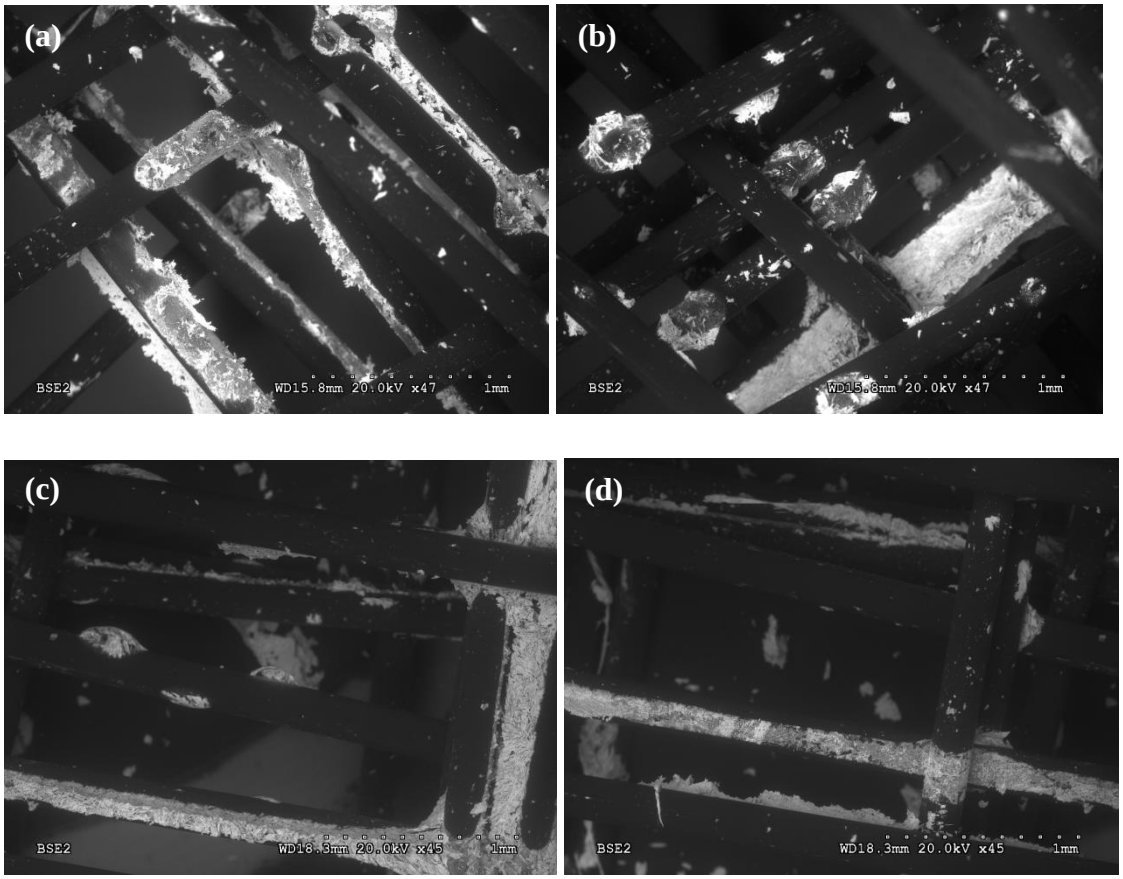

Figure 5-48. SEM image of the monofilament laid structure.

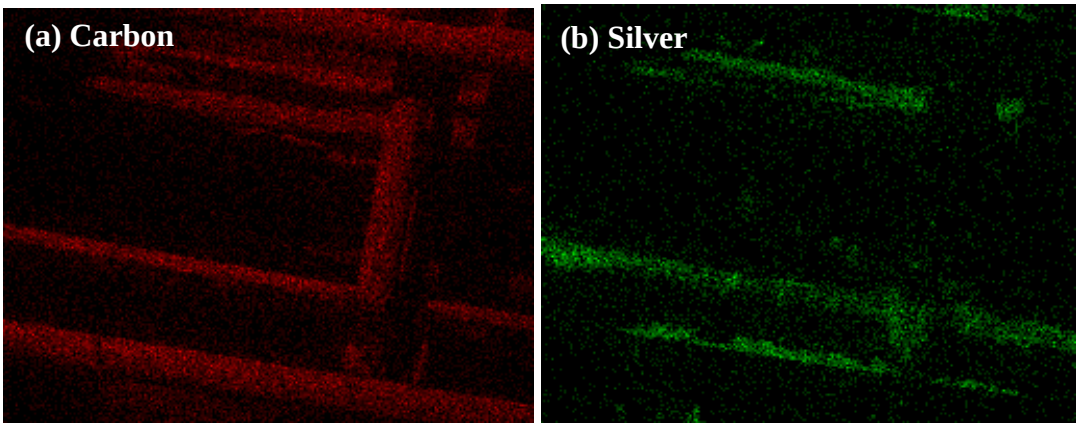

Figure 5-49. EDX elemental mapping of carbon and silver.

5.5.3 Electromechanical characterisation and cardiorespiratory signal acquisition

Electromechanical tests were carried out on the nonwoven structure in order to study its piezo-resistivity.

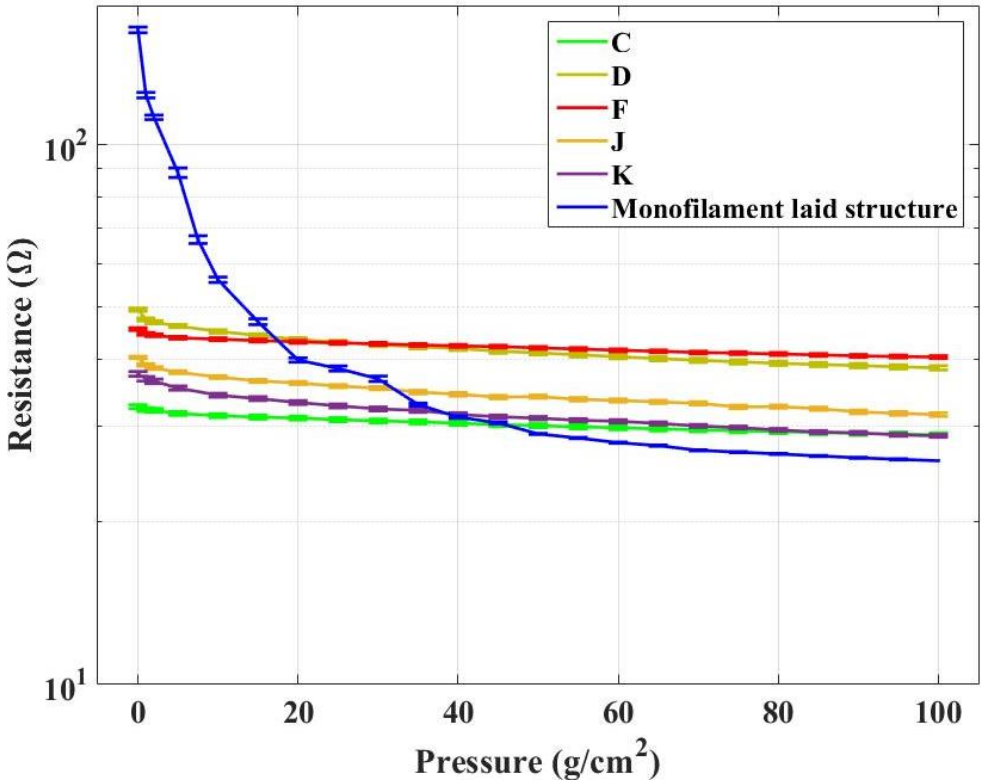

Figure 5-50. Electromechanical compressive strength test.

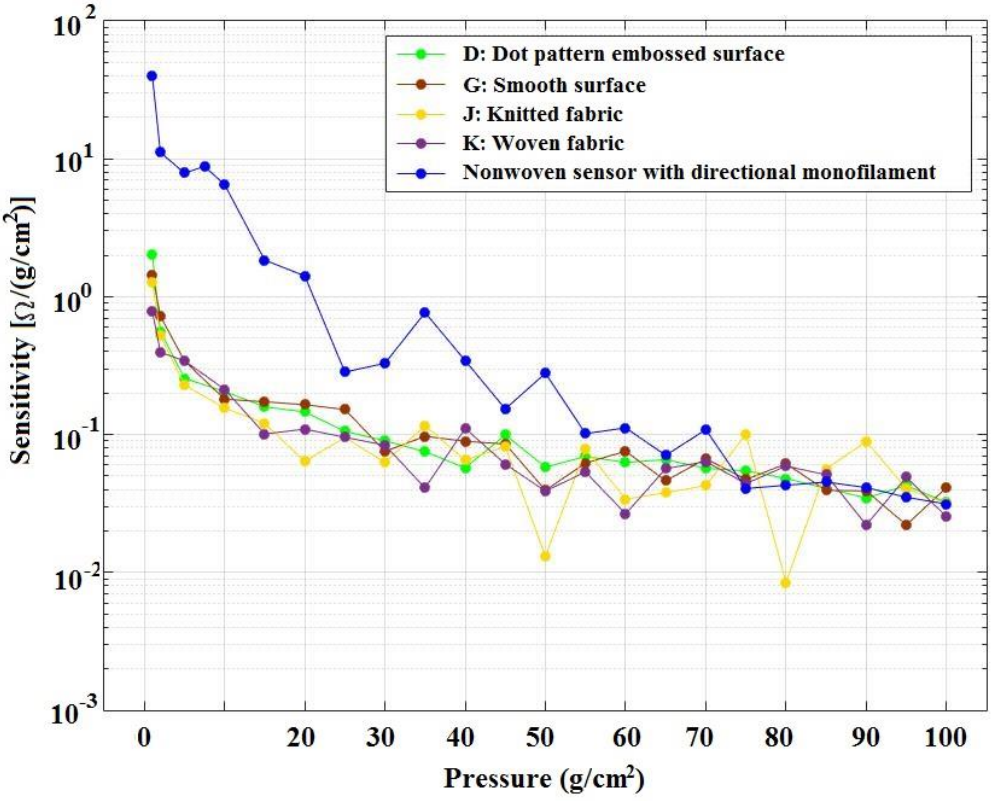

Figure 5-51. The sensitivity of the directional monofilament laid nonwoven sensor.

From **Figure 5-50** and **Figure 5-51**, it can be clearly concluded that the developed directional monofilament laid nonwoven sensor showed superior piezo-resistivity and sensitivity. Apparently, the thorough nanoscale silver coating along the filament surface and at the joint areas created a large amount of potential contacting points for this material. It can be concluded that the nonwoven structure has a high sensitivity from 7.5 g/cm^2 to 40 g/cm^2.

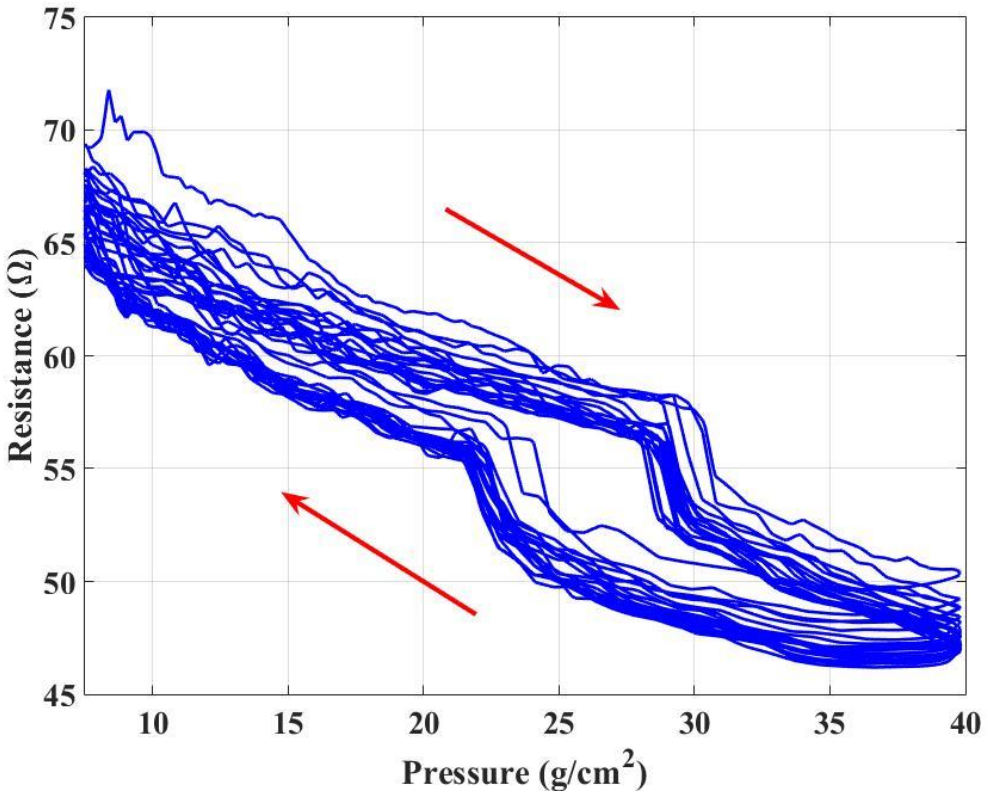

Figure 5-52. Resistance vs. pressure cyclic loading curve of 20 cycles on the HDPE nonwoven structure.

Cyclic loading tests were carried out within this region and the results are shown in **Figure 5-52**. It is clearly shown that the nonwoven structure produced quite repeatable results in 20 cycles. As expected, the resistance hysteresis percentage is higher than the materials tested in section 5.2.2.2. As listed in **Table 5-7**, the average resistance hysteresis loss percentage of the HDPE nonwoven structure reaches 5.70%. This is due to the fact that the heavy HDPE monofilaments have worse flexibility than the fine fibres/yarns used to create nonwoven, knitted or woven fabrics.

Table 5-7. The resistance hysteresis of the HDPE nonwoven structure

No. of cycle	Resistance hysteresis loss ($\Omega\cdot(g/cm^2)$)	Resistance loss percentage
1	115.89	6.03%
2	112.53	5.96%
3	108.11	5.69%
4	121.18	6.44%
5	111.34	5.97%
6	115.00	6.18%
7	105.50	5.71%
8	111.58	6.02%
9	109.22	5.91%
10	108.87	5.90%
11	108.73	5.89%
12	104.95	5.72%
13	102.10	5.57%
14	99.52	5.45%
15	98.08	5.39%
16	100.09	5.49%
17	96.35	5.30%
18	90.92	5.01%
19	96.07	5.28%
20	92.71	5.11%
Average	105.44	5.70%

There are repeatable sharp resistance changes at 30 g/cm^2 on loading and 23 g/cm^2 on unloading cycles, which also can be observed in the quasi-static test result. The slopes of the curve before and after this critical pressure point (30 g/cm^2 for loading and 23 g/cm^2 for unloading) are very similar, indicating the similar piezo-resistive sensitivity and structural change during these periods. The change of resistance over pressure increasing is believed to be caused by that:

(1) the silver agglomerates gathered at the joints or between filaments are getting compressed;
(2) new contact points are created between filament surfaces due to bending;
(3) new contact points are created between joints due to further bending.

As indicated in the structure design, the nonwoven structure was designed to place the joints in separate locations, so to avoid the contacting of the joints in neighbouring layers. Therefore, (3) requires a higher pressure level than (1) and (2); and the piezo-

resistive sensitivity of these 3 statuses should also increase accordingly. Thus, the sharp resistance change at 30 g/cm^2 and 23 g/cm^2 on the loading and unloading cycle can be explained as:

(i) when the pressure has not reached the critical pressure point, the piezo-resistivity changes because of (1) and (2);

(ii) however, during the short period of the pressure has reached the critical point, new contact points are formed between the crossing points as explained in (3);

(iii) after this point, the structure is further compressed, but lacking new contact points to be created; the piezo-resistive sensitivity at this stage changes mainly due to (1). This also explains the reason why the sensitivity after the critical pressure point is slightly lower than before the critical point.

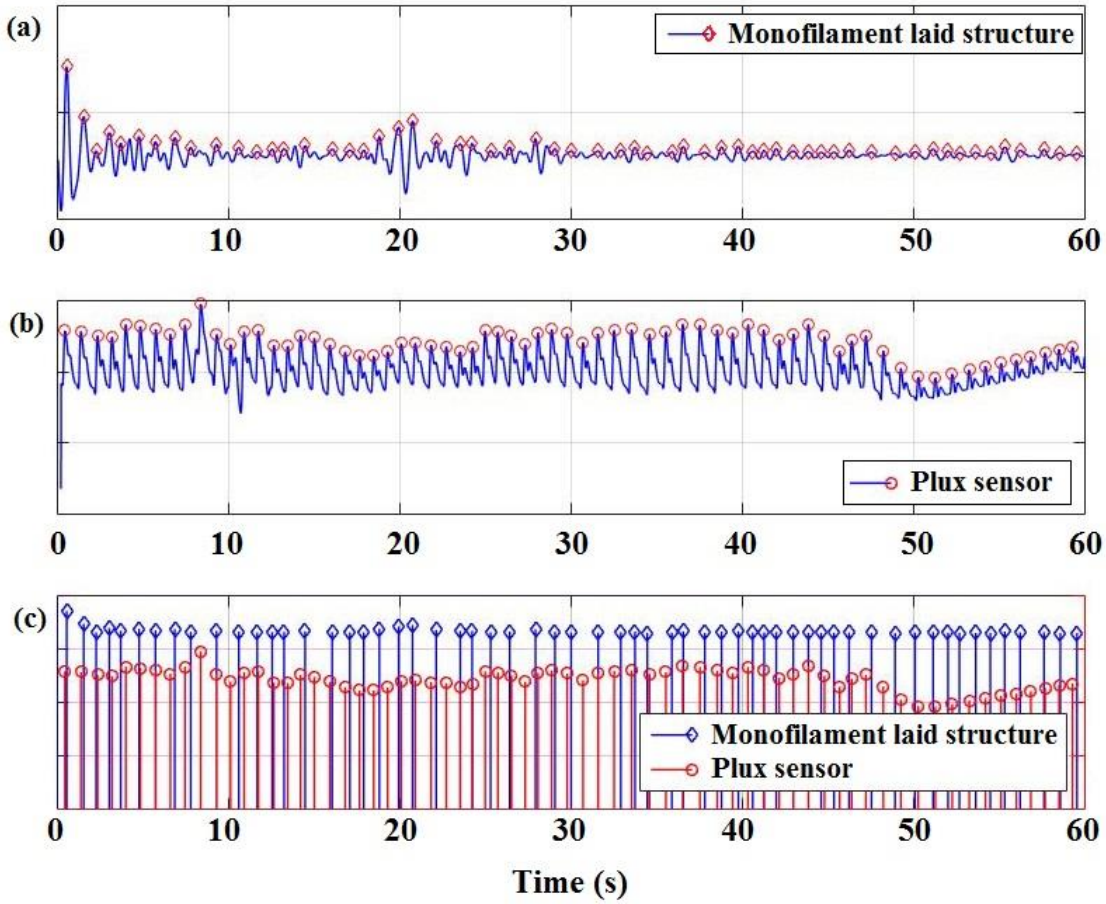

Figure 5-53. Cardiac signal captured by directional monofilament laid nonwovens sensor. (a) Monofilament laid structure; (b) Plux sensor; (c) peak location validation.

Figure 5-53 illustrates the performance of the directional monofilament laid nonwoven sensor in capturing cardiac signals, in which the peak location matching graph shows that the monofilament laid structure captured 59 out of 68 cardiac signals during the

period of 60 seconds. Though the results were encouraging, this was not expected. It is believed that the weak ballistic signal generated from heartbeats will damp within the heavy yarns or fabrics, which was validated by the results of knitted fabric based and woven fabric based sensors. Additionally, the high resistance hysteresis loss percentage would also cause the sensor lack of sensitivity to pick up the weak signals of heart. The thick HDPE (compared with the diameter of the fibres in nonwoven fabrics) should not be ideal to capture the cardiac signals. The success cardiac signal acquisition can only be explained as that the pressure applied on the chest during cardiorespiratory signal capturing test were 25 g/cm^2, which was within the 23-30 g/cm^2 region where the sensor has a superior sensitivity. Compared with the Plux BCG monitoring device, the nonwoven sensor with directional monofilament achieved an accuracy of 84.2% in acquiring the heart signal over a period of five minutes.

However, during testing, it was found that the nanoscale silver particles fell down from the structure. This is believed to be the result of incomplete sintering. In addition, the initial existing silver coating along or in between two monofilaments wore out upon testing. Eventually, the nonwoven sensor fabricated with directional monofilaments lost its electrical conductivity. And due to the randomly formed large silver depositions caused by the incomplete sintering, it was found difficult to produce another reliable sensor material. The bonding process is essential in the creation of such structure in order to obtain a uniform silver particle impregnation for later test procedures. A thermal bonding technology that can prevent the monofilament from shrinkage needs to be investigated. Also, finer monofilaments need to be sourced in order to improve the reliability of the sensor in cardiorespiratory monitoring application and the feasibility for weaker bio-signals. In addition, due to the fact that the monofilaments are quite apart from each other, compared with the fibre distance in nonwoven fabrics, the silver particles were found difficult to be uniformly coated on the monofilament. In order to obtain a more reliable sensor, it is necessary to improve the coating technology for uniform yet partial coating.

In order to further investigate the piezo-resistivity of such structure and due to the limited access to the solutions mentioned above, the nanoscale silver particle coated HDPE monofilaments were replaced by silver coated polyester yarns. The silver coated polyester yarns can be considered equal to a material that the extreme uniform silver

particle coating was achieved. The nonwoven sensor made from directional silver coated polyester yarns are shown in **Figure 5-54**.

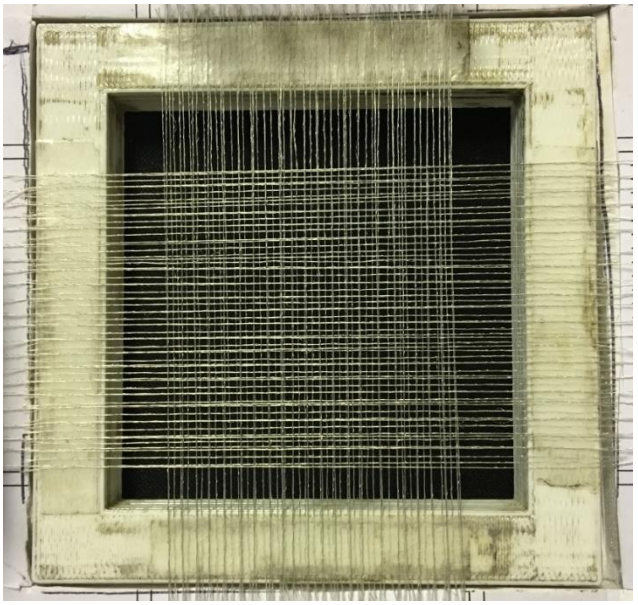

Figure 5-54. Photo of the nonwoven sensor fabricated with directional silver coated polyester yarns.

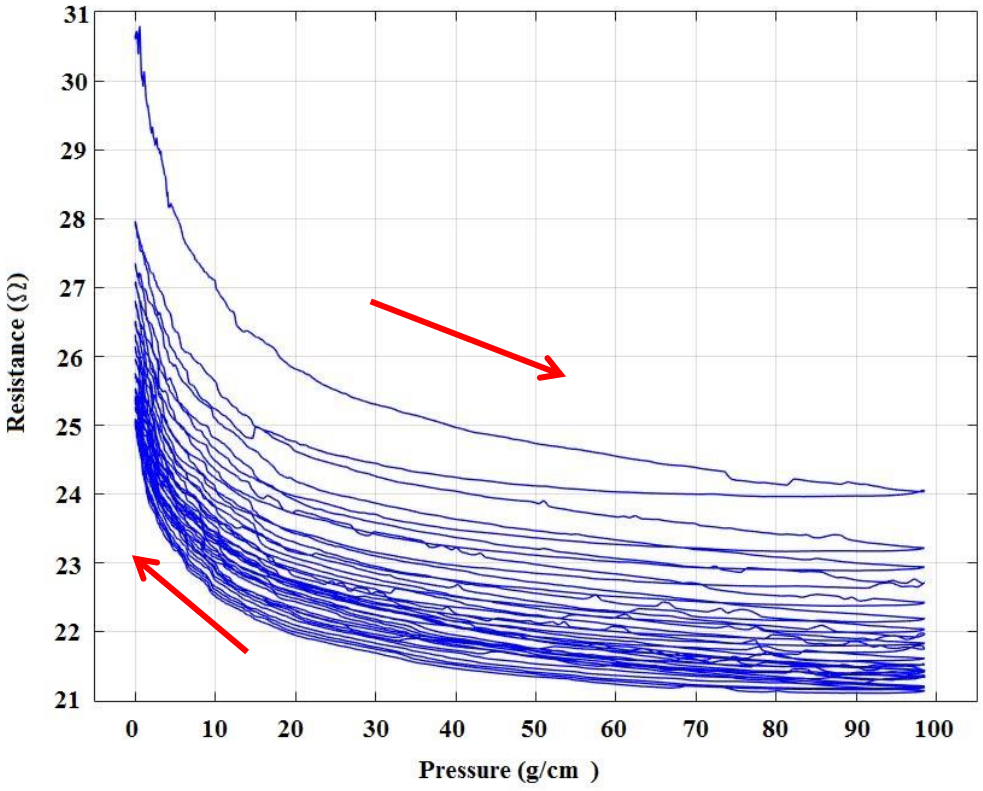

Figure 5-55. Compressive cyclic loading on the nonwoven structure made from silver coated polyester yarns.

Table 5-8. The resistance hysteresis of the silver coated yarn based nonwoven structure

No. of cycle	Resistance hysteresis loss ($\Omega \cdot (g/cm^2)$)	Resistance loss percentage
1	75.38	3.04%
2	48.37	2.03%
3	37.12	1.58%
4	36.13	1.56%
5	37.04	1.62%
6	32.71	1.44%
7	30.93	1.37%
8	32.04	1.43%
9	31.45	1.41%
10	28.74	1.30%
11	34.24	1.55%
12	28.56	1.30%
13	30.66	1.40%
14	20.95	0.96%
15	29.18	1.33%
16	31.54	1.44%
17	29.45	1.35%
18	29.53	1.36%
19	28.88	1.33%
20	28.61	1.32%
Average	34.08	1.51%

This nonwoven sensor showed good repeatability and resistance hysteresis in compressive cyclic loading tests (as shown in **Figure 5-55** and **Table 5-8**). The unbound structure and the elasticity and flexibility of the yarns provided the nonwoven structure with excellent recoverability for compression, resulting in a low average hysteresis loss percentage of 1.51%. However, the fibrous yarn structure prevented the detection of the weak bio-signals; the similar conclusions have been made for knitted fabric based and woven fabric based sensors; as expected, the nonwoven sensor failed to capture the cardiorespiratory signals. Therefore, the empirical modelling was based on static situations.

5.5.4 Empirical modelling

The relationship between the pressure level, the conductance of the nonwoven structure material, piezo-resistivity and the size of the compressive area was studied. According to Pouillet's Law, the electrical resistance (R) can be represented as:

$$R = \rho \times \frac{L}{A}$$ **Equation 5-9**

where: ρ is the resistivity of the material; L is the length of the material in the direction of current flow; A is the cross-section of the material. In the current research, L is the thickness of the nonwoven structure (t), while A represents the size of the sensor area. The dynamic thickness of the sensor can be calculated via:

$$t = t_0 - d$$ **Equation 5-10**

where: d is the deformation of the sensor during the compressive test. Therefore, the resistivity of the piezo-resistive sensor equals to:

$$\rho = R \times \frac{A}{t_0 - d}$$ **Equation 5-11**

Figure 5-56. A Messmer micrometer.

The thickness of the nonwoven structure was measured using a micrometre from Messmer, as shown in **Figure 5-56**. Five measurements were carried out in order to ensure the accuracy of the model. The piezo-resistivity of the nonwoven structure sensor was tested under quasi-static conditions with various sizes of the compressive area, 10 mm by 10 mm, 20 mm by 20 mm, 30 mm by 30 mm and 40 mm by 40 mm. Five tests were carried out for each size of the compressive area and calculated by averaging. The

empirical models for sensor conductance, sensitivity and resistivity and their verification are shown in **Figure 5-57** to **Figure 5-59**. The verification curves were generated from the experiments carried out on an independent test setup of sensor area of 35 mm by 35 mm. The Matlab programme used for creating the empirical model and data points for the models and their verification are provided in Appendix H and I.

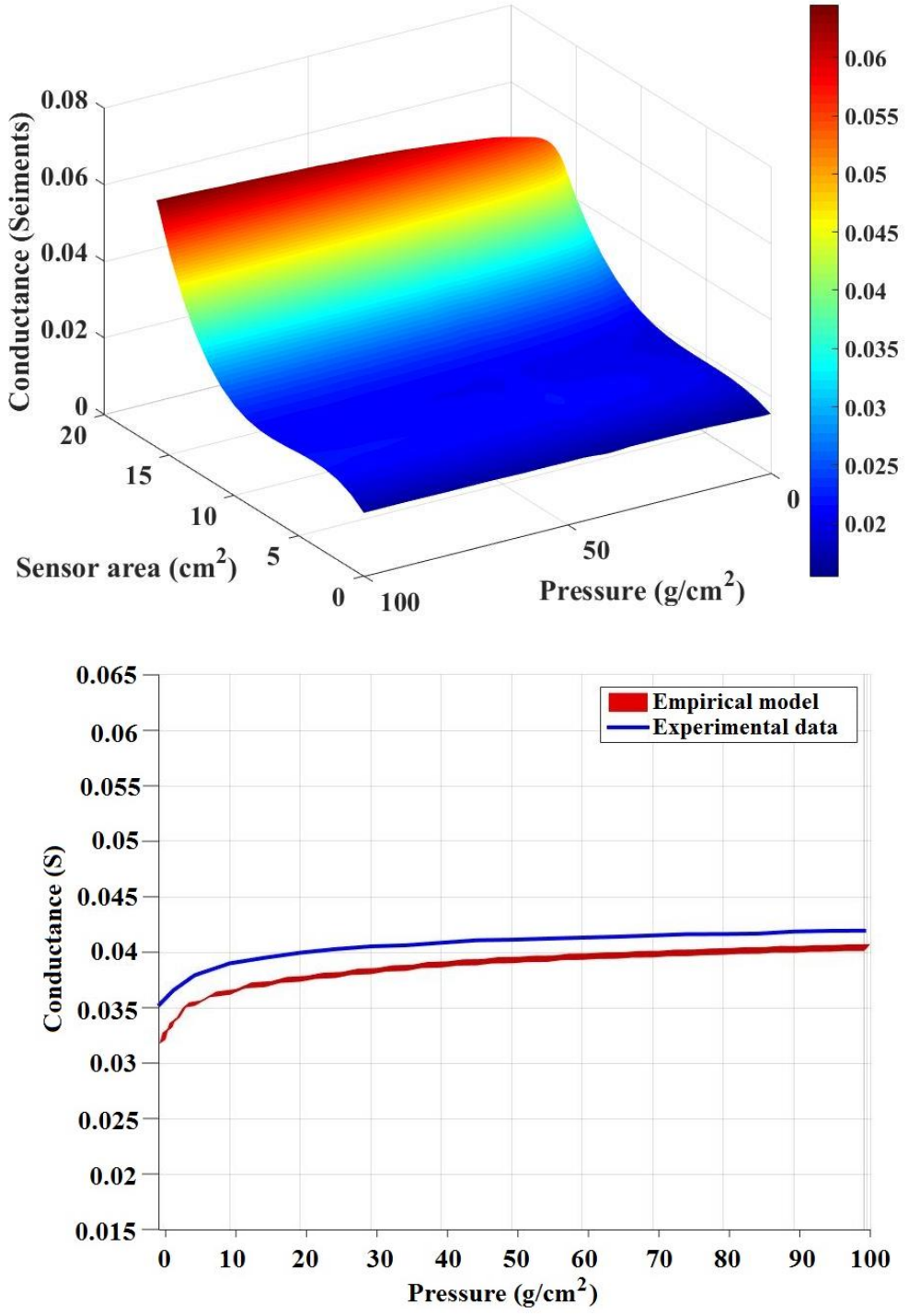

Figure 5-57. The empirical model and verification curve for sensor conductance against variable pressure and sensor area; verification sensor area: 12.25 cm^2.

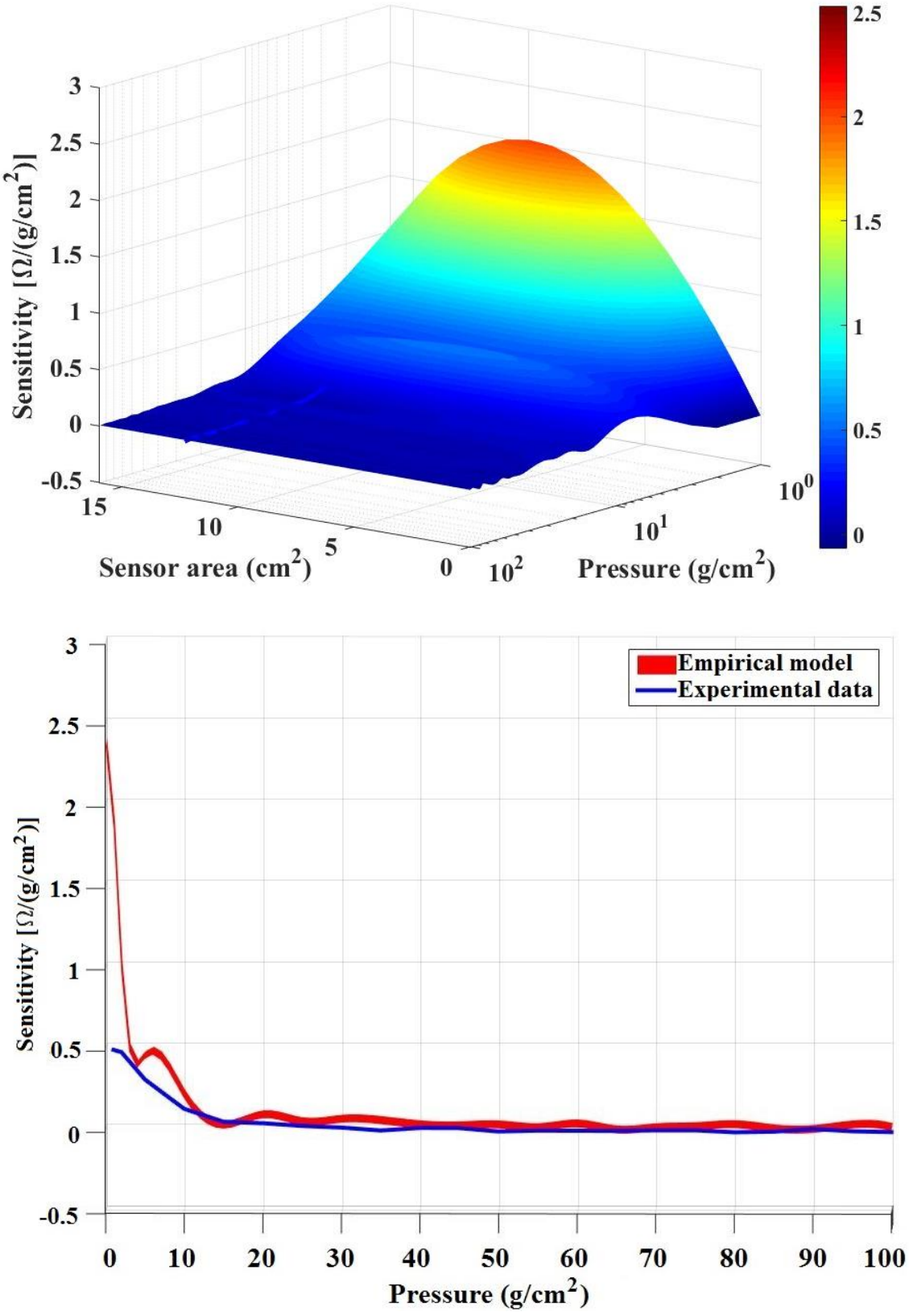

Figure 5-58. The empirical model and verification curve for sensor sensitivity against variable pressure and sensor area; verification sensor area: 12.25 cm^2.

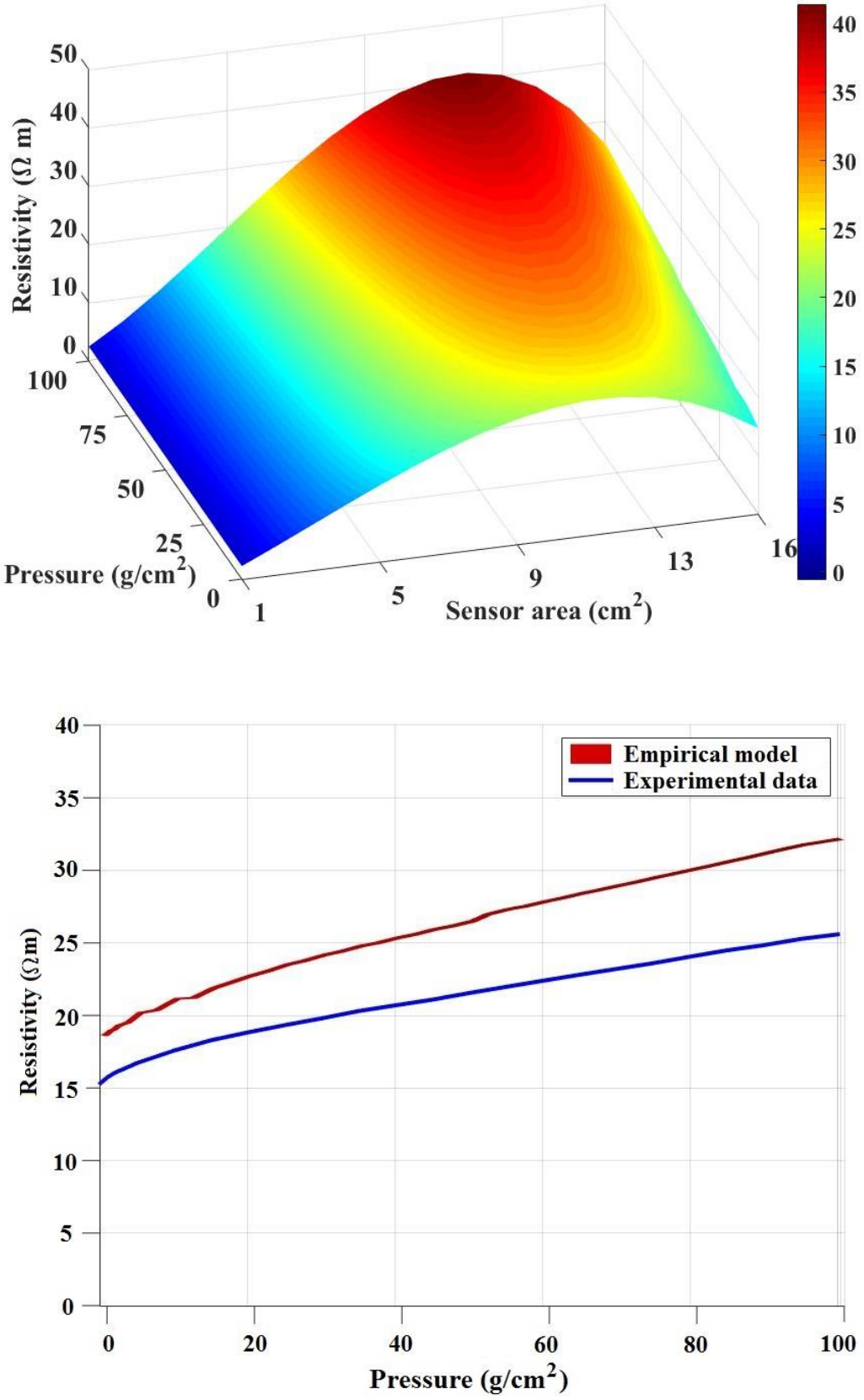

Figure 5-59. The empirical model and verification curve for sensor resistivity against variable pressure and sensor area; verification sensor area: 12.25 cm^2.

From the verification curve for sensor conductance (as shown in **Figure 5-57**), it can be seen that the trends between empirical data and experimental data are very similar to each other, with the minute shift between the values. The high conductance of the nonwoven structure sensor can be achieved by increasing the sensor area and high biasing pressure. However, maintaining high biasing pressure is not always feasible for long-term applications; therefore, increase the sensor area is a more feasible method for acquiring high sensor conductance.

However, in **Figure 5-58**, a large gap can be spotted between the empirical sensor sensitivity and its verification data at near-zero pressure. This is due to the fact the nonwoven structure was tested without any bonding. At near-zero pressure, the silver-coated yarns were free from any fixation. Any noises, vibrations or even wind may affect the results significantly. The verification shows more promising results after reaching 10 g/cm^2. However, the sensitivity becomes practically zero after the pressure exceeds 20 g/cm^2. This explains why the nonwoven structure created by silver-coated yarns failed in capturing the cardiac signals, in which a biasing pressure of 25 g/cm^2 was applied. However, if the biasing pressure is reduced to 10 g/cm^2 in order for the directional-yarn nonwoven sensor to work with a higher sensitivity, the variation of the sensor itself and interferences due to the motion artefacts from breathing are significantly increased to an unaccepted level. This concludes that the directional silver coated polyester yarn laid nonwoven structure was not the optimum sensor for capturing the cardiorespiratory signal under the current test setup. On the other hand, a non-monotonous relationship between the resistivity and sensor area has been found, as illustrated in **Figure 5-59**. The piezo-resistivity of the sensor achieved the maximum value at the sensor area of 8.5 cm^2, and gradually reduces with the change of the sensor area.

Table 5-9 lists the root-mean-square error (RMSE) and correlation coefficient results of the empirical models. The gaps between the empirical data and verifications and the large RMSE value for the resistivity model is due to the limited number of sensor areas tested. However, all the three empirical models show high correlation coefficients over 0.99 with the experimental results. Therefore, these models are still considered being useful to predict the performance of the piezo-resistive material.

Table 5-9. The RMSE and correlation coefficients of the empirical models for the sensor conductance, sensitivity and resistivity.

	RMSE	Correlation coefficient
Conductance (S)	0.00240	0.9941
Sensitivity (Ω g^{-1} cm^2)	0.06618	0.9926
Resistivity (Ωm)	5.90868	0.9987

With the help of these empirical models, the electrical properties of the nonwoven structure can be predicted. Suitable dimension and biasing pressure can be selected for the optimum sensor in order to fulfil various application demands.

5.6 Summary

In this chapter, the results of the experimental work carried out in this research were reported and discussed. In the preliminary tests, the effects of the adhesive webbing fabrics on the piezo-resistivity of the sensor was investigated and it was found that adhesive webbing fabric provided a significant improvement in stabilising the sensor, minimising the motion artefacts between sensor fabric layer and electrode layers, lowering minimum biasing pressure and reducing the overall electrical resistance of the sensor.

From electromechanical compressive strength tests, fabric based piezo-resistive sensors, fabricated from different types of nonwoven fabric, knitted fabric and woven fabric, have been studied in detail. It was found that the sensor material with a higher silver take-up percentage and with a multi-layer structure showed better piezo-resistivity in the quasi-static compressive strength tests. The higher silver take-up percentage provided a higher possibility of creating new electrical paths under compression, therefore resulting in a bigger change in resistance. Addition to the contact points between the fibre joints, the multi-layer structure gave the fabric the capability of establishing new contacts between layers. Among the nonwoven fabric based piezo-resistive sensors, the commercially available nonwoven fabric E performed the best in the aspect of quasi-static compressive strength testing.

In the dynamic cyclic loading tests, it was discovered that the piezo-resistive nonwoven sensors fabricated with sample D, E and G showed good repeatability after 20 cycles. The woven fabric based sensor (sample K) was found with a huge hysteresis loss on the first cycle due to its poor recoverability from compression. The reliability of the knitted fabric based sensor (sample J) reduced after 16 cycles. By calculating the resistance hysteresis loss and resistance hysteresis percentage, it can be concluded that the thermally bonded nonwoven fabric based sensors (sample D and G) had a smaller hysteresis effect than the spunlace nonwoven fabric based sensor (sample E).

RTD effect was observed especially in the woven structure based sensor. As lacking recoverability from compression, the RTD of the woven based sensor was much bigger than other samples.

In the aspect of cardiorespiratory signal capturing, sample D were found with the best performance. It successfully captured both the cardiac and respiratory signals and it even performed better than the commercially available monitoring device in capturing the respiratory signals from motion artefacts. Approaches such as using filtering and developing programme algorithms were carried out in order to improve the reliability and accuracy of the piezo-resistive nonwoven sensor. A Matlab programme used for identification of the peaks in the acquired signals was developed.

In the end, the development of a nonwoven structure with directional monofilaments/yarns was introduced. The nonwoven sensor laid with directional electroconductive monofilaments were found with unique piezo-resistivity, which had a high sensitivity within the pressure range from 23-30 g/cm^2. Based on this investigation, the empirical models on the sensor conductance and piezo-resistivity over variable sensor areas and pressure were calculated and verified by carrying out experiments. These models can be used to provide preliminary information to engineer the nonwoven based pressure and predict its sensor performance.

Chapter Six: Conclusions and future work

6.1 Conclusions

The aim of this research is to develop a new textile-based sensor suitable for weak bio-signal sensing applications. From the previous work, the necessary and urgency in need of developing a non-invasive, flexible and portable sensor, especially for the cardiorespiratory signal monitoring that can be used in daily, long-term and ambulatory condition has been proven. This research focused on the piezo-resistive materials. By impregnating nonwoven materials with electroconductive inks made of the nanoscale silver particle, the nonwoven fabric materials were granted with piezo-resistivity, while retaining the excellent textile properties, such as flexibility and recoverability from compression.

The nonwoven materials were impregnated with nanoscale silver particles by dip-coating technology and sandwiched by functional layers of electrodes and adhesive layers. The developed nanoscale silver particle ink impregnated nonwoven materials were studied under Scanning Electron Microscopy (SEM) and Energy-dispersive X-ray Spectroscopy (EDX) technology in order to understand the morphology of the silver deposition and evaluate the impregnation performance.

From the SEM analysis, four types of silver deposition morphology were found: deposition of the fibre surface; complete coverage over the pore; partial coverage over the pore; deposition along the pore. The conditions in order for these types of deposition to happen were believed to be related to the size of the silver particles, the size of the pore and the diameter of the fibre. Additionally, the thermal sintering process might interference the type of deposition as well.

The area density, thickness and the surface structure of the nonwoven materials have been found related to the impregnation performance. It was discovered that the impregnation results varied based on the area density of the nonwoven materials of the small thickness nonwoven fabrics. When the area density is too high, the fibres on the surface of the nonwoven fabric will be closer to each other, preventing the silver particles from entering the inner structure and resulting in ununiformed silver distribution. However, in the thick nonwoven materials, the nanoscale silver particles were more evenly distributed along the thickness direction than on the planar direction.

The nanoscale silver particles were more likely to be trapped by the fibre joints and the porous area within the fabric structure than on the surface.

It was also found that the thickness of the thermally bond nonwoven fabrics had a major impact on the ink impregnation performance. The thin nonwoven fabric functioned more like a flat, single layer structure. Upon compression, the change in resistance would mostly be acquired from the deformation of the whole structure. Whereas the thick nonwoven materials are multi-layer structures, which allowed the silver particles to be distributed between layers and potentially could create more contact points to show a better piezo-resistivity during compression. This finding was proved in this research that the piezo-resistive sensors fabricated from thick nonwovens performed better than thin nonwoven fabric based sensors.

The dot pattern embossed nonwoven fabrics were found with the combination of the advantages from both thick and thin nonwoven fabrics. The partially bonded surface structure provides the good compressive and piezo-resistivity like thick nonwoven materials, while the embossed area allows a more uniform impregnation performance. The nanoscale silver particle ink impregnated on the knitted and woven structures was found absorbed by yarns, instead of on the fabric/yarn surface.

From the electromechanical characterisation on the nanoscale silver particle ink impregnated nonwoven sensors, it was discovered that the usage of adhesive webbing in the construction of the nonwoven based piezo-resistive sensor was essential and critical. The adhesive webbing fabrics were found an effective method for the improvement on reducing the variation of the sensor under low biasing pressure. It can also be concluded that silver take-up percentage has an effect on the resistance of the sensor. Though the sensor sensitivity at low-pressure region can be improved by increasing the initial sensor resistance, the stability and reliability of the sensor are compromised. The nonwoven materials with a higher silver take-up percentage show better piezo-resistivity. By changing the silver take-up percentage to an appropriate level, the nanoscale silver ink impregnated nonwoven materials can be engineered to achieve high piezo-resistive sensitivity at desired work pressure with controlled variation.

It was also found that the nonwoven materials with a big thickness show better piezo-resistive property in the aspect of compressive testing. The nonwoven fabric based sensors were found requiring fewer cycles in order to provide a reliable signal reading,

comparing with knitted or woven fabric based sensors. The nonwoven materials and knitted fabrics with better compressibility and recoverability also showed a much smaller resistance hysteresis loss. The nonwoven fabric based sensors also suffered less from the resistance time drift than other types of textiles.

In the investigation of the feasibility of using the designed and engineered piezo-resistive material as a cardiorespiratory sensing material, it was found that the piezo-resistive nonwoven based sensors were capable of capturing the respiratory signals under normal and rapid breathing conditions. The dot pattern embossed nonwoven was discovered with the capability of detecting the breathing signals after a strong motion artefact, which was an improvement compared with the commercially available sensor device. As to the knitted fabric based and woven fabric based piezo-resistive sensors, it was found that the weak bio-signals damped in the yarn and fabric structure, resulting in inaccurate and unreliable cardiorespiratory graphs.

A data processing programme including noise filtering and peak justification was developed in order to improve the reliability and accuracy of the piezo-resistive nonwoven sensor. It was found that with the help of the designed programme, the acquired signals showed a much smoother curve, which contained less noise and fluctuations. The piezo-resistive nonwoven cardiorespiratory sensor made from the dot pattern embossed nonwoven materials achieved an accuracy of detecting the cardiorespiratory signal of 87.25% and 95.13% for respiratory and cardiac signals, respectively (averaging from the results from male and female subjects). The sensor also showed a variation less than 5% in the cardiorespiratory acquisition. The response and recovery time of the piezo-resistive sensor were also determined by experiments that the response time of the piezo-resistive nonwoven sensor is 12.65 seconds for heart signal capturing and 17.24 seconds for breathing signal. The piezo-resistive nonwoven sensor requires less recovery time for the cardiac, which is 10.37 seconds, while respiratory signal needs 25.83 seconds to be fully recovered from motion artefacts.

A nonwoven sensor was constructed by laying directional monofilaments/yarns at 0-degree and 90-degree angles in order to simulate the performance of the nonwoven fabric based piezo-resistive sensor. The constructed nonwoven sensor was designed in such a way that the crossing points (contact points between two neighbouring layers) were not stacked right on top of another so that a specific biasing pressure was required

for the crossing points to connect between layers. It was found that the connection of the crossing points between layers could increase the piezo-resistive sensitivity at that point sharply. The biasing pressure for the constructed nonwoven structure to trigger the sensitivity boost was found to be within the region of 23 g/cm^2 to 30 g/cm^2, which will increase the sensitivity from 0.3288 Ω/(g/cm^2) to 0.7665 Ω/(g/cm^2).

The conductance, piezo-resistive sensitivity and resistivity of the nonwoven sensor made with directional silver coat polyester yarns were empirically modelled in order to predict the performance of the nonwoven sensors. The empirical models provided important preliminary information on the conductance, sensitivity and resistivity of the nonwoven sensor varying from 0-100 g/cm^2 pressure and 1-16 cm^2 sensor area. The empirical models were verified by the experimental results tested under an independent sensor area of 12.25 cm^2. The models showed that in the aspect of conductance, a high conductance value can be achieved by increasing the biasing pressure or the sensor area. The sensor with an area size of 16 cm^2 showed high conductance trend over the complete pressure range.

The empirical model showed that the sensitivity of the sensor would drop sharply at near zero pressure. This was due to the fact that the constructed nonwoven sensor with directional silver coated yarns were free from any bonding, the piezo-resistive nonwoven sensor would be affected by any vibration or noise so easily, which caused the huge variation under that biasing pressure. By increasing the pressure, the nonwoven sensor worked with a more reliable sensitivity from 10 g/cm^2 to 20 g/cm^2. Beyond this point, the sensitivity dropped to practically zero. Thus, it can be deduced that improvements should be carried out in order to increase the sensitivity of the directional silver coated yarn based nonwoven sensor under a higher biasing pressure where there is less variation in the sensitivity. A non-monotonous relationship between the resistivity and sensor area has been found in the nonwoven sensor made with directional silver coated yarns. The highest resistivity appears at a sensor area of 8.5 cm^2, while either increasing or decreasing the sensor area will cause a reduction in the resistivity.

6.2 Recommendations for future work

- Silver was chosen as the electroconductive material in this research, due to its electrical property, high cost to performance ratio and availability. Other electroconductive materials such as copper, gold and graphene could be

investigated to study their performance in creating nonwoven fabric based sensors.

- In this research, the morphology of the nanoscale silver particles deposited on the fibres in a nonwoven fabric has been studied and was found to be related to the size of the silver particles, the size of the pore and the diameter of the fibre. Further research can be carried out in the direction of the quantitative relationship between the deposition morphology and these factors.
- The modified surface structure of the dot pattern embossed nonwoven fabrics resulted in good nanoscale silver particle ink impregnation performance. The effects of the modifications on the surface structure can be further studied, such as the type of embossing, depth of the embossing area, size of the embossing area, etc.
- Ways of improving the piezo-resistivity of the nonwoven fabric based pressure sensors have been studied, such as increasing the sensitivity by altering the silver take-up, applying appropriate biasing pressure, optimising sensor area and so on. Other factors may affect the piezo-resistivity of the nonwoven fabric materials as well. Further research can be carried out on the investigation of the effect of the fabric thickness, area density, flexibility and recoverability to compression on the piezo-resistivity of the nonwoven materials.
- The dip-coating method was used in this research in order to create piezo-resistive nonwoven materials. However, during experiments, it was found that the current dip-coating method has difficulties in controlling the exact amount of silver particles being coated. In the future, more work can be conducted in the direction of achieving precise and controllable silver take-up on nonwoven materials, based on dip-coating or other impregnation methods.
- Improvements in the accuracy and reliability of the nonwoven fabric based cardiorespiratory sensor are needed. Also, the direction of investigation can put on the development of reducing the response and recovery time of the nonwoven fabric based sensors.
- The current sensor was the prototype version of a flexible wearable cardiorespiratory sensing device. The integration method in order to apply this sensor to a garment needs to be developed. Also, whether or not this sensor requires shielding from motion artefact or noise requires further investigation.

- In order to simulate the performance of an electroconductive ink impregnated nonwoven material under the compressive situation, a nonwoven type structure was created by laying directional monofilaments/yarns at 0-degree and 90-degree angles without interlacing. The characteristics of such nonwoven structure have been studied; however, the performance of such type of nonwoven structure with monofilaments laid at other angle combinations remains unsurveyed. Also, the type of monofilaments or yarns can be researched in more details.
- The nonwoven structure created in this research was intentionally designed for thermal bonding in order to enhance its mechanical property. However, due to limited access to the thermal bonding technology that can prevent the HDPE from shrinkage, the nonwoven structure was investigated without bonding. The effect of the thermal bonding or any other bonding processes on the piezo-resistivity of such structure needs to be studied further.
- The silver particles coated on the HDPE eventually worn out or fell apart due to poor sintering performance from natural sintering method. Therefore, a new fabrication method suitable this HDPE made nonwoven structure needs to be developed, including altering the silver ink recipe, different bonding methods and low-temperature sinter process and so on.
- Empirical models of the conductance, resistivity and sensitivity were developed. Other types of modelling such as theoretical modelling, mathematical modelling, finite element modelling can be developed in order to characterise the function of such structure further.
- The cardiorespiratory signal was selected as the weak bio-signal to validate the function of the sensor. The sensor parameters were designed for capturing weak bio-signals. However, the feasible methods based on textile materials for acquiring other weak bio-signals need to be studied.

References

[1] Shanahan K. Logan County deputy suffers heart attack while driving on patrol. *KFOR.com*, 22 October 2016.

[2] Cabrero A, Cardenas X. Paramedic commuting to work aids man who suffered heart attack while driving. *KSL*, 19 January 2017.

[3] Key facts & figures | Expert advice from HEART UK https://heartuk.org.uk/press/press-kit/key-facts-figures (accessed 19 August 2017).

[4] Heart Disease Statistics https://www.cardiosmart.org/Heart-Basics/CVD-Stats (accessed 19 August 2017).

[5] Benjamin EJ, Blaha MJ, Chiuve SE, et al. Heart Disease and Stroke Statistics—2017 Update: A Report From the American Heart Association. *Circulation* 2017; 135: e146–e603.

[6] Mozaffarian D, Benjamin EJ, Go AS, et al. Heart Disease and Stroke Statistics—2015 Update. *Circulation* 2015; 131: e29–e322.

[7] Grossman P. The LifeShirt: a multi-function ambulatory system monitoring health, disease, and medical intervention in the real world. *Stud Health Technol Inform* 2004; 108: 133–141.

[8] Teichmann D, Kuhn A, Leonhardt S, et al. The MAIN Shirt: a textile-integrated magnetic induction sensor array. *Sensors (Basel)* 2014; 14: 1039–1056.

[9] Yoo WJ, Jang KW, Seo JK, et al. Development of respiration sensors using plastic optical fiber for respiratory monitoring inside MRI system. *J Opt Soc Korea* 2010; 14: 235–239.

[10] Grlica J, Martinovic T, Dzapo H. Capacitive sensor for respiration monitoring. *SAS 2015 - 2015 IEEE Sensors Appl Symp Proc*. Epub ahead of print 2015. DOI: 10.1109/SAS.2015.7133567.

[11] Kundu SK, Kumagai S, Sasaki M, et al. A Wearable Capacitive Sensor for Monitoring Human Respiratory Rate. *Jpn J Appl Phys* 2013; 52: 04CL05.

[12] Nihtianov SN, Meijer GCM. Application challenges of capacitive sensors with floating targets. *IEEE AFRICON Conf* 2011; 13–15.

[13] WHO. Cardiovascular diseases (CVDs). *WHO* http://www.who.int/mediacentre/factsheets/fs317/en/ (2017, accessed 22 August 2017).

[14] Kaniusas E. *Biomedical Signals and Sensors I Linking Physiological Phenomena and Biosignals*. 2012.

[15] Rangayyan RM. Introduction to Biomedical Signals. In: *Biomedical Signal Analysis*. Hoboken, NJ, USA: John Wiley & Sons, Inc., 2015, pp. 1–69.

[16] Causevic E, Morley RE, Wickerhauser MV, et al. Fast wavelet estimation of weak biosignals. *IEEE Trans Biomed Eng* 2005; 52: 1021–1032.

[17] Ji N, Jiang Y, Yang Z, et al. An active electrode design for weak biosignal measurements. *Int Conf Signal Process Proceedings, ICSP* 2017; 502–507.

[18] Jovic A, Bogunovic N. Classification of biological signals based on nonlinear features. *Melecon 2010 - 2010 15th IEEE Mediterr Electrotech Conf* 2010; 1340–1345.

[19] Muhuthuswamy J. Biomedical Signal Analysis. *Stand Handb Biomed Eng Des* 2004; 18.1-30.

[20] Adochiei NL, David V. QRS time detection using Wavelet Multiresolution Analysis for determining HRV in case of ECG signals with high level noise. *EPE 2012 - Proc 2012 Int Conf Expo Electr Power Eng* 2012; 614–619.

[21] Schofield JRAE. *Electrocardiogram Signal Quality Comparison Between a Dry Electrode and a Standard Wet elctrod over a Period of Extended Wear*. Cleveland State University, 2012.

[22] Rattfält L. *Smartware electrodes for ECG measurements -Design , evaluation and signal processing*. Linköping University, 2013.

[23] Al-Naji A, Gibson K, Lee S-H, et al. Monitoring of Cardiorespiratory Signal: Principles of Remote Measurements and Review of Methods. *IEEE Access* 2017;

PP: 1–1.

[24] O'Connor FG, Kugler JP, Oriscello RG. Sudden death in young athletes: Screening for the needle in a haystack. *Am Acad Fam Physicians* 1998; 57: 2763–2770.

[25] Choi S, Jiang Z. A novel wearable sensor device with conductive fabric and PVDF film for monitoring cardiorespiratory signals. *Sensors Actuators, A Phys* 2006; 128: 317–326.

[26] Bäckman Claes, Kullander Mats. Sweden: EWCO comparative analytical report on Work-related Stress http://www.eurofound.europa.eu/observatories/eurwork/comparative-information/national-contributions/sweden/sweden-ewco-comparative-analytical-report-on-work-related-stress (2010, accessed 26 January 2017).

[27] Avina-Zubieta JA, Thomas J, Sadatsafavi M, et al. Risk of incident cardiovascular events in patients with rheumatoid arthritis: a meta-analysis of observational studies. *Ann Rheum Dis* 2012; 71: 1524–1529.

[28] Metsios GS, Koutedakis Y, Veldhuijzen van Zanten JJCS, et al. Cardiorespiratory fitness levels and their association with cardiovascular profile in patients with rheumatoid arthritis: a cross-sectional study. *Rheumatology* 2015; kev035.

[29] Kokkinos P, Faselis C, Narayan P, et al. Cardiorespiratory Fitness and Incidence of Type 2 Diabetes in United States Veterans on Statin Therapy. *Am J Med* 2017; 1–7.

[30] Ruggero CJ, Petrie T, Sheinbein S, et al. Cardiorespiratory fitness may help in protecting against depression among middle school adolescents. *J Adolesc Heal* 2015; 57: 60–65.

[31] Choi J, Gutierrez-Osuna R. Estimating mental stress using a wearable cardio-respiratory sensor. *Proc IEEE Sensors* 2010; 150–154.

[32] Witt J, Narbonneau F, Schukar M, et al. Medical textiles with embedded fiber optic sensors for monitoring of respiratory movement. *IEEE Sens J* 2012; 12:

246–254.

[33] D'Angelo LT, Weber S, Honda Y, et al. A system for respiratory motion detection using optical fibers embedded into textiles. *Conf Proc IEEE Eng Med Biol Soc* 2008; 2008: 3694–3697.

[34] Pinheiro E, Postolache O, Girão P. Theory and Developments in an Unobtrusive Cardiovascular System Representation: Ballistocardiography. *Open Biomed Eng J* 2010; 4: 201–216.

[35] Gordon JW. Certain Molar Movements of the Human Body produced by the Circulation of the Blood. *J Anat Physiol* 1877; 11: 533–536.

[36] Henderson Y. The mass-movements of the circulation as shown by a recoil curve. *Am J Physiol -- Leg Content* 1905; 14: 287 LP-298.

[37] Hísek K, Niebauer J. *Cardiology Explained*. London: Remedica, 2004.

[38] Walraven G. *Basic arrhythmias*. 8th ed. Pearson, 2016.

[39] Casanella R, Gomez-Clapers J, Pallas-Areny R. On Time Interval Measurements Using BCG. In: *34th Annual International Conference of the IEEE EMBS*. San Diego, 2012, pp. 5034–5037.

[40] Tavakolian K, Zadeh FM, Chuo Y, et al. Development of a novel contactless mechanocardiograph device. *Int J Telemed Appl*; 2008. Epub ahead of print 2008. DOI: 10.1155/2008/436870.

[41] Scott. How To Read An EKG (electrocardiograph) http://www.todayifoundout.com/index.php/2011/10/how-to-read-an-ekg-electrocardiograph/ (2011, accessed 7 December 2017).

[42] Wang F, Tanaka M, Chonan S. Development of a PVDF piezopolymer sensor for unconstrained in-sleep cardiorespiratory monitoring. *J Intell Mater Syst Struct* 2003; 14: 185–190.

[43] Stoppa M, Chiolerio A. Wearable electronics and smart textiles: A critical review. *Sensors (Switzerland)* 2014; 14: 11957–11992.

[44] Loriga G, Taccini N, De Rossi D, et al. Textile sensing interfaces for

cardiopulmonary signs monitoring. *Conf Proc IEEE Eng Med Biol Soc* 2005; 7: 7349–52.

[45] Linz T, Kallmayer C, Aschenbrenner R, et al. Embroidering electrical interconnects with conductive yarn for the integration of flexible electronic modules into fabric. *Proc - Int Symp Wearable Comput ISWC* 2005; 2005: 86–89.

[46] Son J-H, Lee DH, Cho Y-J, et al. *Very Thin Spin-Coated Silver Films via Transparent Silver Ink for Surface Plasmon Resonance Sensor Applications*. 2012. Epub ahead of print 1 July 2012. DOI: 10.1166/jnn.2012.6352.

[47] Ramachandran T, Vigneswaran C. Design and Development of Copper Core Conductive Fabrics for Smart Textiles. *J Ind Text* 2009; 39: 81–93.

[48] Lou C-W. Process of complex core spun yarn containing a metal wire. *Text Res J* 2005; 75: 466–473.

[49] Su C, Chern J-T. Effect of Stainless Steel-Containing Fabrics on Electromagnetic Shielding Effectiveness. *Text Res J* 2004; 74: 51–54.

[50] Lin JH, Lou CW. Electrical Properties of Laminates Made from a New Fabric with PP/Stainless Steel Commingled Yarn. *Text Re* 2003; 73: 322–326.

[51] Zhang W, Tan YY, Wu C, et al. Self-assembly of single walled carbon nanotubes onto cotton to make conductive yarn. *Particuology* 2012; 10: 517–521.

[52] Kim B, Koncar V, Dufour C. Polyaniline-coated PET conductive yarns: Study of electrical, mechanical, and electro-mechanical properties. *J Appl Polym Sci* 2006; 101: 1252–1256.

[53] Chen HC, Lin JH, Lee KC. Electromagnetic Shielding Effectiveness of Copper/Stainless Steel/Polyamide Fiber Co-Woven-Knitted Fabric Reinforced Polypropylene Composites. *J Reinf Plast Compos* 2008; 27: 187–204.

[54] Cheng KB, Ueng TH, Dixon G. Electrostatic Discharge Properties of Stainless Steel/Polyester Woven Fabrics. *Text Res J* 2001; 71: 732–738.

[55] Perumalraj R, Dasaradhan B, Nalankilli G. Copper, stainless steel, glass core yarn, and ply yarn woven fabric composite materials properties. *J Reinf Plast*

Compos 2010; 29: 3074–3082.

[56] Lin J-H, Chen A-P, Hsieh C-T, et al. Physical properties of the functional bamboo charcoal/stainless steel core-sheath yarns and knitted fabrics. *Text Res J* 2011; 81: 567–573.

[57] Cheng KB. Production and Electromagnetic Shielding Effectiveness of the Knitted Stainless Steel/Polyester Fabrics. *J Text Eng Text Mach Soc Japan* 2000; 46: 42–52.

[58] Li L, Au WM, Wan KM, et al. A Resistive Network Model for Conductive Knitting Stitches. *Text Res J* 2010; 80: 935–947.

[59] Ma P, Hu H, Zhu L, et al. Tensile behaviors of co-woven-knitted fabric reinforced composites under various strain rates. *J Compos Mater* 2011; 45: 2495–2506.

[60] Xu Y, Yuan X, Wang N, et al. Comparison of bending properties Co-woven-knitted and Multi-layered biaxial Weft-knitted fabric reinforced composites. *Fibers Polym* 2014; 15: 1288–1294.

[61] Odhiambo SA, De Mey G, Hertleer C, et al. Discharge characteristics of poly(3,4-ethylene dioxythiophene): poly(styrenesulfonate) (PEDOT:PSS) textile batteries; comparison of silver coated yarn electrode devices and pure stainless steel filament yarn electrode devices. *Text Res J* 2014; 84: 347–354.

[62] Roh J, Mann Y, Freed A, et al. Robust and Reliable Fabric and Piezoresistive Multitouch Sensing Surfaces for Musical Controllers. *Proc Int Conf New Interfaces Music Expr* 2011; 393–398.

[63] Luo N, Dai W, Li C, et al. Flexible Piezoresistive Sensor Patch Enabling Ultralow Power Cuffless Blood Pressure Measurement. *Adv Funct Mater* 2016; 26: 1178–1187.

[64] Dai H, Thostenson E, Schumacher T. Processing and Characterization of a Novel Distributed Strain Sensor Using Carbon Nanotube-Based Nonwoven Composites. *Sensors* 2015; 15: 17728–17747.

[65] Dai H, Schumacher T, Thostenson E. Carbon nanotube-based sensing composites

for structural health monitoring of civil infrastructure using non-woven fabrics. In: *Safety, Reliability, Risk and Life-Cycle Performance of Structures and Infrastructures*. CRC Press, 2014, pp. 299–303.

[66] Sadiku M. *Elements of Electromagnetics*. 6th ed. Oxford University Press, 2014.

[67] Bakhoum EG, Cheng MHM. High-sensitivity inductive pressure sensor. *IEEE Trans Instrum Meas* 2011; 60: 2960–2966.

[68] Pedersen M, Ozgur M, Huff MA. *Micro-mechanical capacitive inductive sensor for wireless detection of relative or absolute pressure*. 7017419, United States, 2006.

[69] Cos D de, García-Arribas A, Barandiarán JM. Simplified electronic interfaces for sensors based on inductance changes. *Sensors Actuators, A Phys* 2004; 112: 302–307.

[70] Teichmann D, Foussier J, Buscher M, et al. Textile integration of a magnetic induction sensor for monitoring of cardiorespiratory activity. *IFMBE Proc* 2013; 39 IFMBE: 1350–1353.

[71] Brüllmann G, Fritsch K, Thurnheer R, et al. Respiratory monitoring by inductive plethysmography in unrestrained subjects using position sensor-adjusted calibration. *Respiration* 2009; 79: 112–120.

[72] Fishbein KW, McConville P, Spencer RGS. The lever-coil: A simple, inexpensive sensor for respiratory and cardiac motion in MRI experiments. *Magn Reson Imaging* 2001; 19: 881–889.

[73] Teichmann D, De Matteis D, Bartelt T, et al. A bendable and wearable cardiorespiratory monitoring device fusing two noncontact sensor principles. *IEEE J Biomed Heal Informatics* 2015; 19: 784–793.

[74] Zhang Z, Zheng J, Wu H, et al. Development of a respiratory inductive plethysmography module supporting multiple sensors for wearable systems. *Sensors (Switzerland)* 2012; 12: 13167–13184.

[75] Shah R, Agrawal Y. Introduction to fiber optics: Sensors for biomedical applications. *Indian J Pharm Sci* 2011; 73: 17.

[76] Serway R, Faughn J, Vuille C. *College Physics*. 8th ed. Brooks Cole Pub, 2009.

[77] Zanoon N. The Phenomenon of Total Internal Reflection and Acceleration of Light in Fiber Optics. *Int J Comput Appl* 2014; 107: 19–24.

[78] Liu L, Woolf A, Rodriguez AW, et al. Absolute position total internal reflection microscopy with an optical tweezer. *Proc Natl Acad Sci* 2014; 111: E5609–E5615.

[79] Optical Fiber http://www.thefoa.org/tech/ref/basic/fiber.html (accessed 15 August 2017).

[80] MacFadyen AJ, Jennings BR. Fibre-optic systems for dynamic light scattering — a review. *Opt & Laser Technol* 1990; 22: 175–187.

[81] Peiner E, Scholz D, Fricke K, et al. Microelectromechanical vibration sensor with optical interconnects. *J Microelectromechanical Syst* 1998; 7: 56–60.

[82] Rothmaier M, Clemens F. Textile pressure sensor made of flexible plastic optical fibers. *EMPA Act* 2008; 55.

[83] Gagnadre C, Billon M, Thuillier S. Fibre optic sensor for physiological parameters. *Electron Lett* 1998; 34: 1991–1993.

[84] Maletras F, Augousti AT, Mason J. Construction and calibration of a new design of Fiber Optic Respiratory Plethysmograph (FORP). In: *Optomechanical Design and Engineering 2001*. 2001, pp. 285–293.

[85] Dziuda L, Lewandowski J, Skibniewski F, et al. Fibre-optic sensor for respiration and heart rate monitoring in the mri environment. *Procedia Eng* 2012; 47: 1291–1294.

[86] Suaste-Gómez E, Hernández-Rivera D, Sánchez-Sánchez AS, et al. Electrically insulated sensing of respiratory rate and heartbeat using optical fibers. *Sensors (Basel)* 2014; 14: 21523–21534.

[87] Grattan KT V, Sun T. Fiber optic sensor technology: An overview. *Sensors Actuators, A Phys* 2000; 82: 40–61.

[88] Gao S, Arcos V, Nathan A. Piezoelectric vs. Capacitive Based Force Sensing in

Capacitive Touch Panels. *IEEE Access* 2016; 4: 3769–3774.

[89] Palasagaram JN, Ramadoss R. MEMS-capacitive pressure sensor fabricated using printed-circuit-processing techniques. *IEEE Sens J* 2006; 6: 1374–1375.

[90] Radosavljević GJ, Živanov LD, Smetana W, et al. A wireless embedded resonant pressure sensor fabricated in the standard LTCC technology. *IEEE Sens J* 2009; 9: 1956–1962.

[91] Merritt CR, Nagle HT, Grant E. Textile-based capacitive sensors for respiration monitoring. *IEEE Sens J* 2009; 9: 71–78.

[92] Chavan A V, Member S, Wise KD. Batch-Processed Vacuum-Sealed Capacitive Pressure. 2001; 10: 580–588.

[93] Zhou M-X, Huang Q-A, Zhou W. A novel capacitive pressure sensor based on sandwich structures. *J Microelectromech Syst* 2005; 14: 1272–1282.

[94] Chang W-Y, Chen C-C, Chang C-C, et al. An Enhanced Sensing Application Based on a Flexible Projected Capacitive-Sensing Mattress. *Sensors* 2014; 14: 6922–6937.

[95] Zheng E, Chen B, Wei K, et al. Lower Limb Wearable Capacitive Sensing and Its Applications to Recognizing Human Gaits. *Sensors* 2013; 13: 13334–13355.

[96] Mohammadi-Koushki N, Memarzadeh-Tehran H, Goliaei S. A Wearable Device for Continuous Cardiorespiratory System Monitoring. *Proc - Conf Local Comput Networks, LCN* 2017; 230–235.

[97] González-Sánchez C, Fraile J-C, Pérez-Turiel J, et al. Capacitive Sensing for Non-Invasive Breathing and Heart Monitoring in Non-Restrained, Non-Sedated Laboratory Mice. *Sensors* 2016; 16: 1052.

[98] Fraden J. *Handbook of Modern Sensors*. New York, NY: Springer New York, 2010. Epub ahead of print 2010. DOI: 10.1007/978-1-4419-6466-3.

[99] Paajanen M, Lekkala J, Kirjavainen K. ElectroMechanical Film (EMFi) - a new multipurpose electret material. *Sensors Actuators, A Phys* 2000; 84: 95–102.

[100] Jiménez A, Hernández Á, Ureña J, et al. EMFi-based ultrasonic transducer for

robotics applications. *Sensors Actuators, A Phys* 2008; 148: 342–349.

[101] Choi S, Jiang Z. A wearable cardiorespiratory sensor system for analyzing the sleep condition. *Expert Syst Appl* 2008; 35: 317–329.

[102] Rajala S, Lekkala J. Film-type sensor materials PVDF and EMFi in measurement of cardiorespiratory signals a review. *IEEE Sens J* 2012; 12: 439–446.

[103] Jiang Y, Hamada H, Shiono S, et al. A PVDF-based flexible cardiorespiratory sensor with independently optimized sensitivity to heartbeat and respiration. *Procedia Eng* 2010; 5: 1466–1469.

[104] Chen R, Liu W, Ruan X, et al. A Wearable Pressure Sensor Based on the Array of Polymeric Piezoelectric Fiber with Metal Core. In: Kubota N, Kiguchi K, Liu H, et al. (eds) *9th International Conference, ICIRA*. Tokyo, 2016, pp. 118–124.

[105] Lei K-F, Hsieh Y-Z, Chiu Y-Y, et al. The Structure Design of Piezoelectric Poly(vinylidene Fluoride) (PVDF) Polymer-Based Sensor Patch for the Respiration Monitoring under Dynamic Walking Conditions. *Sensors* 2015; 15: 18801–18812.

[106] Senturia SD (ed). A Piezoresistive Pressure Sensor. In: *Microsystem Design*. Boston, MA: Springer US, 2001, pp. 469–495.

[107] Huang Y, Liu P, Zhang Y, et al. Piezoresistive characteristic of conductive rubber for flexible tactile sensor. *J Wuhan Univ Technol Mater Sci Ed* 2011; 26: 443–448.

[108] Zhang X, Zhao Y, Zhang X. Design and fabrication of a thin and soft tactile force sensor array based on conductive rubber. *Sens Rev* 2012; 32: 273–279.

[109] Wettels N, Santos VJ, Johansson RS, et al. Biomimetic Tactile Sensor Array. *Adv Robot* 2008; 22: 829–849.

[110] Kim K, Lee KR, Kim WH, et al. Polymer-based flexible tactile sensor up to 32x32 arrays integrated with interconnection terminals. *Sensors Actuators, A Phys* 2009; 156: 284–291.

[111] Ohmukai M, Kami Y, Matsuura R. Electrode for Force Sensor of Conductive

Rubber. *J Sens Technol* 2012; 2: 127–131.

[112] Li S, Zhuang X, Xu F, et al. Structure Improvement and Simulation Research of a Three-dimensional Force Flexible Tactile Sensor Based on Conductive Rubber. *Sensors Transducers J* 2011; 132: 47–56.

[113] Shimojo M, Namiki A, Ishikawa M, et al. A tactile sensor sheet using pressure conductive rubber with electrical-wires stitched method. *IEEE Sens J* 2004; 4: 589–596.

[114] Manunza I, Bonfiglio A. Pressure sensing using a completely flexible organic transistor. *Biosens Bioelectron* 2007; 22: 2775–2779.

[115] Heise D, Skubic M. Monitoring pulse and respiration with a non-invasive hydraulic bed sensor. In: *2010 Annual International Conference of the IEEE Engineering in Medicine and Biology Society, EMBC'10*. 2010, pp. 2119–2123.

[116] Zhang Z, Yang GZ. Monitoring cardio-respiratory and posture movements during sleep: What can be achieved by a single motion sensor. *2015 IEEE 12th Int Conf Wearable Implant Body Sens Networks, BSN 2015*. Epub ahead of print 2015. DOI: 10.1109/BSN.2015.7299409.

[117] Taccini N, Loriga G, Pacelli M, et al. Wearable monitoring system for chronic cardio-respiratory diseases. *Conf Proc . Annu Int Conf IEEE Eng Med Biol Soc IEEE Eng Med Biol Soc Annu Conf* 2008; 2008: 3690–3.

[118] Di Rienzo M, Rizzo F, Meriggi P, et al. Applications of a Textile-Based Wearable System in clinics, exercise and under gravitational stress. *Proc 3rd IEEE-EMBS Int Summer Sch Symp Med Devices Biosensors, ISSS-MDBS 2006* 2006; 8–10.

[119] Di Rienzo M, Rizzo F, Meriggi P, et al. Applications of a textile-based wearable system for vital signs monitoring. *Annu Int Conf IEEE Eng Med Biol - Proc* 2006; 2223–2226.

[120] Taylor GL, Chapin WL. *Flexible piezocapacitive and piezoresistive force and pressure sensors*. Google Patents, 2014.

[121] Melnykowycz M, Tschudin M, Clemens F. Piezoresistive Soft Condensed Matter

Sensor for Body-Mounted Vital Function Applications. *Sensors* 2016; 16: 326.

[122] Hamdani S, Fernando A. The Application of a Piezo-Resistive Cardiorespiratory Sensor System in an Automobile Safety Belt. *Sensors* 2015; 15: 7742–7753.

[123] Huang CT, Shen CL, Tang CF, et al. A wearable yarn-based piezo-resistive sensor. *Sensors Actuators, A Phys* 2008; 141: 396–403.

[124] Correia V, Caparros C, Casellas C, et al. Development of inkjet printed strain sensors. *Smart Mater Struct* 2013; 22: 105028.

[125] Rausch J. Printed piezoresistive strain sensors for monitoring of light-weight structures. *Sens Proc* 2011; 216–221.

[126] Cruz S, Dias D, Viana JC, et al. Inkjet Printed Pressure Sensing Platform for Postural Imbalance Monitoring. *IEEE Trans Instrum Meas* 2015; 64: 2813–2820.

[127] Felba J, Nitsch K, Piasecki T, et al. The influence of thermal process on electrical conductivity of microstructures: Made by ink-jet painting with the use of ink containing nano sized silver particles. *2009 9th IEEE Conf Nanotechnol* 2009; 8: 408–411.

[128] Calvert P. Inkjet Printing for Materials and Devices. *Chem Mater* 2001; 13: 3299–3305.

[129] Badri A, Whittaker MR, Zetterlund PB. Modification of graphene/graphene oxide with polymer brushes using controlled/living radical polymerization. *J Polym Sci Part A Polym Chem* 2012; 50: 2981–2992.

[130] Atif R, Inam F. Reasons and remedies for the agglomeration of multilayered graphene and carbon nanotubes in polymers. *Beilstein J Nanotechnol* 2016; 7: 1174–1196.

[131] Yang Y, Rigdon W, Huang X, et al. Enhancing graphene reinforcing potential in composites by hydrogen passivation induced dispersion. *Sci Rep* 2013; 3: 2086.

[132] Kamyshny A, Steinke J, Magdassi S. Metal-based Inkjet Inks for Printed Electronics. *Open Appl Phys J* 2011; 4: 19–36.

[133] Ma PC, Siddiqui NA, Marom G, et al. Dispersion and functionalization of carbon

nanotubes for polymer-based nanocomposites: A review. *Compos Part A Appl Sci Manuf* 2010; 41: 1345–1367.

[134] Abdalla M, Dean D, Adibempe D, et al. The effect of interfacial chemistry on molecular mobility and morphology of multiwalled carbon nanotubes epoxy nanocomposite. *Polymer (Guildf)* 2007; 48: 5662–5670.

[135] Coleman JN, Khan U, Blau WJ, et al. Small but strong: A review of the mechanical properties of carbon nanotube-polymer composites. *Carbon N Y* 2006; 44: 1624–1652.

[136] Yokoi T, Iwamatsu S, Komai S, et al. Chemical modification of carbon nanotubes with organic hydrazines. *Carbon N Y* 2005; 43: 2869–2874.

[137] Green MJ, Behabtu N, Pasquali M, et al. Nanotubes as polymers. *Polymer (Guildf)* 2009; 50: 4979–4997.

[138] Foley TJ, Johnson CE, Higa KT. Inhibition of oxide formation on aluminum nanoparticles by transition metal coating. *Chem Mater* 2005; 17: 4086–4091.

[139] Park BK, Kim D, Jeong S, et al. Direct writing of copper conductive patterns by ink-jet printing. *Thin Solid Films* 2007; 515: 7706–7711.

[140] Grouchko M, Kamyshny A, Magdassi S. Formation of air-stable copper–silver core–shell nanoparticles for inkjet printing. *J Mater Chem* 2009; 19: 3057.

[141] Mallick K, Wang ZL, Pal T. Seed-mediated successive growth of gold particles accomplished by UV irradiation: a photochemical approach for size-controlled synthesis. *J Photochem Photobiol A Chem* 2001; 140: 75–80.

[142] Henglein A, Meisel D. Radiolytic control of the size of colloidal gold nanoparticles. *Langmuir* 1998; 14: 7392–7396.

[143] Pol VG, Gedanken A. Deposition of Gold Nanoparticles on Silica Spheres : A Sonochemical Approach. *Chem Mater* 2003; 15: 1111–1118.

[144] Benson J, Fung CM, Lloyd JS, et al. Direct patterning of gold nanoparticles using flexographic printing for biosensing applications. *Nanoscale Res Lett* 2015; 10: 127.

[145] Jensen GC, Krause CE, Sotzing GA, et al. Inkjet-printed gold nanoparticle electrochemical arrays on plastic. Application to immunodetection of a cancer biomarker protein. *Phys Chem Chem Phys* 2011; 13: 4888.

[146] Dutta J. Gold nanoparticle synthesis in graft copolymer micelles. *Colloid Polym Sci* 1998; 276: 853–859.

[147] Hao Y, Chong Y, Li S, et al. Controlled synthesis of Au nanoparticles in the nanocages of SBA-16: Improved activity and enhanced recyclability for the oxidative esterification of alcohols. *J Phys Chem C* 2012; 116: 6512–6519.

[148] Liu J, Anand M, Roberts CB. Synthesis and extraction of β-D-glucose-stabilized au nanoparticles processed into low-defect, wide-area thin films and ordered arrays using CO 2-expanded liquids. *Langmuir* 2006; 22: 3964–3971.

[149] Meltzer S, Resch R, Koel BE, et al. Fabrication of nanostructures by hydroxylamine seeding of gold nanoparticle templates. *Langmuir* 2001; 17: 1713–1718.

[150] Herrera AP, Resto O, Briano JG, et al. Synthesis and agglomeration of gold nanoparticles in reverse micelles. *Nanotechnology* 2005; 16: S618–S625.

[151] Chandra P, Singh J, Singh A, et al. Gold Nanoparticles and Nanocomposites in Clinical Diagnostics Using Electrochemical Methods. *J Nanoparticles* 2013; 2013: 1–12.

[152] Jayalakshmi A, Kim IC, Kwon YN. Suppression of gold nanoparticle agglomeration and its separation via nylon membranes. *Chinese J Chem Eng* 2017; 25: 931–937.

[153] Pierson JF, Rolin E, Clement-Gendarme C, et al. Effect of the oxygen flow rate on the structure and the properties of Ag-Cu-O sputtered films deposited using a Ag/Cu target with eutectic composition. *Appl Surf Sci* 2008; 254: 6590–6594.

[154] Li WW, Mo LX, Fu JL, et al. Fabrication of Transparent Conductive Film Using Water-Based Nano-Silver Gravure Ink. *Key Eng Mater* 2013; 562–565: 1440–1443.

[155] Walker SB, Lewis JA. Reactive Silver Inks for Patterning High-Conductivity

Features at Mild Temperatures. *J Am Chem Soc* 2012; 134: 1419–1421.

[156] Khondoker MAH, Mun SC, Kim J. Synthesis and characterization of conductive silver ink for electrode printing on cellulose film. *Appl Phys A Mater Sci Process* 2013; 112: 411–418.

[157] Ran J, Mo LX, Li WB, et al. A Nano-Silver Inkjet Conductive Ink with Excellent Adhesion. *Appl Mech Mater* 2012; 262: 501–504.

[158] Li W, Mo L, Fu J, et al. Preparation of Water-based Nano-silver Gravure Conductive Ink Used for Printed Electronics. *Adv Print Packag Technol* 2013; 262: 523–526.

[159] Odom SA, Chayanupatkul S, Blaiszik BJ, et al. A self-healing conductive ink. *Adv Mater* 2012; 24: 2578–2581.

[160] Small WR, Panhuis M n het. Inkjet Printing of Transparent, Electrically Conducting Single-Walled Carbon-Nanotube Composites. *Small* 2007; 3: 1500–1503.

[161] Denneulin A, Bras J, Carcone F, et al. Impact of ink formulation on carbon nanotube network organization within inkjet printed conductive films. *Carbon N Y* 2011; 49: 2603–2614.

[162] Novoselov KS, Geim AK, Morozov S V, et al. Electric Field Effect in Atomically Thin Carbon Films. *Science (80-)* 2004; 306: 666–669.

[163] Tkachev S V., Buslaeva EY, Gubin SP. Graphene: A novel carbon nanomaterial. *Inorg Mater* 2011; 47: 1–10.

[164] Tkachev S V., Buslaeva EY, Naumkin A V., et al. Reduced graphene oxide. *Inorg Mater* 2012; 48: 796–802.

[165] Le T, Lakafosis V, Lin Z, et al. Inkjet-printed graphene-based wireless gas sensor modules. *Proc - Electron Components Technol Conf* 2012; 1003–1008.

[166] Huang L, Huang Y, Liang J, et al. Graphene-based conducting inks for direct inkjet printing of flexible conductive patterns and their applications in electric circuits and chemical sensors. *Nano Res* 2011; 4: 675–684.

[167] Santra S, Hu G, Howe RCT, et al. CMOS integration of inkjet-printed graphene for humidity sensing. *Sci Rep* 2015; 5: 17374.

[168] Yu G, Hu L, Vosgueritchian M, et al. Solution-processed graphene/MnO2 nanostructured textiles for high-performance electrochemical capacitors. *Nano Lett* 2011; 11: 2905–2911.

[169] Molina J, Fernández J, Del Río AI, et al. Chemical and electrochemical study of fabrics coated with reduced graphene oxide. *Appl Surf Sci* 2013; 279: 46–54.

[170] Fugetsu B, Sano E, Yu H, et al. Graphene oxide as dyestuffs for the creation of electrically conductive fabrics. *Carbon N Y* 2010; 48: 3340–3345.

[171] Gu WL, Zhao YN. Graphene Modified Cotton Textiles. *Adv Mater Res* 2011; 331: 93–96.

[172] Li Y, Torah R, Beeby S, et al. An all-inkjet printed flexible capacitor on a textile using a new poly(4-vinylphenol) dielectric ink for wearable applications. *Proc IEEE Sensors* 2012; 25–28.

[173] Cummins G, Desmulliez MPY. Inkjet printing of conductive materials : a review. *Circuit World* 2012; 38: 193–213.

[174] Schiaffino S, Sonin AA. Molten droplet deposition and solidification at low Weber numbers Transport and solidification phenomena in molten microdroplet pileup Molten droplet deposition and solidification at low Weber numbers. *Phys Fluids Appl Phys Lett J Vac Sci Technol B Fluids J Appl Phys Phys Fluids* 1997; 9: 3172–161609.

[175] Rioboo R, Marengo M, Tropea C. Time evolution of liquid drop impact onto solid, dry surfaces. *Exp Fluids* 2002; 33: 112–124.

[176] Smith PJ, Shin DY, Stringer JE, et al. Direct ink-jet printing and low temperature conversion of conductive silver patterns. *J Mater Sci* 2006; 41: 4153–4158.

[177] Doggart J, Wu Y, Zhu S. Inkjet printing narrow electrodes with <50 μm line width and channel length for organic thin-film transistors. *Appl Phys Lett* 2009; 94: 163503.

[178] Öhlund T. *Coated Surfaces for Inkjet-Printed Conductors*. 2012.

[179] Lindblad M, Root A. Atomically controlled preparation of silica on alumina. In: *Preparation of Catalysts VII*. Elsevier Masson SAS, 1998, pp. 817–826.

[180] Tasaltin N, Sanli D, Jonáš A, et al. Preparation and characterization of superhydrophobic surfaces based on hexamethyldisilazane-modified nanoporous alumina. *Nanoscale Res Lett* 2011; 6: 487.

[181] Chinga-Carrasco G, Kuznetsova N, Garaeva M, et al. Bleached and unbleached MFC nanobarriers: properties and hydrophobisation with hexamethyldisilazane. *J Nanoparticle Res* 2012; 14: 1280.

[182] Chinga-Carrasco G, Tobjörk D, Österbacka R. Inkjet-Printed silver nanoparticles on nano-Engineered cellulose films for electrically conducting structures and organic transistors: Concept and challenges. *J Nanoparticle Res*; 14. Epub ahead of print 2012. DOI: 10.1007/s11051-012-1213-x.

[183] Andersson H, Rusu A, Manuilskiy A, et al. System of nano-silver inkjet printed memory cards and PC card reader and programmer. *Microelectronics J* 2011; 42: 21–27.

[184] Bidoki SM, Lewis DM, Clark M, et al. Ink-jet fabrication of electronic components. *J Micromechanics Microengineering* 2007; 17: 967–974.

[185] Lim J, Kim J, Yoon YJ, et al. All-inkjet-printed Metal-Insulator-Metal (MIM) capacitor. *Curr Appl Phys* 2012; 12: e14–e17.

[186] Okhlopkova AA, Shits EY. Structure and properties of teflon composites with natural diamond powders. *Mech Compos Mater* 2004; 40: 145–150.

[187] Xiang F, Wang H, Yao X. Preparation and dielectric properties of bismuth-based dielectric/PTFE microwave composites. *J Eur Ceram Soc* 2006; 26: 1999–2002.

[188] Ko SH, Chung J, Pan H, et al. Fabrication of multilayer passive and active electric components on polymer using inkjet printing and low temperature laser processing. *Sensors Actuators, A Phys* 2007; 134: 161–168.

[189] Wu W, Deconinck A, Lewis JA. Omnidirectional printing of 3D microvascular

networks. *Adv Mater* 2011; 23: 178–183.

[190] Ahn BY, Duoss EB, Motala MJ, et al. Omnidirectional Printing of Flexible, Stretchable, and Spanning Silver Microelectrodes. *Science (80-)* 2009; 323: 1590–1593.

[191] Ahn BY, Walker SB, Slimmer SC, et al. Planar and Three-Dimensional Printing of Conductive Inks. *J Vis Exp* 2011; 1–9.

[192] Guzman G, Dahmani B, Puetz J, et al. Transparent conducting sol-gel ATO coatings for display applications by an improved dip coating technique. *Thin Solid Films* 2006; 502: 281–285.

[193] Robinson JT, Perkins FK, Snow ES, et al. Reduced graphene oxide molecular sensors. *Nano Lett* 2008; 8: 3137–3140.

[194] Zhu C-H, Li L-M, Wang J-H, et al. Three-dimensional highly conductive silver nanowires sponges based on cotton-templated porous structures for stretchable conductors. *RSC Adv* 2017; 7: 51–57.

[195] Rahman MJ, Mieno T. Conductive Cotton Textile from Safely Functionalized Carbon Nanotubes. *J Nanomater*; 2015. Epub ahead of print 2015. DOI: 10.1155/2015/978484.

[196] Ratcliff EL, Lee P a., Armstrong NR. Work function control of hole-selective polymer/ITO anode contacts: an electrochemical doping study. *J Mater Chem* 2010; 20: 2672.

[197] Wang D, Li F, Zhao J, et al. Fabrication of Graphene/Polyaniline Composite Paper via In Situ Anodic Electropolymerization for High-Performance Flexible Electrode. *ACS Nano* 2009; 3: 1745–1752.

[198] Cohen David N, David Y, Katz N, et al. Electro-conductive fabrics based on dip coating of cotton in poly(3-hexylthiophene). *Polym Adv Technol* 2017; 28: 583–589.

[199] Liu S, Hu M, Yang J. A facile way of fabricating flexible and conductive cotton fabric. *J Mater Chem C* 2016; 4: 1320–1325.

[200] Kaynak A, Foitzik R. Methods of coating textiles with soluble conducting polymers. *Res J Text Appar* 2011; 15: 107–113.

[201] Irwin MD, Roberson DA, Olivas RI, et al. Conductive polymer-coated threads as electrical interconnects in e-textiles. *Fibers Polym* 2011; 12: 904–910.

[202] Faustini M, Louis B, Albouy P a, et al. Preparation of Sol - Gel Films by Dip-Coating in Extreme Conditions. *J Phys Chem C* 2010; 114: 7637–7645.

[203] Hwang J, Shoji N, Endo A, et al. Effect of withdrawal speed on film thickness and hexagonal pore-array dimensions of SBA-15 mesoporous silica thin film. *Langmuir* 2014; 30: 15550–15559.

[204] Hoffman L, Nakayama T. Screen Printed Capacitor Dielectrics. *Am Ceram Soc Bull* 1967; 46: 789.

[205] Zhu D, Beeby SP, Tudor MJ, et al. A credit card sized self powered smart sensor node. *Sensors Actuators, A Phys* 2011; 169: 317–325.

[206] Quintana JC, Arduini F, Amine A, et al. Part I: A comparative study of bismuth-modified screen-printed electrodes for lead detection. *Anal Chim Acta* 2011; 707: 171–177.

[207] Wei Y, Torah R, Yang K, et al. Screen printing of a capacitive cantilever-based motion sensor on fabric using a novel sacrificial layer process for smart fabric applications. *Meas Sci Technol* 2013; 24: 75104.

[208] Reddy ASG, Narakathu BB, Atashbar MZ, et al. Gravure printed electrochemical biosensor. *Procedia Eng* 2011; 25: 956–959.

[209] Hwang WJ, Hong JM, Ju BK, et al. A study on the fabrication of organic thin film transistor sensors using gravure printing. *AIP Conf Proc* 2011; 1399: 863–864.

[210] Narakathu BB, Eshkeiti A, Reddy ASG, et al. A novel fully printed and flexible capacitive pressure sensor. *Proc IEEE Sensors* 2012; 26–29.

[211] Chung W-H, Hwang H-J, Lee S-H, et al. In situ monitoring of a flash light sintering process using silver nano-ink for producing flexible electronics.

Nanotechnology 2013; 24: 35202.

[212] Mancosu RD, Quintero, J, A Q, Azevedo RES. Sintering, in Different Temperatures, of Traces of Silver Printed in Flexible Surfaces. In: *11th. International Conference on Thermal Mechanical and Multiphys Simulation and Experiments in Micro-Electronics and Micro-Systems*. Bordeaux, France: EuroSimE 2010, 2010, pp. 1–4.

[213] Falat T, Felba J, Moscicki A, et al. Influence of nano silver filler content on properties of ink-jet printed structures for microelectronics. *Electron Syst Integr Technol Conf ESTC 2010 - Proc* 2010; 5–9.

[214] Ma S, Bromberg V, Liu L, et al. Low temperature plasma sintering of silver nanoparticles. *Appl Surf Sci* 2014; 293: 207–215.

[215] Tobjörk D, Aarnio H, Pulkkinen P, et al. IR-sintering of ink-jet printed metal-nanoparticles on paper. *Thin Solid Films* 2012; 520: 2949–2955.

[216] Polzinger B, Schoen F, Matic V, et al. UV-sintering of inkjet-printed conductive silver tracks. *Proc IEEE Conf Nanotechnol* 2011; 201–204.

[217] Allen ML, Aronniemi M, Mattila T, et al. Electrical sintering of nanoparticle structures. *Nanotechnology* 2008; 19: 175201.

[218] Perelaer J, De Gans BJ, Schubert US. Ink-jet printing and microwave sintering of conductive silver tracks. *Adv Mater* 2006; 18: 2101–2104.

[219] Thostenson ET, Chou T-W. Microwave processing: fundamentals and applications. *Compos Part A Appl Sci Manuf* 1999; 30: 1055–1071.

[220] Cheng DK. *Field and wave electromagnetics*. 2nd ed. Addison-Wesley, 1989.

[221] Magdassi S, Grouchko M, Berezin O, et al. Triggering the sintering of silver nanoparticles at room temperature. *ACS Nano* 2010; 4: 1943–1948.

[222] Werner K. *Manual of textile technology : short-staple spinning series: A practical guide to the blowroom and carding*. 2nd ed. Manchester, 2000.

[223] Zielińska A, Skwarek E, Zaleska A, et al. Preparation of silver nanoparticles with controlled particle size. *Procedia Chem* 2009; 1: 1560–1566.

[224] Yin Y, Li Z-Y, Zhong Z, et al. Synthesis and characterization of stable aqueous dispersions of silver nanoparticles through the Tollens process. *J Mater Chem* 2002; 12: 522–527.

[225] Shenoy RR. *Design of e-textiles for acoustic applications*. Virginia Polytechnic Institute and State University, 2003.

[226] Farringdon J, Moore AJ, Tilbury N, et al. Wearable sensor badge and sensor jacket for context awareness. *Dig Pap Third Int Symp Wearable Comput* 1999; 107–113.

[227] Wijesiriwardana R, Mitcham K, Hurley W, et al. Capacitive fiber-meshed transducers for touch and proximity-sensing applications. *IEEE Sens J* 2005; 5: 989–994.

[228] Hamdani STA, Potluri P, Fernando A. Thermo-mechanical behavior of textile heating fabric based on silver coated polymeric yarn. *Materials (Basel)* 2013; 6: 1072–1089.

[229] Janesch J. Two-wire vs. four-wire resistance measurements: which configuration makes sense for your application? 2013; 1–3.

[230] Hoffmann K. *Applying the wheatstone bridge circuit*. Darmstadt, 2001.

[231] *NI 9219 operating instructions and specifications*. 2009.

[232] Shannon CE. Communication in the Presence of Noise. *Proc IRE* 1949; 37: 10–21.

[233] Miller FP, Vandome AF, McBrewster J. *Nyquist-Shannon Sampling Theorem: Aliasing, Sine Wave, Signal Processing, Nyquist Rate, Nyquist Frequency, Sampling Rate, Shannon-Hartley Theorem, Whittaker-Shannon Interpolation Formula, Reconstruction from Zero Crossings*. Alphascript Publishing, 2010.

[234] Berkow R. *The Merck Manual of Medical Information*. New Jersey: Merck, 1997.

[235] Burr GW, Breitwisch MJ, Franceschini M, et al. Phase change memory technology. *J Vac Sci Technol B, Nanotechnol Microelectron Mater Process*

Meas Phenom 2010; 28: 223–262.

[236] Awasthi M, Shevgoor M, Balasubramonian R. Handling PCM Resistance Drift with Device , Circuit , Architecture , and System Solutions. *Non-Volatile Memories Work*.

[237] Boniardi M, Ielmini D, Lavizzari S, et al. Statistics of resistance drift due to structural relaxation in phase-change memory arrays. *IEEE Trans Electron Devices* 2010; 57: 2690–2696.

[238] Boniardi M, Redaelli A, Pirovano A, et al. A physics-based model of electrical conduction decrease with time in amorphous Ge2 Sb2 Te5. *J Appl Phys*; 105. Epub ahead of print 2009. DOI: 10.1063/1.3109063.

[239] Gao Z. *Optimisation of size, shape and location of resistive knitted electro-textile electrodes for heart signal (ECG) sensing*. The University of Manchester, 2015.

[240] Renz R, Alstädt V, Ehrenstein GW. Hysteresis Measurements for Characterizing the Dynamic Fatigue of R-SMC. *J Reinf Plast Compos* 1988; 7: 413–434.

[241] Ionel DM, Popescu M, McGilp MI, et al. Computation of core losses in electrical machines using improved models for laminated steel. *IEEE Trans Ind Appl* 2007; 43: 1554–1564.

[242] Elmarzougui S, Abdessalem S Ben, Sakli F. Hysteresis measurement for characterising the dynamic fatigue of textile artificial ligaments. *J Text Inst* 2011; 102: 109–113.

[243] Kalanta-zadeh K. *Sensors An introductory Course*. 2013.

Appendix A: Cyclic compressive loading

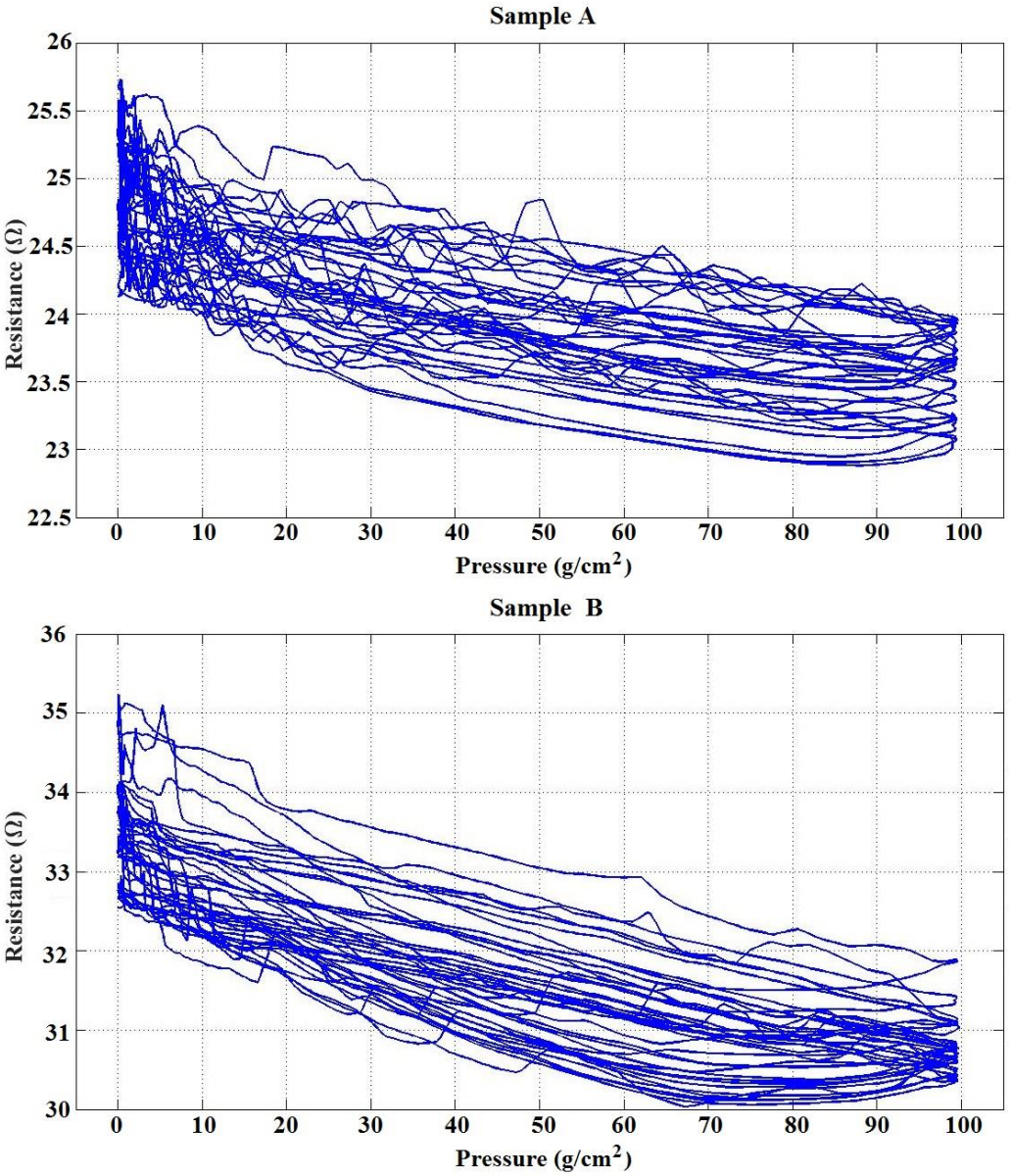

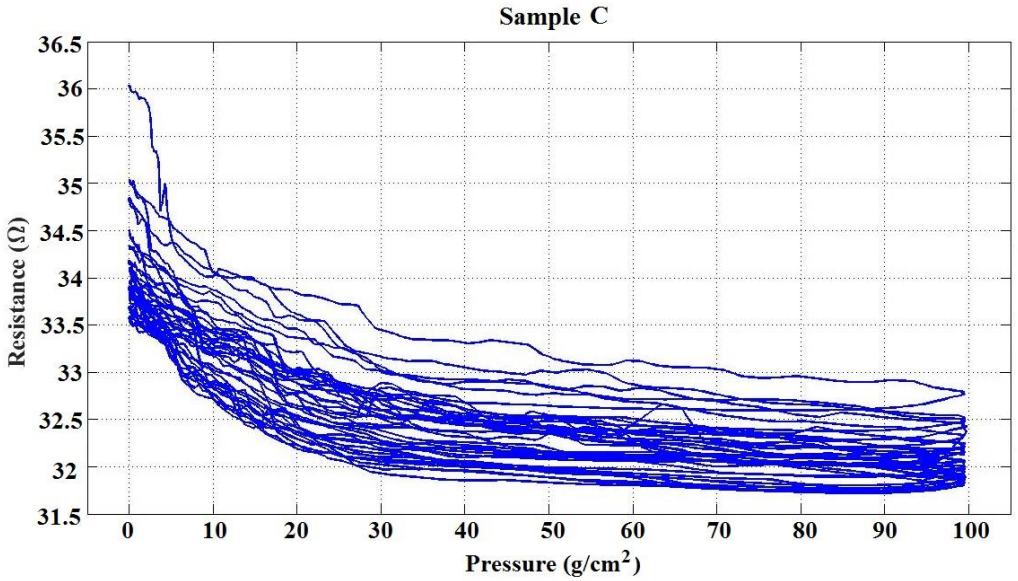
Sample C
Resistance (Ω)
36.5
36
35.5
35
34.5
34
33.5
33
32.5
32
31.5
0
10
20
30
40
50
60
70
80
90
100
Pressure (g/cm2)

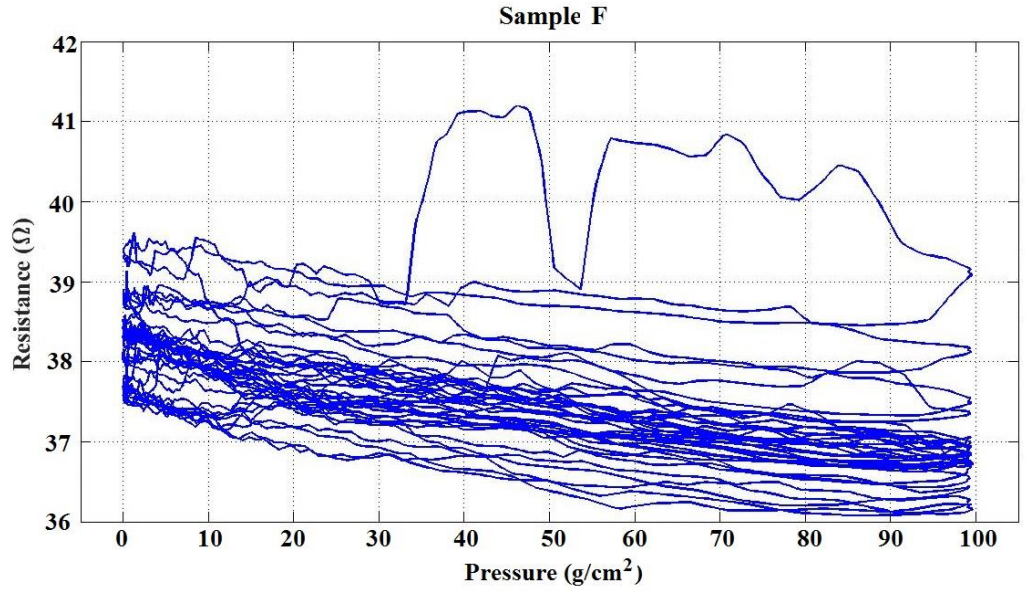
Sample F
Resistance (Ω)
42
41
40
39
38
37
36
0
10
20
30
40
50
60
70
80
90
100
Pressure (g/cm2)

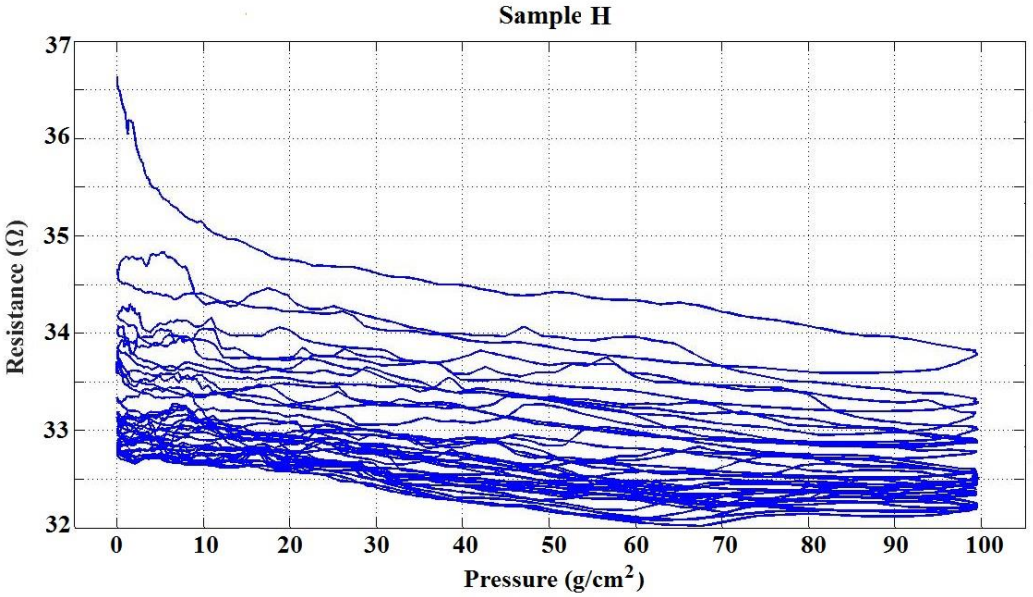
Sample H
Resistance (Ω)
37
36
35
34
33
32
0
10
20
30
40
50
60
70
80
90
100
Pressure (g/cm2)

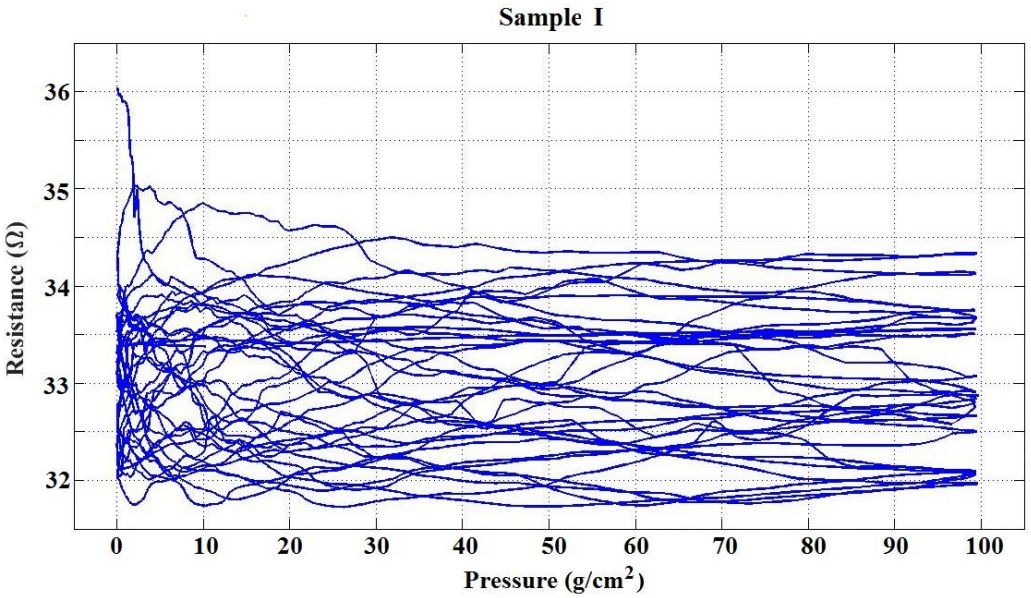
Sample I
Resistance (Ω)
36
35
34
33
32
0
10
20
30
40
50
60
70
80
90
100
Pressure (g/cm2)

Appendix B: Hysteresis analysis of sample D, E, G, J and K

Resistance hysteresis loss of sample D, E, G, J and K in cyclic compressive loading test.

Sample	D	E	G	J	K
Cycle No.	Resistance hysteresis loss ($\Omega\cdot(g/cm^2)$)				
1	70.25	183.37	96.21	104.55	428.70
2	80.15	205.09	107.94	59.25	125.26
3	76.67	160.70	91.42	55.04	99.40
4	83.36	154.63	116.22	41.13	81.23
5	62.43	153.20	105.08	44.01	74.76
6	66.46	150.14	102.05	43.87	68.19
7	59.19	148.11	106.78	34.87	68.60
8	66.61	152.32	106.88	41.60	75.70
9	60.62	156.59	110.03	42.87	71.27
10	66.36	154.77	112.43	41.27	71.52
11	67.05	148.31	114.89	41.73	57.16
12	59.61	150.39	96.74	36.60	62.92
13	58.99	157.56	107.84	35.50	64.01
14	62.03	155.08	110.49	39.53	60.48
15	59.85	150.20	123.69	39.76	67.91
16	58.95	151.11	122.01	39.64	73.69
17	60.97	152.04	109.22	47.79	65.74
18	60.79	151.74	113.81	58.48	76.12
19	57.65	158.31	89.79	60.74	70.22
20	54.38	152.46	137.79	50.38	66.52
Average	64.62	157.31	109.07	47.93	91.47

Resistance hysteresis loss percentage of sample D, E, G, J and K in cyclic compressive loading test.

Sample	D	E	G	J	K
Cycle No.	Resistance loss percentage				
1	2.19%	4.76%	1.81%	2.63%	15.18%
2	2.53%	5.46%	2.06%	1.54%	5.18%
3	2.44%	4.39%	1.78%	1.45%	4.24%
4	2.73%	4.26%	2.25%	1.09%	3.53%
5	2.01%	4.26%	2.05%	1.18%	3.29%
6	2.14%	4.20%	2.00%	1.18%	3.02%
7	1.91%	4.17%	2.09%	0.94%	3.06%
8	2.16%	4.30%	2.10%	1.13%	3.38%
9	1.96%	4.45%	2.16%	1.17%	3.19%
10	2.15%	4.43%	2.21%	1.13%	3.22%
11	2.18%	4.26%	2.27%	1.14%	2.59%
12	1.94%	4.32%	1.92%	1.00%	2.85%
13	1.93%	4.54%	2.14%	0.98%	2.92%
14	2.03%	4.49%	2.20%	1.09%	2.75%
15	1.97%	4.36%	2.47%	1.10%	3.08%
16	1.94%	4.39%	2.44%	1.09%	3.34%
17	2.01%	4.43%	2.19%	1.32%	2.99%
18	2.00%	4.43%	2.29%	1.62%	3.45%
19	1.90%	4.63%	1.82%	1.68%	3.19%
20	1.80%	4.47%	2.77%	1.40%	3.02%
Average	2.10%	4.45%	2.15%	1.29%	3.87%

Appendix C: RTD analysis

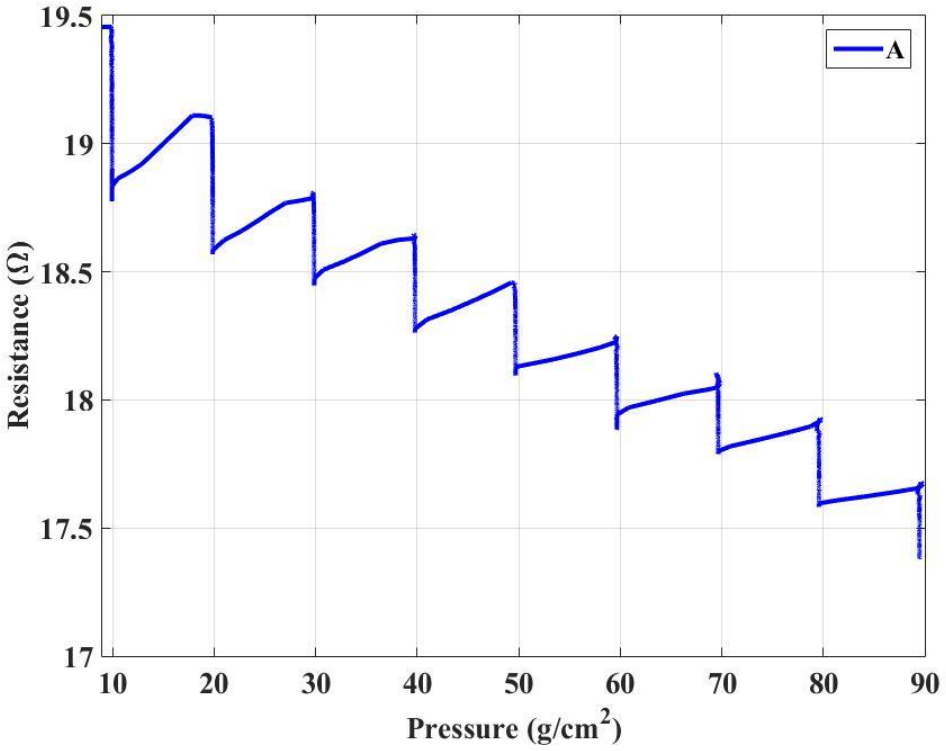

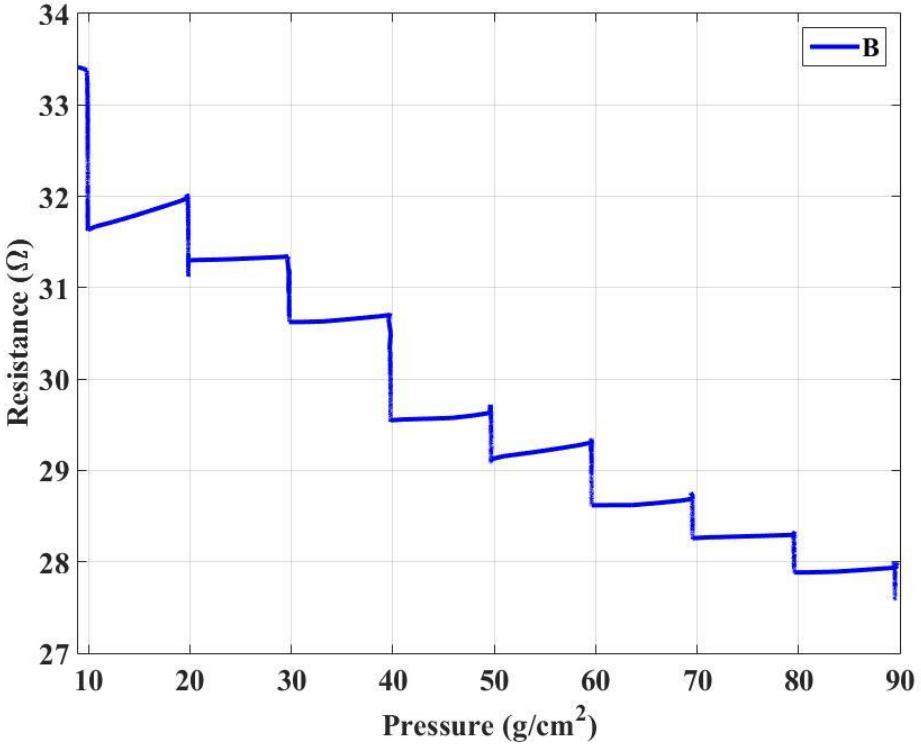

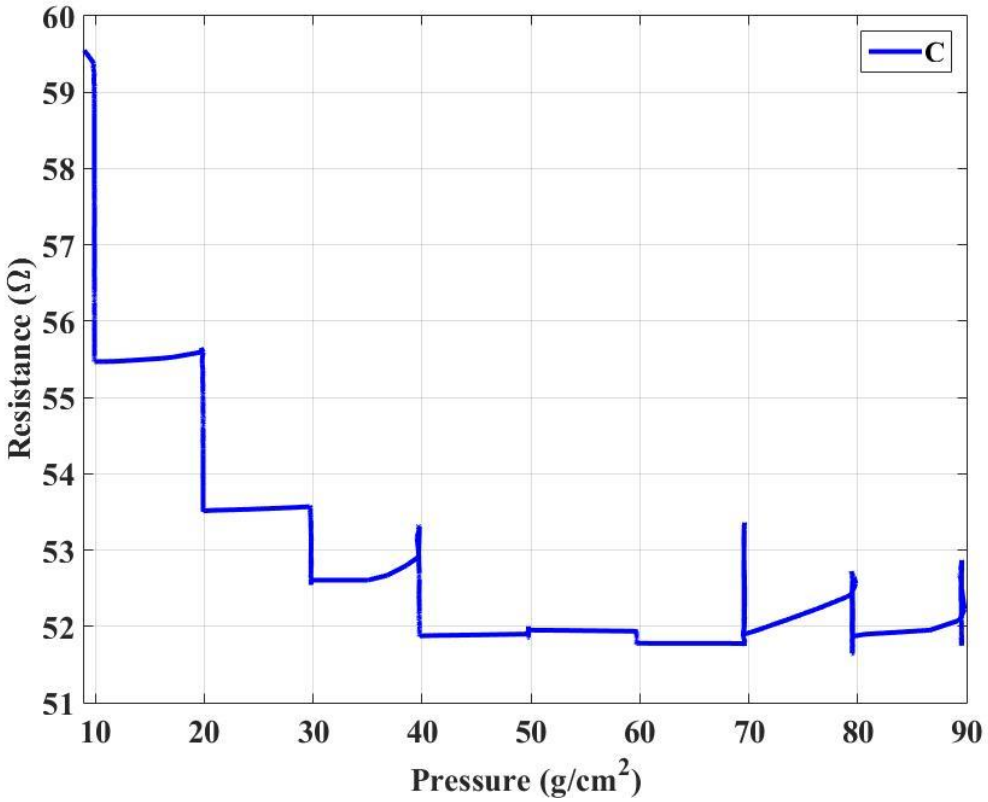
C
Resistance (Ω)
Pressure (g/cm^2)
60
59
58
57
56
55
54
53
52
51
10
20
30
40
50
60
70
80
90

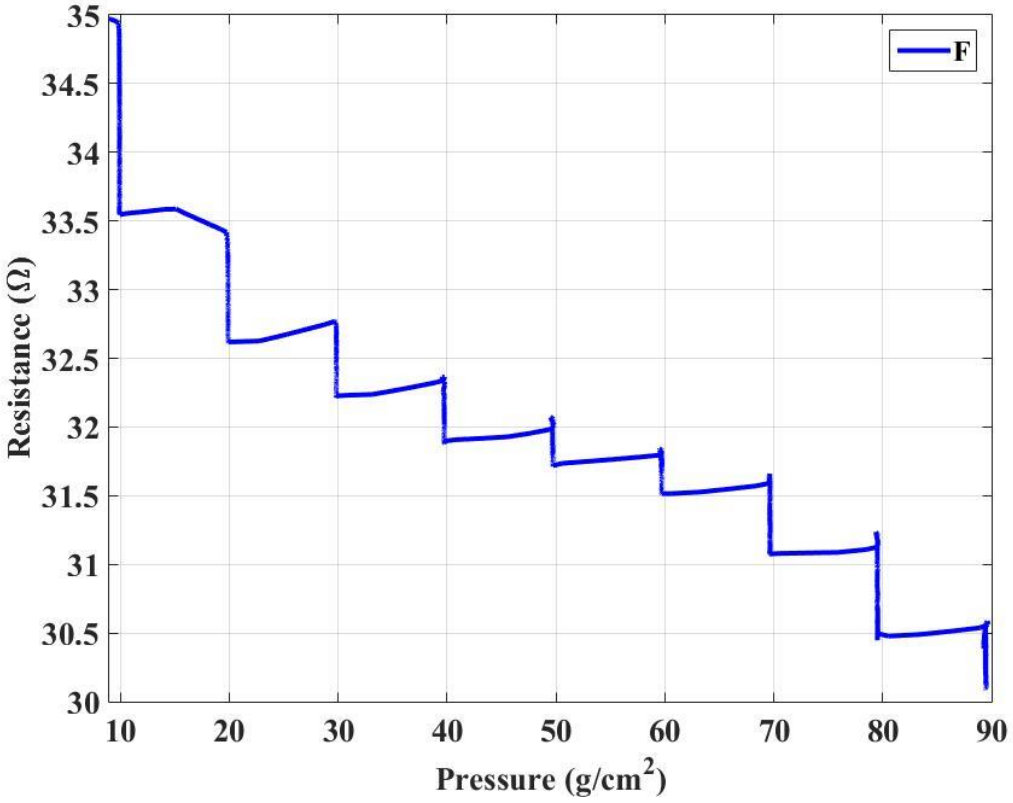
F
Resistance (Ω)
Pressure (g/cm^2)
35
34.5
34
33.5
33
32.5
32
31.5
31
30.5
30
10
20
30
40
50
60
70
80
90

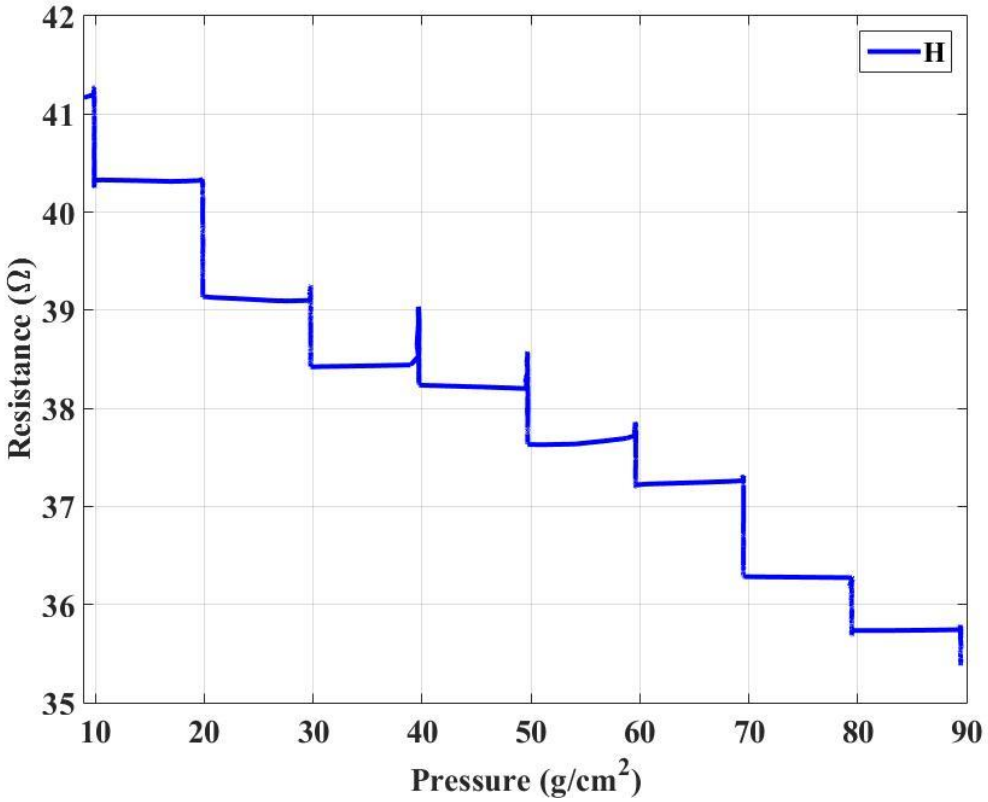
H
Resistance (Ω)
Pressure (g/cm^2)
42
41
40
39
38
37
36
35
10
20
30
40
50
60
70
80
90

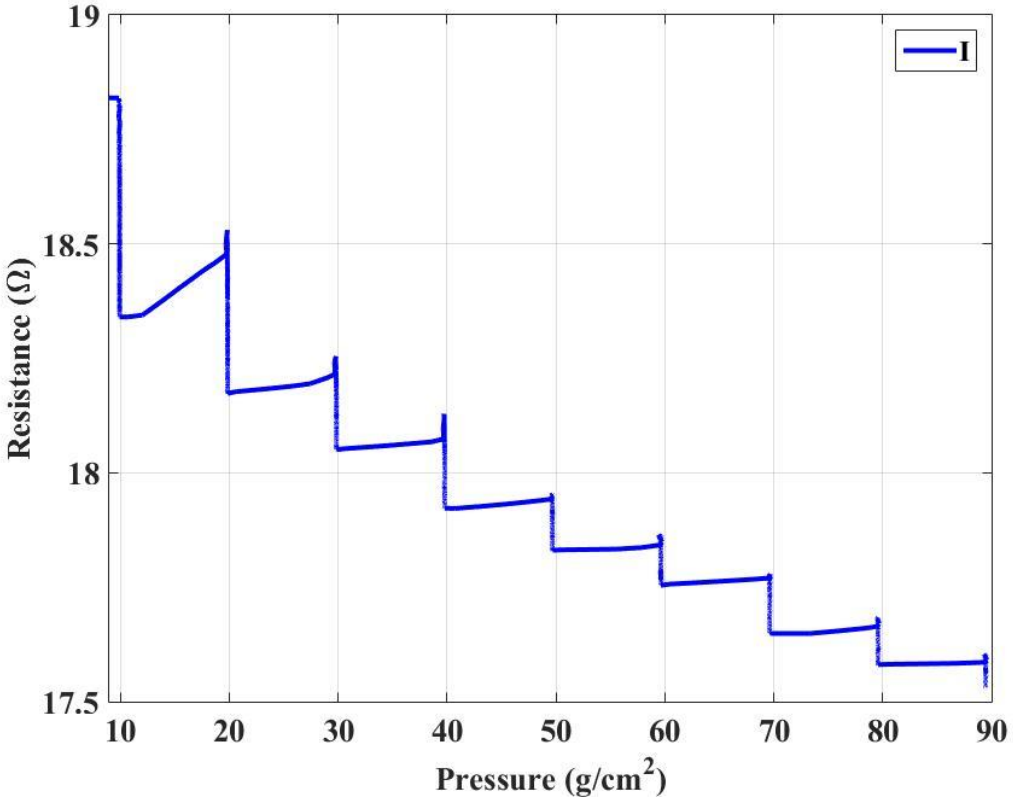
I
Resistance (Ω)
Pressure (g/cm^2)
19
18.5
18
17.5
10
20
30
40
50
60
70
80
90

Appendix D: Respiratory signal capturing

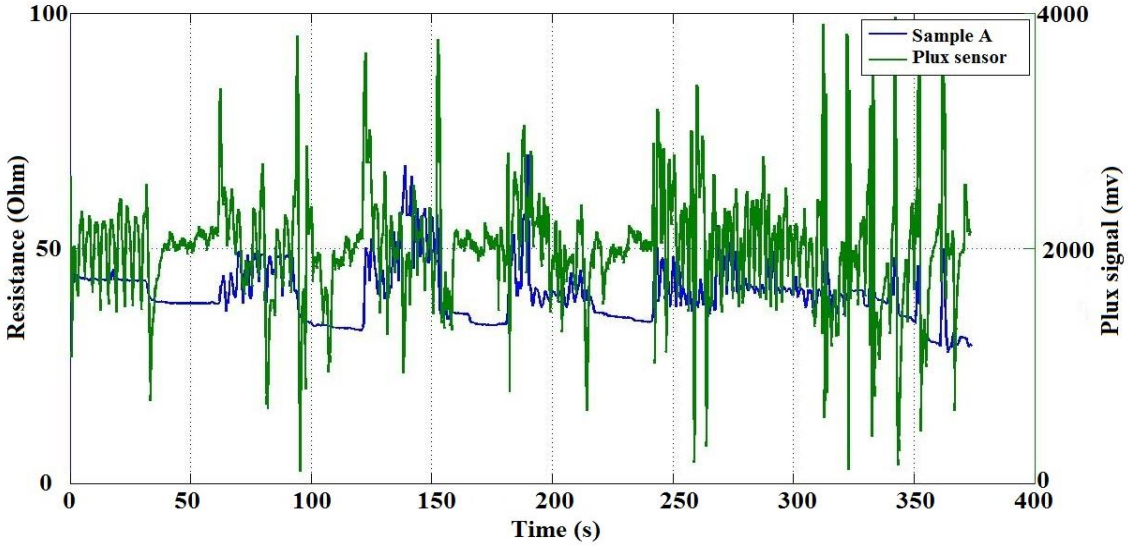

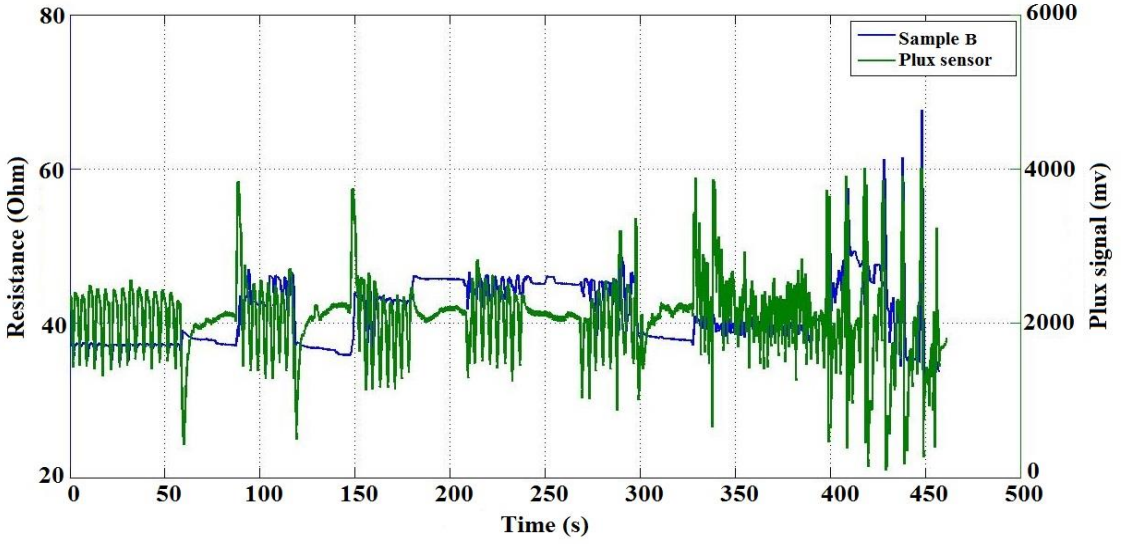

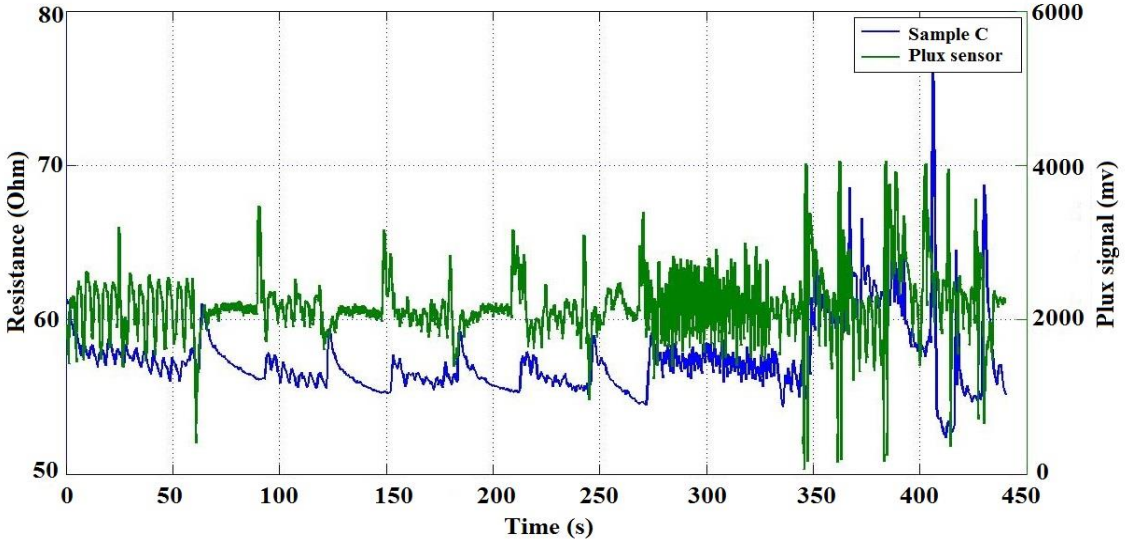

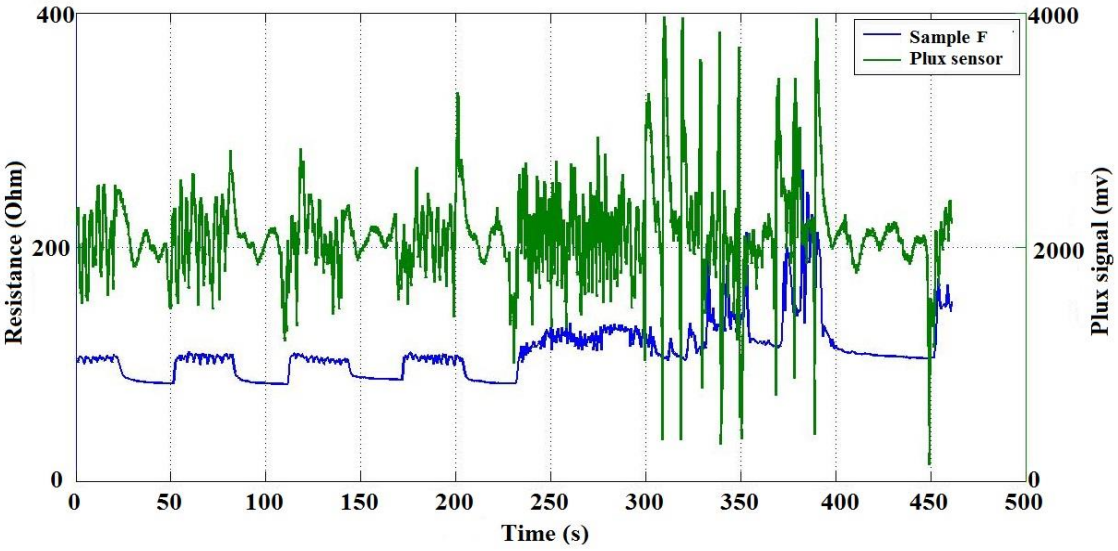
Sample F
Plux sensor
Resistance (Ohm)
Plux signal (mv)
Time (s)
0
200
400
0
2000
4000
0
50
100
150
200
250
300
350
400
450
500

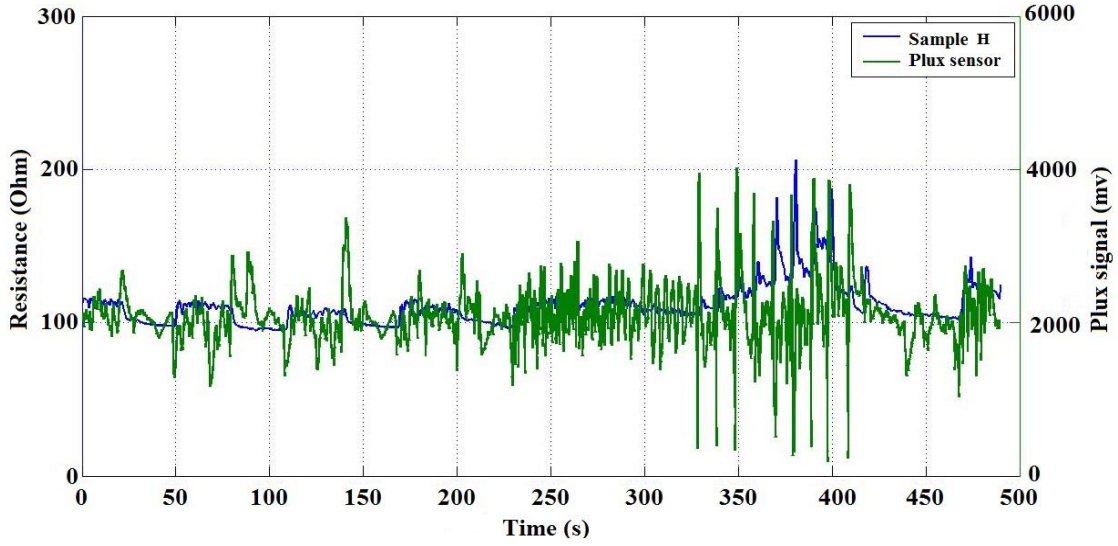
Sample H
Plux sensor
Resistance (Ohm)
Plux signal (mv)
Time (s)
0
100
200
300
0
2000
4000
6000
0
50
100
150
200
250
300
350
400
450
500

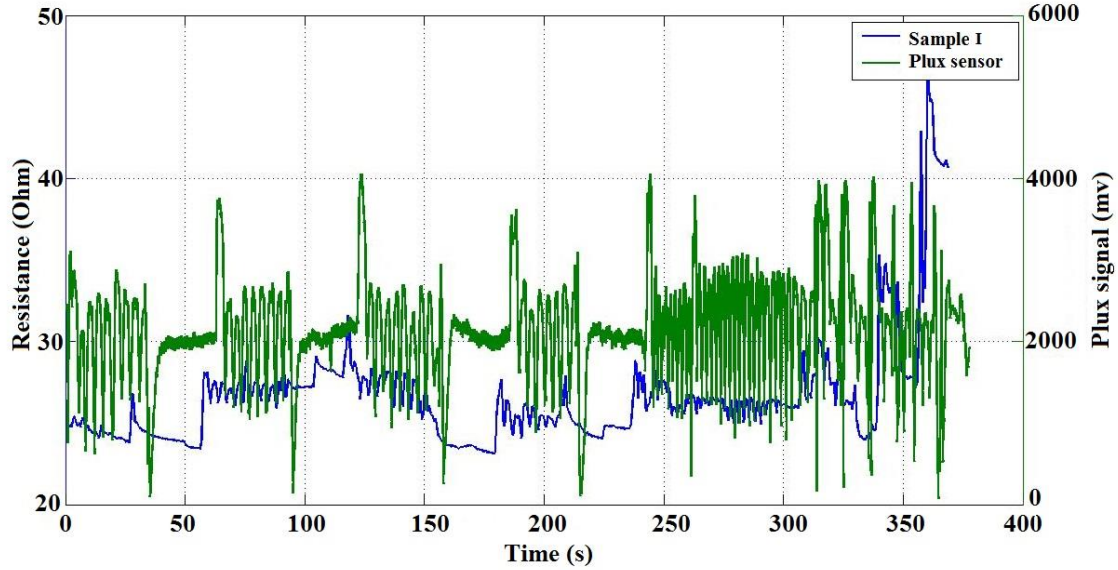
Sample I
Plux sensor
Resistance (Ohm)
Plux signal (mv)
Time (s)
20
30
40
50
0
2000
4000
6000
0
50
100
150
200
250
300
350
400

Appendix E: Cardiac signal capturing

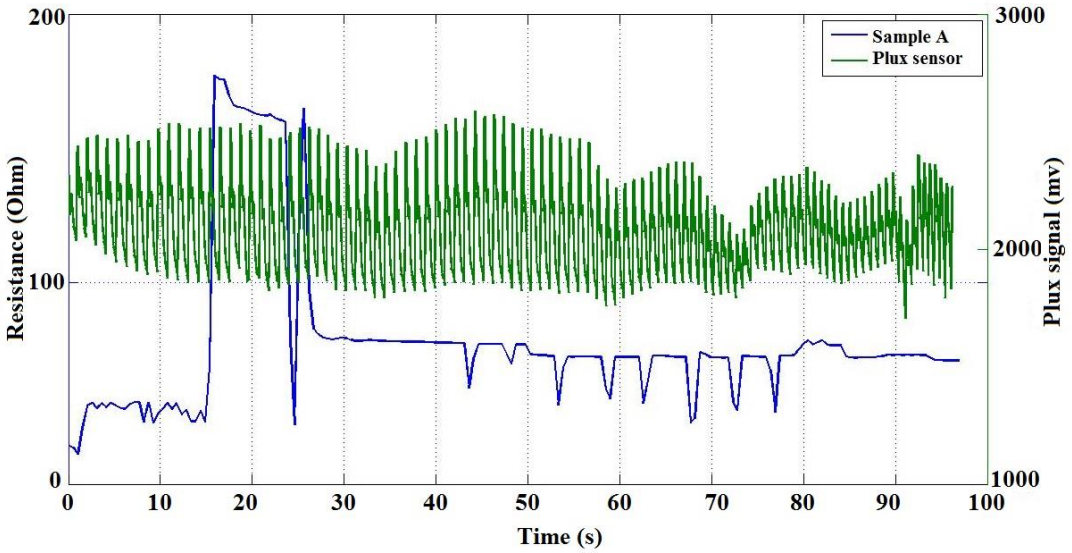

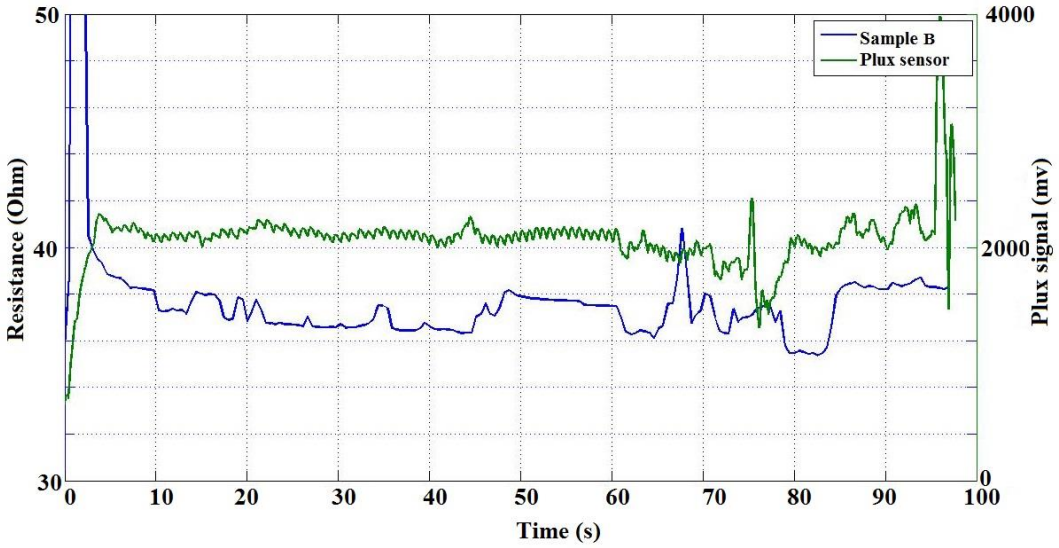

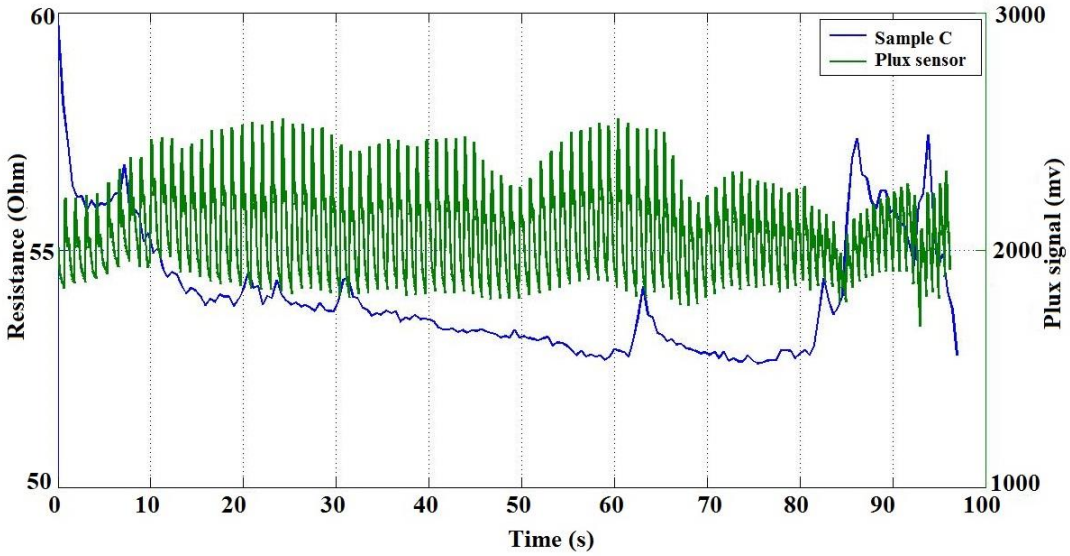

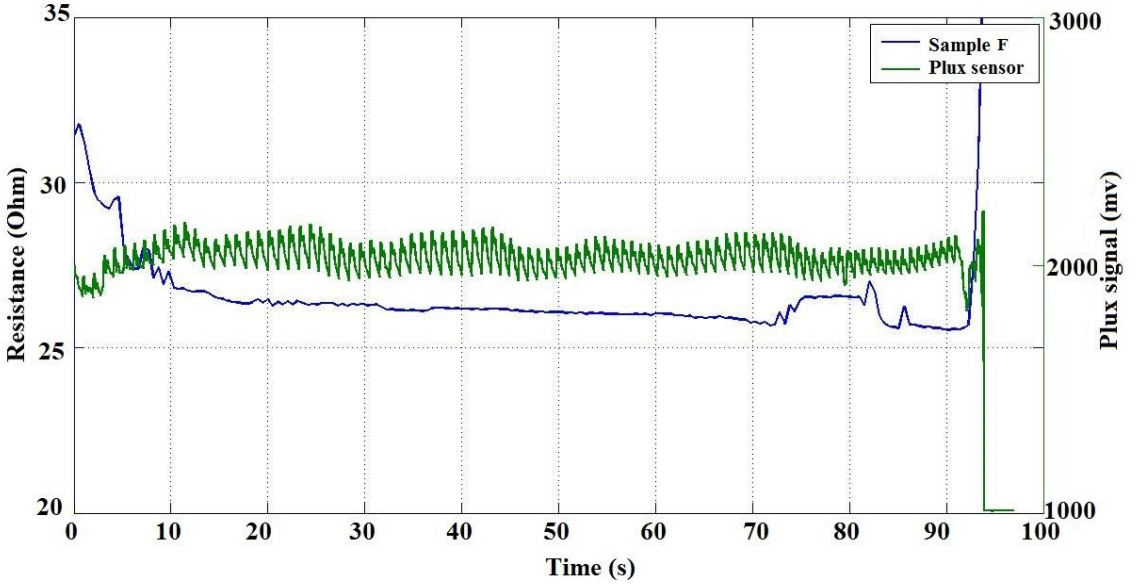
Sample F
Plux sensor
Resistance (Ohm)
Plux signal (mv)
Time (s)
35
30
25
20
3000
2000
1000
0
10
20
30
40
50
60
70
80
90
100

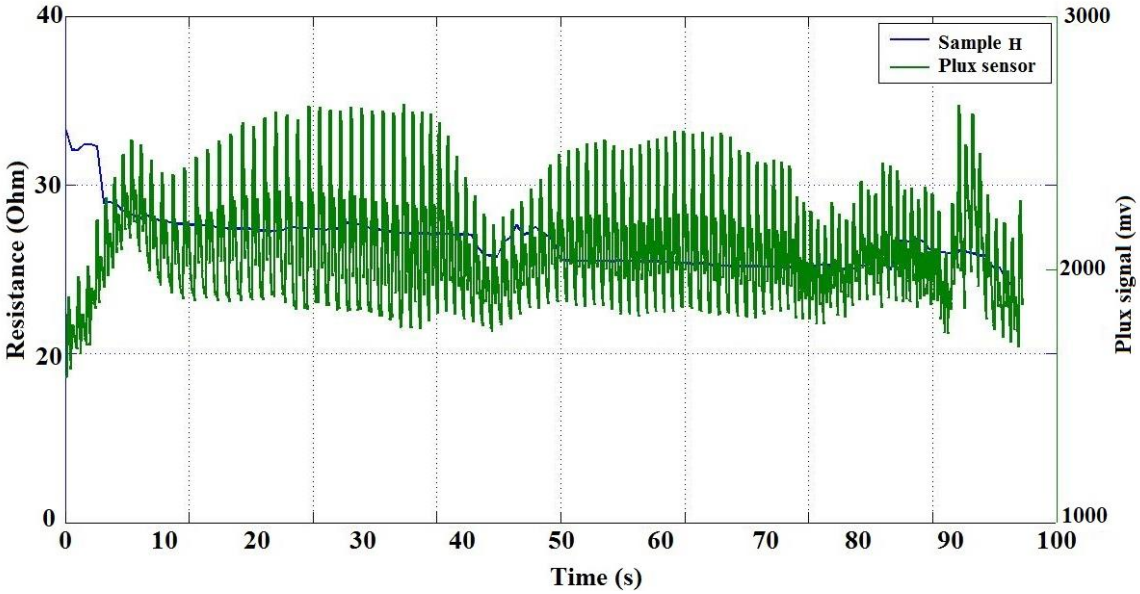
Sample H
Plux sensor
Resistance (Ohm)
Plux signal (mv)
Time (s)
40
30
20
0
3000
2000
1000
0
10
20
30
40
50
60
70
80
90
100

Appendix F: Cardiorespiratory captured with bandpass filter

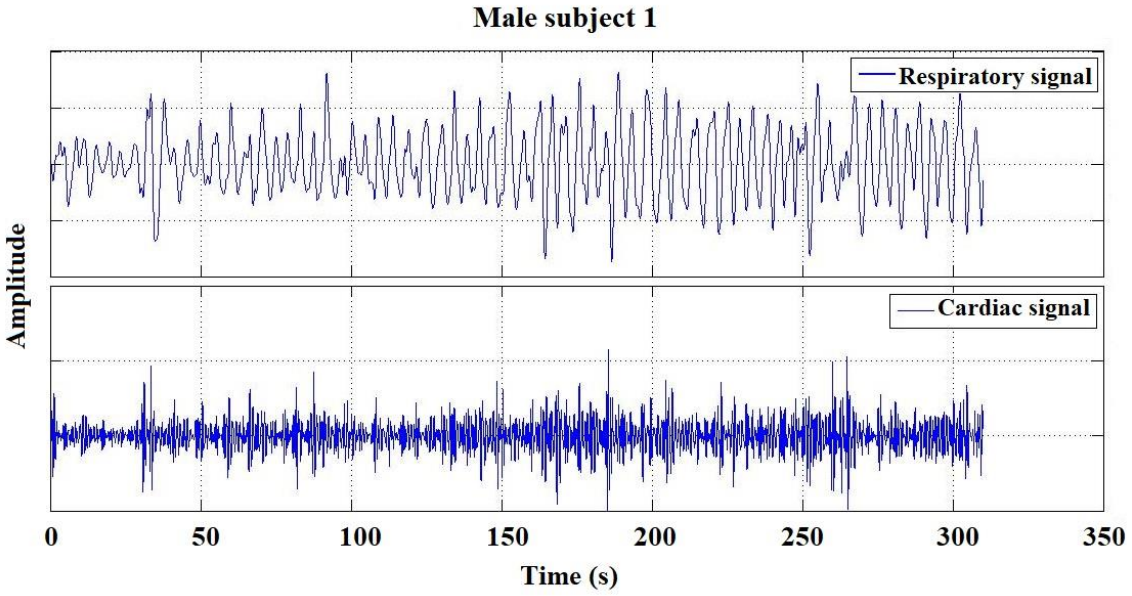

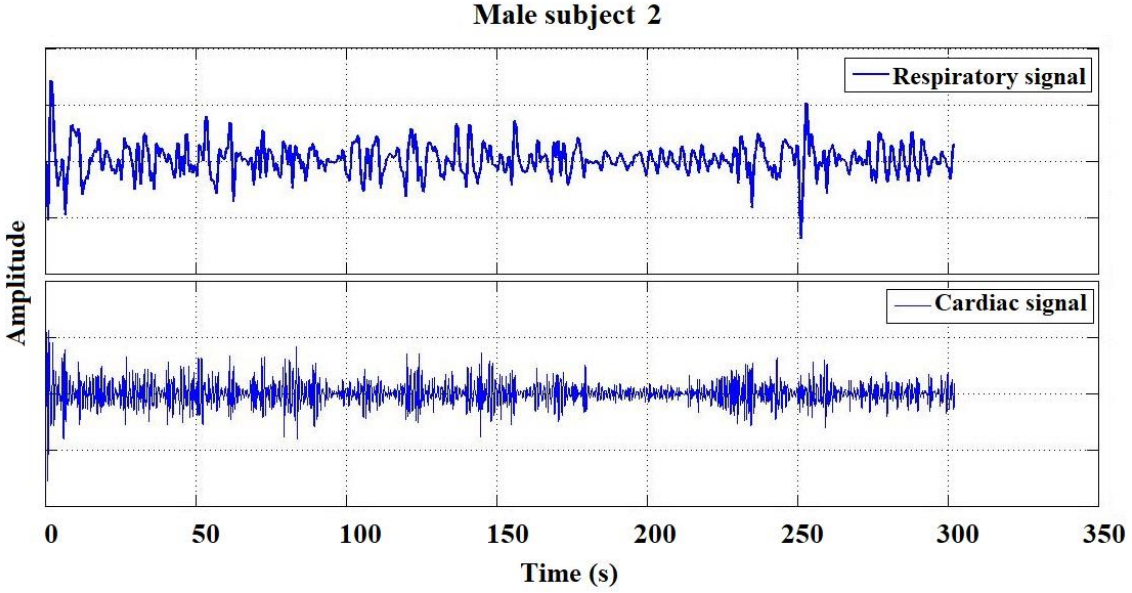

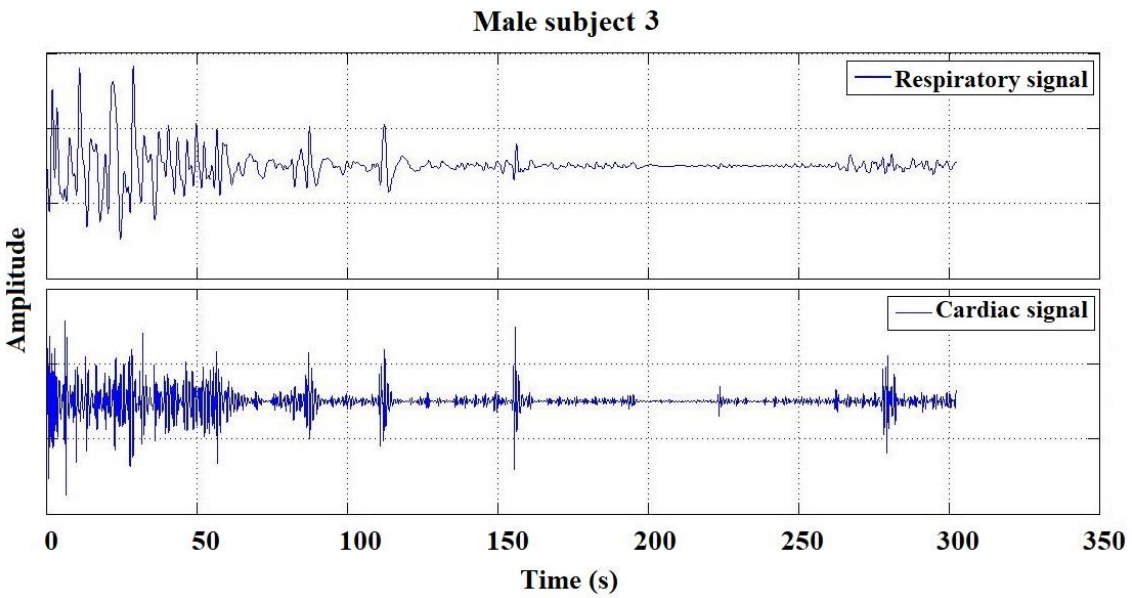
Male subject 3
Respiratory signal
Cardiac signal
Amplitude
0
50
100
150
200
250
300
350
Time (s)

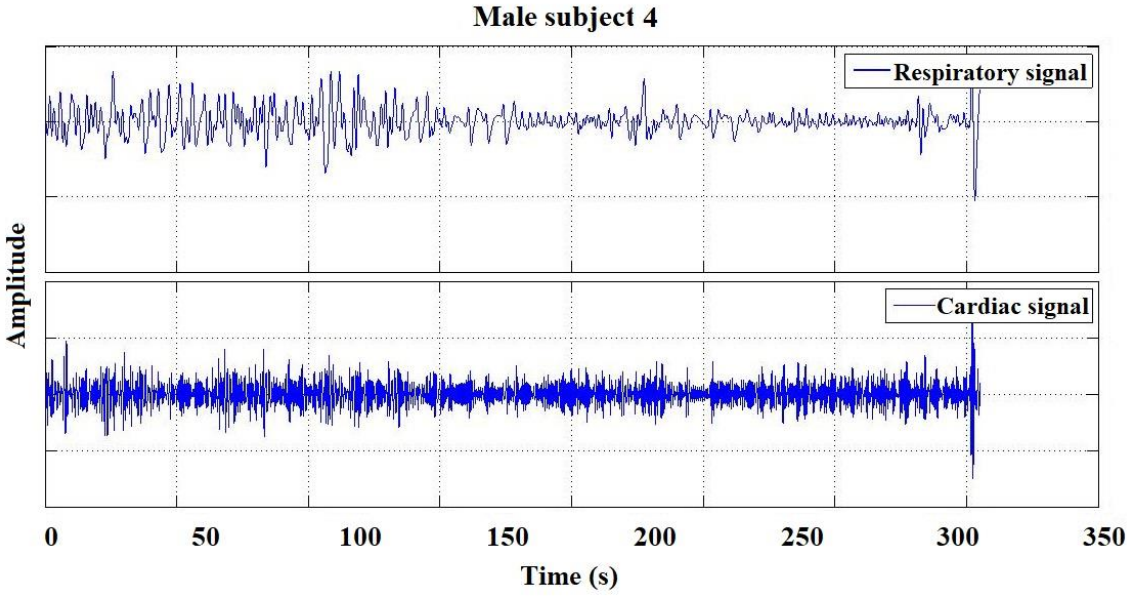
Male subject 4
Respiratory signal
Cardiac signal
Amplitude
0
50
100
150
200
250
300
350
Time (s)

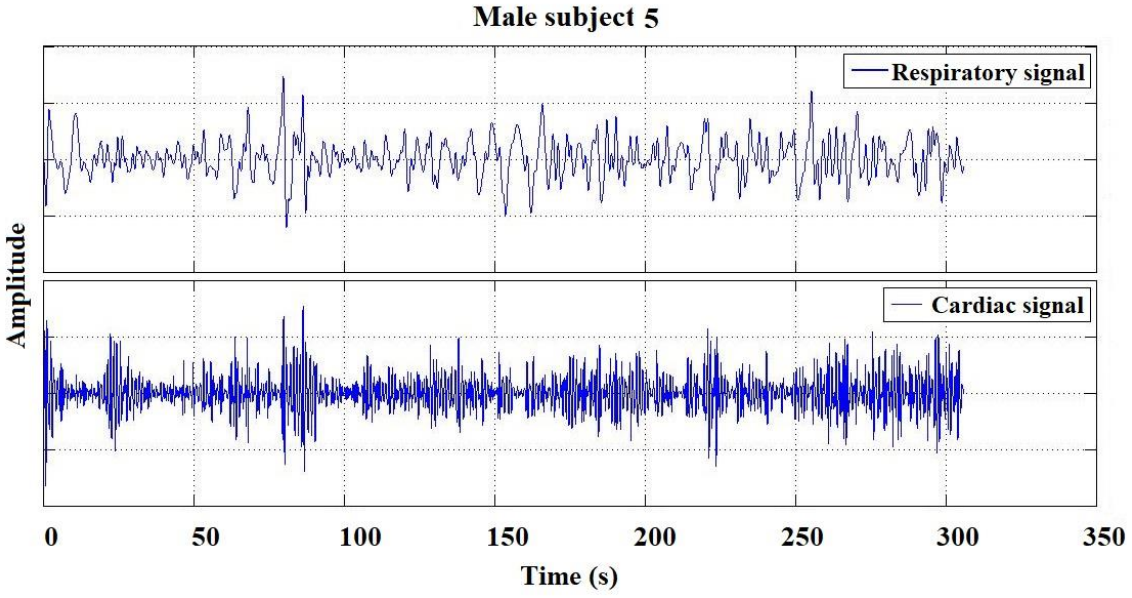
Male subject 5
Respiratory signal
Cardiac signal
Amplitude
0
50
100
150
200
250
300
350
Time (s)

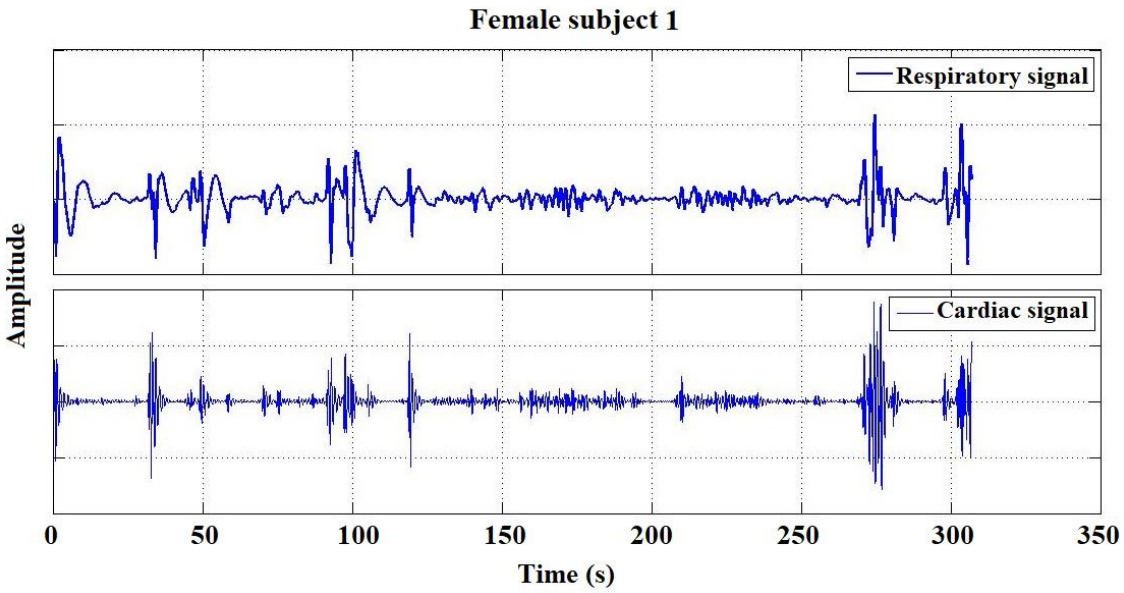
Female subject 1
Respiratory signal
Cardiac signal
Amplitude
0
50
100
150
200
250
300
350
Time (s)

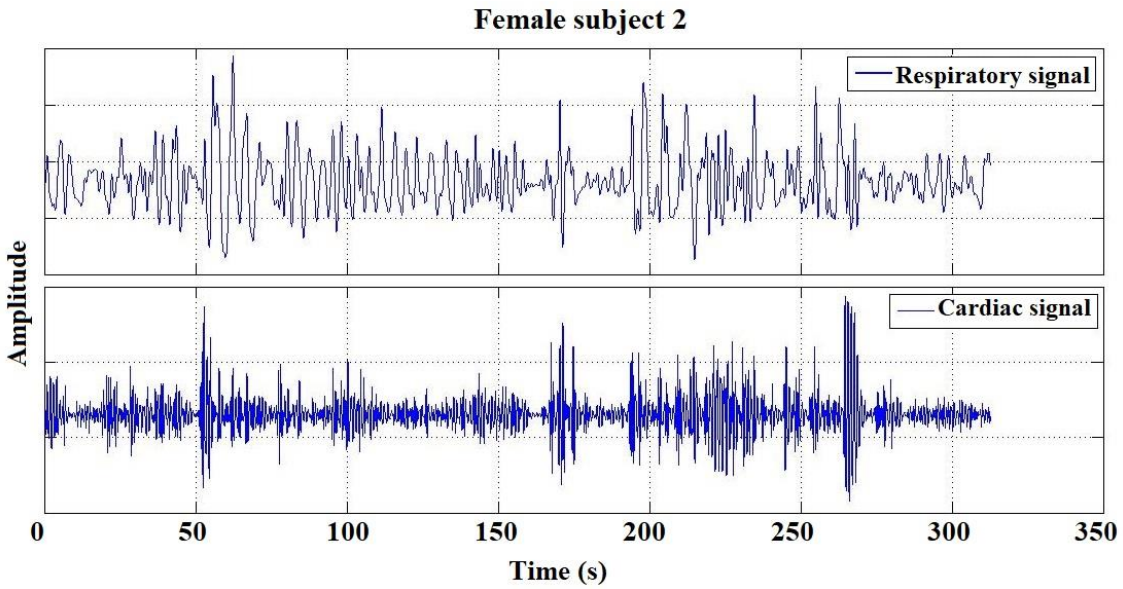
Female subject 2
Respiratory signal
Cardiac signal
Amplitude
0
50
100
150
200
250
300
350
Time (s)

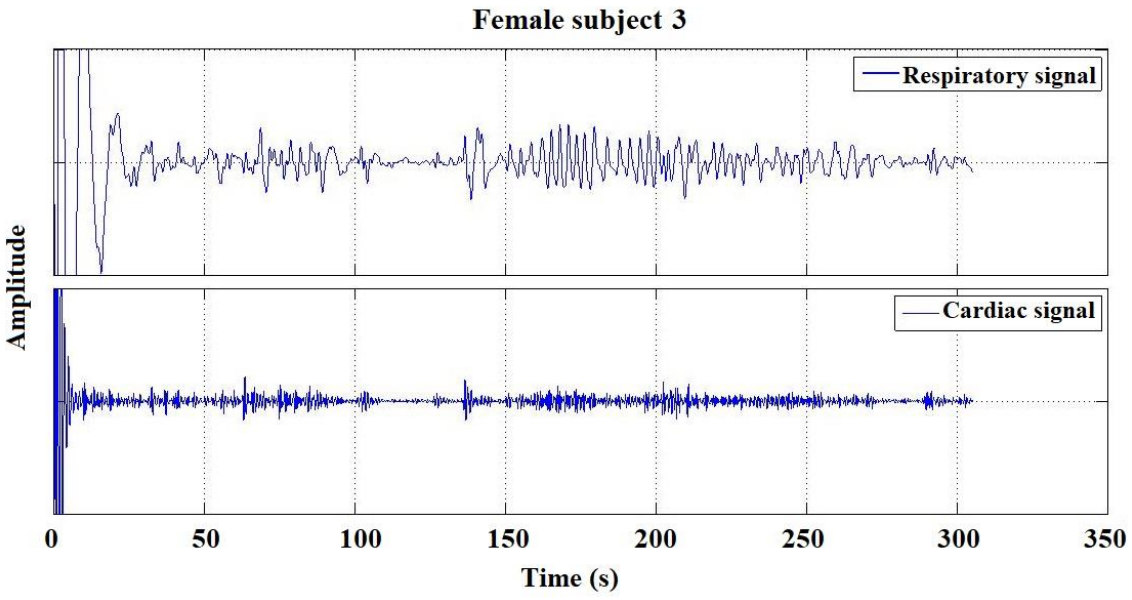
Female subject 3
Respiratory signal
Cardiac signal
Amplitude
0
50
100
150
200
250
300
350
Time (s)

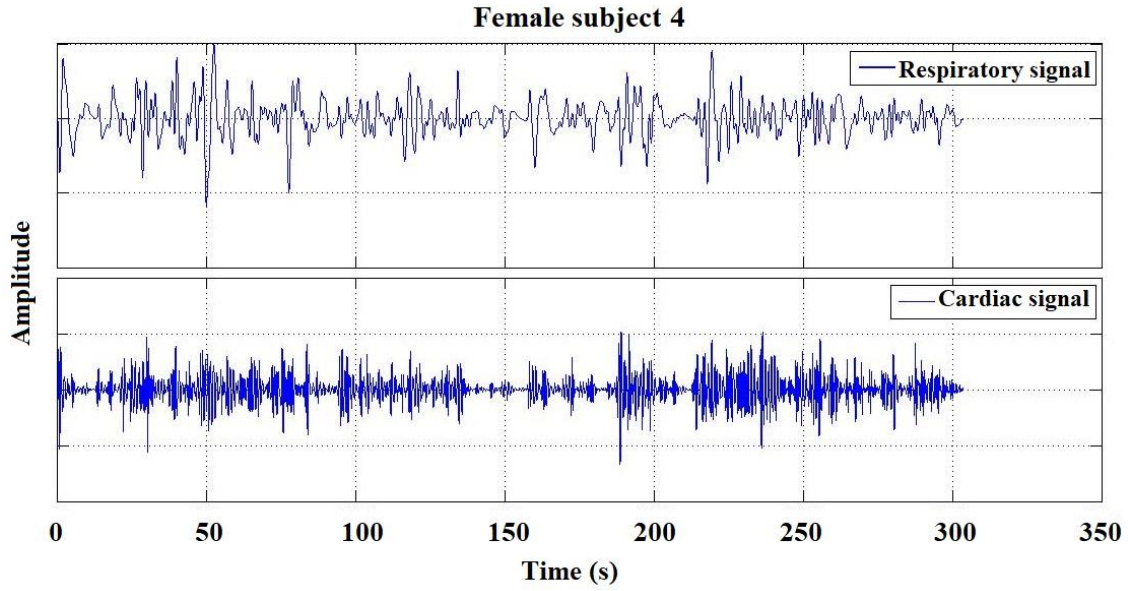
Female subject 4
Respiratory signal
Cardiac signal
Amplitude
0
50
100
150
200
250
300
350
Time (s)

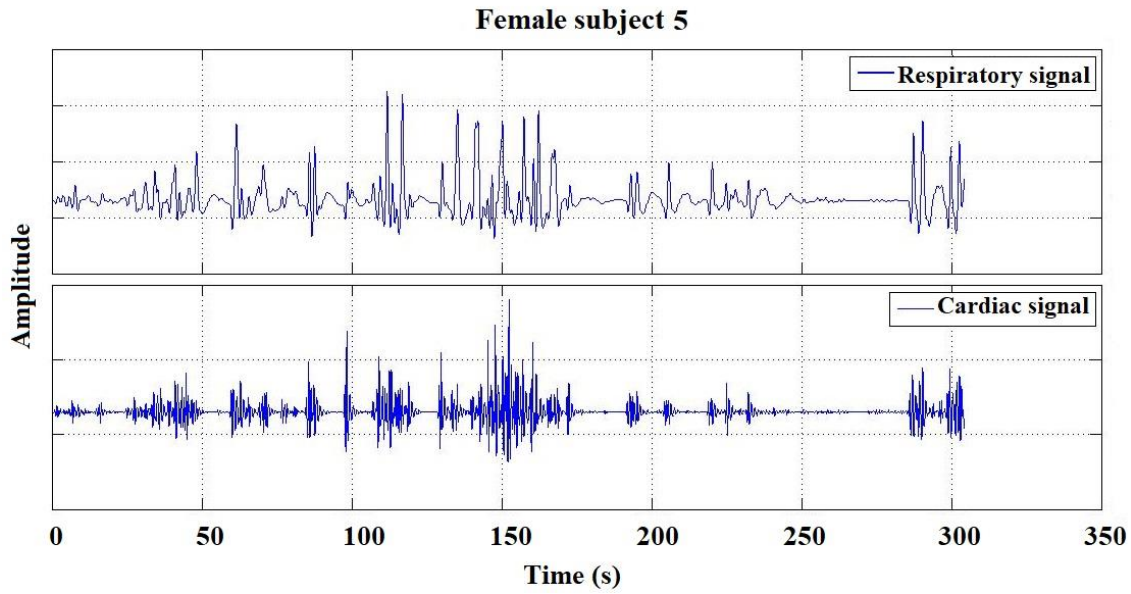
Female subject 5
Respiratory signal
Cardiac signal
Amplitude
0
50
100
150
200
250
300
350
Time (s)

Appendix G: Matlab programme for cardiorespiratory signal peak justification and validation

```
clear all
%%%%%%%%%%%%%%%%%%%%%%%%%%
hdata=xlsread('heart resistance.xlsx',2);
bdata=xlsread('breathing resistance.xlsx',2);
pdata=xlsread('plux data.xlsx');
%%%%%%%%%%%%%%%%%%%%%%%%%%
figure
 subplot(3,1,1);
 [ph,lh]=findpeaks(hdata(:,2),'minpeakdistance',35);
plot(hdata(:,1),hdata(:,2),'b',hdata(lh,1),ph,'dr');
 subplot(3,1,2);
 [pph,lph]=findpeaks(pdata(:,3),'minpeakdistance',200);
 plot(pdata(:,1),pdata(:,3),'b',pdata(lph,1),pph,'or');
 subplot(3,1,3);
 [ax,H1,H2]=plotyy(hdata(lh,1),ph,pdata(lph,1),pph,'stem','stem');
 set(H1,'marker','d','markeredgecolor','b'); set(H2,'marker','o','markeredgecolor','r');
 figure
 subplot(3,1,1);
```

```
 [pb,lb]=findpeaks(bdata(:,2),'minpeakdistance',300);
plot(bdata(:,1),bdata(:,2),'b',bdata(lb,1),pb,'dr')
 subplot(3,1,2);
[ppb,lpb]=findpeaks(pdata(:,4),'minpeakdistance',900);
 plot(pdata(:,1),pdata(:,4),'b',pdata(lpb,1),ppb,'or');
 subplot(3,1,3);
 [ax,H1,H2]=plotyy(bdata(lb,1),pb,pdata(lpb,1),ppb,'stem','stem');
 set(H1,'marker','d','markeredgecolor','b'); set(H2,'marker','o','markeredgecolor','r');
```

Appendix H: Matlab programme for creating the empirical models

```
clear all

figure

% sensor area in [16 9 4 1]

x=xlsread('Book_XYZ.xlsx',1);

% pressure in 0 1 2 5 10 15 20 25 30 35 40 45 50 55 60 65 70 75 80 85 90 95 100]

y=xlsread('Book_XYZ.xlsx',2); );

%Conductance/Resistivity/Sensitivity

z=xlsread('Book_XYZ.xlsx',3);

% Creating meshgrid

Xq=0:1:16;

Yq=0:1:100;

[Xq,Yq] = meshgrid(Xq,Yq);

zq=interp2(x,y,z,Xq,Yq,'cubic');


surf(Xq,Yq,zq/1000)

shading interp
```

Appendix I: Data points used to calculate empirical models and their verifications

Sensitivity (Ohm g^{-1} cm^2)	Sensor area (cm^2)				Verification
Pressure (g/cm^2)	16	9	4	1	12.25
1	0.9921646	2.008301	1.238915	0.310229	0.507658
2	0.7157082	1.034271	0.687656	0.168826	0.493965
5	0.364934467	0.505023	0.440004	0.260687	0.325207
10	0.11618272	0.222753	0.195382	0.190289	0.145122
15	0.08206324	0.057246	0.122952	0.092004	0.066036
20	0.05055672	0.085719	0.070833	0.082131	0.05677
25	0.03425684	0.0454	0.050559	0.062952	0.040179
30	0.03578908	0.045678	0.027096	0.055817	0.030056
35	0.0300208	0.034405	0.012965	0.040833	0.012044
40	0.0314078	0.031596	0.042551	0.037984	0.027793
45	0.02122028	0.03	0.0386	0.022594	0.026711
50	0.02083748	0.02544	0.02135	0.015571	0.006017
55	0.0120082	0.012086	0.018041	0.013751	0.011444
60	0.01984812	0.019935	0.004125	0.016438	0.010411
65	0.0096464	0.01188	0.038149	0.018262	0.009856
70	0.01187044	0.018506	0.026605	0.007738	0.013006
75	0.01197584	0.011428	0.007638	0.010174	0.013284
80	0.00980788	0.019021	0.009169	0.027157	0.00102
85	0.0092272	0.011275	0.023846	0.006582	0.004708
90	0.01215812	0.00258	0.015189	0.008451	0.021413
95	0.00868184	0.021476	0.008641	0.011054	0.007312
100	0.00691996	0.009243	0.008486	0.005915	0.002167

Conductance (S)	Sensor area (cm^2)				Verification
Pressure (g/cm^2)	16	9	4	1	12.25
0	0.047634064	0.019788	0.01848	0.016953	0.035279
1	0.049996962	0.01991	0.019192	0.017317	0.035922
2	0.051852409	0.019977	0.019581	0.017526	0.036571
5	0.054973135	0.020294	0.02018	0.017941	0.037924
10	0.056786594	0.020694	0.020644	0.018261	0.038997
15	0.058141314	0.020893	0.020766	0.018468	0.039506
20	0.059008573	0.021073	0.020953	0.01859	0.039954
25	0.059611076	0.021214	0.021053	0.018678	0.040277
30	0.060253811	0.02134	0.021155	0.018725	0.040522
35	0.060803741	0.021434	0.021232	0.018748	0.040621
40	0.061389926	0.021521	0.021714	0.018823	0.040852
45	0.061792414	0.021574	0.021348	0.018892	0.041076
50	0.062192811	0.02161	0.021407	0.01893	0.041127
55	0.062425917	0.021642	0.021434	0.018962	0.041224
60	0.062815068	0.021681	0.02148	0.018955	0.041313
65	0.063005957	0.021724	0.021508	0.019024	0.041397
70	0.063242455	0.021742	0.02155	0.019072	0.041509
75	0.063482858	0.021766	0.021577	0.01909	0.041623
80	0.063681108	0.021831	0.021621	0.019102	0.041632
85	0.063868754	0.021846	0.021648	0.019146	0.041673
90	0.064117698	0.021826	0.021654	0.019174	0.04186
95	0.064296655	0.021853	0.021704	0.01919	0.041924
100	0.064440012	0.021867	0.021726	0.019205	0.041943

Resistivity (Ohm m)	Sensor area (cm^2)				Verification
Pressure (g/cm^2)	16	9	4	1	12.25
0	14.83631081	21.51104	10.42136	2.232176	15.33731
1	15.10222204	21.93823	10.54896	2.232571	15.75898
2	15.28131864	22.37549	10.73352	2.234308	16.06153
5	15.82063498	23.53765	11.10785	2.231587	16.72814
10	16.27512617	24.91957	11.56217	2.235243	17.58252
15	16.40821779	26.12655	11.88712	2.253666	18.29145
20	17.23858396	26.97887	12.18157	2.267359	18.83338
25	17.94668044	27.80783	12.44004	2.281071	19.3311
30	18.52395365	28.53578	12.68969	2.29358	19.79962
35	19.06339892	29.21742	12.93523	2.307686	20.30183
40	19.54119489	29.85352	13.12182	2.320333	20.69684
45	20.04508427	30.49899	13.30009	2.335485	21.086
50	20.52151177	31.09763	13.48483	2.350924	21.54435
55	21.64352039	31.71933	13.66551	2.365812	21.96898
60	22.0952327	32.31258	13.8686	2.379117	22.39111
65	22.62216293	32.90587	14.01144	2.391308	22.80727
70	23.13172846	33.46357	14.1587	2.405544	23.20758
75	23.64952515	34.05084	14.32524	2.418235	23.60421
80	24.17929648	34.60735	14.49117	2.426175	24.05664
85	24.72502118	35.18534	14.62827	2.439067	24.4894
90	25.26391684	35.78491	14.77244	2.45547	24.84576
95	25.85298398	36.33197	14.9267	2.465947	25.27601
100	26.25604946	36.74624	15.02395	2.473737	25.5863